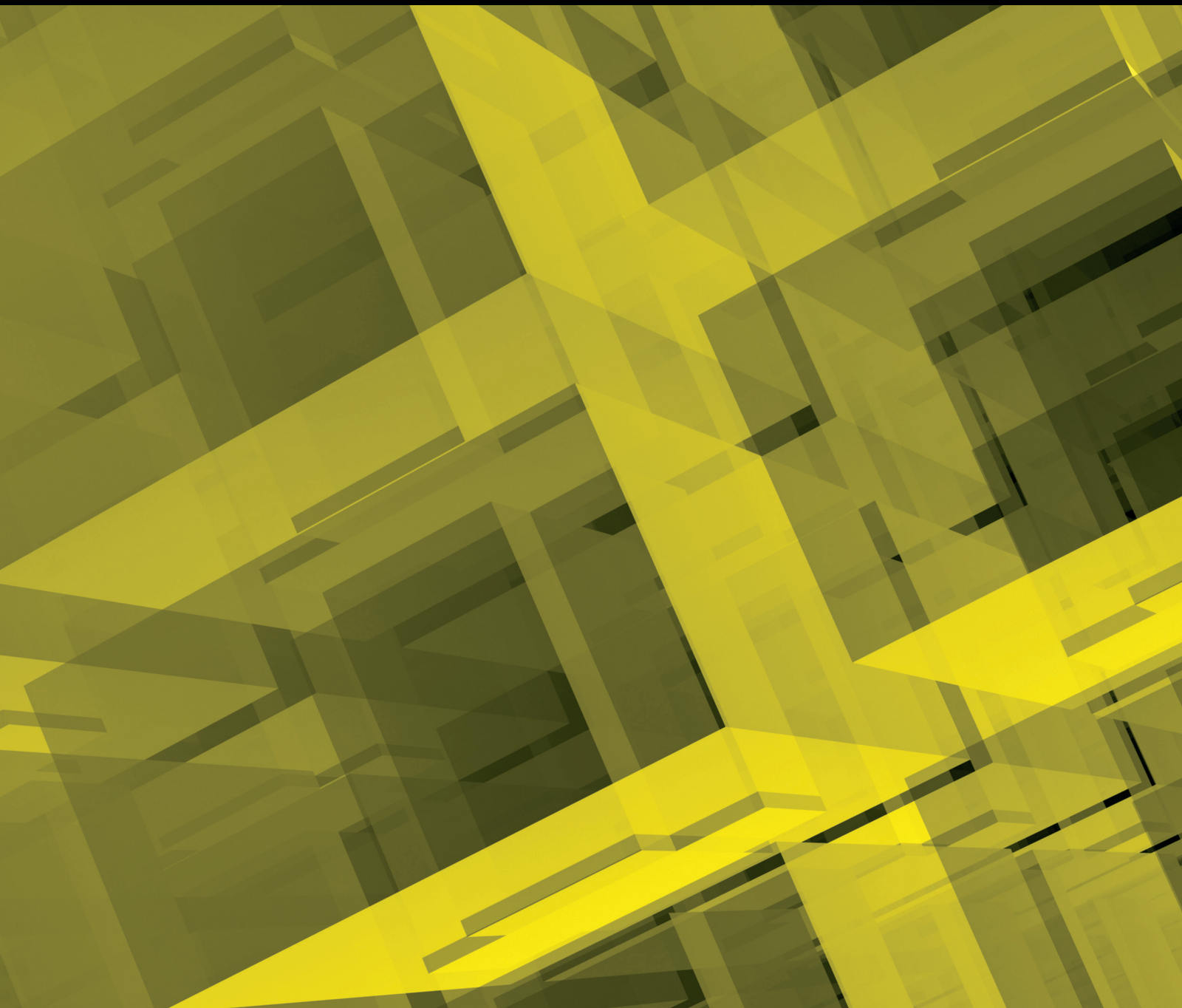


Advanced Techniques in Computational Mechanics

Guest Editors: Luís Godinho, Daniel Dias-da-Costa, António Tadeu,
and Delfim Soares Jr.





Advanced Techniques in Computational Mechanics

Journal of Applied Mathematics

Advanced Techniques in Computational Mechanics

Guest Editors: Luís Godinho, Daniel Dias-da-Costa,
António Tadeu, and Delfim Soares Jr.



Copyright © 2014 Hindawi Publishing Corporation. All rights reserved.

This is a special issue published in “Journal of Applied Mathematics.” All articles are open access articles distributed under the Creative Commons Attribution License, which permits unrestricted use, distribution, and reproduction in any medium, provided the original work is properly cited.

Editorial Board

Saeid Abbasbandy, Iran
Mina B. Abd-El-Malek, Egypt
Mohamed A. Abdou, Egypt
Subhas Abel, India
Carlos J. S. Alves, Portugal
Mohamad Alwash, USA
Igor Andrianov, Germany
Sabri Arik, Turkey
Ali R. Ashrafi, Iran
Francis T.K. Au, Hong Kong
Olivier Bahn, Canada
Antonio Bandera, Spain
Roberto Barrio, Spain
Alfredo Bellen, Italy
Jafar Biazar, Iran
Anjan Biswas, Saudi Arabia
Stephane P.A. Bordas, USA
James Robert Buchanan, USA
Alberto Cabada, Spain
Xiao Chuan Cai, USA
Zhenfu Cao, China
Jinde Cao, China
Yijia Cao, China
Alexandre Carvalho, Brazil
Song Cen, China
Tai-Ping Chang, Taiwan
Wei-Der Chang, Taiwan
Shih-sen Chang, China
Xinkai Chen, Japan
Rushan Chen, China
Ke Chen, UK
Jin Cheng, China
Eric Cheng, Hong Kong
Ching-Hsue Cheng, Taiwan
Qi Cheng, USA
Francisco Chiclana, UK
Jen-Tzung Chien, Taiwan
Han H. Choi, Republic of Korea
S. H. Chowdhury, Malaysia
Hung-Yuan Chung, Taiwan
Carlos Conca, Chile
Vitor Costa, Portugal
Livija Cveticanin, Serbia
Orazio Descalzi, Chile
Kai Diethelm, Germany

Urmila Diwekar, USA
Vit Dolejsi, Czech Republic
Bo-Qing Dong, China
Magdy A. Ezzat, Egypt
Meng Fan, China
Ya Ping Fang, China
Didier Felbacq, France
Antonio J. M. Ferreira, Portugal
Michel Fliess, France
Marco A. Fontelos, Spain
Huijun Gao, China
Xin-Lin Gao, USA
B. J. Geurts, The Netherlands
Pablo González-Vera, Spain
Laurent Gosse, Italy
Keshlan S. Govinder, South Africa
Jose L. Gracia, Spain
Zhi-Hong Guan, China
Nicola Guglielmi, Italy
Kerim Guney, Turkey
Vijay Gupta, India
Saman K. Halgamuge, Australia
Abdelmagid S. Hamouda, Qatar
Maoan Han, China
Bo Han, China
Pierre Hansen, Canada
Ferenc Hartung, Hungary
Xiao-Qiao He, China
Luis J. Herrera, Spain
Ying Hu, France
Ning Hu, Japan
Jianguo Huang, China
Dan Huang, China
Zhilong L. Huang, China
Gerardo Iovane, Italy
Anuar Ishak, Malaysia
Takeshi Iwamoto, Japan
George Jaiani, Georgia
Zhongxiao Jia, China
Xing Jin, China
Zhen Jin, China
Zlatko Jovanoski, Australia
Tadeusz Kaczorek, Poland
Ido Kanter, Israel
Abdul Hamid Kara, South Africa

Hamid Reza Karimi, Norway
Dogan Kaya, Turkey
Chaudry Masood Khaliq, South Africa
Khalil Khanafer, USA
Hyunsung Kim, Korea
Younjea Kim, Republic of Korea
Jong Hae Kim, Republic of Korea
Kazutake Komori, Japan
Vadim A. Krysko, Russia
Jin L. Kuang, Singapore
Miroslaw Lachowicz, Poland
Hak-Keung Lam, UK
Tak-Wah Lam, Hong Kong
Peter G L Leach, Cyprus
Jaehong Lee, Republic of Korea
Jinsong Leng, China
Edson D. Leonel, Brazil
Xiang Li, China
Yongkun Li, China
Wan-Tong Li, China
Jin Liang, China
Ching-Jong Liao, Taiwan
Chong Lin, China
Yansheng Liu, China
Shutian Liu, China
Kang Liu, USA
Weiqing Liu, China
Chongxin Liu, China
Chein-Shan Liu, Taiwan
Tao Liu, China
Zhijun Liu, China
Fei Liu, China
Jose L. López, Spain
Shiping Lu, China
Hongbing Lu, China
Li Ma, China
Ruyun Ma, China
Nazim I. Mahmudov, Turkey
Oluwole Daniel Makinde, South Africa
Francisco J. Marcellán, Spain
Guiomar Martín-Herrán, Spain
Nicola Mastronardi, Italy
Panayotis Takis Mathiopoulos, Greece
Michael McAleer, The Netherlands
Stephane Metens, France

Michael Meylan, Australia
Alain Miranville, France
Ram N. Mohapatra, USA
Cristinel Mortici, Romania
Jaime E. Munoz Rivera, Brazil
Javier Murillo, Spain
Roberto Natalini, Italy
Srinivasan Natesan, India
Roger Ohayon, France
Javier Oliver, Spain
Donal O'Regan, Ireland
M. Ostoj-Starzewski, USA
Turgut Öziş, Turkey
Claudio Padra, Argentina
R. M. Palhares, Brazil
Francesco Pellicano, Italy
Juan Manuel Peña, Spain
Ricardo Perera, Spain
Malgorzata Peszynska, USA
Allan C. Peterson, USA
Vu Ngoc Phat, Vietnam
Andrew Pickering, Spain
Hector Pomares, Spain
Mario Primicerio, Italy
Morteza Rafei, The Netherlands
Laura Rebollo-Neira, UK
Roberto Renò, Italy
Ignacio Rojas, Spain
Carla Roque, Portugal
Debasish Roy, India
Samir Saker, Egypt
Miguel A. F. Sanjuan, Spain
Wolfgang Schmidt, Germany
Mehmet Sezer, Turkey
Naseer Shahzad, Saudi Arabia
Hui-Shen Shen, China

Jian Hua Shen, China
Yong Shi, China
Yasuhide Shindo, Japan
Patrick Siarry, France
Fernando Simões, Portugal
Theodore E. Simos, Greece
Francesco Soldovieri, Italy
A.-M. A. Soliman, Egypt
Qiankun Song, China
Xinyu Song, China
Yuri N. Sotskov, Belarus
Niclas Strömberg, Sweden
Ray K.L. Su, Hong Kong
Chengjun Sun, USA
Jitao Sun, China
Wenyu Sun, China
Ying Tan, China
XianHua Tang, China
San-Yi Tang, China
Zhidong Teng, China
Engang Tian, China
Alexander Timokha, Norway
Mariano Torrisi, Italy
Jung-Fa Tsai, Taiwan
Ch. Tsitouras, Greece
Kuppalapalle Vajravelu, USA
Alvaro Valencia, Chile
Erik Van Vleck, USA
Ezio Venturino, Italy
Jesus Vigo-Aguiar, Spain
Michael N. Vrahatis, Greece
Yaonan Wang, China
Mingxin Wang, China
Guangchen Wang, China
Qing-Wen Wang, China
Baolin Wang, China

Junjie Wei, China
Li Weili, China
Martin Weiser, Germany
Frank Werner, Germany
Shanhe Wu, China
Shi-Liang Wu, China
Yonghui Xia, China
Tiecheng Xia, China
Gongnan Xie, China
Daoyi Xu, China
Yuesheng Xu, USA
Chao Yan, USA
Chao Yang, China
Suh-Yuh Yang, Taiwan
Her-Terng Yau, Taiwan
Guan H. Yeoh, Australia
Bo Yu, China
Xiaohui Yuan, China
Jinyun Yuan, Brazil
Guisheng Zhai, Japan
Jianming Zhan, China
Jian-gang Zhang, China
Jifeng Zhang, China
Heping Zhang, China
Zhihua Zhang, China
Sheng Zhang, China
Liang Zhang, China
Jingxin Zhang, Australia
Chongbin Zhao, Australia
Shan Zhao, USA
Renat Zhdanov, USA
Bin Zhou, China
Goangseup Zi, Korea
J. D. Hoenderkamp, The Netherlands

Contents

Advanced Techniques in Computational Mechanics, Luís Godinho, Daniel Dias-da-Costa, António Tadeu, and Delfim Soares Jr.

Volume 2014, Article ID 785181, 2 pages

Numerical Study on the Charge Transport in a Space between Concentric Circular Cylinders,

Y. K. Suh and K. H. Baek

Volume 2014, Article ID 340916, 18 pages

A Numerical Scheme Based on an Immersed Boundary Method for Compressible Turbulent Flows with Shocks: Application to Two-Dimensional Flows around Cylinders, Shun Takahashi, Taku Nonomura, and Kota Fukuda

Volume 2014, Article ID 252478, 21 pages

Numerical Treatment of a Modified MacCormack Scheme in a Nondimensional Form of the Water Quality Models in a Nonuniform Flow Stream, Nopparat Pochai

Volume 2014, Article ID 274263, 8 pages

Eddy Heat Conduction and Nonlinear Stability of a Darcy Lapwood System Analysed by the Finite Spectral Method, Jónas Eliasson

Volume 2014, Article ID 695425, 10 pages

An Overview of Recent Advances in the Iterative Analysis of Coupled Models for Wave Propagation,

D. Soares Jr. and L. Godinho

Volume 2014, Article ID 426283, 21 pages

Experiment and Application of Market-Based Control for Engineering Structures, Gang Li, Wen Wang, and Hong-Nan Li

Volume 2013, Article ID 219537, 12 pages

The Numerical Solution of Linear Sixth Order Boundary Value Problems with Quartic B-Splines,

Mingzhu Li, Lijuan Chen, and Qiang Ma

Volume 2013, Article ID 962165, 7 pages

A Conjugate Gradient Method with Global Convergence for Large-Scale Unconstrained Optimization Problems, Shengwei Yao, Xiwen Lu, and Zengxin Wei

Volume 2013, Article ID 730454, 9 pages

Path Transmissibility Analysis Considering Two Types of Correlations in Hydropower Stations,

Baoping Zhi and Zhenyue Ma

Volume 2013, Article ID 802546, 9 pages

Editorial

Advanced Techniques in Computational Mechanics

Luís Godinho,¹ Daniel Dias-da-Costa,^{2,3} António Tadeu,¹ and Delfim Soares Jr.⁴

¹ CICC, Department of Civil Engineering, University of Coimbra, 3030-788 Coimbra, Portugal

² School of Civil Engineering, The University of Sydney, NSW 2006, Australia

³ INESCC, Department of Civil Engineering, University of Coimbra, 3030-788 Coimbra, Portugal

⁴ Structural Engineering Department, Federal University of Juiz de Fora, 36036-330 Juiz de Fora, MG, Brazil

Correspondence should be addressed to Luís Godinho; lgodinho@dec.uc.pt

Received 9 April 2014; Accepted 9 April 2014; Published 17 April 2014

Copyright © 2014 Luís Godinho et al. This is an open access article distributed under the Creative Commons Attribution License, which permits unrestricted use, distribution, and reproduction in any medium, provided the original work is properly cited.

Computational mechanics has suffered significant developments in the last decades. Novel numerical models have been proposed to model solid and fluid problems, as well as to deal with solid-fluid interaction. Many of these methods are based in a spatial description of the model by points (such as in Meshless methods) or in enrichment strategies of the classic finite element method (such as in the GFEM, XFEM, or EFEM). In many cases, these methods became more efficient and accurate than classical formulations and are very competitive in applied mechanics. All contributions included in this special issue address this challenging and broad topic that we, as editors, have the pleasure to share with the readers. We would like to thank all the authors for their commitment in this issue, as well as the reviewers for their critical and detailed assessment.

This special issue is composed of eight research papers and one review paper. The covered subjects are very broad, including topics such as fluid mechanics, solid mechanics, and optimization problems. Below, a very brief overview of the featured works is given.

The “*Numerical study on the charge transport in a space between concentric circular cylinders*,” by Y. K. Suh and K. H. Baek, addresses what the authors call essential elements of numerical solution methods for the charge transport equations. The authors argue on the uttermost importance of maintaining the conservation property in convective terms because of the numerical accuracy, in particular at low reaction rates.

In the work entitled “*A numerical scheme based on an immersed boundary method for compressible turbulent flows with shocks: application to two-dimensional flows around*

cylinders,” S. Takahashi et al. develop a computational code adopting immersed boundary methods for compressible gas-particle multiphase turbulent flows. A second-order pseudo skew-symmetric form with minimum dissipation models the turbulent flow region, while the monotone upstream-centred scheme for conservation laws scheme is employed in the shock region.

The paper by N. Pochai, entitled “*Numerical treatment of a modified MacCormack scheme in a nondimensional form of the water quality models in a nonuniform flow stream*,” makes use of two mathematical models to simulate water quality in a nonuniform flow stream. The author proposes an alteration to the MacCormack method that is more accurate than the classic method, without a significant loss of computational efficiency.

The work by J. Eliasson, entitled “*Eddy heat conduction and nonlinear stability of a Darcy Lapwood system analysed by the finite spectral method*,” proposes a finite Fourier transform to perform linear and nonlinear stability analyses of a Darcy-Lapwood system of convective rolls. The author shows how many modes are unstable, the wave number instability band within each mode, the maximum growth rate (most critical) wave numbers on each mode, and the nonlinear growth rates for each amplitude as a function of the porous Rayleigh number.

In the paper “*Experiment and application of market-based control for engineering structures*,” by G. Li et al., an experimental study on the vibration control of a single-degree-of-freedom model is carried out to verify market-based control (MBC) strategy effect. The authors’ results reveal that the MBC strategy can reduce both displacement

and acceleration responses. Additionally, the authors apply the MBC strategy to a long-span bridge considering the travelling wave effect.

M. Li et al. propose a quartic B-spline method for solving linear sixth order boundary value problems in the paper entitled "*The numerical solution of linear sixth order boundary value Problems with quartic B-splines.*" Their method converts the boundary problem to solve a system of linear equations and obtains coefficients of the corresponding B-spline functions. Two numerical examples are used to verify the theoretical framework and validate the method.

The paper "*A conjugate gradient method with global convergence for large-scale unconstrained optimization problems,*" by S. Yao et al, proposes a conjugate gradient method that is similar to Dai-Liao conjugate gradient method, but with better convergence properties. This is shown using different test problems.

B. Zhi and Z. Ma, in the paper "*Path transmissibility analysis considering two types of correlations in hydropower stations,*" present their research on disturbance- and parameter-related transfer paths in a practical situation related to hydropower station units and powerhouses. The authors state that their results indicate that the proposed methods can efficiently reduce the disturbance range and accurately analyse the transfer paths of hydraulic-source vertical vibration in hydropower stations.

Finally, a review paper by D. Soares Jr. and L. Godinho, entitled "*An overview of recent advances in the iterative analysis of coupled models for wave propagation,*" presents an overview of the application of iterative procedures for coupling between different methods in wave propagation analysis. Both frequency- and time-domain analyses are addressed in acoustic, mechanical, and electromagnetic wave propagation problems.

Luís Godinho
Daniel Dias-da-Costa
António Tadeu
Delfim Soares Jr.

Research Article

Numerical Study on the Charge Transport in a Space between Concentric Circular Cylinders

Y. K. Suh and K. H. Baek

Department of Mechanical Engineering, Dong-A University, Busan 604-714, Republic of Korea

Correspondence should be addressed to Y. K. Suh; yksuh@dau.ac.kr

Received 8 October 2013; Accepted 10 February 2014; Published 27 March 2014

Academic Editor: Delfim Soares Jr.

Copyright © 2014 Y. K. Suh and K. H. Baek. This is an open access article distributed under the Creative Commons Attribution License, which permits unrestricted use, distribution, and reproduction in any medium, provided the original work is properly cited.

Electrification is one of the key factors to be considered in the design of power transformers utilizing dielectric liquid as a coolant. Compared with enormous quantity of experimental and analytical studies on electrification, numerical simulations are very few. This paper describes essential elements of numerical solution methods for the charge transport equations in a space between concentric cylinders. It is found that maintaining the conservation property of the convective terms in the governing equations is of the uttermost importance for numerical accuracy, in particular at low reaction rates. Parametric study on the charge transport on the axial plane of the annular space with a predetermined velocity shows that when the convection effect is weak the solutions tend to a one-dimensional nature, where diffusion is simply balanced by conduction. As the convection effect is increased the contours of charge distribution approach the fluid streamlines. Thus, when the conduction effect is weak, charge distribution tends to be uniform and the role of the convection effect becomes insignificant. At an increased conduction effect, on the other hand, the fluid motion transports the charge within the electric double layers toward the top and bottom boundaries leading to an increased amount of total charge in the domain.

1. Introduction

When a dielectric liquid containing impurities is in contact with a solid surface, a certain physicochemical process occurs at the interface yielding free ions near the surface of the liquid. Usually negative ions are adsorbed to the solid surface and the positive ions are diffused away forming the electric double layer (to be referred to as EDL). Since the positive ions are mobile, they are convected by the fluid flow giving rise to the streaming current, which is called flow electrification. Problem occurs when they are accumulated in a certain location downstream resulting in locally high electric-field intensity which can cause electrical discharge, breakdown, and local failure of the device employing the liquid transport.

Electrification becomes one of the key factors to be considered in the design of electrical devices utilizing dielectric liquid (mineral or ester oil) as a coolant, such as power transformers. Demand for increased capacity from the users of power transformers tempts designers to increase the oil flow rate for increased cooling capacity, which, however,

brings increased electrification and makes the device more susceptible to the electrical failure.

Studies on electrification and discharge with full-scale transformers were carried out by Higaki et al. [1, 2] and Tamura et al. [3]. They inserted numerous sensors to measure the charge distribution within transformers and measured the local leakage current through the solid surfaces. Higaki et al. [1, 2] demonstrated that the point of maximum electric field on the solid surface, calculated by solving the potential equation with the leakage currents being used as the boundary conditions, was consistent with the point of discharge actually observed from the experiment. Tamura et al. [3] presented a diagram in the parameter space where high flow rate was shown to lead to electrical discharge.

In order to perform more fundamental studies, researchers have considered simple experimental apparatus other than actual transformers, which is easier to build and easier to measure data with, such as electrical charge tendency (ECT). In addition, how to interpret the measured data in relation to the actual transformers is also an important

issue in selecting suitable geometries for study. Most of the initial studies focused on the flow between parallel plates and circular pipes [4–7]. A spinning disk system was used by Kedzia and Willner [8] and Gibbings [9] in their experimental and theoretical studies on electrification. In order to attain a fully developed flow in a compact space Washabaugh [10] and Washabaugh and Zahn [11, 12] used a circular Couette system. Moreau and Touchard [13] conducted an experimental study to show that an impinging jet can result in a surface current with an order of magnitude larger than that with the parallel flow. The swing cylinder system, where the inner cylinder shows back-and-forth rotation, was also used in [14] to study ECT.

With the simple flow apparatus in hand, researchers can perform investigations on the effect of various factors on the electrification independently. There are many factors influencing electrification or ECT. They can be categorized into two kinds, fluid/flow properties and electrical properties. Included in the former are flow rate, geometrical features determined by the fluid path, and fluid viscosity, while in the latter electrical conductivity and permittivity are the key elements; the operating temperature and material degradation may influence many of these properties, such as viscosity, conductivity and permittivity. Properties of the pressboard such as chemical composition of the material and surface roughness may also influence the ECT. General understanding of the effect of various parameters on ECT and design aspect for avoiding discharge in transformers was given in [15, 16].

Touchard [17] and Touchard [18] included detailed kinetics of wall surface reaction in the formulation of the charge flux through planar and circular duct to attain a reasonable matching with experimental data. Moreau et al. [19] measured ECT for a flow passing through a filter made of degraded pressboard to show that a degraded surface enhances the charge accumulation and that small amount of additive (i.e., BTA) can reduce ECT. The effect of additive was further studied in [20, 21], and by using a flow-loop apparatus, Bourgeois et al. [21] addressed the mechanism of the enhancement of ECT in terms of the carboxyl group. Aksamit and Zmarzly [22] also studied the inhibition of flow electrification with the additive C_{60} . Developing advanced models for the wall reaction that can well fit the experimental data is one of the most important issues in the study of electrification. Cabaleiro et al. [23] and El-Adawy et al. [24] for instance demonstrated that the wall-reaction constant must be varied depending on the other parameters such as flow rate in order to fit the experimental data. Cabaleiro et al. [25] performed analysis on ECT within a shallow rectangular duct with a more complex model for the wall reaction. Paillat et al. [26] showed that inclusion of the effect of the fluid shear stress in the physicochemical process at the interface provides a much better agreement with experimental data at high laminar Reynolds numbers. El-Adawy et al. [27] conducted numerical simulation for the foundation of EDL without the convection effect and calculated ECT in the presence of fluid flow with source terms representing the ion dissociation and recombination in the bulk. Kobayashi

et al. [28] paid attention to the competitive role of oil and pressboard in the electrification process. Okabe et al. [29] investigated the effect of the compounds in oil on ECT and showed that increase of ECT was mostly caused by the oxidation of sulfides. In [30], both the transient and steady-state data of the electrification experiment could be matched with the one-dimensional model for ion transport by using a hybrid boundary condition, where a constant flux as well as the flux proportional to the local ionic concentration was employed. Due to environmental problems, the electrical power industry considers using substitutive oils in transformers. Paillat et al. [31] investigated experimentally the electrification property of ester oil compared with conventional mineral oil, in particular in terms of ECT. They confirmed that charge accumulation with ester oil is one or two orders of magnitude larger than that with mineral oil.

Most studies on electrification even with simple geometry have been performed experimentally and/or analytically, and numerical studies, at least in a two-dimensional space, are very few. In [13], numerical simulation was performed for the impinging jet configuration by using the authors' in-house code. In [27], two-dimensional numerical simulation was performed to investigate the transient development of EDL and surface current by using comprehensive models incorporating ion dissociation and recombination of molecules not only in liquid but also in solid. The authors also included in their simulation the wall reaction model representing the combination of cation in the solid and anion in the fluid. In the second stage in their simulation they considered a fully developed parabolic velocity profile to investigate the time-dependent flow electrification. Their numerical results are qualitatively in line with experimental results and knowledge.

The main purpose of the present study is to develop a two-dimensional numerical code and perform simulations for charge transport in a confined space under a various range of parameters. In particular, we select as the computational domain the annulus between concentric cylinders, following [10–12]. We are concerned with the axisymmetric secondary flow developed on the axial plane at supercritical Reynolds numbers. One of the most important issues to be addressed in this study is the effect of nondimensional parameters on the numerical solutions as well as their accuracy. Aside from the one- and two-dimensional in-house codes, we also use the commercial software COMSOL and exact and approximate analytical solutions of the one-dimensional problem for verification of the numerical solutions. The present in-depth analysis of the characteristics of the equations governing the charge transport in relation to the numerical solutions may play an important role in the development of more practical simulation codes and in interpretation of the numerical results obtained either by an in-house or a commercial code.

2. Mathematical Formulation

We consider transport of a space charge density distributed in an annulus space between two concentric circular cylinders

of radii R_1 and R_2 , respectively, caused by diffusion, convection, and electrical conduction. The governing equations for the problem can be written as follows:

$$\frac{\partial q^*}{\partial t^*} + \nabla_* \cdot \mathbf{J}^* = 0, \quad (1a)$$

$$\nabla_* \cdot \varepsilon \mathbf{E}^* = q^*, \quad (1b)$$

$$\frac{\partial \mathbf{u}^*}{\partial t^*} + (\mathbf{u}^* \cdot \nabla_*) \mathbf{u}^* = -\frac{1}{\rho} \nabla_* p^* + \nu \nabla_*^2 \mathbf{u}^* + q^* \mathbf{E}^*, \quad (1c)$$

$$\nabla_* \cdot \mathbf{u}^* = 0, \quad (1d)$$

where t^* is the time, q^* the charge density, \mathbf{u}^* the fluid velocity, p^* the pressure, \mathbf{E}^* the electric field related to the electric potential ϕ^* as $\mathbf{E}^* = -\nabla_* \phi^*$, ∇_* the gradient operator, and

$$\mathbf{J}^* = -D \nabla_* q^* + q^* \mathbf{u}^* + \sigma \mathbf{E}^* \quad (2)$$

the current density (or charge flux). Further, ρ is the fluid density, ν the kinematic viscosity of the fluid, D the diffusivity of the species (i.e., charge carriers), σ the electrical conductivity, and ε the electrical permittivity, all of which are assumed to be constant in this study.

It is assumed that metals or pressboards in contact with dielectric liquid create charges (or they may be adsorbed) by certain chemical reaction, and we simply employ the model used in [10–12] dictating that the charge flux from the electrode surface to the liquid is proportional to the local space charge density, reading

$$J_r^* = -k_1^* (q^* - q_{1w}^*) \quad \text{at } r^* = R_1, \quad (3a)$$

$$J_r^* = k_2^* (q^* - q_{2w}^*) \quad \text{at } r^* = R_2, \quad (3b)$$

where J_r^* denotes the radial component of \mathbf{J}^* , q_{iw}^* the wall charge density at $r^* = R_i$ ($i = 1$ for the inner and $i = 2$ for the outer cylinder surface, resp.), and k_i^* the reaction rate at the surface i . Between the two cylinder surfaces, we could connect a resistor and/or apply a potential difference, but in this study we only consider a short circuit. So, the boundary conditions for the potential read

$$\phi^* = 0 \quad \text{at } r^* = R_1, \quad r^* = R_2. \quad (4)$$

We may apply no-slip and impermeable conditions on the solid walls surrounding the fluid. Boundary conditions on the upper and lower ends of the domain will be addressed after dimensionless equations are presented.

The fluid flow within the annulus can be assumed to be created by two kinds of forcing; one is by the rotation of the inner cylinder and the other by the so-called induced charge electroosmotic effect. While the former is driven by the boundary condition for the Navier-Stokes equation (1c), the latter comes from the last term in (1c), that is, the Coulomb-force term, which couples the fluid flow and the charge

transport problem. Apparently, the fluid velocity created by the two effects contributes to the convection of the charge, that is, the second term in (2).

As a first step in our series of studies on the charge transport within an annulus, we in this paper focus on steady and axisymmetric solutions. Then the azimuthal component of the fluid velocity does not contribute to the charge transport. Thus, even the circular Couette flow driven by the inner cylinder's rotation has no effect on the charge transport when it is stable, which is relevant at low Reynolds numbers exhibiting only the primary azimuthal flow (referred to as steady circular Couette flow; see, e.g., Liao et al. [32]); here, the Reynolds number may be based on the tangential velocity of the inner cylinder and the gap between the two cylinders, $d \equiv R_2 - R_1$. As the Reynolds number is increased, the primary flow becomes unstable and creates a secondary flow in the axial plane (referred to as “steady axisymmetric Taylor vortex flow”; Liao et al. [32]), which now plays an important role in the convective transport of charge. It is this type of flow that is used in the calculation of the convective terms in the charge transport equation (1a); for more complex supercritical flow regimes in the circular Couette flow system, such as nonaxisymmetric flow and travelling waves, one can refer to Koschmieder [33].

In the present study, convection due to the induced charge electroosmotic flow effect is assumed to be negligible compared with the effect of the secondary flow caused by the flow instability mentioned above following El-Adawy et al. [27]. This is valid in particular at low diffusivity of the charge carriers, D . Thus, we can decouple the fluid flow from the charge transport problem and are allowed to impose an arbitrary velocity field (but without losing the physical relevance, of course).

Based on the above reasoning, we can write the governing equations for the dimensionless charge density q and the dimensionless potential ϕ in dimensionless form as follows:

$$\begin{aligned} & - \left[\frac{1}{r} \frac{\partial}{\partial r} \left(r \frac{\partial q}{\partial r} \right) + \frac{\partial^2 q}{\partial z^2} \right] + P \left[\frac{1}{r} \frac{\partial}{\partial r} (ruq) + \frac{\partial}{\partial z} (wq) \right] + Qq \\ & = 0, \end{aligned} \quad (5a)$$

$$\frac{1}{r} \frac{\partial}{\partial r} \left(r \frac{\partial \phi}{\partial r} \right) + \frac{\partial^2 \phi}{\partial z^2} = -q. \quad (5b)$$

Here, $(r, z) = (r^*, z^*)/d$, $(u, w) = (u^*, w^*)/U$, $q = q^*/q_{1w}^*$, $\phi = \phi^*/[d^2 q_{1w}^*/\varepsilon]$, and $\mathbf{E} = -\nabla \phi = \mathbf{E}^*/[dq_{1w}^*/\varepsilon]$ are dimensionless variables. Further, we define $\mathbf{J} = \mathbf{J}^*/(Dq_{1w}^*/d)$. The dimensionless parameters $P = Ud/D$ and $Q = \sigma d^2/(\varepsilon D)$ may be considered as the ratio of time scales; $P = \tau_{\text{dif}}/\tau_{\text{conv}}$ and $Q = \tau_{\text{dif}}/\tau_{\text{cond}}$, where $\tau_{\text{dif}} \equiv d^2/D$ is the diffusion time scale, $\tau_{\text{conv}} \equiv d/U$ the convection time scale, and $\tau_{\text{cond}} \equiv \varepsilon/\sigma$ the conduction time scale.

Boundary conditions for q can be written in terms of the dimensionless radial component of the charge flux, $J_r \equiv -\partial q/\partial r - Q\partial\phi/\partial r$, as follows:

$$J_r = -k_1 (q - 1) \quad \text{at } r = r_1, \quad (6a)$$

$$J_r = k_2 (q - q_{2w}) \quad \text{at } r = r_2, \quad (6b)$$

where $k_i = k_i^*/(D/d)$, $r_i = R_i/d$, and $q_{2w} = q_{2w}^*/q_{1w}^*$; note that $q_{1w} = 1$. Boundary conditions for ϕ are simply

$$\phi = 0 \quad \text{at } r = r_1, r = r_2. \quad (7)$$

As for the conditions on the upper and lower boundaries we apply zero gradient for q and ϕ :

$$\frac{\partial q}{\partial z} = \frac{\partial \phi}{\partial z} = 0 \quad \text{at } z = 0, z = h, \quad (8)$$

where h corresponds to the dimensionless height of the domain, that is, the recirculating flow cell, whose dimensional quantity is defined as H ; that is, $h = H/d$. In this study h is set as $H = d$ or $h = 1$.

The fact that ϕ does not explicitly appear in (5a) may mislead to the conclusion that (5a) is decoupled from (5b), but it is not the case because it appears in boundary conditions (6a) and (6b).

3. Analytic Solutions of 1D Transport Equation

When the convection effect is neglected, we may well assume, in view of the boundary conditions, that solutions are independent of z . Then the system of equations reduces to a one-dimensional transport problem, where only the diffusion and conduction effects are present:

$$\frac{d^2 q}{dr^2} + \frac{1}{r} \frac{dq}{dr} - Qq = 0, \quad (9a)$$

$$\frac{d^2 \phi}{dr^2} + \frac{1}{r} \frac{d\phi}{dr} + q = 0. \quad (9b)$$

The general solution to (9a) takes the following form:

$$q = C_1 I_0 \left(\frac{r}{\lambda} \right) + C_2 K_0 \left(\frac{r}{\lambda} \right), \quad (10)$$

where I_0 and K_0 denote the modified Bessel function of the first and second kind, respectively, of order zero, and $\lambda = 1/\sqrt{Q}$ corresponds to the dimensionless thickness of EDL adjacent to the cylinder surfaces where charge is mainly distributed. Eliminating the third terms on the left-hand side of (9a) and (9b) and integrating the result twice with respect to r yield

$$\phi = -\lambda^2 q - C_3 \ln r + C_4. \quad (11)$$

Four constants, C_1 through C_4 , in (10) and (11) can be obtained from the boundary conditions (6a), (6b), and (7) as follows:

$$\begin{aligned} C_1 &= \frac{-K_{02} + K_{01}q_{2w} + [(K_{02}/s_1 + K_{01}/s_2)/\lambda^2] C_3}{I_{02}K_{01} - I_{01}K_{02}}, \\ C_2 &= \frac{I_{02} - I_{01}q_{2w} - [(I_{02}/s_1 + I_{01}/s_2)/\lambda^2] C_3}{I_{02}K_{01} - I_{01}K_{02}}, \\ C_3 &= \frac{s_1 s_2 \lambda^2 (1 - q_{2w})}{s_1 s_2 \ln(r_2/r_1) + s_1 + s_2}, \\ C_4 &= \frac{\lambda^2 [s_1 s_2 \ln(r_2/r_1) + s_1 + s_2 q_{2w}]}{s_1 s_2 \ln(r_2/r_1) + s_1 + s_2}, \end{aligned} \quad (12)$$

where $s_i = k_i r_i$, $I_{0i} = I_0(r_i/\lambda)$, and $K_{0i} = K_0(r_i/\lambda)$ are constants.

For the case with $\lambda \ll 1$, we are allowed to approximate the governing equations and obtain the solutions in terms of more familiar functions. We let $q = f(r)/\sqrt{r}$ and then (9a) becomes

$$\frac{d^2 f}{dr^2} - \left(\frac{1}{\lambda^2} - \frac{1}{4r^2} \right) f = 0. \quad (13)$$

Under the assumption of $\lambda \ll r$ (thin-layer approximation), we can ignore the second term in the bracket. Solving the resultant equation is straight forward, and we arrive at

$$q = \frac{1}{\sqrt{r}} \left\{ \frac{q_1 \sqrt{r_1} \sinh[(r_2 - r)/\lambda]}{\sinh(1/\lambda)} + \frac{q_2 \sqrt{r_2} \sinh[(r - r_1)/\lambda]}{\sinh(1/\lambda)} \right\}, \quad (14)$$

where the unknown constant q_i stands for the value of q at $r = r_i$. Solution (14) is shown to be the same as that provided in [10]. In fact, the solution form (14) can also be derived from the leading order terms in the asymptotic expansion of I_0 and K_0 in (10) for large argument [34]. Equation (11) is still used for obtaining ϕ after q is obtained from (14). Applying boundary conditions (6a), (6b), and (7), we get

$$q_1 = 1 - \frac{(1 - q_{2w})}{s_1 B}, \quad (15a)$$

$$q_2 = q_{2w} + \frac{(1 - q_{2w})}{s_2 B}, \quad (15b)$$

where $B = (s_1 + s_2)/(s_1 s_2) + \ln(r_2/r_1)$.

4. Numerical Solutions of Full 2D Transport Equations

When the velocity field is arbitrarily imposed, we must use numerical methods to solve the 2D charge transport problem

governed by (5a) and (5b) under the boundary conditions (6a)–(8). We performed two kinds of numerical simulation, one using a self-developed (in-house) code and the other using the commercial code COMSOL.

We briefly address first the numerical method employed in the in-house code. Although the steady-state solutions are our primary concern, we add the transient term to the left-hand side of (5a) in order to facilitate the relaxation method. There are two key factors in developing the numerical schemes which must be borne in mind for the successful run of the simulation, numerical instability and accuracy. When convection is dominant, as is common in engineering applications, the convection terms themselves become the primary cause of the numerical instability when the central difference schemes are used. For this reason, in this study we employed the second-order upwind method to discretize the convection terms. Secondly, numerical accuracy can be maintained by constructing a variable grid system. Another key factor affecting numerical accuracy turns out to be the conservation property of the numerical schemes employed for discretization of the equations. Using the conservative form of the convection terms and employing the finite volume method in discretization turns out to be of the uttermost importance for maintaining the numerical accuracy.

Since λ usually remains very small, we expect thin layers, that is, EDLs, near the surfaces $r = r_1$ and $r = r_2$. To resolve such thin layers, we construct fine grids there. Along the radial direction, for instance, we use the algebraic function

$$r = r_1 + \frac{[3 + 2a_r \xi (3 - 2\xi)] \xi}{3 + 2a_r} \quad (16)$$

for the range $0 \leq \xi \leq 1$, where a_r is a control parameter for the variable grid along the radial direction; the case with $a_r = 0$ corresponds to no grid refinement and a larger value of a_r means finer grids near the surfaces. Usually we take $a_r = 3$ or larger. We use a similar function for the variable grids along the z direction, where the refinement of the grids is controlled by a_z , which is usually taken as 3.

Both q and ϕ are defined at the point “0” (to be referred to as $q_{i,j}$ and $\phi_{i,j}$), the center of the grid cell being of the size $\Delta r_i^0 \times \Delta z_j^0$ as shown in Figure 1. Before discretizing the governing equation (5a), we first integrate it over the grid cell. Then we use the central difference scheme in discretization of the first-order derivatives for the diffusion terms at the surrounding four points denoted as “e,” “n,” “w,” and “s” in Figure 1. We then need to evaluate the values of q at those four points arising from the convection terms. As mentioned before, choosing upwind methods in that evaluation is very important in establishing numerical stability. In this work, we employ the second-order upwind algorithm. For instance, when the radial component of the velocity at the point “e,” u_e , is positive, we construct the second-order polynomial in r with $q_{i-1,j}$, $q_{i,j}$, and $q_{i+1,j}$ and evaluate the result at the point “e” to get

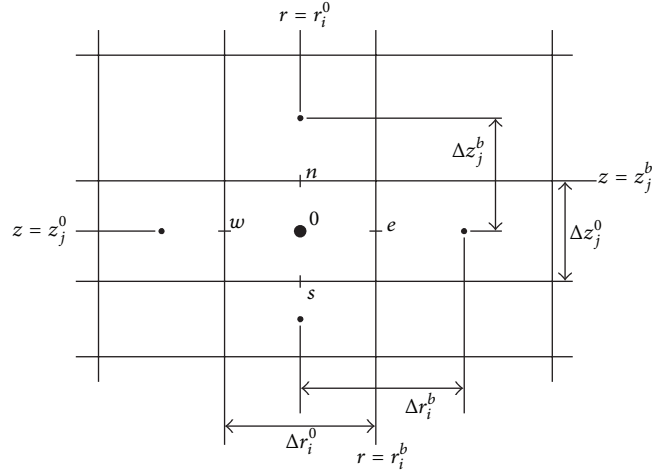


FIGURE 1: Notation for grid sizes, coordinates, and points in the variable grid system.

$$q_e = \frac{-(\Delta r_i^b)^2 q_{i-1,j}}{4\Delta r_{i-1}^b (\Delta r_{i-1}^b + \Delta r_i^b)} + \frac{(2\Delta r_{i-1}^b + \Delta r_i^b) q_{i,j}}{4\Delta r_{i-1}^b} + \frac{(2\Delta r_{i-1}^b + \Delta r_i^b) q_{i+1,j}}{4(\Delta r_{i-1}^b + \Delta r_i^b)}. \quad (17)$$

Similarly, when u_e is negative, the polynomial is constructed with $q_{i,j}$, $q_{i+1,j}$, $q_{i+2,j}$, and so on. The Poisson equation (5b) for ϕ is treated in the same way as for the diffusion terms in (5a). We use the backward Euler method to discretize the transient term in (5a), which corresponds to the simplest stable algorithm. Since the accuracy of the solutions is independent of the time step Δt chosen so as to make the solutions converged, we take the larger time step if possible to speed up the calculation.

The two algebraic systems of equations constructed in this way are solved by using the SOR (successive-over relaxation) method in a coupled manner. Relaxation parameter for (5a) is usually taken as smaller than that for (5b) due to the convection terms.

In the use of the commercial software COMSOL, we employ two models, “transport of a diluted species” and “electrostatics.” The original form of the model however leads to numerical instability due to the fact that the conductivity is set to be proportional to the charge density in the original model, whereas in this study the conductivity is set to be constant. So, we modified the model in such a way that the conduction term is excluded from the charge flux \mathbf{J} but treated as a source. Boundary conditions (3a) and (3b), written in terms of the flux, must also be modified for the same reason. On the other hand, COMSOL allows us to use not only the conservative but also the nonconservative form for the convection terms. We will see that the nonconservative form leads to significant errors compared with the conservative form. The grid system is constructed on the same principle as applied in developing the in-house code; that is, fine grids are built near the cylinder surfaces to resolve thin EDLs.

The velocity field we are interested in is the secondary Taylor-vortex flow observed in the axial plane caused by hydrodynamic instability. Instead of using the exact solution of the secondary flow given from the numerical simulation of the Navier-Stokes equations or the experimental measurement, we set the flow in an arbitrary manner but with physical relevance if possible. For this, we assume that the axial plane between the coaxial cylinders is occupied by the series of spatially periodic flow cells. The velocity components u and w then can be written in a separation-of-variable form like

$$u = \frac{\pi\psi(r)}{hr} \cos\left(\frac{\pi z}{h}\right), \quad w = -\frac{1}{r} \frac{d\psi(r)}{dr} \sin\left(\frac{\pi z}{h}\right), \quad (18)$$

where ψ is a kind of stream function for the axisymmetric velocity field. To determine the functional form of $\psi(r)$, we assume that $\psi(r)$ is a quadratic function (or rw is a linear function) of r in the bulk, while rw exponentially approaches zero as $r \rightarrow r_1$ or $r \rightarrow r_2$. Then we let

$$\begin{aligned} \psi(r) = & c_0 + c_1 r + c_2 r^2 + c_3 \exp[-\beta_1(r - r_1)] \\ & + c_4 \exp[-\beta_2(r_2 - r)], \end{aligned} \quad (19)$$

where five unknown constants c_0 – c_4 are determined from the four restrictions

$$\psi(r_1) = \psi(r_2) = 0, \quad \frac{d\psi}{dr}(r_1) = \frac{d\psi}{dr}(r_2) = 0, \quad (20)$$

and the normalization condition for w on $z = h/2$,

$$\psi(r_m) = -\frac{r_m^2 - r_1^2}{2}. \quad (21)$$

Here r_m denotes the radial coordinate of the point in the bulk on $z = h/2$ where w vanishes; that is,

$$\frac{d\psi}{dr}(r_m) = 0. \quad (22)$$

Note that the spatially averaged vertical velocity component at $z = h/2$ (averaged over $r_1 \leq r \leq r_m$) is now 1. The two parameters β_1 and β_2 control the boundary-layer thickness near the cylinder walls, where the steep distribution of w along the normal to the wall is expected; larger β_i means a thinner layer. Figure 2 illustrates typical profiles of the velocity component $w(r, h/2)$ for different sets of β_1 and β_2 . It clearly shows that larger β_i yields a thinner layer and each wall-layer thickness can be controlled separately.

We have also prepared 1D code applicable to the case where no fluid motion exists so that the convection terms vanish. The numerical schemes are identical to those employed in the 2D code except that the variables' dependence on z has been removed in the 1D code.

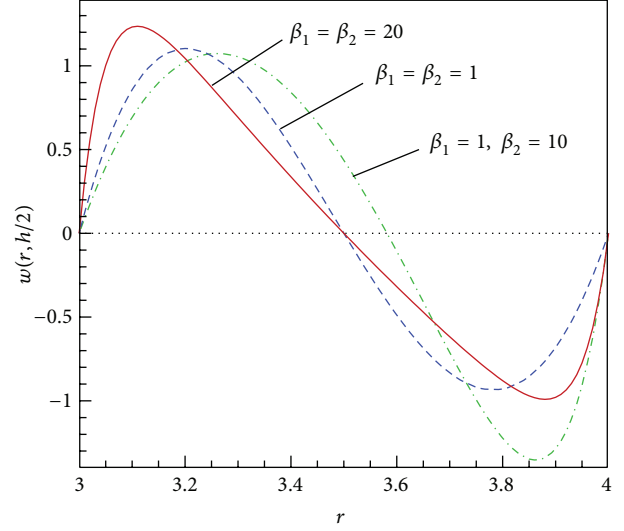


FIGURE 2: Typical profiles of the velocity component w on $z = h/2$ given with three different sets of β_1 and β_2 .

5. Results and Discussion

The standard parameter set is given as follows [10]:

$$\begin{aligned} R_1 &= 76.2 \text{ [mm]}, & R_2 &= 101.6 \text{ [mm]}, \\ \varepsilon &= 2 \times 8.85 \times 10^{-12} \text{ [s} \cdot \text{S/m]}, \\ k_1^* &\equiv k_{10}^* = 2.84 \times 10^{-6} \text{ [m/s]}, \\ k_2^* &\equiv k_{20}^* = 3.12 \times 10^{-6} \text{ [m/s]}, \\ \sigma &= \sigma_0 = 20 \times 10^{-12} \text{ [S/m]}, \\ q_{1w}^* &= 7.71 \times 10^{-3} \text{ [C/m}^3\text{]}, \\ q_{2w}^* &= 1.84 \times 10^{-3} \text{ [C/m}^3\text{]}. \end{aligned} \quad (23)$$

The diffusivity is set at $D = 8.86 \times 10^{-11} \text{ [m}^2\text{/s]}$ in Washabaugh [10]. However, in laminar flow with such a very low diffusivity, numerical simulation in general requires a very long time and the EDLs near the cylinder surfaces are too thin to be effectively resolved by a reasonably fine grid system. It also turned out that the conservation property cannot be established with such low diffusivity. Since we are concerned with laminar flow in this study, we assume much higher diffusivity than the original value, usually in the range $O(10^{-5}) \sim O(10^{-6}) \text{ [m}^2\text{/s]}$. So, in this study we set $D_0 \equiv 10^{-6} \text{ [m}^2\text{/s]}$ as the standard diffusivity. Increasing the diffusivity is equivalent to decreasing the geometric scale as can be seen from the definition of the two main dimensionless parameters, P and Q appearing in (5a). Other parameters to be varied here are k_i^* and σ . So, we set the following: $D = \alpha_D D_0$, $k_i^* = \alpha_{ki} k_{i0}^*$, and $\sigma = \alpha_\sigma \sigma_0$, where α_D , α_{ki} , and α_σ are multiplying factors. The reference velocity will vary in the range $U = 10^{-6} \sim 1 \text{ [m/s]}$, and the control parameters for the

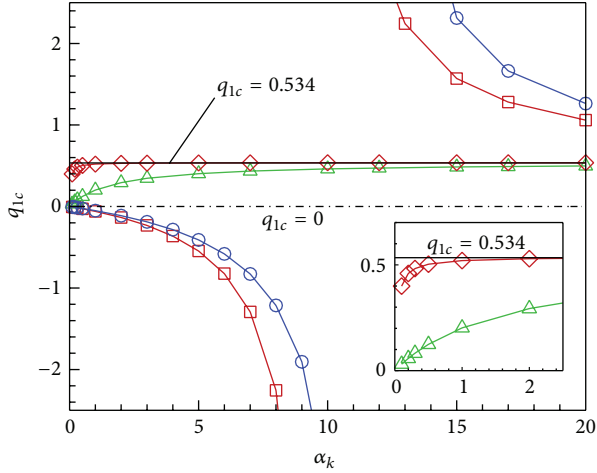


FIGURE 3: Dependence of q_{1c} , the value of q_1 at $z = h/2$, on the conservation property of the convection terms and the specific form of the source terms in the charge transport equation given from COMSOL simulation with the number of grid elements being 12,000. The diffusivity factor is set at $\alpha_D = 88.6$ and the reference velocity at $U = 1$ [m/s]. Solid lines with square symbols are given by CN-SC (convection terms in a nonconservative form and the source term written in terms of the charge), solid lines with circles by CN-SE (convection terms in a nonconservative form and the source term written in terms of the electric field), solid line with deltas by CC-SC (convection terms in a conservative form and the source term written in terms of the charge), and solid line with diamond symbols by CC-SE (convection terms in a conservative form and the source term written in terms of the electric field). The solid line without symbols, $q_{1c} = 0.534$, denotes the numerical solution obtained by the 2D in-house code.

velocity profiles will be set at $\beta_1 = \beta_2 = 20$, except where otherwise mentioned.

Figure 3 shows the sensitive dependence of the numerical solutions given by the COMSOL simulations on the conservation property of the convection terms and the form of the source term. The diffusivity factor is set at $\alpha_D = 88.6$ in the simulations; then, we get $P = 287$ and $Q = 8.23$. Here CC means that the convection terms are treated with the conservative form, that is, with the form shown in (5a) (second term). CN means that the convection terms are treated with the nonconservative form, that is, with $P[u\partial q/\partial r + w\partial q/\partial z]$. Further, SC means that the source term is written as Qq (like the third term in (5a)), whereas SE means that it is written as $Q\nabla \cdot \mathbf{E}$. When the nonconservative form for the convection terms (CN) is used, the results vary enormously with α_k ($\equiv \alpha_{k1} = \alpha_{k2}$), and at low values of α_k it can even be negative, which is physically irrelevant. We also conducted the grid-dependence test with different grids. At $\alpha_k = 0.1$, the in-house code gives $q_{1c} = 0.534$ with grids 51×51 , whereas it gives $q_{1c} = 0.536$ with 101×101 , showing a very small change. The scheme CC-SE in COMSOL on the other hand gives $q_{1c} = 0.399$ with the number of grid elements 12,000, but it gives $q_{1c} = 0.502$ with 33,000 elements and $q_{1c} = 0.524$ with 61,000 elements, indicating that as the

grids are refined the data approaches the value given by the in-house code. We also confirm that the in-house code yields the same result regardless of α_k . We also developed an in-house code which uses the nonconservative convection terms. For the same parameter set given above and for $\alpha_k = 1$, we get $q_{1c} = 0.025$ with the grids 51×51 and $q_{1c} = 0.113$ with the grids 101×101 , both being much smaller than the correct value $q_{1c} = 0.534$. This implies that the conservative property of the convection terms is one of the most important factors regarding numerical accuracy.

The fact that the numerical solutions are sensitively dependent on the form of the convection or conduction (source) term in the governing equations implies that a small error in the equations can yield a significantly different solution. In order to explore the reason, we perform a simple analysis with the one-dimensional equation without convection effect:

$$q'' - \lambda^2 q = \delta, \quad (24a)$$

$$\phi'' + q = 0, \quad (24b)$$

where the prime denotes differentiation with respect to the new variable $x = r - r_1$ and δ is an arbitrary small error which is supposed to be contained in the charge transport equation due to the use of different forms of each term. In fact, the above equations can be derived from (9a) and (9b) under the limit of very large cylinders, $r \rightarrow \infty$. The boundary conditions to be satisfied are

$$J_r \equiv -(q' + \lambda^2 \phi') = -k_1 (q - 1) \quad \text{at } x = 0, \quad (25a)$$

$$-(q' + \lambda^2 \phi') = \kappa k_1 (q - q_{2w}) \quad \text{at } x = 1, \quad (25b)$$

$$\phi = 0 \quad \text{at } x = 0, 1. \quad (25c)$$

Here, k_1 is taken to be very small, and $\kappa \equiv k_2/k_1 = O(1)$; we calculate $k_1 = 8.1 \times 10^{-4}$ with the standard parameter set and $D = 8.86 \times 10^{-5}$ [m²/s]. Then, after some algebraic work we derive

$$q_1 = q_2 = \frac{1 + \kappa q_{2w} - \delta/k_1}{1 + \kappa}. \quad (26)$$

This gives $q_1 = q_2 = 0.601$ for $\delta = 0$ (no error), which is not so much different from $q_{1c} = 0.534$ given from the two-dimensional simulation (see Figure 3). More importantly, we see from (26) that even a small value of δ can bring a significantly different value of q_1 as long as k_1 remains small. It can even produce a negative value of q_1 when $\delta > k_1(1 + \kappa q_{2w})$.

On the other hand, the numerical data of q_{1c} given from the 2D in-house code with the conservative convection terms are almost invariant of the parameter k_1 as shown in Figure 3. This can be understood from the expansion of (15a) for small k_1 reading

$$q_1 = 1 - (1 - q_{2w}) \frac{\kappa r_2 \ln(r_2/r_1)}{r_1 + \kappa r_2} + O(k_1). \quad (27)$$

Equation (27) clearly indicates that q_1 , which can also be shown to be the same as q_2 for small k_1 , is independent of k_1 to the leading order. In passing, evaluation of (27) gives $q_1 = 0.547$, which differs only 2% from the 2D result $q_{1c} = 0.534$ (see Figure 3). This agreement is remarkable considering that in 2D simulations q_1 is also a function of z .

Figure 4(a) shows the distribution of $q(r)$ and $Q\phi(r)$ obtained numerically from the 1D code for the case without convection effect; the graph is almost indistinguishable from the one given by the analytical solutions (11) and (14). We confirm an almost linear relationship between q and ϕ as described in (11); C_3 is small because k_1 is small. Since the charge is positive everywhere, the second derivative of the potential is negative, as can be seen from (24b), being consistent with Figure 4(a). Figure 4(b) shows the distribution of the total amount of the charge flux times the radius, $(rJ_r)_{\text{tot}}$, and the two contributions, $(rJ_r)_{\text{dif}}$ and $(rJ_r)_{\text{cond}}$ obtained from the 1D code. Since the charge is large near both walls and small in between the two, the diffusion must occur from the walls to the central region so that $(rJ_r)_{\text{dif}} > 0$ on the left-hand side and $(rJ_r)_{\text{dif}} < 0$ on the right-hand side as shown in Figure 4(b). On the other hand, since the electric field is directed from the central region toward the walls, the charge receives Coulomb force in the same direction as the field vector, and so the sign of $(rJ_r)_{\text{cond}}$ is the reverse of that of $(rJ_r)_{\text{dif}}$ as shown in Figure 4(b). We will see below that those two can make balance with each other independently of the charge input or output through the walls. First, we note from Figure 4(b) that $(rJ_r)_{\text{tot}}$ is much smaller than the other two contributions. As addressed before, this is caused by the smallness of k_i . Since $(rJ_r)_{\text{tot}}$ is positive, the charge is transmitted from the inner to the outer cylinder side, which is physically correct because $q_{1w} = 1$ is higher than q_{2w} . This implies that for a small value of k_i the diffusive charge flux is balanced by the conductive flux. We confirm from the 1D simulation that setting $q_{2w} = q_{1w} = 1$ produces $(rJ_r)_{\text{tot}} = 0$ although the distributions of $(rJ_r)_{\text{dif}}$ and $(rJ_r)_{\text{cond}}$ are similar to those of Figure 4(b). This means that the nonzero charge distribution can be established as long as the wall charge is assigned with a nonzero value.

Two important dimensionless parameters explicitly appearing in the governing equations (5a) and (5b) are P and Q , and exploring the influence of these parameters on the solutions' behavior is the main purpose of this study. The former represents the importance of the convection terms compared with the diffusion terms, whereas the latter is related to the thickness of EDL as $\lambda = 1/\sqrt{Q}$. Under the standard parameter set and $U = 1$ [m/s], we calculate $P = 2.54 \times 10^4$ and $Q = 729$. In the following parametric study, we will start with small values of P and Q , and see how the solution structures vary with increase of these parameters.

Figure 5 shows the numerical results of the 2D code given at $\alpha_\sigma = 0.001$ and $U = 10^{-5}$ [m/s] at which $P = 0.254$ and $Q = 0.729$. P remains small enough that the distributions of q (Figure 5(a)) and ϕ (Figure 5(b)) are almost one-dimensional being invariant of z . The diffusive charge-flux vector, $\mathbf{J}_{\text{dif}} \equiv -\nabla q$ (Figure 5(c)), and the conductive charge-flux vector, $\mathbf{J}_{\text{cond}} \equiv -Q\nabla\phi$ (Figure 5(d)), also reveal a one-dimensional

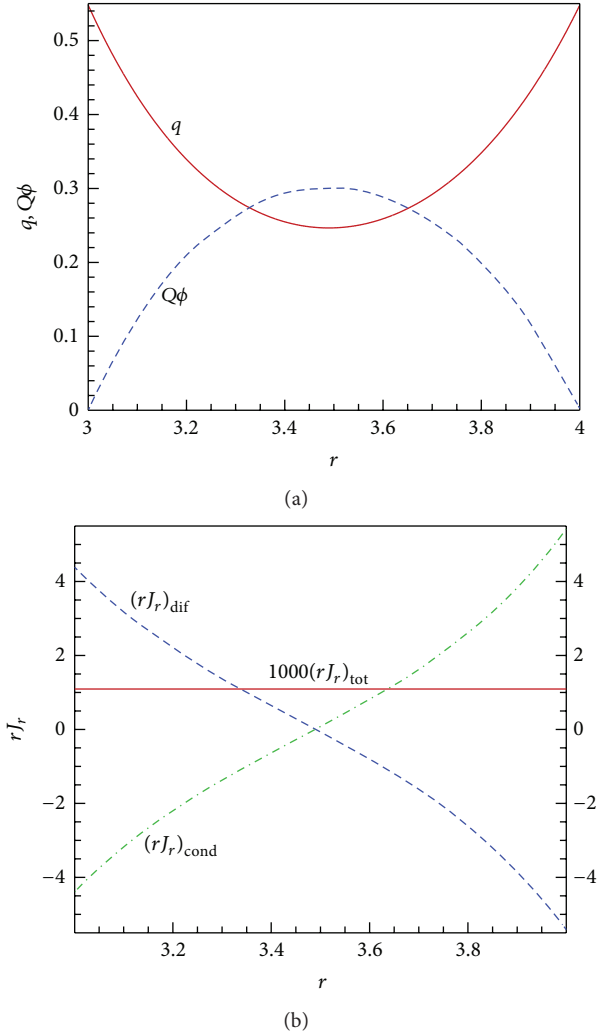


FIGURE 4: Numerical results of 1D simulation with $\alpha_D = 88.6$; (a) distribution of $q(r)$ (solid line) and $Q\phi(r)$ (dashed line) and (b) distribution of $(rJ_r)_{\text{dif}}$ (dashed line), $(rJ_r)_{\text{cond}}$ (dash-dot line), and $1000(rJ_r)_{\text{tot}}$ (solid line).

nature; they are almost heading for the radial direction and are balanced by each other. On the other hand, the convective charge-flux vector, $\mathbf{J}_{\text{conv}} \equiv \mathbf{P}uq$ (Figure 5(e)), is almost in the same pattern as the velocity vector, \mathbf{u} , because the charge distribution is nearly uniform as shown in Figure 5(a). The total charge-flux vector, $\mathbf{J}_{\text{tot}} \equiv \mathbf{J}_{\text{dif}} + \mathbf{J}_{\text{conv}} + \mathbf{J}_{\text{cond}}$ (Figure 5(f)), then looks not so much different from \mathbf{J}_{conv} , because although \mathbf{J}_{dif} and \mathbf{J}_{cond} are in the same order of magnitude as \mathbf{J}_{conv} , they combine to become much smaller than each one, as discussed above. The stream traces of the total charge flux (Figure 5(f)) show that the wall charge at $r = r_1$ is diffused into the domain, convected along the streamlines, and finally diffused into the wall at $r = r_2$. In the bulk, the total charge-flux vector plot shows a recirculating pattern like the fluid velocity vector. Figure 6 shows a sketch of the passage through which the charge is transmitted from the inner wall at $r = r_1$ to the outer

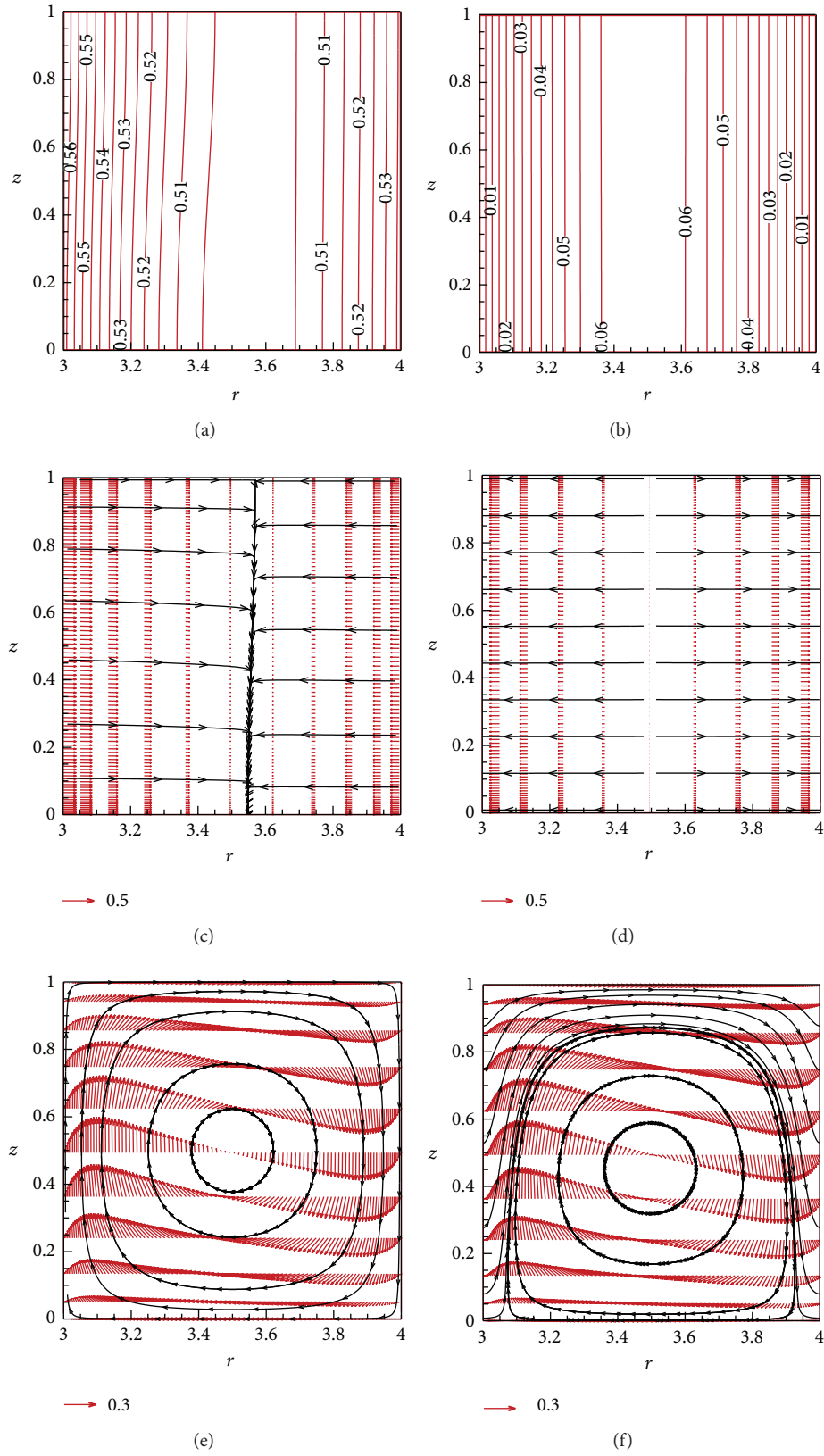


FIGURE 5: Numerical results of 2D simulation at $\alpha_\sigma = 10^{-3}$ and $U = 10^{-5}$ [m/s]; (a) contours of q , (b) contours of ϕ , (c) J_{dif} , (d) J_{cond} , (e) J_{conv} , and (f) J_{tot} .

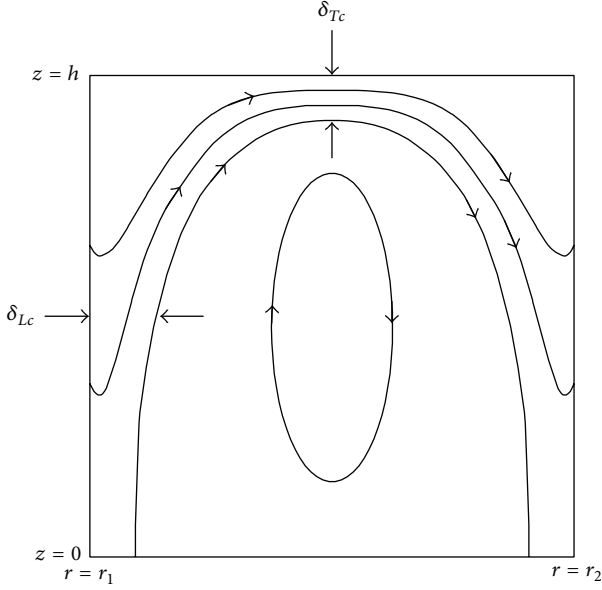


FIGURE 6: Passage of the charge transmission from the inner cylindrical wall at $r = r_1$ to the outer cylindrical wall at $r = r_2$. Also shown are the thickness of the passage at $z = h/2$ on the inner wall, δ_{Lc} , and that at $r = r_c$ on the top wall, δ_{Tc} .

wall at $r = r_2$ together with the definition of the thicknesses of the passage, δ_{Lc} and δ_{Tc} at particular places.

At a reference velocity 10 times higher, $U = 10^{-4}$ [m/s], we get $P = 2.54$ and $Q = 0.729$. Distribution of q (Figure 7(a)) shows deviation from the one-dimensional structure, while ϕ (Figure 7(b)) still keeps its one-dimensional nature. Accordingly, \mathbf{J}_{dif} is somewhat deteriorated (Figure 7(c)), but \mathbf{J}_{cond} is still heading for the radial direction (Figure 7(d)). The sum of the two flux vectors, $\mathbf{J}_{\text{dif}} + \mathbf{J}_{\text{cond}}$ (Figure 7(e)), now shows much decreased level caused by their mutual balance but with complex stream-trace structure. The total flux vector, \mathbf{J}_{tot} (Figure 7(f)), then shows that most of the bulk region is composed of the recirculating pattern and simultaneously the passage near the walls responsible for the wall-to-wall charge transmission is more narrowed than in Figure 5(f) with smaller U .

Further increase of U (at $U = 10^{-3}$ [m/s]; $P = 25.4$, $Q = 0.729$) tends to make the contours of q the closed-curve style in particular in the bulk (Figure 8(a)). Thus the diffusive flux vectors (Figure 8(c)) focus on the center of the contours of q , where q is minimized. However variation of q is not so significant that the contours of ϕ still show the one-dimensional nature (Figure 8(b)). Thus, the conductive flux vectors (Figure 8(d)) are heading for the radial direction. The pattern of $\mathbf{J}_{\text{dif}} + \mathbf{J}_{\text{cond}}$ (Figure 8(e)) is now more complex than Figure 7(e) but its magnitude still remains at low value. The charge transmission passages near the walls at $r = r_1$ and $r = r_2$ become thinner than Figure 7(f) because the convective effect is more pronounced.

When U is further increased, the contour plot of q tends to the streamline pattern of the fluid flow and the diffusive flux vector plot shows the radial inward pattern more clearly than

Figure 8(c), but the distribution of ϕ and the conductive flux vector plot are qualitatively the same as Figures 8(b) and 8(d). The total charge-flux vector plot also tends more closely to the convective flux vector plot, because the convective effect is more dominant at higher values of U (or equivalently at larger values of P). The thickness of the transmission passage becomes smaller at larger U . We measure the dimensionless thickness δ_{Lc} as 0.094 at $U = 10^{-5}$ [m/s] (from Figure 5(f)), 0.024 at $U = 10^{-4}$ [m/s] (from Figure 7(f)), 0.0070 at $U = 10^{-3}$ [m/s] (from Figure 8(f)), 0.0016 at $U = 10^{-2}$ [m/s], and so forth. We also measure δ_{Tc} as 0.127 at $U = 10^{-5}$ [m/s], 0.014 at $U = 10^{-4}$ [m/s], 0.0014 at $U = 10^{-3}$ [m/s], 0.00014 at $U = 10^{-2}$ [m/s], and so forth. This indicates that the amount of charge transmitted through the walls per unit area and unit time is almost independent of U at high values of U .

As U is increased at a fixed σ , the contour of q tends to follow the fluid streamline pattern because, when the fluid circulates along its closed path with high velocity, the fluid circulation time, that is, τ_{conv} , becomes so short compared with τ_{dif} and τ_{cond} that the diffusive or conductive action does not have enough time to modify the value of q but must leave it to remain at a constant value specific to the circulation path. That is, we can estimate for large value of U the relation $q = q(\Psi)$, where Ψ is the stream function reading $\Psi = \psi(r) \sin(\pi z/h)$ in this study. This can be also proved from (5a). At the limit $P \rightarrow \infty$, (5a) becomes $\nabla \cdot (\mathbf{u}q) \approx 0$ or equivalently $(\mathbf{u} \cdot \nabla)q \approx 0$ (from the continuity equation). In terms of the material derivative, this can be written as $Dq/Dt = 0$, indicating that $q = \text{constant}$ along the streamline, on which Ψ is set as constant.

In order to confirm the above reasoning, we calculate the Lagrangian variation of q of a fluid particle while it flows along the given streamline. Figure 9 shows the numerical results obtained at various reference velocities and at fixed $\alpha_\sigma = 10^{-3}$. The abscissa s indicates the distance travelled by the fluid particle along the closed streamline specified by the initial point, normalized by the total length of the streamline. So, $s = 0$ means the starting point and $s = 1$ the final point, which is set to be the same as the initial point. The figure clearly demonstrates that as the reference velocity increases, the charge density variation is more uniform because the time taken for one complete circulation is decreased accordingly. It also reveals that the inner streamline starting at $(r, z) = (r_c, 0.2)$ (Figure 9(b)) shows smaller variation of q than the outer one starting at $(r, z) = (r_c, 0.02)$ (Figure 9(a)) for the same parameter set; this is also consistent with the above reasoning because the former requires a smaller circulation time than the latter. The overall level of q is observed to increase as U is increased in particular near $s = 0.5$, because the contour of q tends to the plume structure when U is increased (partly shown in Figure 8(a) near $z = 0$ and 1).

Now we investigate the effect of σ on the charge-transport behavior at fixed $U = 10^{-4}$ [m/s]. Figure 10 shows the numerical results given at $\alpha_\sigma = 0.1$ ($P = 2.54$, $Q = 72.9$). Compared with Figure 7(a) for σ being 100 times smaller, the level of q is significantly decreased in the bulk, because λ is decreased by the factor 0.1. As a result, the level of ϕ is also decreased (Figure 10(b)). The vector plots of \mathbf{J}_{dif} (Figure 10(c))

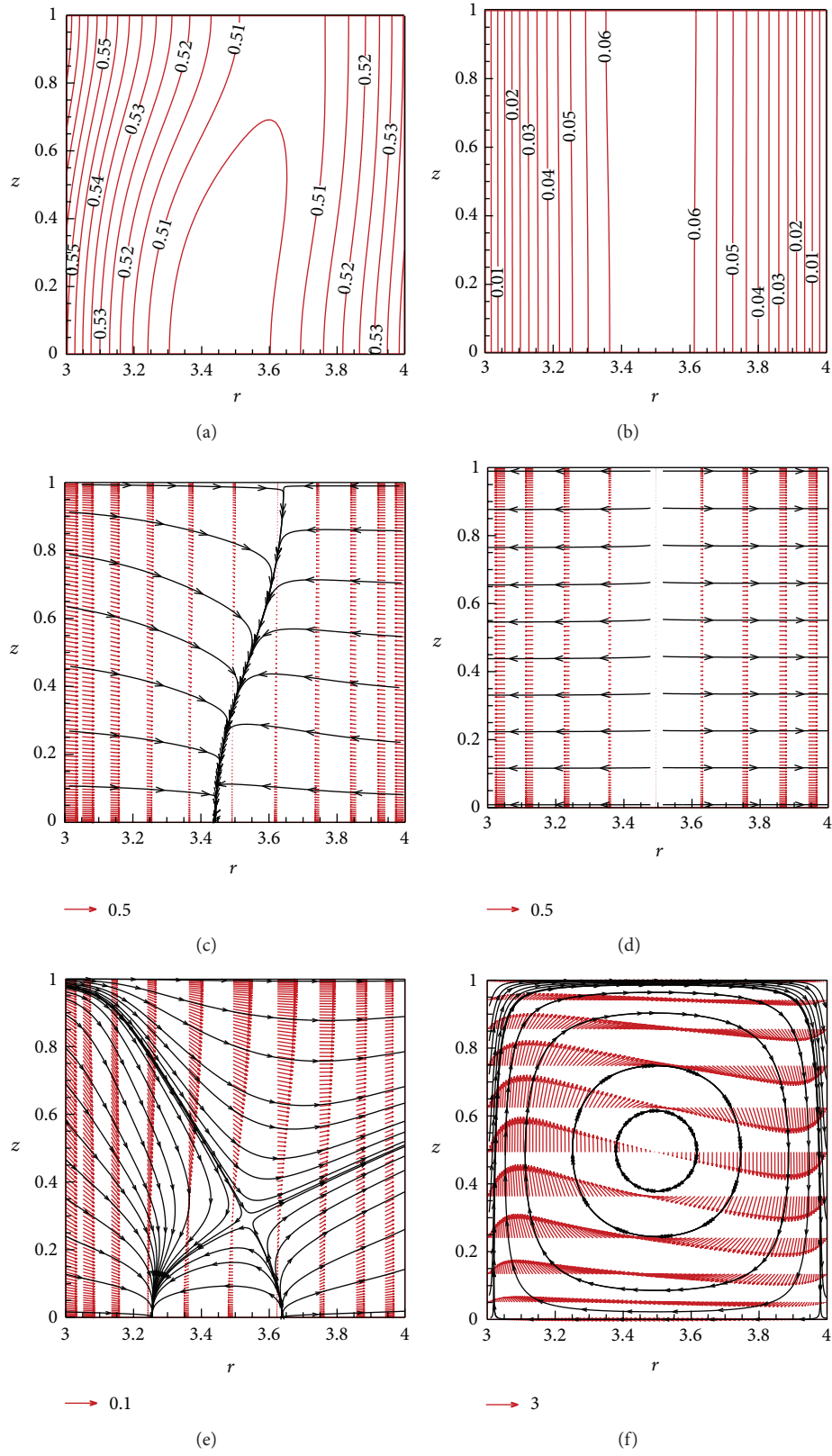


FIGURE 7: Numerical results of 2D simulation at $\alpha_\sigma = 10^{-3}$ and $U = 10^{-4}$ [m/s]; (a) contours of q , (b) contours of ϕ , (c) \mathbf{J}_{dif} , (d) \mathbf{J}_{cond} , (e) $\mathbf{J}_{\text{dif}} + \mathbf{J}_{\text{cond}}$, and (f) \mathbf{J}_{tot} .

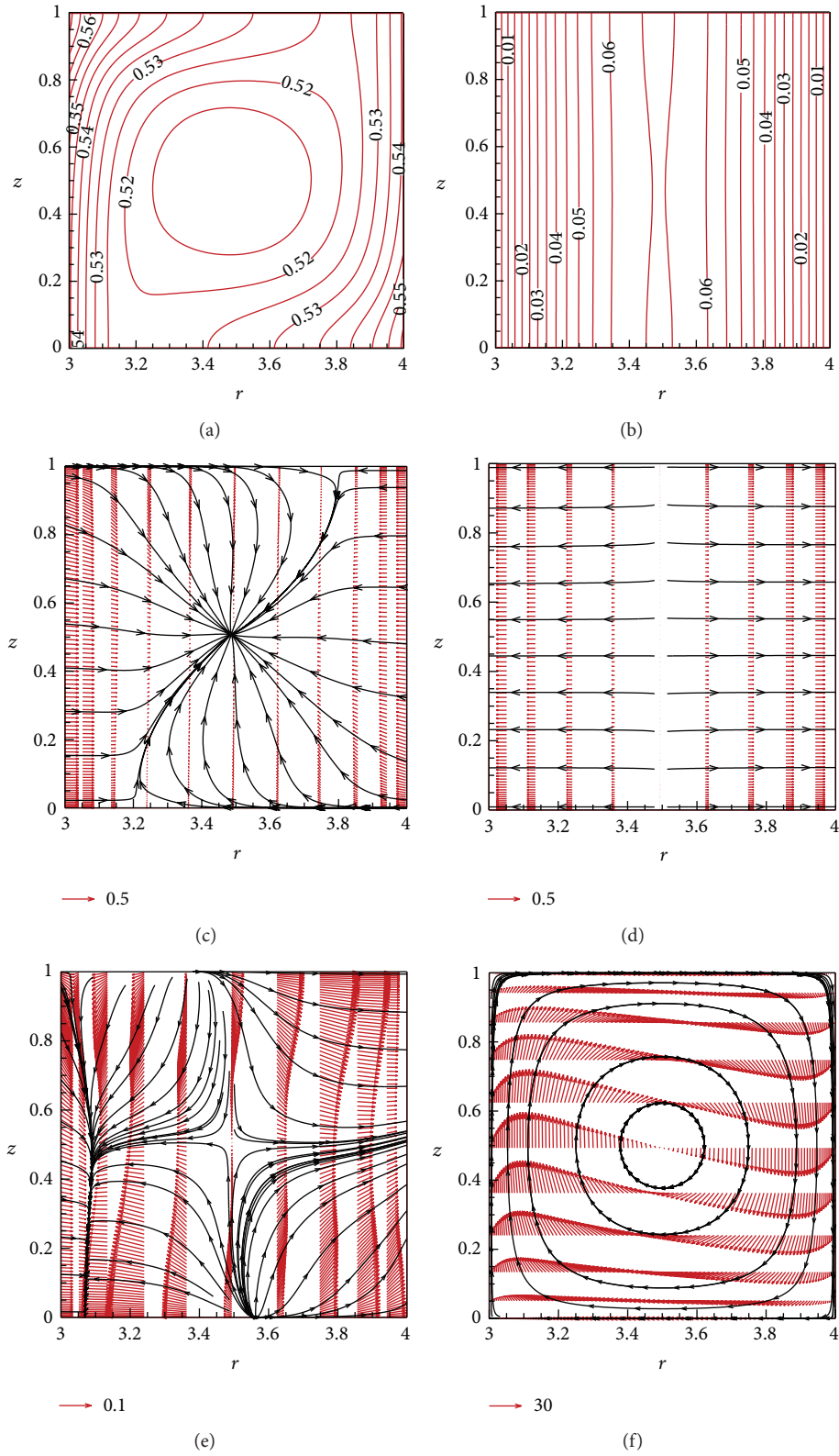


FIGURE 8: Numerical results of 2D simulation at $\alpha_\sigma = 10^{-3}$ and $U = 10^{-3}$ [m/s]; (a) contours of q , (b) contours of ϕ , (c) \mathbf{J}_{dif} , (d) \mathbf{J}_{cond} , (e) $\mathbf{J}_{\text{dif}} + \mathbf{J}_{\text{cond}}$, and (f) \mathbf{J}_{tot} .

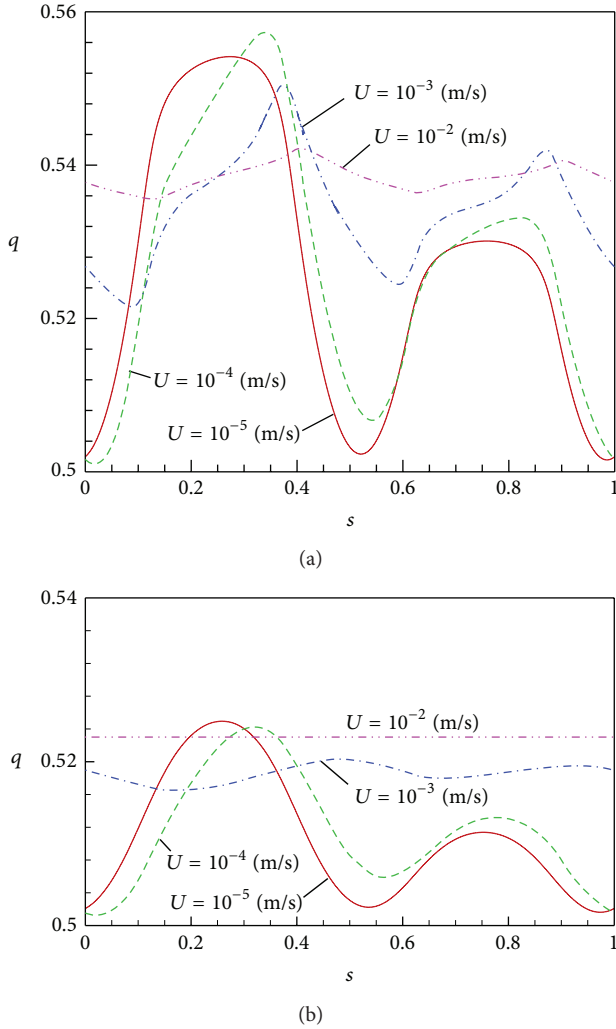


FIGURE 9: Lagrangian variation of the charge density versus the normalized distance travelling from the initial point of a fluid particle while flowing along the streamline, numerically given at the four reference velocities indicated and at $\alpha_\sigma = 10^{-3}$. Initial points are (a) $(r, z) = (r_c, 0.02)$ and (b) $(r, z) = (r_c, 0.2)$.

and J_{cond} (Figure 10(d)) show the one-dimensional nature and they are not qualitatively so much different from Figures 7(c) and 7(d), respectively. However, their magnitude is increased significantly, in particular near the walls, of course. The level of their sum, $J_{\text{dif}} + J_{\text{cond}}$ (Figure 10(e)), is accordingly increased but not so much as J_{dif} and J_{cond} . On the other hand, J_{tot} (Figure 10(f)) differs from Figure 7(f) significantly. Its magnitude is about 3 times smaller than Figure 7(f), because at $\alpha_\sigma = 0.1$ the charge density q decreases sharply with the normal distance from the walls, which causes J_{conv} to be reduced; note that in this parameter set, too, the contribution of J_{conv} to J_{tot} is dominant over the other fluxes. On the other hand, in the central region near $r = r_c$, the level of q is much lowered so that the levels of J_{conv} and J_{tot} must also be low

there. Thus, in order to satisfy the charge conservation, the passage of the charge transmission near the top wall must be wider than that near the side walls, $\delta_{Tc} > \delta_{Lc}$. In other words, at a high enough value of σ , the central region is dominated by the diffusive and conductive flux but not by the convective flux, whereas the EDLs are dominated by the convective flux, except for the very thin EDLs closer to the walls where the diffusion terms should be more effective because the fluid velocity remains very small.

As α_σ is further increased, the EDLs are clearly distinguished from the bulk as shown in Figure 11(a) for the radial distribution of q and ϕ at $z = h/2$. Since $q \approx 0$ in the bulk (to be referred to as “charge depletion zone”), ϕ must be a logarithmic function of r as indicated in (11) and shown in Figure 11(a). Thus the electric field is nonzero in the bulk causing $J_{\text{cond}} \equiv Q\sigma E$ to be finite there. The diffusive flux and convective flux must vanish in the bulk, because $q \approx 0$ there. Then, the total flux must be dominated by the conductive flux, which can be confirmed from Figures 11(b), 11(c), and 11(f), where the patterns of stream trace of the fluxes look similar to each other near the central region, $r = r_c$. On the other hand, the EDLs are dominated by the convective flux. At this parameter set, the level of J_{tot} shown in Figures 11(e) and 11(f) is further decreased from Figure 10(f) because of the decreased EDL thickness. We also observe that δ_{Tc} is increased significantly with increase of σ . Measurement of δ_{Tc} from the simulation results gives $\delta_{Tc} = 0.021$ at $\alpha_\sigma = 0.01$, 0.079 at $\alpha_\sigma = 0.1$, and 0.386 at $\alpha_\sigma = 1$, while δ_{Lc} is not so much changed upon σ ; we measure $\delta_{Lc} = 0.028$ at $\alpha_\sigma = 0.01$, 0.034 at $\alpha_\sigma = 0.1$, and 0.038 at $\alpha_\sigma = 1$.

We can estimate the dependence of the charge density distribution on σ from the Lagrangian variation of q for various values of α_σ as shown in Figure 12. On the streamline having the initial point at $(0.5, 0.02)$, the overall level of q decreases with α_σ , but the range of variation is rather increased up to $\alpha_\sigma = 0.1$ (Figure 12(a)). The latter result can be understood from the fact that as α_σ is increased the wall charge q_i remains almost constant (we measure only 4% change for the range $10^{-3} \leq \alpha_\sigma \leq 1$) but the charge depletion zone begins to appear near $\alpha_\sigma = 0.1$. As α_σ is further increased, EDLs become thinner while the charge depletion zone becomes wider, which causes the variation of q to be smaller as shown in Figure 12(a). We can also give a qualitatively similar description as to the Lagrangian variation of q of the fluid particle on the streamline with the initial point at $(r_c, 0.2)$ (Figure 12(b)). In particular, the level of q vanishes all the way through the streamline at $\alpha_\sigma = 1$ implying that charge depletion zone should encompass the region surrounded by the streamline.

A typical solution structure of the charge transport equations with α_σ and U sufficiently high is shown in Figure 13. We can say that the given value of α_σ is high enough in that the EDLs are thin and the charge depletion zone is wide. We can also say that the given value of U is high enough in that contours of q in the regions near $z = 0$ and $z = 1$ show the plume structure, which then causes the charge to accumulate there and makes the contour of ϕ to be of a saddle type near the center point at $(r_c, h/2)$.

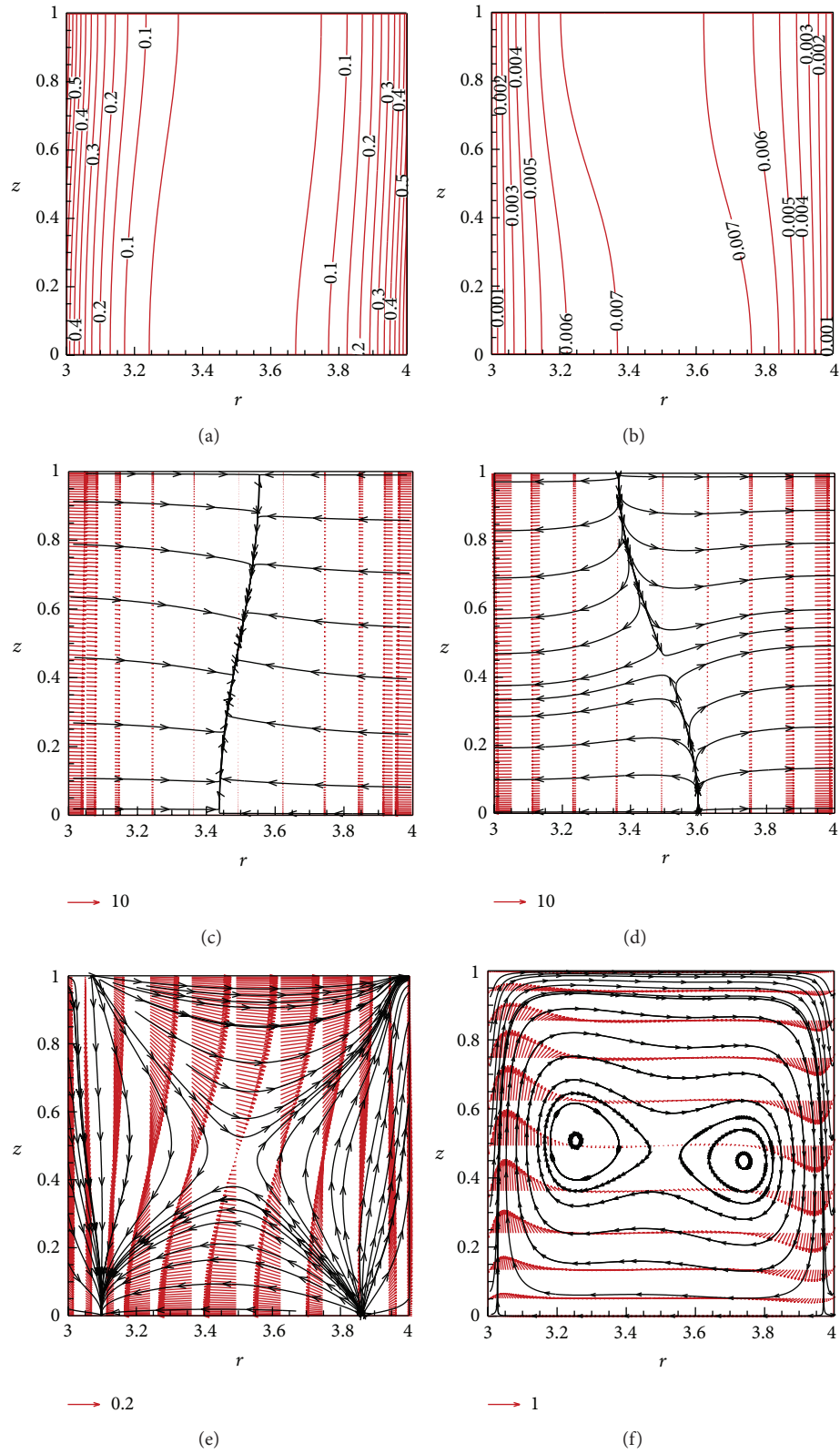


FIGURE 10: Numerical results of 2D simulation at $\alpha_\sigma = 0.1$ and $U = 10^{-4}$ [m/s]; (a) contours of q , (b) contours of ϕ , (c) \mathbf{J}_{dif} , (d) \mathbf{J}_{cond} , (e) $\mathbf{J}_{\text{dif}} + \mathbf{J}_{\text{cond}}$, and (f) \mathbf{J}_{tot} .

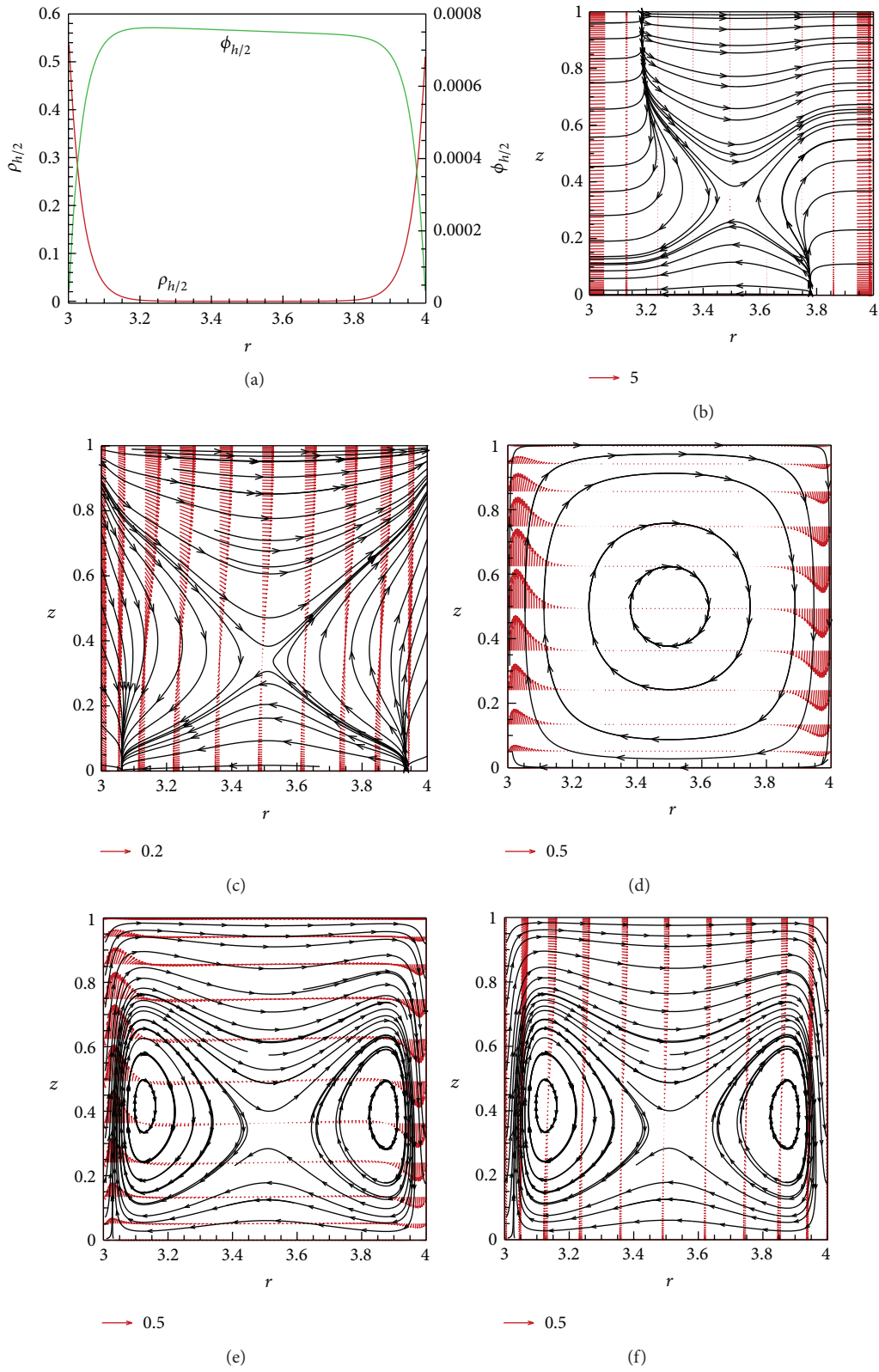


FIGURE 11: Numerical results of 2D simulation at $\alpha_\sigma = 1$ and $U = 10^{-4}$ [m/s]; (a) radial distributions of q and ϕ on $z = h/2$, (b) \mathbf{J}_{cond} , (c) $\mathbf{J}_{\text{dif}} + \mathbf{J}_{\text{cond}}$, (d) \mathbf{J}_{conv} , (e) \mathbf{J}_{tot} showing its r -profile, and (f) \mathbf{J}_{tot} showing its z -profile.

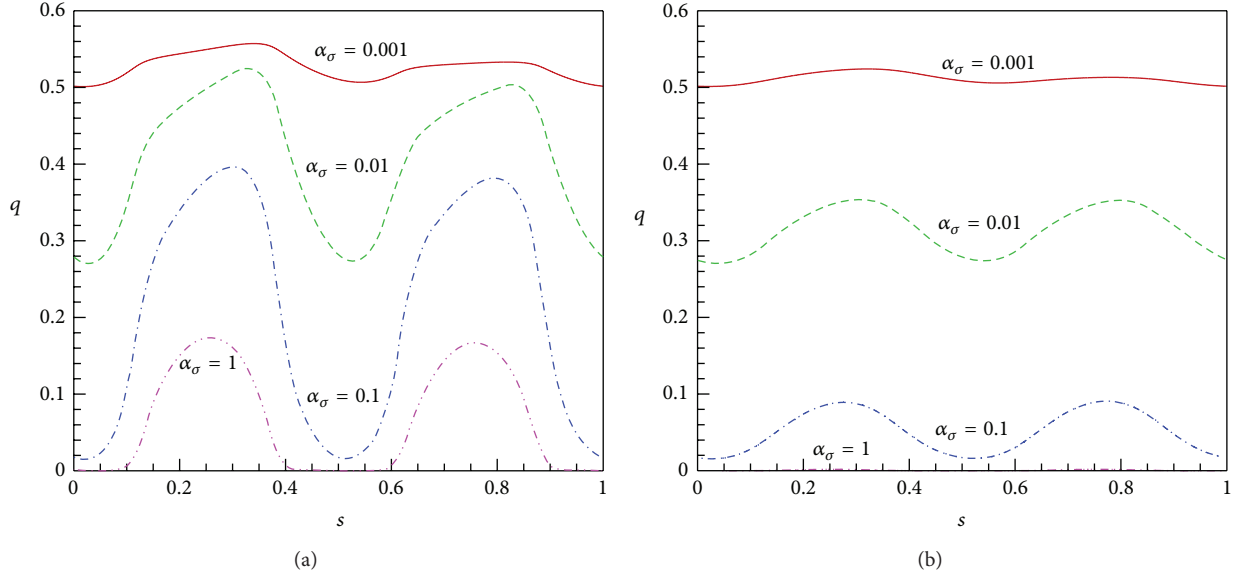


FIGURE 12: Lagrangian variation of the charge density versus the normalized distance travelling from the initial point of a fluid particle while flowing along the streamline, numerically given at the three indicated values of α_σ and at $U = 10^{-4}$ [m/s]. Initial points are (a) $(r, z) = (r_c, 0.02)$ and (b) $(r, z) = (r_c, 0.2)$.

Electrification is known to be directly related to the amount of charge accumulated in the bulk, which in this study is quantified by the averaged charge density

$$q_{av} = \frac{2}{h(r_2^2 - r_1^2)} \int_A r q dr dz. \quad (28)$$

Figure 14 shows variation of q_{av} obtained from the 2D code for various U values. In the limit $U \rightarrow 0$, q_{av} asymptotes to a constant value, because the charge distribution tends to the 1D structure (see, e.g., Figure 5(a)). As U increases, q_{av} also increases, because the fluid conveys the charge within the EDLs to the top ($z = 1$) and bottom ($z = 0$) boundaries of the domain, leading to the plume structure there (see, e.g., Figures 8(a) and 13(a)). The amount of increase however depends on the value of σ . At low values of α_σ , the level of q is high but its spatial variation is small (Figures 7(a) and 8(a)) so that even the plume structure brings a slight increase of q_{av} upon U as shown in Figure 14(a). On the other hand, at high values of α_σ , thin EDLs appear distinctively and a nonzero value of q is detected only within the EDLs. In this case, existence of the convection effect would sweep the charge carriers within EDLs toward the top and bottom boundaries, giving rise to additional thin layers of nonzero charge (i.e., plume structure) there. Since increase of U tends to make the overall level of q higher in those additional layers, we expect more increase of q_{av} upon U , as shown in Figure 14(a), than is the case with lower α_σ (Figure 14(b)).

6. Conclusions

We studied the physics of charge transport in an annulus between concentric circular cylinders from theoretical and

numerical analysis by using a commercial software COMSOL and 2D in-house code.

We have found that the conservation property of the convective terms in the charge transport equation affects numerical accuracy significantly. In both the COMSOL and in-house code simulations, keeping the convective terms in conservative form is essential in maintaining the numerical accuracy. In COMSOL, the conductive terms being treated as sources must also be written in the gradient-of-field form, not in the form of charge so as not to deteriorate the numerical accuracy. Such sensitive dependence of the numerical solutions' accuracy on a small error in the governing equations can be explained in terms of 1D simplified equations.

In the absence of the convection effect, the analytical and numerical solutions of the 1D equations show that the diffusive charge flux is balanced by the conductive flux and the sum of the two fluxes yields the total flux which remains much smaller than the two fluxes for small values of k_i .

The effect of two dimensionless parameters, P and Q , on the solution structure is then studied from the simulation with 2D in-house code. At low values of P , the solutions tend to a one-dimensional nature being independent of z . Increase of P caused by increase of U tends to make the convective effect dominate over the diffusive or conductive effect and the contour of q tends to follow the fluid's streamline pattern, because the time taken by the fluid particle for one complete circulation along the streamline becomes so short that the diffusive or conductive action is ineffective. At low values of Q , on the other hand, q tends to be uniformly distributed, because the diffusion effect is strong compared with conduction. Accordingly, P is less effective at low values of Q ; spatially averaged value of q increases only 2.2% when U increases from 10^{-5} [m/s] to 0.1 [m/s] at $\alpha_\sigma = 10^{-3}$ fixed,

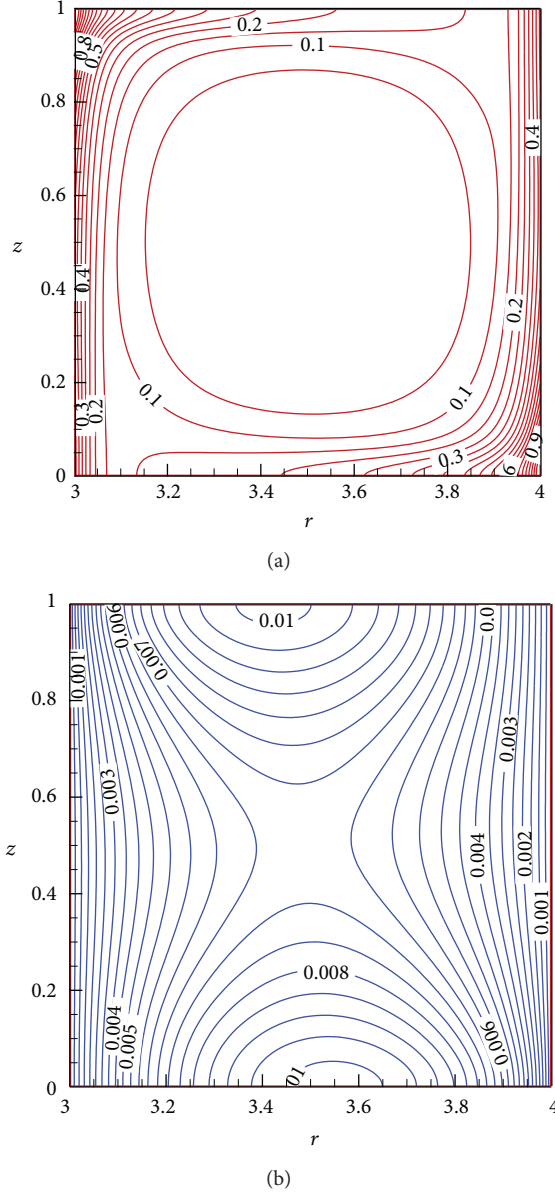


FIGURE 13: Typical solution structure of the system of charge transport equations given numerically at $\alpha_\sigma = 0.2$ and $U = 0.01$ [m/s]; contours of (a) q and (b) ϕ .

whereas it increases 42% at $\alpha_\sigma = 0.2$ for the same increase of U .

Increase of Q caused by increase of σ makes the EDLs thinner and the charge depletion zone wider. Thickness of the passage near the inner and outer walls through which the charge is transmitted from one wall to the other also decreases as Q is increased.

Conflict of Interests

The authors declare that there is no conflict of interests regarding the publication of this paper.

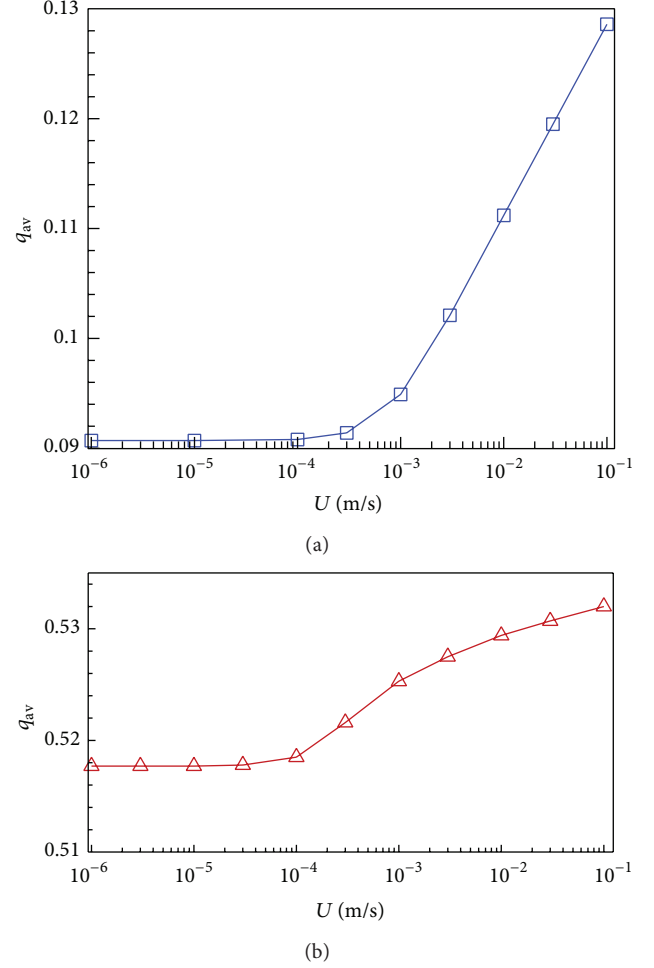


FIGURE 14: Volume-averaged charge density within the annulus given numerically at (a) $\alpha_\sigma = 0.2$ and (b) $\alpha_\sigma = 10^{-3}$.

Acknowledgments

This work was supported by the National Research Foundation of Korea (NRF) Grant funded by the Korean government (MSIP) (no. 2009-0083510). This work was also supported by the Human Resources Development Program (no. 20114030200030) of the Korean Institute of Energy Technology Evaluation and Planning (KETEP) grant funded by the Korean government Ministry of Trade, Industry and Energy. This paper has been read by Professor M. Duffy.

References

- [1] M. Higaki, Y. Kako, M. Moriyama, M. Hirano, K. Hiraishi, and K. Kurita, "Static electrification and partial discharges caused by oil flow in forced oil cooled core type transformers," *IEEE Transactions Power Apparatus and Systems*, vol. 98, no. 4, pp. 1259–1267, 1979.
- [2] M. Higaki, H. Miyao, K. Endou, and H. Ohtani, "A calculation of potential distribution caused by static electrification owing to oil flow in a oil flow in a oil-paper insulation system and its application to partial discharge phenomena in oil," *IEEE*

- Transactions Power Apparatus and Systems*, vol. 98, no. 4, pp. 1275–1282, 1979.
- [3] R. Tamura, Y. Miura, T. Watanabe, T. Ishii, N. Yamada, and T. Nitta, "Static electrification by forced oil flow in large power transformer," *IEEE Transactions on Power Apparatus and Systems*, vol. 99, no. 1, pp. 335–343, 1980.
 - [4] H. L. Walmsley and G. Woodford, "The generation of electric currents by the laminar flow of dielectric liquids," *Journal of Physics D: Applied Physics*, vol. 14, no. 10, article 011, pp. 1761–1782, 1981.
 - [5] H. L. Walmsley, "The generation of electric currents by the turbulent flow of dielectric liquids. II. Pipes of finite length," *Journal of Physics D: Applied Physics*, vol. 16, no. 4, article 016, pp. 553–572, 1983.
 - [6] S. Jayaram, "Effect of streaming potential on heat transfer in transformer oil," *IEEE Transactions on Dielectrics and Electrical Insulation*, vol. 3, no. 3, pp. 410–416, 1996.
 - [7] C.-S. Huh and J.-I. Jeong, "Method to observe the change of charges in an electric double layer between pressboard and the insulating oil in a power transformer," *IEEE Proceedings on Electric Power Applications*, vol. 147, no. 1, pp. 83–86, 2000.
 - [8] J. Kedzia and B. Willner, "Electrification current in the spinning disk system," *IEEE Transactions on Dielectrics and Electrical Insulation*, vol. 1, no. 1, pp. 58–62, 1994.
 - [9] J. C. Gibbings, "Rotating disc studies of streaming current," *Journal of Electrostatics*, vol. 67, no. 4, pp. 559–561, 2009.
 - [10] A. P. Washabaugh, *Flow induced electrification of liquid insulated systems [MIT thesis]*, 1994.
 - [11] A. P. Washabaugh and M. Zahn, "Flow electrification measurements of transformer insulation using a Couette flow facility," *IEEE Transactions on Dielectrics and Electrical Insulation*, vol. 3, no. 2, pp. 161–181, 1996.
 - [12] A. P. Washabaugh and M. Zahn, "A chemical reaction-based boundary condition for flow electrification," *IEEE Transactions on Dielectrics and Electrical Insulation*, vol. 4, no. 6, pp. 688–709, 1997.
 - [13] O. Moreau and G. G. Touchard, "Experimental study and modeling of static electrification in power transformers," *IEEE Transactions on Industry Applications*, vol. 37, no. 4, pp. 971–977, 2001.
 - [14] D. Zmarzly, "Streaming electrification measurements in swinging cylinder system," *IEEE Transactions on Dielectrics and Electrical Insulation*, vol. 19, no. 5, pp. 1665–1672.
 - [15] K. J. Nelson, "Dielectric fluids in motion," *IEEE Electrical Insulation Magazine*, vol. 10, no. 3, pp. 16–28, 1994.
 - [16] J. A. Palmer and J. K. Nelson, "Practical implications of transformer flow electrification studies," *Journal of Electrostatics*, vol. 40–41, pp. 693–698, 1997.
 - [17] G. G. Touchard, "A physicochemical explanation for flow electrification in low-conductivity liquids in contact with a corroding wall," *IEEE Transactions on Industry Applications*, vol. 32, no. 5, pp. 1051–1057, 1996.
 - [18] G. Touchard, "Flow electrification of liquids," *Journal of Electrostatics*, vol. 51–52, no. 1–4, pp. 440–447, 2001.
 - [19] E. Moreau, T. Paillat, and G. Touchard, "Flow electrification in high power transformers: BTA effect on pressboard degraded by electrical discharges," *IEEE Transactions on Dielectrics and Electrical Insulation*, vol. 10, no. 1, pp. 15–21, 2003.
 - [20] A. Bourgeois, T. Paillat, O. Moreau, G. Mortha, and G. Touchard, "Flow electrification in power transformers: salt-type additive as a potential remedy?" *Journal of Electrostatics*, vol. 63, no. 6–10, pp. 877–882, 2005.
 - [21] A. Bourgeois, G. Mortha, T. Paillat, G. Touchard, O. Moreau, and Y. Bertrand, "Flow electrification in power transformers: study of a potential remedy," *IEEE Transactions on Dielectrics and Electrical Insulation*, vol. 13, no. 3, pp. 650–655, 2006.
 - [22] P. Aksamit and D. Zmarzly, "C₆₀ as flow electrification inhibitor in mineral insulating oil," *Journal of Electrostatics*, vol. 69, no. 3, pp. 195–199, 2011.
 - [23] J. M. Cabaleiro, T. Paillat, O. Moreau, and G. Touchard, "Flow electrification of dielectric liquids in insulating channels: Limits to the application of the classical wall current expression," *Journal of Electrostatics*, vol. 66, no. 1–2, pp. 79–83, 2008.
 - [24] M. El-Adawy, J. M. Cabaleiro, T. Paillat, O. Moreau, and G. Touchard, "Experimental determination of space charge density associated with flow electrification phenomenon: application to power transformers," *Journal of Electrostatics*, vol. 67, no. 2–3, pp. 354–358, 2009.
 - [25] J. M. Cabaleiro, T. Paillat, O. Moreau, and G. Touchard, "Electrical double layer's development analysis: application to flow electrification in power transformers," *IEEE Transactions on Industry Applications*, vol. 45, no. 2, pp. 597–605, 2009.
 - [26] T. Paillat, J. Cabaleiro, H. Romat, and G. Touchard, "Flow electrification process: the physicochemical corroding model revisited," *IEEE Transactions on Dielectrics and Electrical Insulation*, vol. 16, no. 2, pp. 359–363, 2009.
 - [27] M. El-Adawy, T. Paillat, G. Touchard, and J. M. Cabaleiro, "Numerical simulation of the electrical double layer development: physicochemical model at the solid and dielectric liquid interface for laminar flow electrification phenomenon," *IEEE Transactions on Dielectrics and Electrical Insulation*, vol. 18, no. 5, pp. 1463–1475, 2011.
 - [28] T. Kobayashi, K. Yajima, S. Yamada, T. Amimoto, and N. Hosokawa, "Increase of static electrification in an aged oil-immersed transformer," *Electrical Engineering in Japan*, vol. 167, no. 3, pp. 10–19, 2009.
 - [29] S. Okabe, M. Kotoh, M. Tsuchie, and T. Amimoto, "Influence of various compounds on electrostatic charging tendency in insulating oil," *Electrical Engineering in Japan*, vol. 176, no. 3, pp. 29–36, 2011.
 - [30] D. A. Bogachev, S. Martemianov, and T. Paillat, "Modelling of electrification in steady state and transient regimes," *Journal of Electrostatics*, vol. 70, pp. 517–523, 2012.
 - [31] T. Paillat, Y. Z. G. Morin, and C. Perrier, "Ester oils and flow electrification hazards in power transformers," *IEEE Transactions on Dielectrics and Electrical Insulation*, vol. 19, no. 5, pp. 1537–1543, 2012.
 - [32] C. B. Liao, S. J. Jane, and D. L. Young, "Numerical simulation of three-dimensional Couette-Taylor flows," *International Journal for Numerical Methods in Fluids*, vol. 29, pp. 827–847, 1999.
 - [33] E. L. Koschmieder, *Benard Cells and Taylor Vortices*, Cambridge University Press, 1993.
 - [34] M. Abramowitz and I. A. Stegun, *Handbook of Mathematical Functions*, Dover, 1972.

Research Article

A Numerical Scheme Based on an Immersed Boundary Method for Compressible Turbulent Flows with Shocks: Application to Two-Dimensional Flows around Cylinders

Shun Takahashi,¹ Taku Nonomura,² and Kota Fukuda³

¹ Department of Prime Mover Engineering, Tokai University, Hiratsuka, Kanagawa 259-1292, Japan

² Department of Space Flight Systems, Institute of Space and Astronautical Science, Japan Aerospace Exploration Agency, Sagami-hara, Kanagawa 252-5210, Japan

³ Department of Aeronautics and Astronautics, Tokai University, Hiratsuka, Kanagawa 259-1292, Japan

Correspondence should be addressed to Shun Takahashi; takahasi@tokai-u.jp

Received 12 October 2013; Accepted 31 December 2013; Published 6 March 2014

Academic Editor: Luís Godinho

Copyright © 2014 Shun Takahashi et al. This is an open access article distributed under the Creative Commons Attribution License, which permits unrestricted use, distribution, and reproduction in any medium, provided the original work is properly cited.

A computational code adopting immersed boundary methods for compressible gas-particle multiphase turbulent flows is developed and validated through two-dimensional numerical experiments. The turbulent flow region is modeled by a second-order pseudo skew-symmetric form with minimum dissipation, while the monotone upstream-centered scheme for conservation laws (MUSCL) scheme is employed in the shock region. The present scheme is applied to the flow around a two-dimensional cylinder under various freestream Mach numbers. Compared with the original MUSCL scheme, the minimum dissipation enabled by the pseudo skew-symmetric form significantly improves the resolution of the vortex generated in the wake while retaining the shock capturing ability. In addition, the resulting aerodynamic force is significantly improved. Also, the present scheme is successfully applied to moving two-cylinder problems.

1. Introduction

The acoustic waves from rocket plumes are sufficiently strong to damage the satellites inside the fairing of a rocket. These waves are widely assessed by empirical prediction methods [1], but the low accuracy of these methods renders them unsuitable for new rocket launch sites. To improve the prediction accuracy of acoustic waves from rocket plumes, a sophisticated model based on the underlying physics is required. Numerical simulations are an essential component of new model development [2–5]. The behavior of acoustic waves from rocket plumes is difficult to predict, because actual plumes are very hot, with very high speed, and of the multiple phase conditions. In real rocket systems, acoustic waves are suppressed by a water injection system installed at the rocket launch site. Fukuda et al. [6] showed that rarefaction or absorption of acoustic waves by particles exerts no significant effect and that acoustic waves might be primarily attenuated

by interactions between particles and turbulence. However, this scenario is not well modeled in their study. To more accurately evaluate acoustic wave suppression by particle-turbulence interactions, further fundamental analyses are necessary. Therefore, we consider a multiscale analysis of gas-particle multiphase high-speed compressible flows. Because the target is a rocket plume, we propose a simultaneous treatment of the turbulence and the shock waves. Figure 1 shows an overview of the proposed numerical approach. The simultaneous high-resolution simulation of the particles and turbulence is conducted on the microscale, the large eddy simulation (LES) modeling only the particle behavior is conducted on the intermediate scale, and the complex flow fields are modeled by the Reynolds-averaged Navier-Stokes (RANS) simulation.

Speeds of these scattering particles cover a wide range of Mach numbers from subsonic to supersonic, while Reynolds numbers are quite low since the sizes of the particles are small.

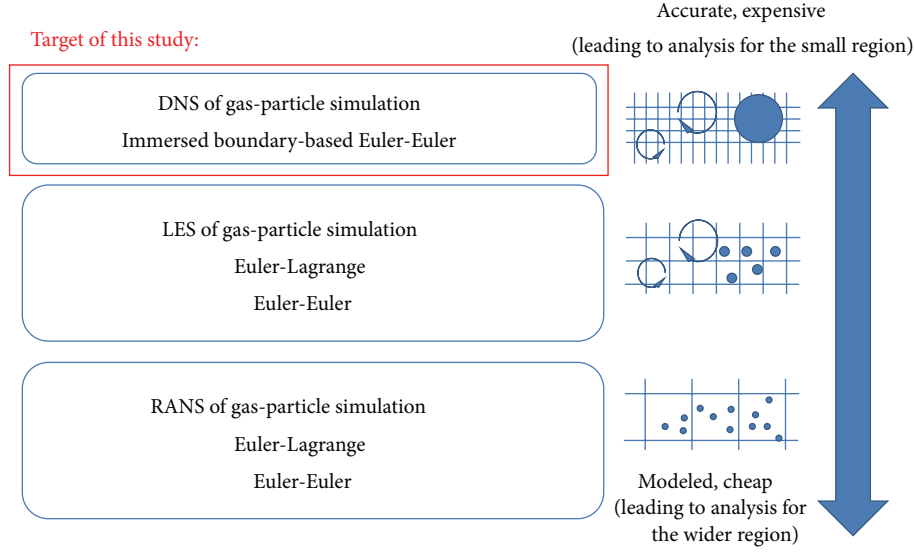


FIGURE 1: Overview of the proposed gas-particle simulation.

Therefore, flowfields around the small particles can be solved by flow simulation without any turbulence models though the flowfield is macroscopically turbulent. There are several kinds of numerical methods to solve the problem treating a number of moving objects, such as dynamic mesh method [7] or overset method [8]. However, simple implementation and rapid computation are difficult to achieve in using these methods because additional numerical processes are included in the flow simulation like mesh regeneration or interpolation between computational grids. We select level set method [9] to track a number of moving particles in this study. There are some other options to trace many moving objects with high accuracy like phase field method or front tracking method. However, our main focus is investigation of the acoustic wave characteristics under interference between turbulence and particles. Therefore, level set method is selected based on computational efficiency. The represented boundaries by level set method are imposed by immersed boundary method [10] in equally spaced Cartesian mesh in this study. Immersed boundary method (IBM) is widely used in the community of Cartesian mesh method from the simplicity and applicability. The methodology of IBM can be classified into several categories such as continuous forcing method [11], direct forcing method, and ghost-cell method [10]. Although IBM was originally proposed and used for incompressible flow simulations, it is also applied to compressible flow simulations [12–15], recently. Takahashi et al. have been developing several Cartesian flow solvers [15–21] and investigating the performance of this kind of numerical method. Based on the background, we adopted ghost-cell method [10, 15] with equally spaced Cartesian mesh by the points of simple implementation, robustness, and extensibility.

Here, we should recall our flow features that consist of both turbulence and shocks. In general, an upwind scheme is often employed to evaluate inviscid fluxes in IBM flow

solver to stabilize a flow with numerical dissipation. The dissipation is not preferable to solve our flows of turbulence part clearly, while it should be added appropriately to capture the shocks in a part of our flows. In other words, we should minimize numerical dissipation in the turbulent region, while the dissipation must be added to prevent spurious oscillations around shocks. In resolving both the turbulence and shock waves, dissipation switching scheme can play a major role. In this study, a switching procedure for numerical dissipation is introduced and examined through the two-dimensional test cases. This study overviews the computational code and demonstrates its efficacy in simulations of two-dimensional static cylinder flows under various Mach number conditions. The present numerical method is developed to three-dimensional problem of interference among turbulence, shocks, and particles with high-performance parallel computing based on the previous studies [16, 17, 20, 21].

2. Computational Methods

2.1. Governing Equations and Numerical Method. In the present study, flows are governed by two-dimensional compressible Navier-Stokes equations. No averaging or filtering process is involved and the flows are solved without any turbulence models:

$$\frac{\partial Q}{\partial t} + \frac{\partial E}{\partial x} + \frac{\partial F}{\partial y} = \frac{\partial E_v}{\partial x} + \frac{\partial F_v}{\partial y}$$

$$Q = \begin{bmatrix} \rho \\ \rho u \\ \rho v \\ \rho e \end{bmatrix}, \quad E = \begin{bmatrix} \rho u \\ \rho u^2 + p \\ \rho uv \\ (\rho e + p)u \end{bmatrix}, \quad F = \begin{bmatrix} \rho v \\ \rho vu \\ \rho v^2 + p \\ (\rho e + p)v \end{bmatrix},$$

$$E_v = \begin{bmatrix} 0 \\ \tau_{xx} \\ \tau_{xy} \\ \tau_{xx}u + \tau_{xy}v + \kappa T_x \end{bmatrix}, \quad F_v = \begin{bmatrix} 0 \\ \tau_{yx} \\ \tau_{yy} \\ \tau_{yx}u + \tau_{yy}v + \kappa T_y \end{bmatrix}, \quad (1)$$

where E and F are the inviscid fluxes in the x - and y -directions, respectively, E_v and F_v are the corresponding viscous fluxes, and Q contains the conservative variables. Here the stress tensor components are given as

$$\begin{aligned} \tau_{xx} &= \frac{2}{3}\mu(2u_x - v_y), & \tau_{xy} &= \tau_{yx} = \mu(u_y + v_x), \\ \tau_{yy} &= \frac{2}{3}\mu(2v_y - u_x). \end{aligned} \quad (2)$$

The pressure p is related to the total energy e per unit mass by the equation of state:

$$\rho e = \frac{p}{\gamma - 1} + \frac{1}{2}\rho(u^2 + v^2). \quad (3)$$

The heat flux term in the equation of total energy is computed by

$$\kappa T_x = \frac{\mu}{\text{Pr}} \frac{\gamma}{\gamma - 1} \left(\frac{p}{\rho} \right)_x, \quad \kappa T_y = \frac{\mu}{\text{Pr}} \frac{\gamma}{\gamma - 1} \left(\frac{p}{\rho} \right)_y, \quad (4)$$

where the equation is transformed by the ideal gas equation and Prandtl number as follows:

$$C_p T = e + \frac{p}{\rho} - \frac{1}{2}(u^2 + v^2), \quad \text{Pr} = \frac{C_p \mu}{\kappa}. \quad (5)$$

All variables are nondimensionalized by the freestream conditions of density, sound speed, and unit length. The above equations are discretized on an equally spaced Cartesian mesh with a cell-centered arrangement. To eliminate additional numerical dissipation everywhere, except in the vicinities of shock waves and potential flows, the inviscid terms are computed by a hybrid scheme that combines the pseudo skew-symmetric central difference scheme [22] with the monotone upstream-centered scheme for conservation laws (MUSCL)-Roe scheme [23, 24]. The flux in the turbulent region is modeled by a pseudo skew-symmetric central difference scheme with a minimum dissipation term as follows:

$$\begin{aligned} E_{i+1/2, \text{turbulent}} &= E_{i+1/2, \text{cent}} + \sigma_{i+1/2, \text{cent}}, \\ E_{i+1/2, \text{cent}} &= \begin{bmatrix} \frac{1}{4}(\rho_i + \rho_{i+1})(u_i + u_{i+1}) \\ \frac{1}{8}(\rho_i + \rho_{i+1})(u_i + u_{i+1})^2 + \frac{1}{2}(\rho_i + \rho_{i+1}) \\ \frac{1}{8}(\rho_i + \rho_{i+1})(u_i + u_{i+1})(v_i + v_{i+1}) \\ \frac{1}{4}(\rho_i e_i + \rho_{i+1} e_{i+1} + p_i + p_{i+1})(u_i + u_{i+1}) \end{bmatrix}, \\ \sigma_{i+1/2, \text{cent}} &= \frac{1}{4}\chi(\rho_i + \rho_{i+1})(u_i + u_{i+1}) \begin{bmatrix} 0 \\ u_{i+1/2, R} - u_{i+1/2, L} \\ v_{i+1/2, R} - v_{i+1/2, L} \\ e_{i+1/2, R} - e_{i+1/2, L} \end{bmatrix}. \end{aligned} \quad (6)$$

Here the subscript i denotes the quantity on the i th grid point and subscripts L and R denote the left- and right-side states, respectively, interpolated by the third-order MUSCL scheme [24] with van Albada's limiter [25].

On the other hand, the flux in the shock and potential flow region, computed by the second-order MUSCL-Roe scheme, is written as follows:

$$E_{i+1/2, \text{shock}} = \frac{1}{2}(E_i + E_{i+1} + |A_{i+1/2, \text{Roe}}|(Q_{i+1/2, R} - Q_{i+1/2, L})), \quad (7)$$

where A is the flux Jacobian and the subscript Roe denotes the Roe-averaged quantity of the left and right states. Here

$$|A| = R|\Lambda|L, \quad (8)$$

where R and L are the right and left eigenmatrices of A , respectively, and $\Lambda = LAR$ is a diagonal matrix.

The symmetric central difference part of (8) can be replaced by that of the pseudo skew-symmetric form without losing the formal order of accuracy of the equation. The proposed scheme adopts the following new form of (7):

$$E_{i+1/2, \text{shock}} = E_{i+1/2, \text{cent}} + \frac{1}{2}(|A_{i+1/2, \text{Roe}}|(Q_{i+1/2, R} - Q_{i+1/2, L})). \quad (9)$$

Combining this with the digital switching function, we obtain the following hybrid scheme:

$$\begin{aligned} E_{i+1/2} &= (1 - \beta_{i+1/2})E_{i+1/2, \text{turbulent}} + \beta_{i+1/2}E_{i+1/2, \text{shock}} \\ &= E_{i+1/2, \text{cent}} + (1 - \beta_{i+1/2})\sigma_{i+1/2} \\ &\quad + \beta_{i+1/2} \frac{1}{2}(|A_{i+1/2, \text{Roe}}|(Q_{i+1/2, R} - Q_{i+1/2, L})). \end{aligned} \quad (10)$$

Excessive dissipation is added to the shock or potential flow region when beta is unity, whereas dissipation is minimized when beta is zero. $\beta_{i+1/2}$ is defined in terms of the Ducros-type sensor [26] as follows:

$$\begin{aligned} \beta_{i+1/2} &= \min(1, \phi_i + \phi_{i+1}), \\ \phi &= \begin{cases} 0 & \frac{|\nabla \cdot u|^2}{|\nabla \cdot u|^2 + |\nabla \times u|^2 + \varepsilon} < \theta \\ 1 & \frac{|\nabla \cdot u|^2}{|\nabla \cdot u|^2 + |\nabla \times u|^2 + \varepsilon} \geq \theta. \end{cases} \end{aligned} \quad (11)$$

Here $\varepsilon = 10^{-15}$ is a small value that prevents division by zero and $\theta = 0.6$ is the switching threshold. The divergence and rotation in (11) are computed by a second-order finite difference scheme. In the present study, the Ducros-type sensor [26] alone is used in both the shock and potential flow regions, although previous studies have combined this sensor with the Jameson sensor [27] in the shock region [26, 28]. Furthermore, in one of our proposed schemes, $\beta_{i+1/2}$ is set to unity in cells close to the body. Finally, the flux derivative is approximated as follows:

$$\frac{\partial E}{\partial x} = \frac{E_{i+1/2} - E_{i-1/2}}{\Delta x}. \quad (12)$$

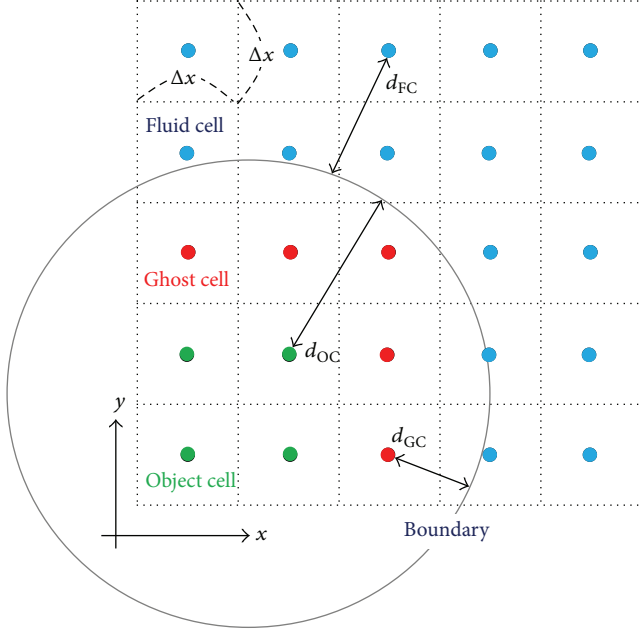


FIGURE 2: Cell construction and classification in the present level set method.

The derivative $\partial F/\partial y$ is obtained similarly.

The diffusive terms are treated by a second-order, central difference scheme using the mid-point flux. The time marching is conducted by the three-stage total variation diminishing Runge-Kutta scheme [29]. In this study, time increment is determined as follows:

$$\Delta t = c \frac{\Delta x}{a_{\infty} + |u_{\infty}| + |v_{\infty}| + |u_{\text{obj}}| + |v_{\text{obj}}|}. \quad (13)$$

2.2. Boundary Representation. The boundary is defined by the level set method [9, 14]. The level set function is determined in whole cells as a signed distance from the object boundary. A schematic of the cells around a boundary is shown in Figure 2. The level set method effectively computes the normal vector from the object surface on the basis of a gradient operation. In the present study, flows around multiple moving objects are solved by extending the level set method to multiple level set functions based on simple minimum distance approach [8].

On the basis of the level set function (14), all cells are classified into three categories: fluid cell, ghost cell, and object cell, as shown in Figure 2. The ghost cells behave as guard cells between the fluid and object regions and are assigned in two layers under the present definition as follows:

$$\begin{aligned} d_{\text{FC}} &> 0, & d_{\text{GC}} &\leq 0, & d_{\text{GC}} &\geq -2\sqrt{2}\Delta x, \\ d_{\text{OC}} &< -2\sqrt{2}\Delta x. \end{aligned} \quad (14)$$

Ghost cells are used for imposing boundary condition in the present method [10, 15]. An image point set in the region of fluid cells is used to collect flow information for a ghost cell. A primary advantage of the present ghost-cell

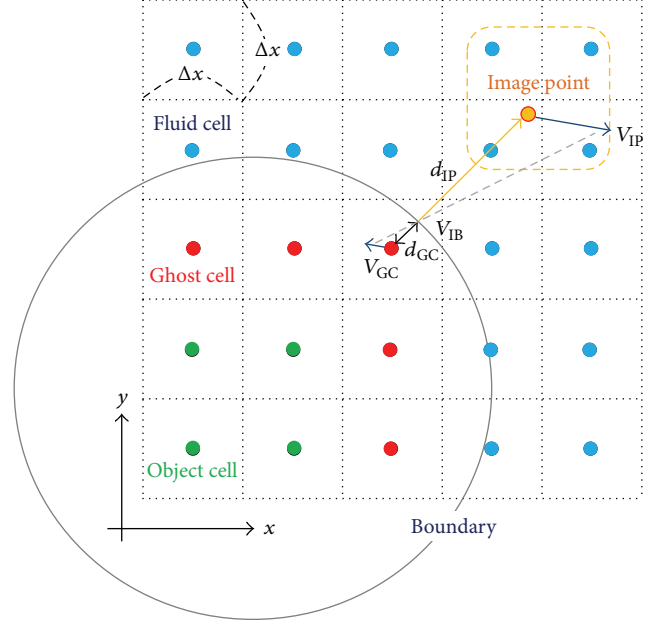


FIGURE 3: Schematic of the present ghost cell approach with image point.

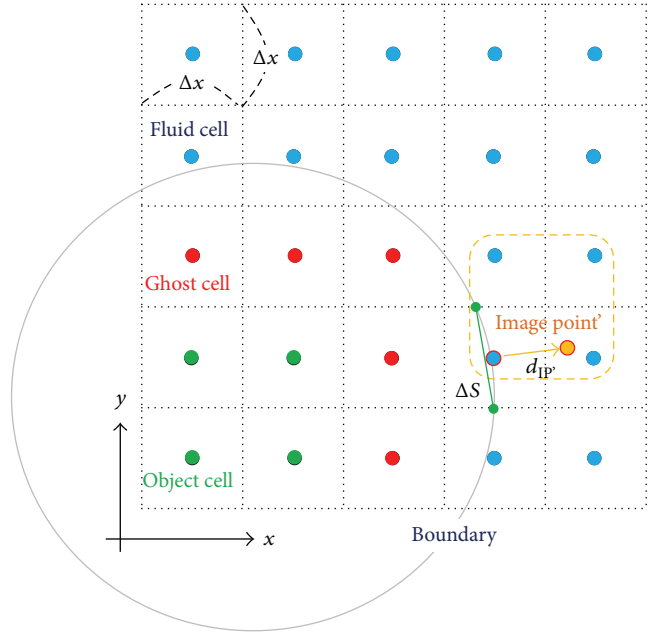


FIGURE 4: Image point projected from a fluid cell to compute the fluid force on the surface.

method adopting the image point approach is its robustness. A schematic of the present immersed boundary method is shown in Figure 3. The image point is located at the edge of a probe that extends from a ghost cell through the object boundary in the direction normal to the surface. The length of the probe, denoted as d_{IP} in Figure 3, is an important parameter that eliminates recursive interpolation. Here we fix the length of d_{IP} as 1.75 times the mesh size, considering

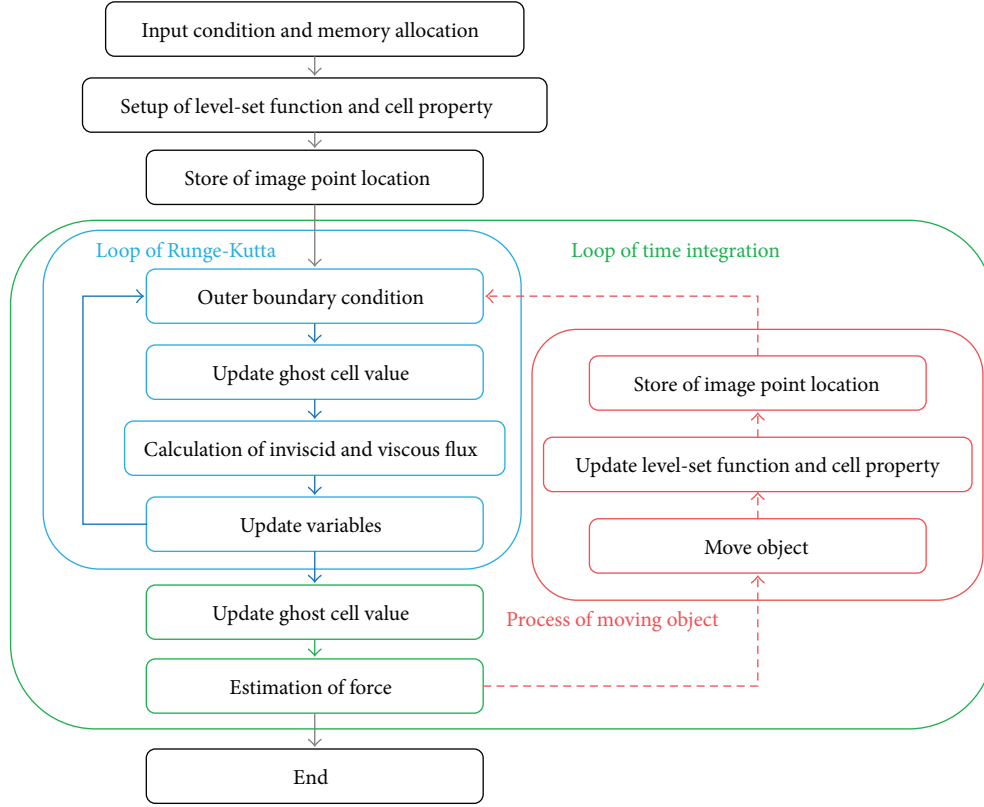


FIGURE 5: Flowchart of the present numerical method.

the extension to the three-dimensional problem. Because the probe is longer than $\sqrt{3}$ times the mesh size, the nodes enclosed by the orange dotted square in Figure 3 are classified only as fluid cells. The primitive variables on the image point are interpolated by the bilinear function based on the surrounding cells. Finally, the value of the ghost cell is defined by the value of the image point. The flow velocity, computed by (15), is assumed to be linearly distributed along the probe from the boundary point to image point. For the pressure and density, a Neumann condition is assumed on the boundary and the ghost cell is assigned the value of its corresponding image point:

$$\mathbf{V}_{GC} = \mathbf{V}_{IP} - \frac{d_{IP} + d_{GC}}{d_{IP}} (\mathbf{V}_{IP} - \mathbf{V}_{IB}). \quad (15)$$

2.3. Estimation of Friction Force. The fluid force acting on an object is estimated by surface integration. Fluid forces must be evaluated at both ghost and fluid cells because the object boundary can straddle both cells, as shown in Figure 4. For the ghost cells, the image point for the immersed boundary method is directly available for calculating the fluid force on the surface. In the case of fluid cells, on the other hand, the small distance between the surface and fluid cell can magnify the friction force wrongly. Therefore, the friction force on the fluid cell is estimated by using the image point method with changed probe length to $\sqrt{2}/2$ times the mesh

size. This value $\sqrt{2}/2$ is determined to adopt only fluid cells as interpolation cells for the image point. In this case, the viscous force is estimated by (16). The velocity component in the following equation corresponds to the component parallel to the boundary:

$$f_{IB} = \mu \frac{V_{IP'} - V_{IB}}{d_{IP'} + d_{FC}} \Delta S. \quad (16)$$

Our code supports a simpler but accurate force estimation method without the information of a level set function [30], but this option is not considered here.

2.4. Outer Boundary Conditions. While supersonic flows can be solved by applying Neumann conditions at the outer boundary, this approach can induce instabilities in subsonic flow simulations. Therefore, we apply a sponge region [31] near the outer boundary to suppress sound reflections with imposing a Dirichlet condition on the density at the outflow boundary. This boundary condition ensures numerical stability of flows with vortical wakes.

2.5. Coding Flowchart. Figure 5 shows a flowchart of the computational procedures. The loop of the three-stage Runge-Kutta time integration is iterated three times in the blue box. Immediately before flux computation, the ghost cells that specify the inner boundary condition of the fluid-cell neighboring boundary are updated. If the flows contain

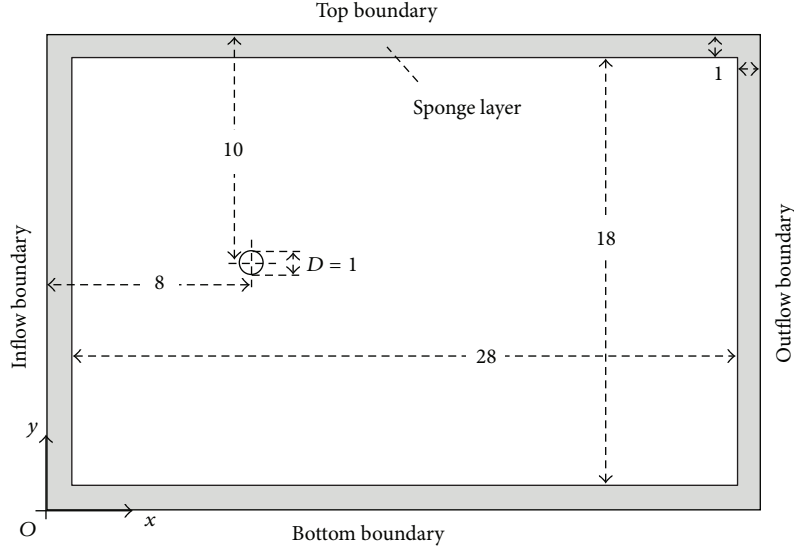
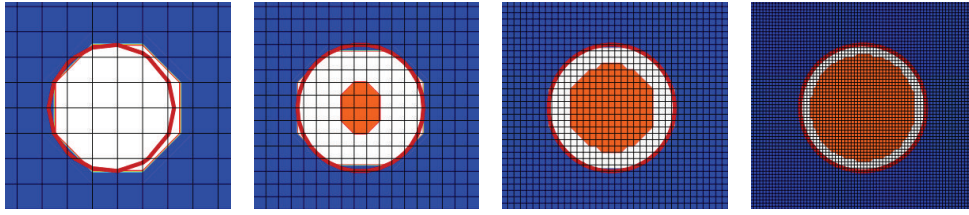


FIGURE 6: Schematic of the computational domain.

FIGURE 7: Computational meshes around a cylinder ($dx = 0.2D, 0.1D, 0.05D, 0.025D$).

moving objects, the level set function, cell classification, and image point identification are reexecuted before the Runge-Kutta loop as shown in the red box. Prior to computing the viscous forces using the ghost cell values, the ghost cells are again updated.

3. Computational Result of Flow around a Two-Dimensional Circular Cylinder

3.1. Computational Condition. The proposed scheme is evaluated through a series of numerical tests. The proposed schemes are compared with the conventional MUSCL-Roe scheme at different grid resolutions. Three methods for estimating the inviscid flux as shown in Table 1 are compared: (A) the present scheme (10) over the whole region, (B) enforcing the MUSCL-Roe scheme for nearby objects and the present scheme for other regions, and (C) the MUSCL-Roe scheme over the whole region. In the present implementation, there is no difference about the computational cost to calculate the fluxes based on (A), (B), and (C). The characteristics of the schemes are investigated on subsonic and supersonic flows around a two-dimensional circular cylinder. The Reynolds number, based on the cylinder diameter and freestream values (including viscosity), is fixed at 300, while the freestream Mach numbers are varied as Mach 0.3, 1.2, and 2.0. Four

mesh sizes are compared: $0.200D$, $0.100D$, $0.050D$, and $0.025D$, where the diameter D of the circular cylinder is fixed at 1. The parameters in all trials are summarized in Table 2. The computational domain is shown in Figure 6. We investigated the validity to employ the size of computational domain with comparing square domain of $40D$. The flow simulations are conducted with a Courant number of 0.4. It was confirmed that there was no significant effect about the Courant number with comparing results from Courant number 0.2. Dirichlet conditions are imposed on all flow variables at the inflow boundary and on density alone at the outflow boundary. Other variables are assigned Neumann conditions at the outflow boundary. Neumann conditions are imposed at the top and bottom boundaries for all variables. The circular cylinders represented by the four mesh sizes are illustrated in Figure 7. The black solid lines are grid lines connecting cell centers. The bold red line is the boundary of the circular cylinder immersed in the Cartesian mesh. The blue, white, and red regions show fluid, ghost, and object cells, respectively. The boundary layer thickness is roughly estimated as $1/\sqrt{Re}$, that is, $0.058D$. Consequently, the boundary layer is discretized by two or three cells in using $0.025D$ mesh size at Reynolds number 300.

In addition, the present results are compared with the recent “state-of-the-art” WENO body-fitted coordinate computational code. This code is based on the sixth-order

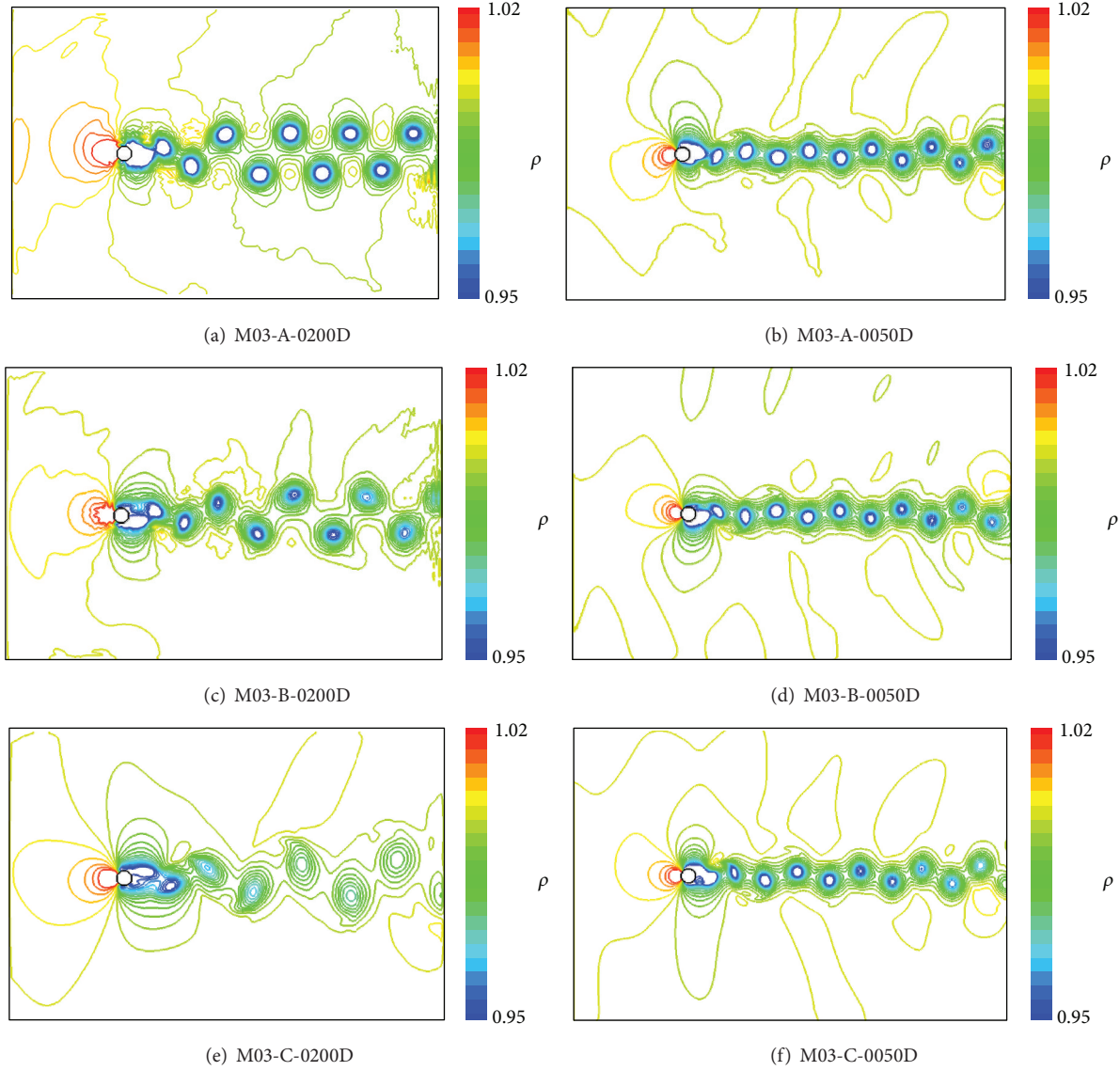


FIGURE 8: Density contours in Mach 0.3.

WENO-CU developed by Hu et al. [32] and extended to the body-fitted coordinate system by Nonomura et al. [33]. The number of grid points is 208×177 . The result obtained by this code is used as a reference solution. We confirmed that the 208×177 mesh is sufficiently fine to generate a reference solution by comparing the results with those obtained on a finer grid (410×268). The results output by this code are presented in the Appendix.

3.2. Comparison of Computational Results at M 0.3. Figure 8 shows the density distribution at Mach 0.3. The top, central, and bottom columns show the results from schemes A, B, and C, respectively. The left and right panels were computed on mesh sizes of $0.200D$ and $0.050D$, respectively. Clearly, the vortices are collapsed when the MUSCL-Roe scheme is implemented on the coarse mesh (M03-C-0200D; bottom left of Figure 8). On the other hand, the present scheme

A preserves the flow features at all mesh resolutions. All schemes yield similar results on the fine mesh.

The differences among the three schemes are confirmed from pressure distributions and the time history of aerodynamic coefficients at mesh size $0.050D$. The results are shown in Figure 9. In scheme A, although high vortex resolution is achieved in the pressure contours, pressure oscillation is also observed near the cylinder. The oscillation is not preferable for stable computation. On the other hand, scheme C yields smooth pressure distribution and history of aerodynamic coefficients. The vortices in scheme C are more dissipative than those of scheme A. The strong features of schemes A and C, vortex conservation and pressure oscillation suppression, are realized in scheme B.

Figure 10 plots the distributions of the switching parameter β in (11). Schemes A and B are adopted at mesh sizes $0.100D$ and $0.025D$. The black and white regions are

TABLE 1: Numerical schemes for estimating inviscid flux.

Scheme type	Scheme A	Scheme B	Scheme C
	Present scheme for all regions	Present scheme + MUSCL-Roe scheme for nearby objects	MUSCL-Roe scheme

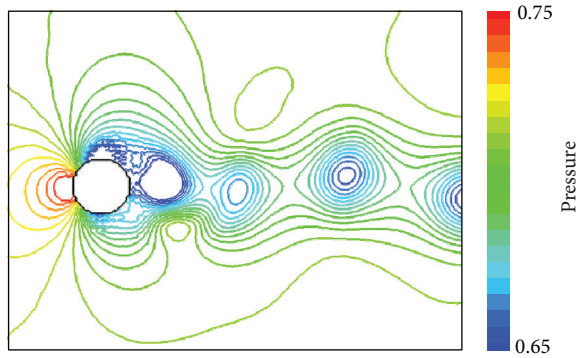
TABLE 2: Test cases.

Re	Mach	Scheme	Mesh size	Case
300	0.3	A (10)	0.2D	M03-A-0200D
			0.1D	M03-A-0100D
			0.05D	M03-A-0050D
			0.025D	M03-A-0025D
		B ((10) and MUSCL-Roe [22, 23] for nearby body)	0.2D	M03-B-0200D
			0.1D	M03-B-0100D
			0.05D	M03-B-0050D
			0.025D	M03-B-0025D
		C (MUSCL-Roe [22, 23])	0.2D	M03-C-0200D
			0.1D	M03-C-0100D
			0.05D	M03-C-0050D
			0.025D	M03-C-0025D
300	1.2	A (10)	0.2D	M12-A-0200D
			0.1D	M12-A-0100D
			0.05D	M12-A-0050D
			0.025D	M12-A-0025D
		B ((10) and MUSCL-Roe [22, 23] for nearby body)	0.2D	M12-B-0200D
			0.1D	M12-B-0100D
			0.05D	M12-B-0050D
			0.025D	M12-B-0025D
		C (MUSCL-Roe [22, 23])	0.2D	M12-C-0200D
			0.1D	M12-C-0100D
			0.05D	M12-C-0050D
			0.025D	M12-C-0025D
300	2.0	A (10)	0.2D	M20-A-0200D
			0.1D	M20-A-0100D
			0.05D	M20-A-0050D
			0.025D	M20-A-0025D
		B ((10) and MUSCL-Roe [22, 23] for nearby body)	0.2D	M20-B-0200D
			0.1D	M20-B-0100D
			0.05D	M20-B-0050D
			0.025D	M20-B-0025D
		C (MUSCL-Roe [22, 23])	0.2D	M20-C-0200D
			0.1D	M20-C-0100D
			0.05D	M20-C-0050D
			0.025D	M20-C-0025D

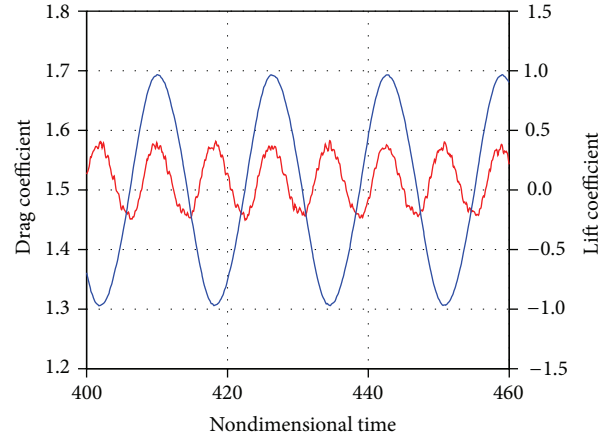
solved by the present scheme (10) and MUSCL-Roe [22, 23] scheme, respectively. On the coarse mesh, the switching function is rendered ineffective by numerical error and small perturbation. In scheme B, however, where the MUSCL-Roe scheme is applied only near the object, the performance of the switching function is superior to that of scheme A.

While the switching scheme improves at finer mesh resolution in both cases, scheme B shows good performance at all mesh resolutions.

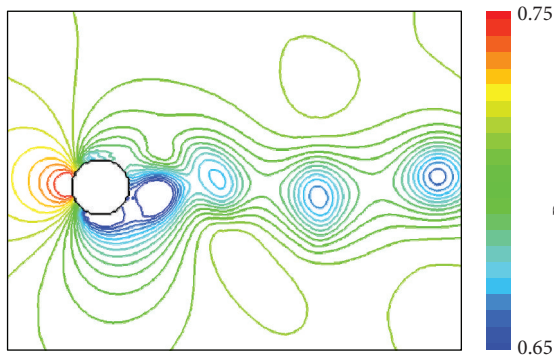
Figure 11 summarizes the results at Mach 0.3. The reference values were obtained from a boundary-fitted mesh simulation shown in the Appendix. Although grid convergence



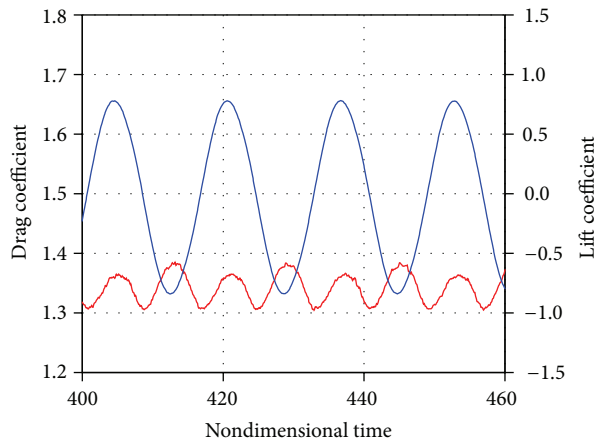
(a) M03-A-0050D



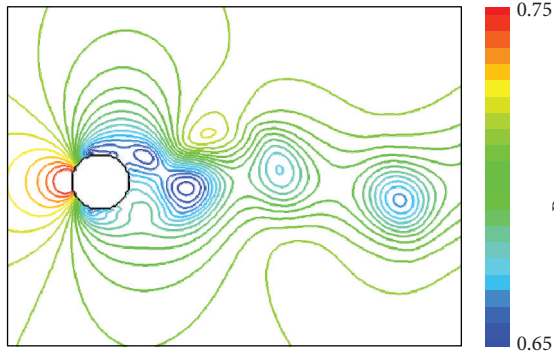
(b) M03-A-0050D



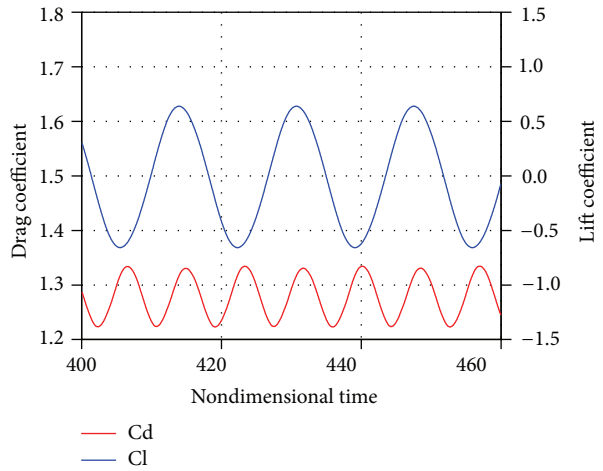
(c) M03-B-0050D



(d) M03-B-0050D



(e) M03-C-0050D



(f) M03-C-0050D

FIGURE 9: Pressure contours (left) and time variation of aerodynamic coefficient (right).

is almost obtained for the lift coefficient amplitudes, Strouhal number, and average drag coefficient, the convergence is not monotonic. One of the reasons of the inflected convergence that can occur is interference between the present switching scheme of different spatial accuracy (third-order

MUSCL-Roe and second-order pseudo skew-symmetric) and immersed boundary method. The lift and drag coefficients are overestimated and underestimated, respectively, in schemes A and C. In the case of scheme B, the lift and drag coefficients are intermediate between schemes A and C.

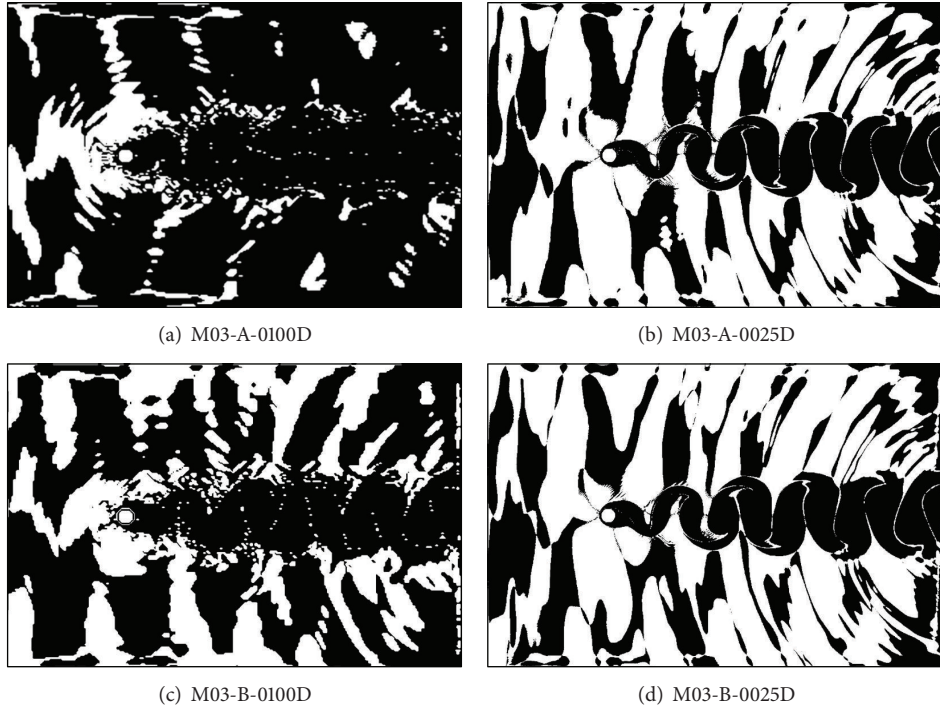
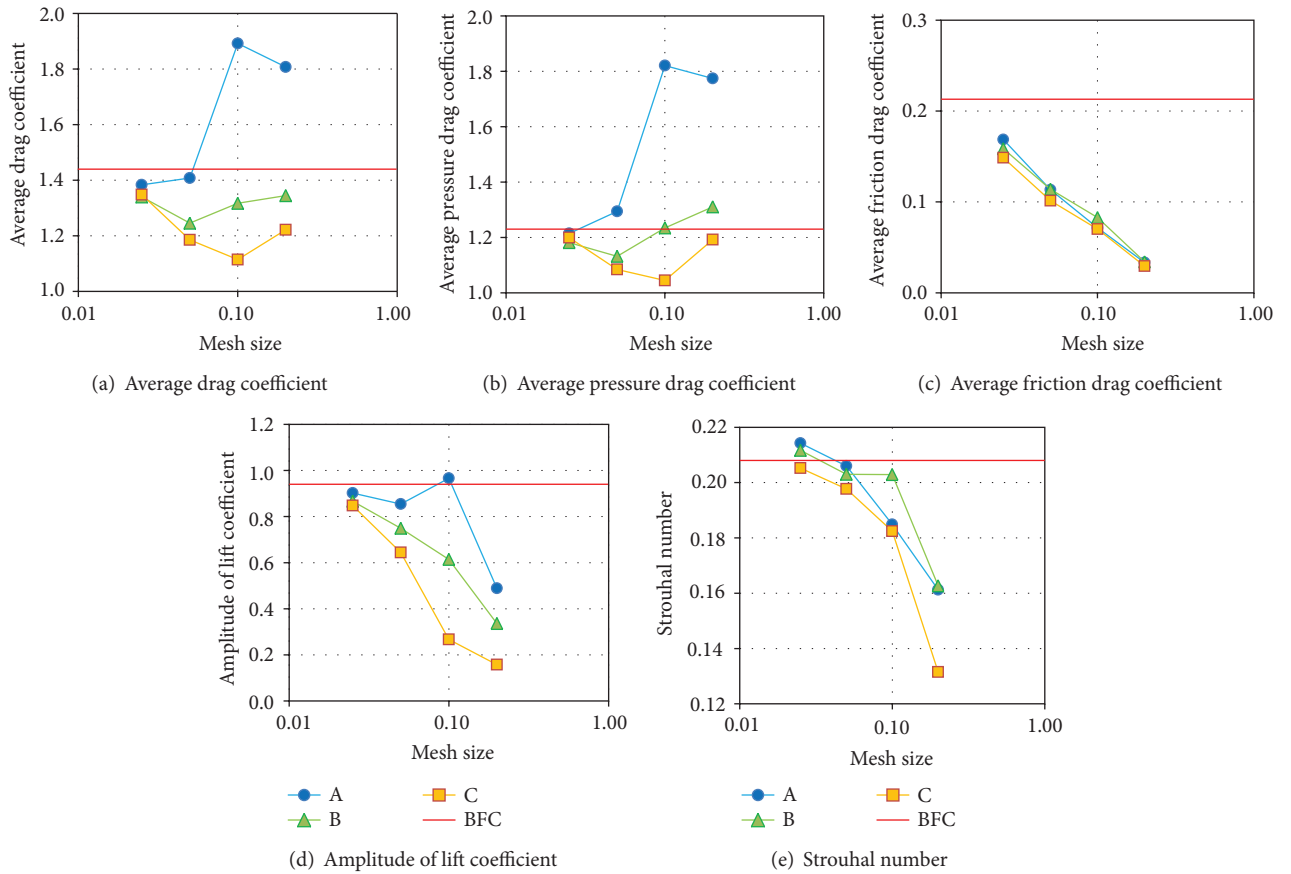
FIGURE 10: Visualization of switching parameter β (white: $\beta = 1$, black: $\beta = 0$).

FIGURE 11: Effect of mesh size on aerodynamic coefficients at Mach 0.3. The red lines are reference values.

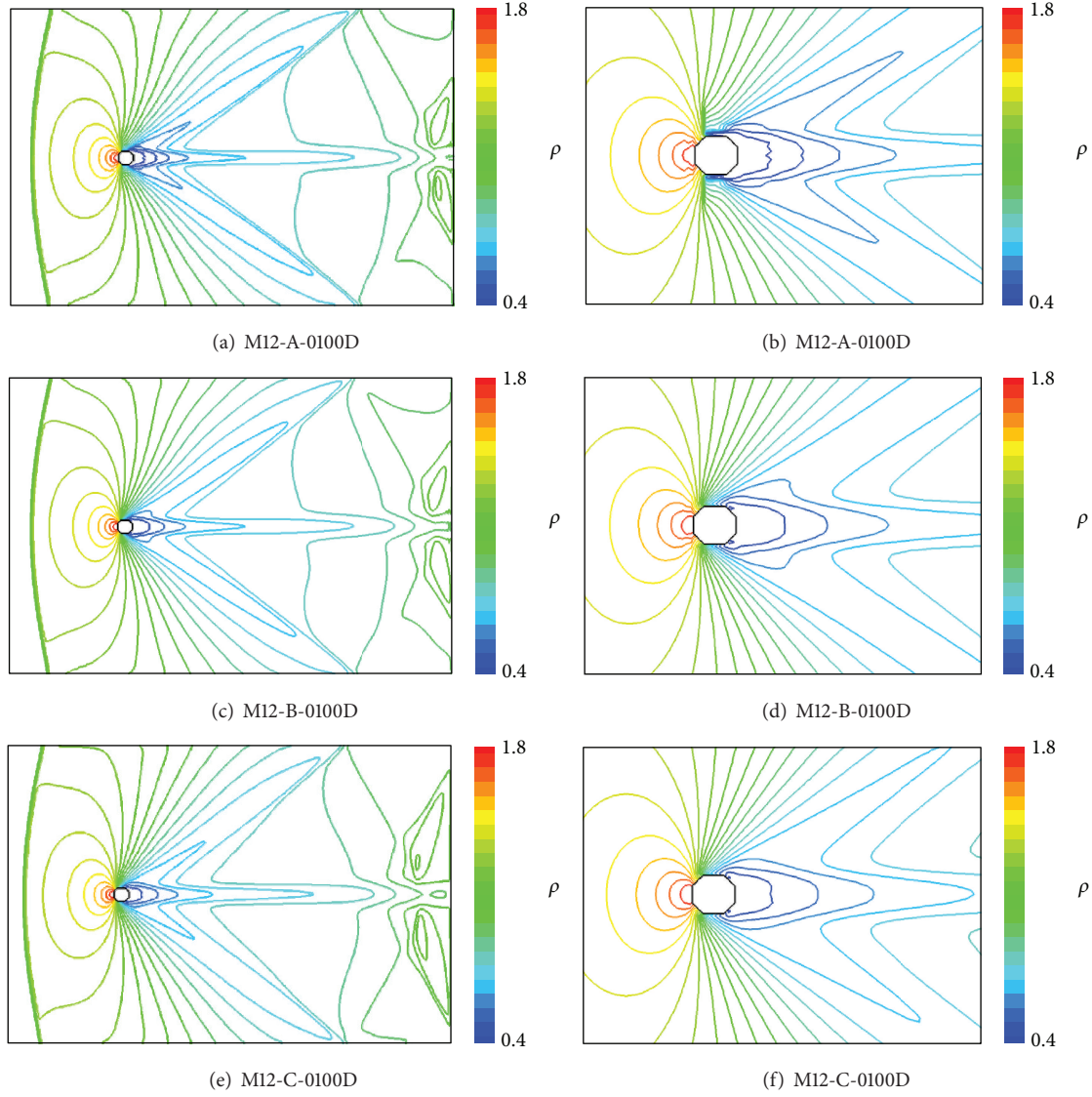


FIGURE 12: Density contours in Mach 1.2.

The friction drag coefficient follows the same trend in all schemes and never completely converges. The boundary layer, which is discretized by several grid points even in the finest grid resolution $0.025D$, is not sufficiently resolved to show grid convergence since the thickness is roughly estimated by $D/\sqrt{\text{Re}}$ as $0.058D$.

3.3. Comparison of Computational Results at $M 1.2$. Figure 12 plots the density contours over the whole computational region and in the near field of the object at mesh size $0.100D$. Obtained flowfield becomes almost symmetrically different from the previous subsonic case. The trend of the flow resolution is similar to the previously discussed subsonic case. Scheme A captures a sharper distribution than scheme C but develops weak numerical oscillation. Reasonable results are obtained by scheme B, in which regions far and near the object are evolved under schemes A and C, respectively.

The distribution of β at mesh size $0.100D$ is similar among the three schemes (Figure 13). At Mach 1.2, the white region (solved by scheme C) enlarges relative to that at Mach 0.3. The dependency of drag coefficient on grid resolution is similar to that of Mach 0.3 (Figure 14), although the drag coefficients are more similar among the three schemes. A likely reason for this trend is that the region solved by scheme C becomes wider in Mach 1.2 than in Mach 0.3.

3.4. Comparison of Computational Results at $M 2.0$. At Mach 2.0, the flows computed by scheme A destabilize even under various restart conditions probably because the present scheme consists of little numerical dissipation. Figure 15 plots the density distribution calculated by schemes B and C at mesh size $0.100D$. While the distributions yielded by both schemes are very similar, those of scheme B are slightly sharper than those of scheme C.

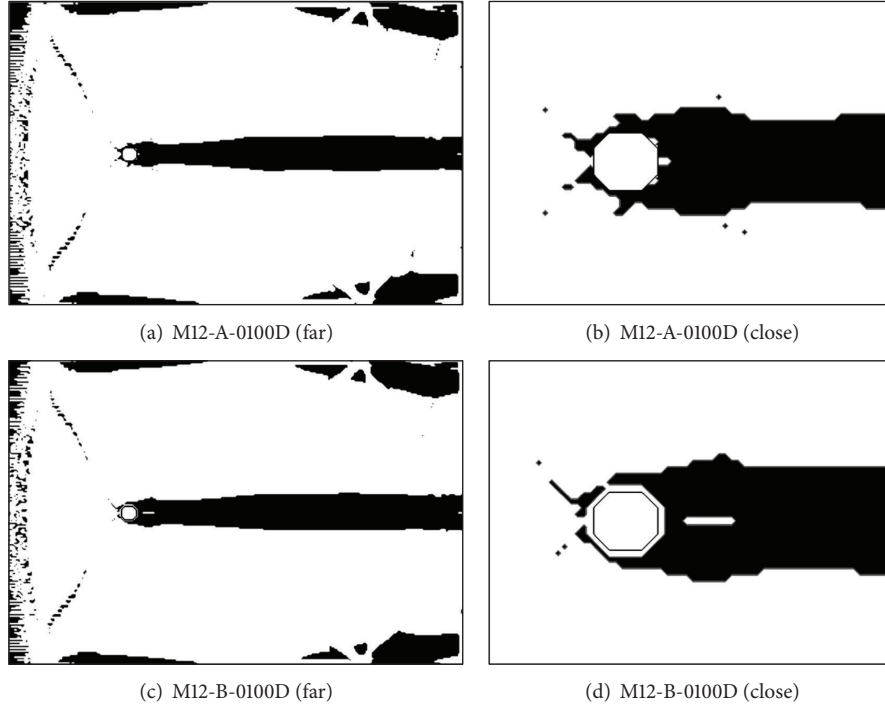


FIGURE 13: Visualization of switching parameter β (white: $\beta = 1$, black: $\beta = 0$).

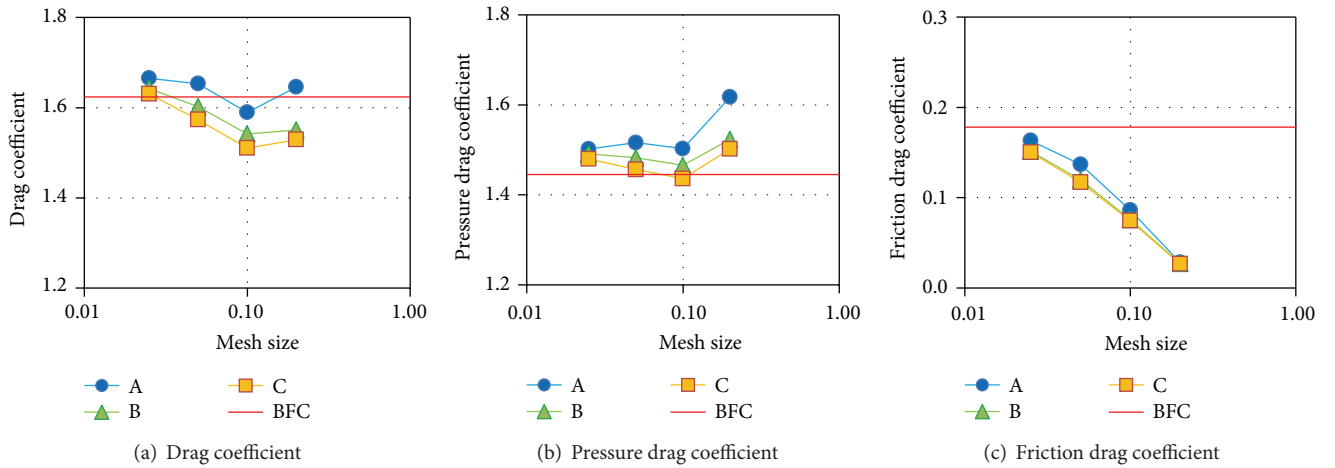


FIGURE 14: Effect of mesh size on aerodynamic coefficients at Mach 1.2. The red lines are reference values.

The distributions of the switching parameter β at mesh sizes $0.100D$ and $0.025D$ are displayed in Figure 16. Both distributions are obtained from scheme B because computations by scheme A blow up. The black regions solved by the central difference scheme appear both upstream and downstream of the cylinder. Thus, the present switching scheme adequately captures nondissipative flows. However, the drag coefficients calculated by schemes B and C are very similar, a likely consequence of the wide MUSCL-Roe region (see Figure 17). Thus, while the wake resolution is unambiguously clarified, the drag coefficients are not affected.

3.5. Comparison of Surface Pressure Coefficient at M 1.2 and M 2.0. Here, surface pressure coefficients in supersonic cases are compared with BFC results to investigate resolution near the boundary. Figure 18 shows the pressure coefficient distributions obtained from all schemes with fine ($0.025D$) and coarse ($0.100D$) mesh resolutions. The present results from fine and coarse meshes are drawn by circles and other symbols, respectively. Discrepancies are observed between BFC and results from coarse meshes, while almost agreements are obtained in the cases of fine mesh resolution. In the case of M 1.2, however, the stagnation pressure is

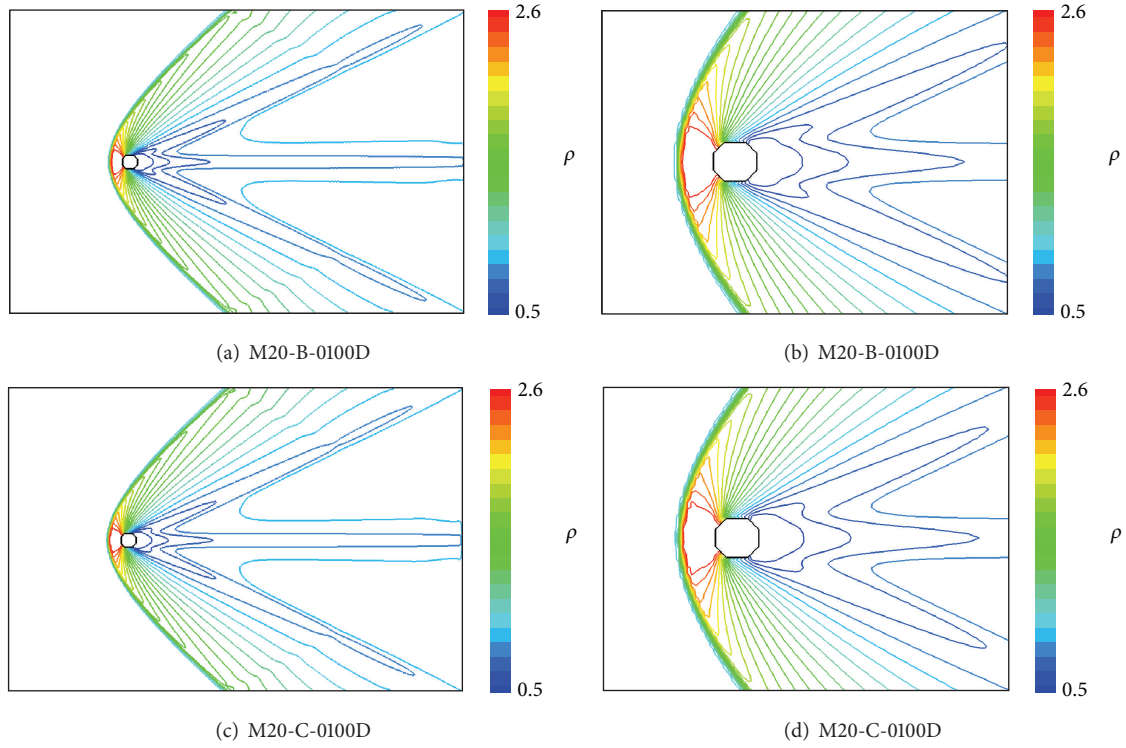
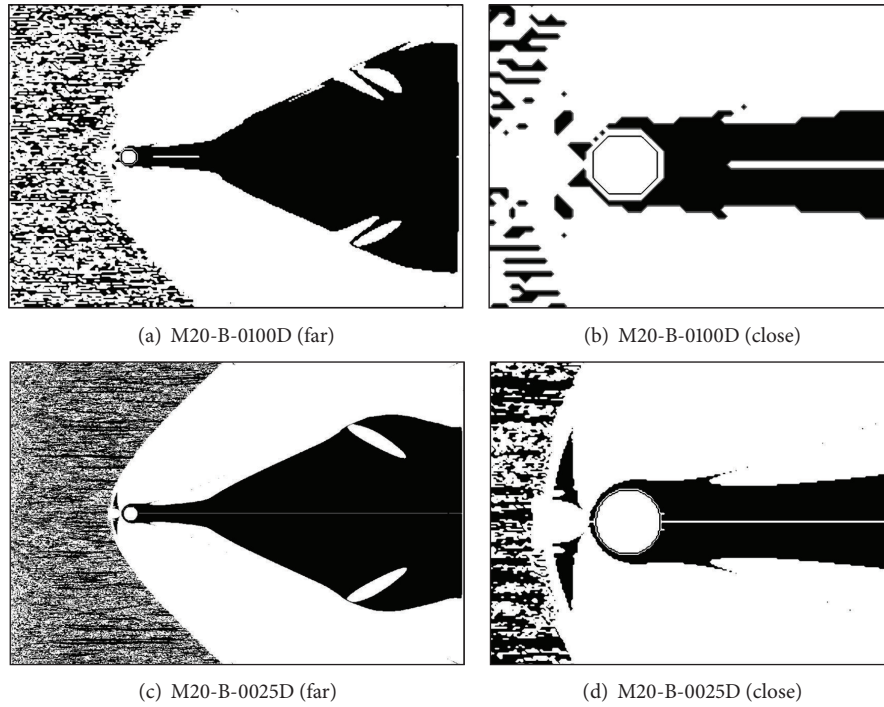


FIGURE 15: Density contours in Mach 2.0.

FIGURE 16: Visualization of switching parameter β (white: $\beta = 1$, black: $\beta = 0$).

overestimated rather than BFC even in all cases of fine mesh. It can be affected from the size of upstream region from the cylinder and the location of the shock wave. Although scheme A shows oscillatory distributions due to the characteristic of the central difference scheme, schemes B and C show almost

same distributions without the feature. In the case of coarse meshes, the beginning of the adverse pressure gradient is not captured clearly; that is, the resolution of the present IBM should be investigated precisely in addition to the effect of the mesh resolution.

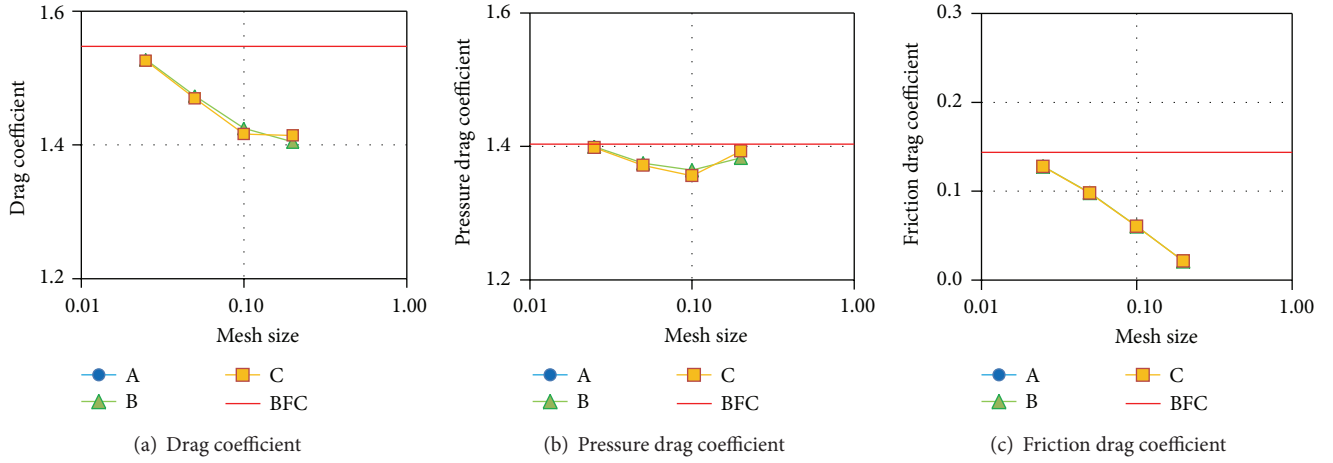


FIGURE 17: Effect of mesh size on drag coefficients at Mach 2.0. The red lines are reference values.

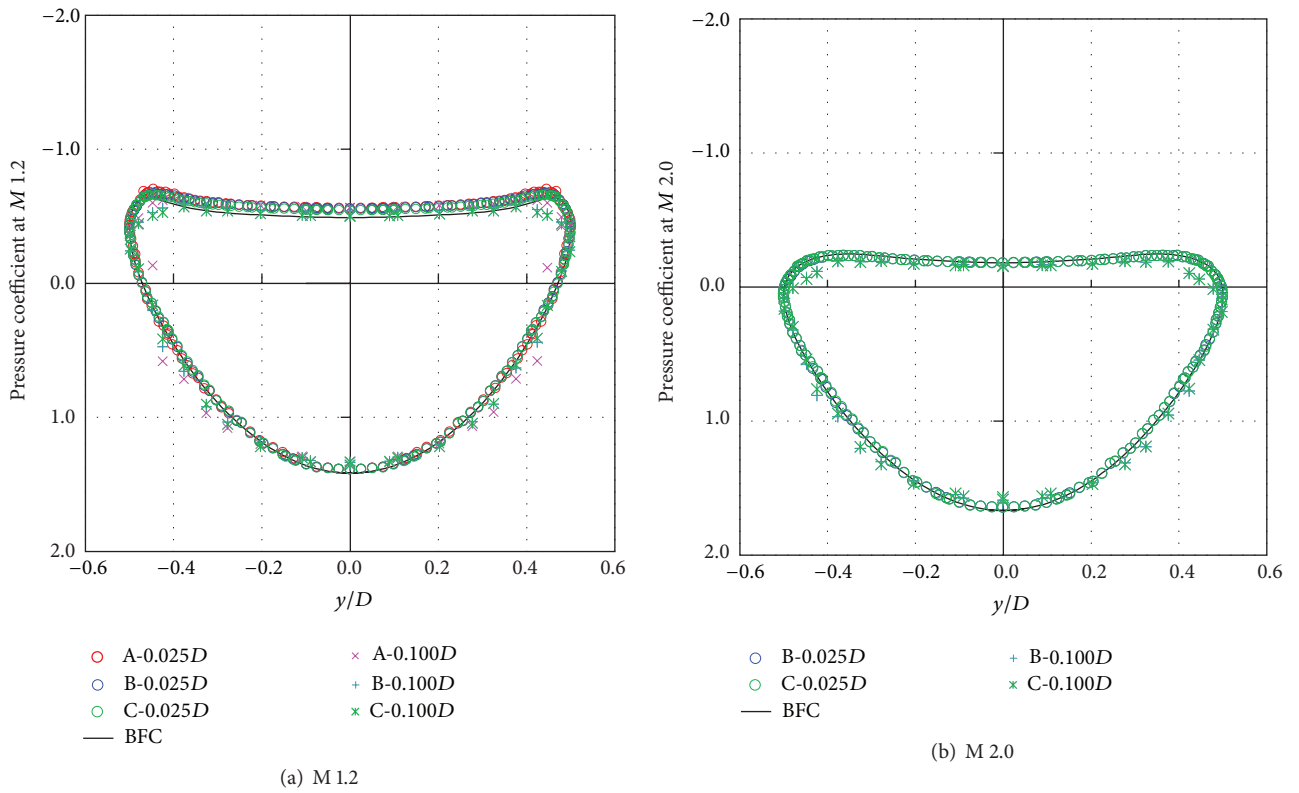


FIGURE 18: Surface pressure coefficient distributions at M 1.2 and M 2.0.

4. Flow Simulation around Relatively Moving Cylinders

The present study aims to solve flows around multiple moving objects. To this end, we simulate the flows induced by two moving cylinders at Mach 1.2. Schematics of the applications are shown in Figure 19. All cylinders in this section are forced to move with fixed velocities and directions. All computations are performed by scheme B, and the diameters D of all cylinders are 1. The Reynolds number, based on

the moving velocity, flow viscosity, and cylinder diameter, is fixed at 300. For comparison, the simulations are conducted on two mesh sizes: $0.050D$ and $0.025D$. In flow simulations with moving objects, the flow simulations are conducted with a Courant number of 0.4. Cartesian meshes can cause the so-called “fresh cell” problem because the cell properties alter with the moving boundary [34]. In this study, although we do not employ any special treatment for the fresh cell problem, the computations are accurate and stable.

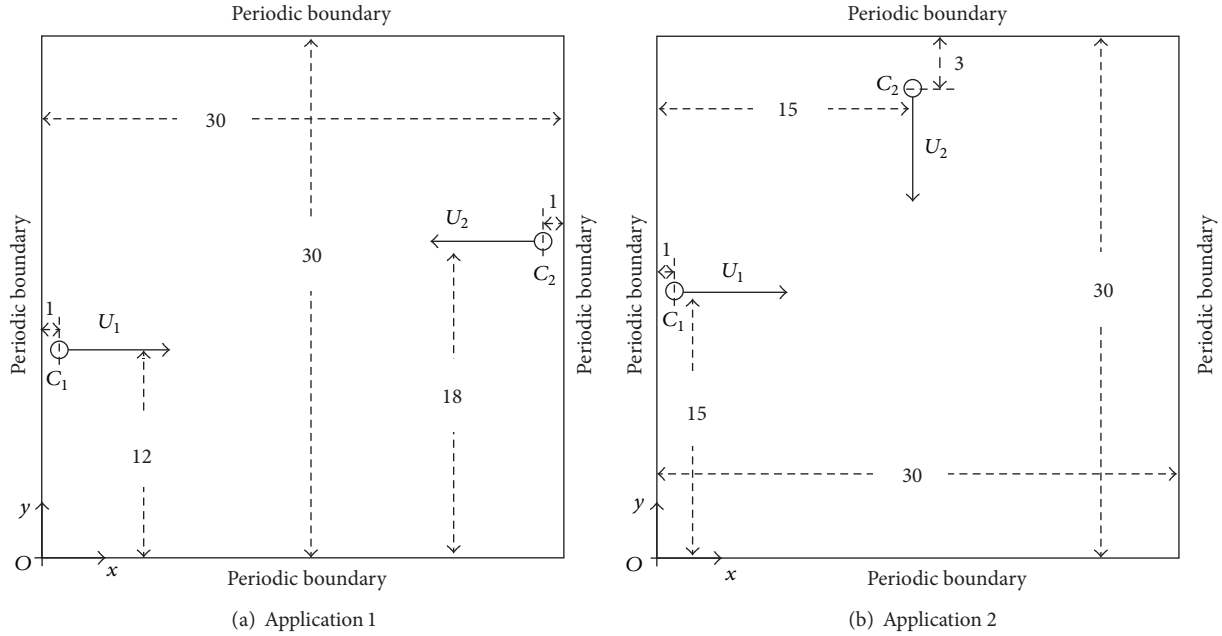


FIGURE 19: Computational configurations of the applications discussed in the text.

4.1. Application 1: Passing Cylinders over Each Other. In the first application, flow is simulated around cylinders passing each other along the x -axis. Figure 20 plots the distributions of density and vorticity magnitude at nondimensional times $t = 8.2, 13.6, 19.1$, and 23.2 . The shock wave generated by a moving cylinder interacts with the wake of the partner cylinder. Vortices are generated from the interaction between the shock wave and shear layer of the wake.

Figure 21 displays the distribution of the switching parameter β at $t = 23.2$. The distribution of β around a moving cylinder is similar to that around a fixed cylinder. The black region, solved by the central difference scheme, spreads in the wake and vortical regions. The nondissipative scheme encourages instabilities to develop in the shear layer.

The fluid force, estimated by surface integration on each object, is normalized identically to the usual aerodynamic coefficient based on the velocity of moving objects. Figure 22 plots the axial force coefficient calculated in this manner, as a function of nondimensional time. The red and blue lines represent the coefficients of cylinders C_1 and C_2 , respectively. The solid and dotted lines represent coarse and fine meshes, respectively. The coefficients are almost independent of grid resolution. Apart from the initial impulse, most of the variation is caused by the shock wave intercepting from the partner cylinder. Along the x -axis, the force coefficient jumps at $t = 11.1$ as the shock wave strikes and then decreases nonlinearly under interference between the shock wave from the partner cylinder and shear layer in the cylinder's own wake. Finally, the coefficient returns to its initial value, having been reduced by half following the nonlinear variation. Along the y -axis,

on the other hand, the force coefficient peaks around 0.7 as the shock wave arrives. Thus, the numerical method allows quantitative evaluation of the fluid force around the moving cylinders.

4.2. Application 2: Crossing Cylinders. The second application is flow simulation around crossing cylinders. In this flow-field, the shock wave, wake, and objects mutually interact. Figure 23 shows the distributions of density and vorticity magnitude at $t = 7.8, 12.9, 18.1$, and 22.0 . The shock waves propagated from the cylinders diagonally interfere ahead of the cylinders at $t = 7.8$. The shear flow in the wake is disordered following the crossing at $t = 18.1$. The flows formed by the interaction of wake and shocks are resolved well by the present switching scheme (see Figure 24).

As in application 1, we now evaluate the axial force coefficients around a pair of crossing cylinders. The temporal changes are plotted in Figure 25. Initially, the axial force on C_1 is enlarged by the shock wave and shear flow from C_2 , similar to application 1. However, the force coefficient falls to zero, negated by the shear flow of C_2 . Along the x -axis, the mesh size introduces a 10% variation in the peak coefficient of C_2 (occurring around $t = 10$). At the peak, the flows are highly compressed by the shock waves from C_1 and C_2 . Moreover, the shock wave is damped by the shear flow around the cylinder. While the grid resolution affects the sharpness of both shock wave and shear flow, the decreased peak value at the higher grid resolution may be attributable to excitation of the shear flow around C_2 . Along the y -axis, the force coefficient of C_2 enhances around $t = 10$, as the circulation around C_2 is diminished by C_1 intercepting the shear flow.

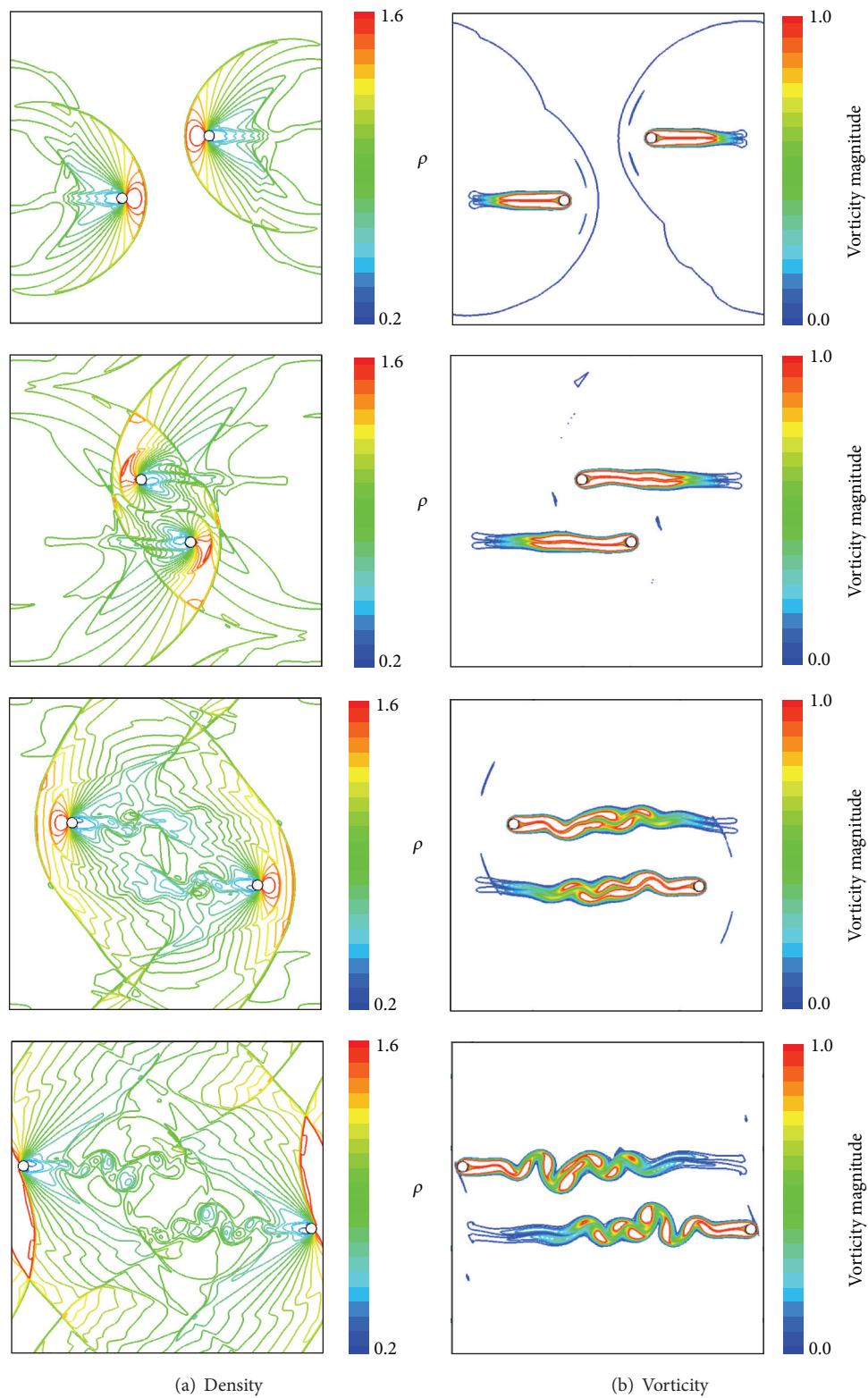


FIGURE 20: Density and vorticity contours at nondimensional times = 8.2, 13.6, 19.1, and 23.2 with $dx = 0.025D$.

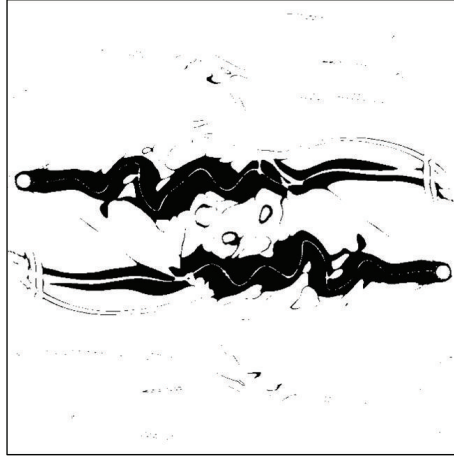
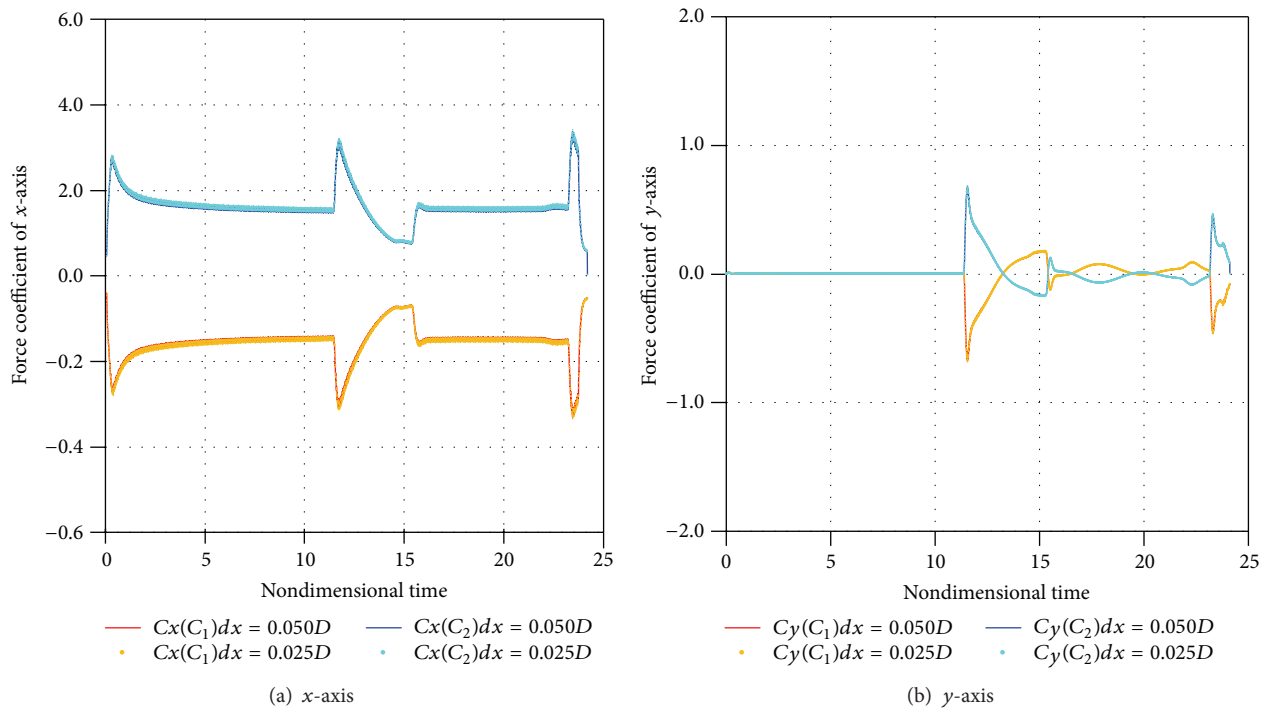
FIGURE 21: Visualization of switching parameter β at $t = 23.2$ with $dx = 0.025D$.

FIGURE 22: Temporal variation of axial force coefficient.

5. Conclusions

To enable simulation of high-speed gas-particle multiphase flows, we developed a high-resolution computational code that captures shock behavior and applied it to the compressible Navier-Stokes equations on an equally spaced Cartesian mesh. The second-order pseudo skew-symmetric and MUSCL-Roe schemes, together with the immersed boundary method, were combined into a hybrid scheme. The hybrid scheme yielded much higher vortex resolution than the MUSCL-Roe scheme while capturing the shock waves with the same effectiveness. The scheme was evaluated on Mach 0.3 subsonic flows and Mach 1.2 and 2.0 supersonic flows

around a two-dimensional circular cylinder at $Re = 300$. The high resolution enabled accurate estimation of the aerodynamic forces. The modified hybrid scheme, which enforces the MUSCL-Roe scheme only around nearby objects, showed more accurate and stable characteristics than the original hybrid scheme because it dampens oscillations near the body. These oscillations are induced by the insufficient grid resolution near the object. The effectiveness of the scheme was emphasized in the flow simulations on coarse meshes.

Moreover, flows were simulated around two moving cylinders at Mach 1.2. The results of these simulations verified the applicability and robustness of the proposed method. Grid convergence results were obtained and the flow features,

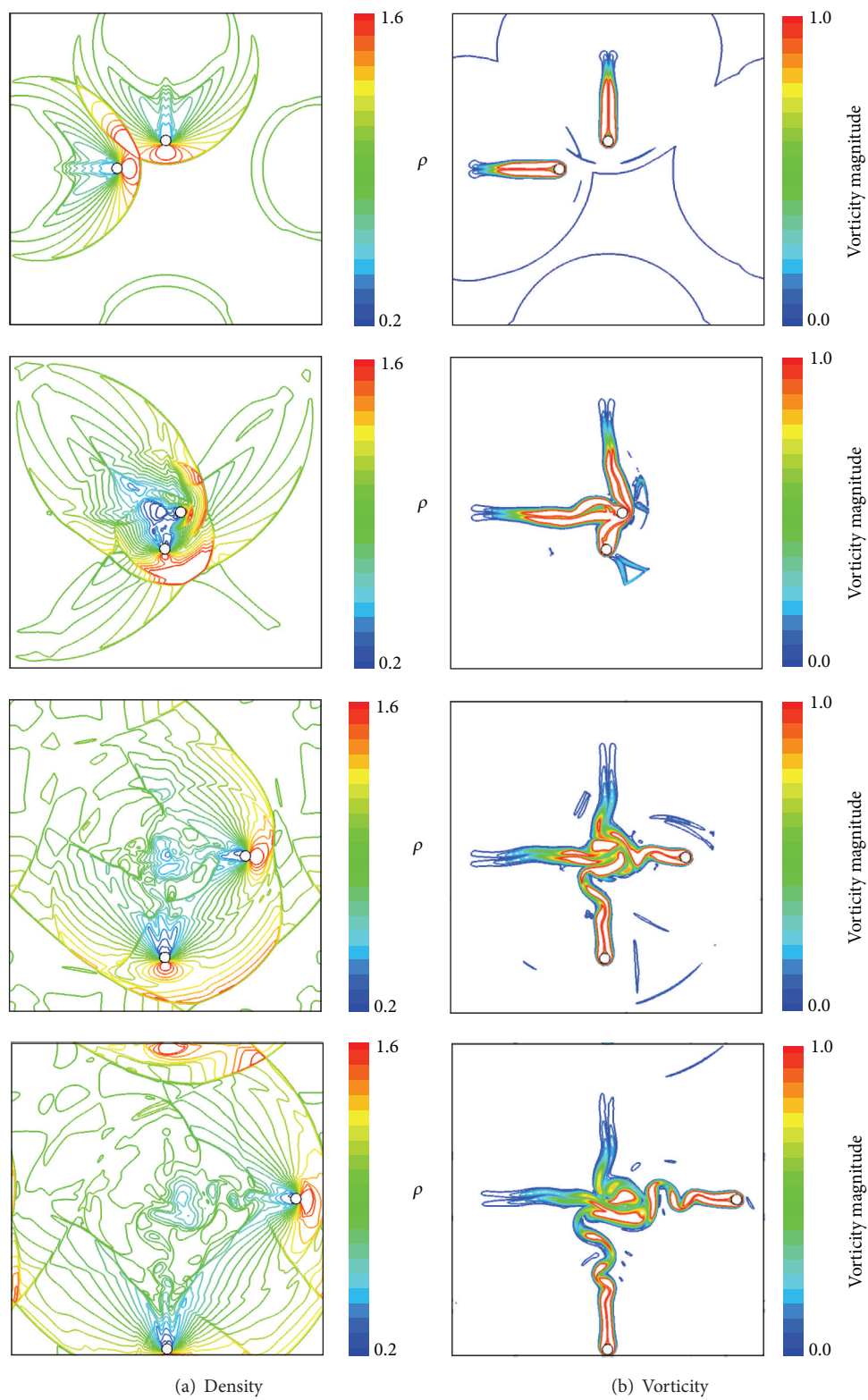


FIGURE 23: Density and vorticity contours around two crossing cylinders at nondimensional times = 7.8, 12.9, 18.1, and 22.0 with $dx = 0.025D$.



FIGURE 24: Visualization of switching parameter β at $t = 23.2$ with $dx = 0.025D$ (white: $\beta = 1$, black: $\beta = 0$).

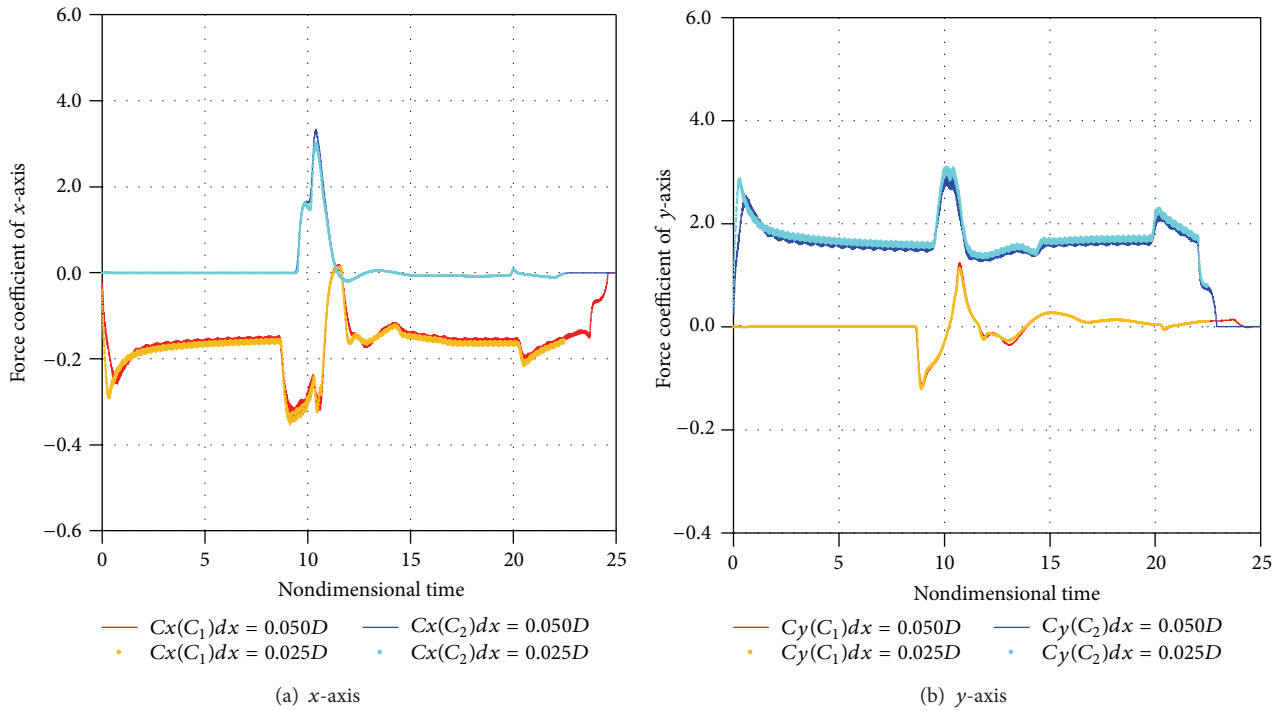


FIGURE 25: Temporal variation of axial force coefficient.

including interference among shock waves, shear flows, and objects, were well captured by the code developed in this study.

Our main focus is characteristics of acoustic wave in flow involving turbulence, shocks, and particles. Now we develop the present numerical method to three-dimensional simulation with investigating the applicability to turbulence and computational performance carefully to achieve high performance parallel computing. In near future, detailed phenomenon of this problem is going to be clarified from large-scale gas-particle flow simulation by using over billion computational cells.

Appendix

The flowfields obtained by the body-fitted coordinate code are shown in Figure 26.

Nomenclature

- a : Speed of sound
- c : Courant number
- C_p : Specific heat at constant pressure
- d : Distance from object boundary (= value of level set function)
- D : Cylinder diameter

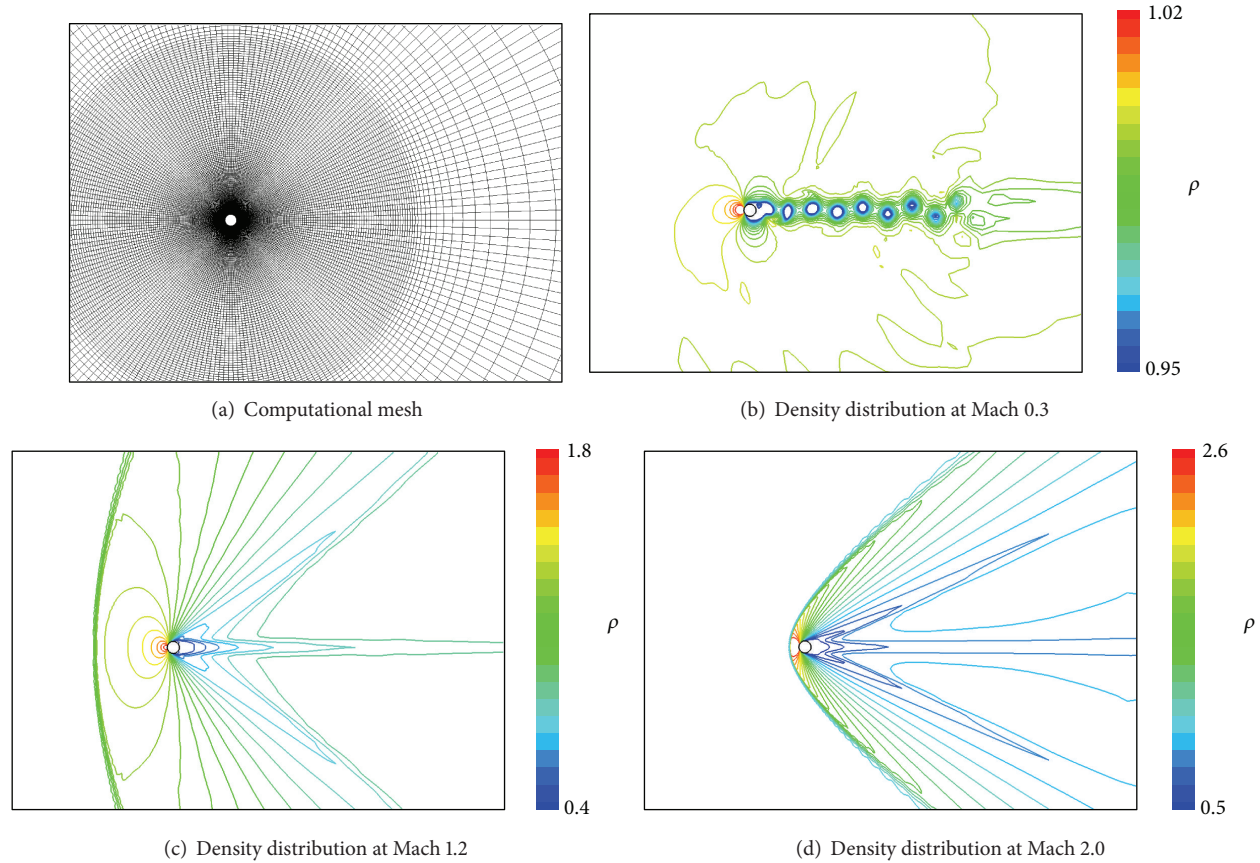


FIGURE 26: Density distribution computed by body-fitted coordinate code [24], simulating flow around a two-dimensional cylinder.

e : Total energy per unit mass
 E : Conservative variable vector
 E : Inviscid flux vector along the x -axis
 E_v : Viscous flux vector along the x -axis
 F : Inviscid flux vector along the y -axis
 F_v : Viscous flux vector along the y -axis
 p : Pressure
 Pr : Prandtl number
 Q : Conservative variable vector (used as a solution vector in this study)
 Re : Reynolds number
 t : Time
 u : Horizontal (x -axis) velocity component
 v : Vertical (y -axis) velocity component
 \mathbf{V} : Velocity vector
 x : Horizontal Cartesian coordinate
 y : Vertical Cartesian coordinate
 ρ : Density
 γ : Specific heat ratio
 β : Switching function of inviscid scheme
 μ : Viscosity
 τ_{ij} : Viscous stress tensor
 κ : Thermal conductance.

Subscripts

∞ : Freestream value
 IP : Image point
 FC : Fluid cell
 GC : Ghost cell
 OC : Object cell
 obj : Object value.

Conflict of Interests

The authors declare that there is no conflict of interests regarding the publication of this paper.

Authors' Contribution

Shun Takahashi and Taku Nonomura equally contributed to this paper.

Acknowledgments

This research is partially supported by KAKENHI (24656-522). The computations are carried out by NEC SX-9 at the Cyber Science Center of Tohoku University.

References

- [1] K. M. Eldred, "Acoustic Loads Generated by Propulsion System," NASA SP-8072, 1972.
- [2] K. Fujii, T. Nonomura, and S. Tsutsumi, "Toward accurate simulation and analysis of strong acoustic wave phenomena: a review from the experience of our study on rocket problems," *International Journal for Numerical Methods in Fluids*, vol. 64, no. 10–12, pp. 1412–1432, 2010.
- [3] T. Nonomura and K. Fujii, "Recent efforts for rocket plume acoustics," in *Computational Fluid Dynamics Review 2010*, pp. 421–446, World Scientific Company, 2010.
- [4] T. Nonomura and K. Fujii, "Overexpansion effects on characteristics of mach waves from a supersonic cold jet," *AIAA Journal*, vol. 49, no. 10, pp. 2282–2294, 2011.
- [5] T. Nonomura, Y. Goto, and K. Fujii, "Aeroacoustic waves generated from a supersonic jet impinging on an inclined flat plate," *International Journal of Aeroacoustics*, vol. 10, no. 4, pp. 401–426, 2011.
- [6] K. Fukuda, S. Tsutsumi, K. Ui, T. Ishii, R. Takaki, and K. Fujii, "An acoustic impedance model for evaluating the ground effect of static-firing tests on a rocket motor," *Transactions of the Japan Society for Aeronautical and Space Sciences*, vol. 54, no. 184, pp. 120–129, 2011.
- [7] S. Takahashi, W. Yamazaki, and K. Nakahashi, "Aerodynamic design exploration of flapping wing, viewpoint of shape and kinematics," in *Proceedings of the 45th AIAA Aerospace Sciences Meeting*, pp. 5772–5781, January 2007.
- [8] S. Takahashi, I. Monjugawa, and K. Nakahashi, "Unsteady flow computations around moving airfoils by overset unstructured grid method," *Transactions of the Japan Society for Aeronautical and Space Sciences*, vol. 51, no. 172, pp. 78–85, 2008.
- [9] J. A. Sethian and P. Smereka, "Level set methods for fluid interfaces," *Annual Review of Fluid Mechanics*, vol. 35, pp. 341–372, 2003.
- [10] R. Mittal and G. Iaccarino, "Immersed boundary methods," *Annual Review of Fluid Mechanics*, vol. 37, pp. 239–261, 2005.
- [11] L. Zhu and C. S. Peskin, "Interaction of two flapping filaments in a flowing soap film," *Physics of Fluids*, vol. 15, no. 7, pp. 1954–1960, 2003.
- [12] S. K. Sambasivan and H. S. UdayKumar, "Ghost fluid method for strong shock interactions part 2: immersed solid boundaries," *AIAA Journal*, vol. 47, no. 12, pp. 2923–2937, 2009.
- [13] X. Y. Hu, B. C. Khoo, N. A. Adams, and F. L. Huang, "A conservative interface method for compressible flows," *Journal of Computational Physics*, vol. 219, no. 2, pp. 553–578, 2006.
- [14] M. D. de Tullio, P. de Palma, G. Iaccarino, G. Pascazio, and M. Napolitano, "An immersed boundary method for compressible flows using local grid refinement," *Journal of Computational Physics*, vol. 225, no. 2, pp. 2098–2117, 2007.
- [15] K. Nakahashi, "Immersed boundary method for compressible Euler equations in the building-cube method," in *Proceedings of the 20th AIAA computational fluid dynamics conference*, 2011.
- [16] S. Takahashi, T. Ishida, K. Nakahashi et al., "Study of high resolution incompressible flow simulation based on Cartesian mesh," in *Proceedings of the 47th AIAA Aerospace Sciences Meeting including the New Horizons Forum and Aerospace Exposition*, January 2009.
- [17] D. Sasaki, S. Takahashi, T. Ishida et al., "Large-scale flow computation of complex geometries by building-cube method," in *High Performance Computing on Vector Systems 2009*, pp. 167–178, 2010.
- [18] T. Ishida and K. Nakahashi, "Immersed boundary method for compressible turbulent flow computations in building-cube method," in *Proceedings of the 21st AIAA Computational Fluid Dynamics Conference*, 2013.
- [19] R. Sakai, S. Obayashi, Y. Matsuo, and K. Nakahashi, "Practical large-eddy simulation for complex turbulent flowfield with adaptive cartesian mesh and data compression technique," in *Proceedings of the 21st AIAA Computational Fluid Dynamics Conference*, 2013.
- [20] K. Komatsu, T. Soga, R. Egawa et al., "Parallel processing of the Building-Cube Method on a GPU platform," *Computers and Fluids*, vol. 45, no. 1, pp. 122–128, 2011.
- [21] S. Takahashi, T. Ishida, and K. Nakahashi, "Parallel computation of incompressible flow using Building-Cube method," in *Parallel Computational Fluid Dynamics 2007*, vol. 67 of *Lecture Notes in Computational Science and Engineering*, pp. 195–200, 2009.
- [22] L. Georges, G. Winckelmans, and P. Geuzaine, "Improving shock-free compressible RANS solvers for LES on unstructured meshes," *Journal of Computational and Applied Mathematics*, vol. 215, no. 2, pp. 419–428, 2008.
- [23] P. L. Roe, "Approximate Riemann solvers, parameter vectors, and difference schemes," *Journal of Computational Physics*, vol. 43, no. 2, pp. 357–372, 1981.
- [24] B. van Leer, "Towards the ultimate conservative difference scheme. IV: a new approach to numerical convection," *Journal of Computational Physics*, vol. 23, no. 3, pp. 276–299, 1977.
- [25] G. van Albada, B. van Leer, and W. Roberts, "A comparative study of computational methods in cosmic gas dynamics," *Astronautics and Astrophysics*, vol. 108, pp. 76–84, 1982.
- [26] F. Ducros, V. Ferrand, F. Nicoud et al., "Large-Eddy simulation of the Shock/Turbulence interaction," *Journal of Computational Physics*, vol. 152, no. 2, pp. 517–549, 1999.
- [27] A. Jameson, W. Schmidt, and E. Turkel, "Numerical solution of the Euler equations by finite volume methods using Runge Kutta time stepping schemes," in *Proceedings of the 14th AIAA Fluid and Plasma Dynamics Conference*, 1981.
- [28] S. Teramoto, "Large-eddy simulation of transitional boundary layer with impinging shock wave," *AIAA Journal*, vol. 43, no. 11, pp. 2354–2363, 2005.
- [29] S. Gottlieb and C.-W. Shu, "Total variation diminishing Runge-Kutta schemes," *Mathematics of Computation*, vol. 67, no. 221, pp. 73–85, 1998.
- [30] J. Onishi and T. Nonomura, "Notes on the simple evaluation of the force on bodies in immersed boundary methods for fluid computation," Submitted for publication.
- [31] J. B. Freund, "Proposed inflow/outflow boundary condition for direct computation of aerodynamic sound," *AIAA Journal*, vol. 35, no. 4, pp. 740–742, 1997.
- [32] X. Y. Hu, Q. Wang, and N. A. Adams, "An adaptive central-upwind weighted essentially non-oscillatory scheme," *Journal of Computational Physics*, vol. 229, no. 23, pp. 8952–8965, 2010.
- [33] T. Nonomura, D. Terakado, Y. Abe, and K. Fujii, "A new technique for finite difference WENO with geometric conservation law," in *Proceedings of the 21st AIAA Computational Fluid Dynamics Conference*, 2013.
- [34] J. H. Seo and R. Mittal, "A sharp-interface immersed boundary method with improved mass conservation and reduced spurious pressure oscillations," *Journal of Computational Physics*, vol. 230, no. 19, pp. 7347–7363, 2011.

Research Article

Numerical Treatment of a Modified MacCormack Scheme in a Nondimensional Form of the Water Quality Models in a Nonuniform Flow Stream

Nopparat Pochai^{1,2}

¹ Department of Mathematics, Faculty of Science, King Mongkut's Institute of Technology Ladkrabang, Bangkok 10520, Thailand

² Centre of Excellence in Mathematics, Commission on Higher Education (CHE), Si Ayutthaya Road, Bangkok 10400, Thailand

Correspondence should be addressed to Nopparat Pochai; nop_math@yahoo.com

Received 1 September 2013; Revised 17 December 2013; Accepted 17 December 2013; Published 23 February 2014

Academic Editor: Luís Godinho

Copyright © 2014 Nopparat Pochai. This is an open access article distributed under the Creative Commons Attribution License, which permits unrestricted use, distribution, and reproduction in any medium, provided the original work is properly cited.

Two mathematical models are used to simulate water quality in a nonuniform flow stream. The first model is the hydrodynamic model that provides the velocity field and the elevation of water. The second model is the dispersion model that provides the pollutant concentration field. Both models are formulated in one-dimensional equations. The traditional Crank-Nicolson method is also used in the hydrodynamic model. At each step, the flow velocity fields calculated from the first model are the input into the second model as the field data. A modified MacCormack method is subsequently employed in the second model. This paper proposes a simply remarkable alteration to the MacCormack method so as to make it more accurate without any significant loss of computational efficiency. The results obtained indicate that the proposed modified MacCormack scheme does improve the prediction accuracy compared to that of the traditional MacCormack method.

1. Introduction

In general, the amount of pollution levels in a stream can be measured via data collection from a real of field data site. It is somehow rather difficult and complex, and the results obtained tentatively deviate in the measurement from one point in each time/place to another when the water flow in the stream is not uniform. In water quality modelling for nonuniform flow stream, the general governing equations used are the hydrodynamic model and the dispersion model. The one-dimensional shallow water equation and advection-dispersion-reaction equation is govern the first and the second models, respectively.

Numerous numerical techniques for solving such models are available. In [1], the finite element method for solving a steady water pollution control to achieve a minimum cost is presented. The numerical techniques for solving the uniform flow of stream water quality model, especially the one-dimensional advection-dispersion-reaction equation, are presented in [2–6].

The nonuniform flow model requires data concerned with the velocity of the current at any point and any time in the domain. The hydrodynamics model provides the velocity field and tidal elevation of the water. In [7–10], they used the hydrodynamics model and the advection-dispersion equation to approximate the velocity of the water current in bay, uniform reservoir, and stream, respectively. Among these numerical techniques, the finite difference methods, including both explicit and implicit schemes, are mostly used for one-dimensional domain such as in longitudinal stream systems [11, 12].

There are two mathematical models used to simulate water quality in a nonuniform water flow systems. The first is the hydrodynamic model that provides the velocity field and the elevation of water. The second is the dispersion model that gives the pollutant concentration field. A couple of models are formulated in one-dimensional equations. The traditional Crank-Nicolson method is used in the hydrodynamic model. At each step, the calculated flow velocity fields of the first

model are input into the second model as the field data [9, 10, 13].

The numerical techniques to solve the nonuniform flow of stream water quality model containing one-dimensional advection-dispersion-reaction equation have been presented in [10] using the fully implicit scheme: Crank-Nicolson method is used to solve the hydrodynamic model and backward time central space (BTCS) for dispersion model, respectively. In [13], the Crank-Nicolson method is also used to solve the hydrodynamic model, while the explicit Saul'yev scheme is used to solve the dispersion model.

Their research on finite difference techniques for the dispersion model has concentrated on computation accuracy and numerical stability. Many complicated numerical techniques, such as the QUICK scheme, the Lax-Wendroff scheme, and the Crandall scheme, have been studied to increase performances. These techniques have focused on advantages in terms of stability and higher order accuracy [3].

The simple finite difference schemes become more attractive for model use. The simple explicit methods include the forward time-central space (FTCS) scheme, the MacCormack scheme, and the Saul'yev scheme, and the implicit schemes include the backward time-central space (BTCS) scheme, and the Crank-Nicolson scheme [12]. These schemes are either first-order or second-order accurate and have the advantages in programming and computing without losing much accuracy and thus they are used for many model applications [3].

A third-order upwind scheme for the advection-diffusion equation using a simple spreadsheets simulation is proposed in [14]. In [15], a new flux splitting scheme is proposed. The scheme is robust and converges as fast as the Roe Splitting. The Godunov-mixed methods for advection-dispersion equations are introduced in [16]. A time-splitting approach for advection-dispersion equations is also considered. In addition, [17] proposes a time-splitting method for multi-dimensional advection-diffusion equations that advection is approximated by a Godunov-type procedure, and diffusion is approximated by a low-order mixed finite element method. In [18], the flux-limiting solution techniques for simulation of reaction diffusion convection system are proposed. A composite scheme to solves the scalar transport equation in a two-dimensional space that accurately resolve sharp profiles in the flow is introduced. The total variation diminishing implicit Runge-Kutta methods for dissipative advection-diffusion problems in astrophysics is proposed in [19]. They derive dissipative space discretizations and demonstrate that together with specially adapted total-variation-diminishing (TVD) or strongly stable Runge-Kutta time discretizations with adaptive step-size control this yields reliable and efficient integrators for the underlying high-dimensional nonlinear evolution equations.

In this research, we propose simple revisions to the MacCormack scheme that improve its accuracy for the problem of water quality measurement in a nonuniform water flow in a stream. In the following sections, the formulation of the traditional MacCormack scheme is reviewed. The revision of the modified MacCormack scheme is proposed.

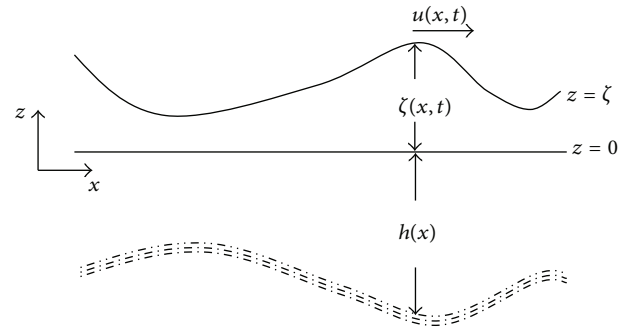


FIGURE 1: The shallow water system.

The results from the hydrodynamic model are the data of the water flow velocity for the advection-dispersion-reaction equation which provides the pollutant concentration field. The term of friction forces, due to the drag of sides of the stream, is considered. The theoretical solution of the model at the end point of the domain that guarantees the accuracy of the approximate solution is presented in [9, 10, 13].

The stream has a simple one-space dimension as shown in Figure 1. By averaging the equation over the depth, discarding the term due to the Coriolis force, it follows that the one-dimensional shallow water and the advection-dispersion-reaction equations are applicable. We use the Crank-Nicolson scheme, the traditional MacCormack scheme, and the Modified MacCormack scheme to approximate the velocity, the elevation, and the pollutant concentration from the first and the second models, respectively.

2. Model Formulation

2.1. The Hydrodynamic Model. In this section, we derive a simple hydrodynamic model for describing water current and elevation by one-dimensional shallow water equation. We make the usual assumption in the continuity and momentum balance; that is, we assume that the Coriolis, shearing stresses, and the surface wind are small [7, 9, 10, 20]; we obtain the one-dimensional shallow water equations:

$$\begin{aligned} \frac{\partial \zeta}{\partial t} + \frac{\partial}{\partial x} [(h + \zeta) u] &= 0, \\ \frac{\partial u}{\partial t} + g \frac{\partial \zeta}{\partial x} &= 0, \end{aligned} \quad (1)$$

where x is the longitudinal distance along the stream (m), t is time (s), $h(x)$ is the depth measured from the mean water level to the stream bed (m), $\zeta(x, t)$ is the elevation from the mean water level to the temporary water surface or the tidal elevation (m/s), and $u(x, t)$ is the velocity components (m/s), for all $x \in [0, l]$.

Assume that h is a constant and $\zeta \ll h$. Then (1) lead to

$$\begin{aligned} \frac{\partial \zeta}{\partial t} + h \frac{\partial u}{\partial x} &= 0, \\ \frac{\partial u}{\partial t} + g \frac{\partial \zeta}{\partial x} &= 0. \end{aligned} \quad (2)$$

We will consider the equation in the dimensionless problem by letting $U = u/\sqrt{gh}$, $X = x/l$, $Z = \zeta/h$, and $T = t\sqrt{gh}/l$. Substituting them into (2) leads to

$$\begin{aligned}\frac{\partial Z}{\partial T} + \frac{\partial U}{\partial X} &= 0, \\ \frac{\partial U}{\partial T} + \frac{\partial Z}{\partial X} &= 0.\end{aligned}\quad (3)$$

In [9, 10, 13], they introduce a damping term into (3) to represent the frictional forces due to the drag of sides of the stream,

$$\begin{aligned}\frac{\partial Z}{\partial T} + \frac{\partial U}{\partial X} &= 0, \\ \frac{\partial U}{\partial T} + \frac{\partial Z}{\partial X} &= -U,\end{aligned}\quad (4)$$

with the initial conditions at $t = 0$ and $0 \leq X \leq 1$ are $Z = 0$ and $U = 0$. The boundary conditions for $t > 0$ are specified: $Z = e^{it}$ at $X = 0$ and $\partial Z/\partial X = 0$ at $X = 1$. The system of (4) is called the damped equation. We solve the damped equation by using the finite difference method. In order to solve (4) in $[0, 1] \times [0, T]$, it is convenient to use u, d for U and Z , respectively:

$$\begin{aligned}\frac{\partial u}{\partial t} + \frac{\partial d}{\partial x} &= -u, \\ \frac{\partial d}{\partial t} + \frac{\partial u}{\partial x} &= 0,\end{aligned}\quad (5)$$

with the initial conditions $u = 0$, $d = 0$, at $t = 0$, and the boundary conditions $d(0, t) = f(t)$ and $\partial d/\partial x = 0$ at $x = 1$.

2.2. Dispersion Model. In a stream water quality model, the governing equations are the dynamic one-dimensional advection-dispersion-reaction equations (ADREs). A simplified representation by averaging the equation over the depth is shown in [2–4, 6, 10] as follows:

$$\frac{\partial C}{\partial t} + u \frac{\partial C}{\partial x} = D \frac{\partial^2 C}{\partial x^2} - KC, \quad (6)$$

where $C(x, t)$ is the concentration averaged in depth at the point x and at time t , D is the diffusion coefficient, K is the mass decay rate, and $u(x, t)$ is the velocity component for all $x \in [0, 1]$. We will consider the model with the following conditions. The initial condition $C(x, 0) = 0$ at $t = 0$ for all $x > 0$. The boundary conditions $C(0, t) = C_0$ at $x = 0$ and $\partial C/\partial x = 0$ at $x = 1$ where C_0 is a constant.

3. Crank-Nicolson Method for the Hydrodynamic Model

The hydrodynamic model provides the velocity field and elevation of the water. Then the calculated results of the model will be the input into the dispersion model which provides the pollutant concentration field. We will follow the

numerical techniques of [9]. To find the water velocity and water elevation from (5), we make the following change to variables $v = e^t u$ and substitute it into (5). Therefore,

$$\begin{aligned}\frac{\partial v}{\partial t} + e^t \frac{\partial d}{\partial x} &= 0, \\ \frac{\partial d}{\partial t} + e^{-t} \frac{\partial v}{\partial x} &= 0.\end{aligned}\quad (7)$$

Equations (7) can be written in the matrix form

$$\begin{pmatrix} v \\ d \end{pmatrix}_t + \begin{bmatrix} 0 & e^t \\ e^{-t} & 0 \end{bmatrix} \begin{pmatrix} v \\ d \end{pmatrix}_x = \begin{pmatrix} 0 \\ 0 \end{pmatrix}. \quad (8)$$

That is

$$U_t + AU_x = \bar{0}, \quad (9)$$

where

$$\begin{aligned}A &= \begin{bmatrix} 0 & e^t \\ e^{-t} & 0 \end{bmatrix}, \\ U &= \begin{pmatrix} v \\ d \end{pmatrix}, \quad \begin{pmatrix} v \\ d \end{pmatrix}_t = \begin{pmatrix} \frac{\partial v}{\partial t} \\ \frac{\partial d}{\partial t} \end{pmatrix},\end{aligned}\quad (10)$$

with the initial condition $d = v = 0$ at $t = 0$. The left boundary condition for $x = 0$, $t > 0$ is specified: $d(0, t) = \sin t$ and $\partial v/\partial x = -e^t \cos t$, and the right boundary condition for $x = 1$, $t > 0$ is specified: $\partial d/\partial x = 0$ and $v(0, t) = 0$.

We now discretize (9) by dividing the interval $[0, 1]$ into M subintervals such that $M\Delta x = 1$ and the interval $[0, T]$ into N subintervals such that $N\Delta t = T$. We can then approximate $d(x_i, t_n)$ by d_i^n , value of the difference approximation of $d(x, t)$ at point $x = i\Delta x$ and $t = n\Delta t$, where $0 \leq i \leq M$ and $0 \leq n \leq N$, and similarly defined for v_i^n and U_i^n . The grid point (x_n, t_n) is defined by $x_i = i\Delta x$ for all $i = 0, 1, 2, \dots, M$ and $t_n = n\Delta t$ for all $n = 0, 1, 2, \dots, N$ in which M and N are positive integers. Using the Crank-Nicolson method [21] to (9), the following finite difference equation can be obtained:

$$\left[I - \frac{1}{4} \lambda A (\Delta_x + \nabla_x) \right] U_i^{n+1} = \left[I + \frac{1}{4} \lambda A (\Delta_x + \nabla_x) \right] U_i^n, \quad (11)$$

where

$$\begin{aligned}U_i^n &= \begin{pmatrix} v_i^n \\ d_i^n \end{pmatrix}, \quad \Delta_x U_i^n = U_{i+1}^n - U_i^n, \\ \nabla_x U_i^n &= U_i^n - U_{i-1}^n,\end{aligned}\quad (12)$$

I is the unit matrix of order 2, and $\lambda = \Delta t/\Delta x$. Applying the initial and boundary conditions given in (7), it can be obtained the general form

$$G^{n+1} \bar{U}^{n+1} = E^n \bar{U}^n + F^n, \quad (13)$$

where

$$G^{n+1} = \begin{bmatrix} 1 & 0 & 0 & -\frac{\lambda}{4}a_1^{n+1} & 0 & 0 \\ \frac{\lambda}{4}a_2^{n+1} & 1 & -\frac{\lambda}{4}a_2^{n+1} & 0 & 0 & 0 \\ 0 & \frac{\lambda}{4}a_1^{n+1} & 1 & 0 & 0 & -\frac{\lambda}{4}a_1^{n+1} \\ \frac{\lambda}{4}a_2^{n+1} & 0 & 0 & 1 & -\frac{\lambda}{4}a_2^{n+1} & 0 \\ \ddots & \ddots & \ddots & \ddots & \ddots & \ddots \\ 0 & 0 & 0 & \frac{\lambda}{4}a_1^{n+1} & 1 & -\frac{\lambda}{4}a_1^{n+1} \\ 0 & 0 & \frac{\lambda}{4}a_2^{n+1} & 0 & 0 & 1 \end{bmatrix},$$

$$E^n = \begin{bmatrix} 1 & 0 & 0 & -\frac{\lambda}{4}a_1^n & 0 & 0 \\ -\frac{\lambda}{4}a_2^n & 1 & \frac{\lambda}{4}a_2^n & 0 & 0 & 0 \\ 0 & -\frac{\lambda}{4}a_1^n & 1 & 0 & 0 & \frac{\lambda}{4}a_1^n \\ -\frac{\lambda}{4}a_2^n & 0 & 0 & 1 & \frac{\lambda}{4}a_2^n & 0 \\ \ddots & \ddots & \ddots & \ddots & \ddots & \ddots \\ 0 & 0 & 0 & -\frac{\lambda}{4}a_1^n & 1 & \frac{\lambda}{4}a_1^n \\ 0 & 0 & -\frac{\lambda}{4}a_2^n & 0 & 0 & 1 \end{bmatrix},$$

$$\bar{U}^n = \begin{pmatrix} U_1^n \\ U_2^n \\ \vdots \\ U_{M-1}^n \end{pmatrix},$$

$$F^n = \begin{pmatrix} -\frac{\lambda}{4}a_1^{n+1} \sin(t_{n+1}) - \frac{\lambda}{4}a_1^n \sin(t_n) \\ -\frac{\lambda}{4}a_2^{n+1} \Delta x e^{-t_{n+1}} \cos(t_{n+1}) - \frac{\lambda}{4}a_2^n \Delta x e^{-t_n} \cos(t_n) \\ 0 \\ 0 \\ \vdots \\ 0 \\ 0 \end{pmatrix}, \quad (14)$$

where $a_1^n = e^{t_n}$, $a_2^n = e^{-t_n}$, and $t_n = n\Delta t$ for all $n = 0, 1, 2, \dots, N$. The Crank-Nicolson scheme is unconditionally stable [12, 21].

4. A Modified MacCormack Scheme for the Advection-Dispersion-Reaction Equation

4.1. The Traditional MacCormack Scheme. First of all, we consider the traditional MacCormack scheme. The scheme is an explicit finite difference scheme with predictor-corrector two-step method. The first step is a modification of forward time central space (FTCS) by changing the central space evaluation at time n to a forward space evaluation. This step is a forward time forward space (FTFS) scheme. The FTFS scheme approximates the temporal and spacial derivatives and the decay in (6) with the following discretization.

We can then approximate $C(x_i, t_n)$ by C_i^n , the value of the difference approximation of $C(x, t)$ at point $x = i\Delta x$ and $t = n\Delta t$, where $0 \leq i \leq M$ and $0 \leq n \leq N$. The grid point (x_n, t_n) is

defined by $x_i = i\Delta x$ for all $i = 0, 1, 2, \dots, M$ and $t_n = n\Delta t$ for all $n = 0, 1, 2, \dots, N$ in which M and N are positive integers. Taking the forward time forward space technique [3, 21] into (6), we get the following discretization:

$$\begin{aligned} C &\cong C_i^n, \\ \frac{\partial C}{\partial t} &\cong \frac{C_i^{n+1} - C_i^n}{\Delta t}, \\ \frac{\partial C}{\partial x} &\cong \frac{C_{i+1}^n - C_i^n}{\Delta x}, \\ \frac{\partial^2 C}{\partial x^2} &\cong \frac{C_{i+1}^n - 2C_i^n + C_{i-1}^n}{(\Delta x)^2}, \\ u &\cong \bar{U}_i^n. \end{aligned} \quad (15)$$

Note that \bar{U}_i^n are obtained by the Crank-Nicolson method with the hydrodynamic model of (5) that are presented in [9, 10, 13].

Substituting (15) into (6), we get

$$\begin{aligned} &\frac{C_i^{n+1} - C_i^n}{\Delta t} + \bar{U}_i^n \left(\frac{C_{i+1}^n - C_i^n}{\Delta x} \right) \\ &= D \left(\frac{C_{i+1}^n - 2C_i^n + C_{i-1}^n}{(\Delta x)^2} \right) - KC_i^n, \end{aligned} \quad (16)$$

for $1 \leq i \leq M$ and $0 \leq n \leq N - 1$. Substitute the difference equation into (16), and then define slope S_{i_1} as

$$S_{i_1} = -\bar{U}_i^n \left(\frac{C_{i+1}^n - C_i^n}{\Delta x} \right) + D \left(\frac{C_{i+1}^n - 2C_i^n + C_{i-1}^n}{(\Delta x)^2} \right) - KC_i^n. \quad (17)$$

Let $\lambda = D\Delta t/(\Delta x)^2$ and $\gamma_i^{n+1} = (\Delta t/\Delta x)\bar{U}_i^{n+1}$, and then define $\hat{\gamma}_i^n = \gamma_i^n/\Delta t = \bar{U}_i^n/\Delta x$ and $\hat{\lambda} = D/(\Delta x)^2 = \lambda/\Delta t$. Equation (17) takes a simplified form:

$$S_{i_1} = -\hat{\gamma}_i^n (C_{i+1}^n - C_i^n) + \hat{\lambda} (C_{i+1}^n - 2C_i^n + C_{i-1}^n) - KC_i^n, \quad (18)$$

or

$$S_{i_1} = (\hat{\lambda} - \hat{\gamma}_i^n) C_{i+1}^n - (2\hat{\lambda} - \hat{\gamma}_i^n + K) C_i^n + \hat{\lambda} C_{i-1}^n. \quad (19)$$

For upper boundary, where $i = 1$, plug the known value of the left boundary $C_0^n = C_0$ to (19) in the right hand side; we obtain

$$S_{1_1} = (\hat{\lambda} - \hat{\gamma}_1^n) C_2^n - (2\hat{\lambda} - \hat{\gamma}_1^n + K) C_1^n + \hat{\lambda} C_0. \quad (20)$$

For the lower boundary, where $i = M$, substitute the approximate unknown value of the right boundary by the forward difference approximation to $\partial C/\partial x = 0$. Let $C_M = C_{M-1}$ and rearrange; we obtain

$$S_{M_1} = -(\hat{\lambda} + K) C_{M-1}^n + \hat{\lambda} C_{M-2}^n. \quad (21)$$

Taking the Euler formula, we obtain the MacCormack predictor step formulation:

$$C_i^{n+1} = C_i^n + S_{i_1} \Delta t. \quad (22)$$

The second step is a modified backward time central space (BTCS) scheme by changing the central space evaluation time n with a backward space evaluation. It is essentially a backward time backward space (BTBS) scheme. The BTBS scheme approximates the temporal and spacial derivatives and the decay in (6) with the following discretization:

$$\begin{aligned} C &\cong \frac{1}{2} (C_i^n + C_i^{n+1}), \\ \frac{\partial C}{\partial t} &\cong \frac{C_i^{n+1} - C_i^n}{\Delta t}, \\ \frac{\partial C}{\partial x} &\cong \frac{C_i^{n+1} - C_{i-1}^{n+1}}{\Delta x}, \\ \frac{\partial^2 C}{\partial x^2} &\cong \frac{1}{2} \left(\frac{C_{i+1}^n - 2C_i^n + C_{i-1}^n}{(\Delta x)^2} + \frac{C_{i+1}^{n+1} - 2C_i^{n+1} + C_{i-1}^{n+1}}{(\Delta x)^2} \right). \end{aligned} \quad (23)$$

Because the values at time level $n+1$ have been calculated in predictor step, the second step is also explicit. It follows that the slope base on their predictor points can be calculated as follows:

$$S_{i_2} = \lambda C_{i+1}^{n+1} - (2\lambda + \gamma_i^{n+1} + K) C_i^{n+1} + (\lambda + \gamma_i^{n+1}) C_{i-1}^{n+1}. \quad (24)$$

For upper boundary, where $i = 1$, plug the known value of the left boundary $C_0^{n+1} = C_0$ to (24) in the right hand side. We obtain

$$S_{i_2} = \lambda C_2^{n+1} - (2\lambda + \gamma_1^{n+1} + K) C_1^{n+1} + (\lambda + \gamma_1^{n+1}) C_0. \quad (25)$$

For the lower boundary, where $i = M$, substitute the approximate unknown value of the right boundary by the backward difference approximation to $\partial C / \partial x = 0$. Let $C_{M+1} = C_M$ and rearrange; then, we obtain

$$\begin{aligned} S_{M_2} &= \lambda C_M^{n+1} - (2\lambda + \gamma_M^{n+1} + K) C_M^{n+1} \\ &\quad + (\lambda + \gamma_M^{n+1}) C_{M-1}^{n+1}. \end{aligned} \quad (26)$$

From both of the steps, the MacCormack scheme takes the following form:

$$C_i^{n+1} = C_i^n + \frac{\Delta t}{2} (S_{i_1} + S_{i_2}). \quad (27)$$

The MacCormack scheme is conditionally stable subject to constraints in (16). The stability requirements for the scheme are [22]

$$\begin{aligned} \lambda &= \frac{D \Delta t}{(\Delta x)^2} < \frac{1}{2}, \\ \gamma_i^n &= \frac{\widehat{U}_i^n \Delta t}{\Delta x} < 0.9, \end{aligned} \quad (28)$$

where λ is the diffusion number (dimensionless) and γ_i^n is the advection number or Courant number (dimensionless).

4.2. The Modified MacCormack Scheme. Since the derivative approximation during discretization is not centered, numerical dispersion will be introduced. The dispersion coefficients used in the dispersion model would take the value obtained by subtracting the numerical dispersion from the real data of the stream. The amounts of the numerical dispersion introduced by backward space denoted by Dn_1 and forward time denoted by Dn_2 schemes as follow [3, 12]:

$$\begin{aligned} Dn_{1i}^n &= \frac{\Delta x}{2} \widehat{U}_i^n, \\ Dn_{2i}^n &= -\frac{\Delta x}{2} (\widehat{U}_i^n)^2. \end{aligned} \quad (29)$$

There are temporal and spacial numerical dispersion in both predictor and corrector steps since the scheme uses forward time forward space difference for prediction and backward time backward space difference for correction. From (29), the numerical dispersion for forward time forward space prediction step and backward time backward space correction step are

$$\begin{aligned} D_{n_{\text{prdi}}}^n &= -\frac{\Delta x}{2} \widehat{U}_i^n - \frac{\Delta t}{2} (\widehat{U}_i^n)^2, \\ D_{n_{\text{crdi}}}^n &= \frac{\Delta x}{2} \widehat{U}_i^n + \frac{\Delta t}{2} (\widehat{U}_i^n)^2. \end{aligned} \quad (30)$$

The modified MacCormack scheme uses the following corrected dispersion, rather than the real dispersion coefficients for calculation in both prediction and correction steps:

$$\begin{aligned} D_{1i}^n &= D_{\text{real}} - D_{n_{\text{prdi}}}^n, \\ D_{2i}^n &= D_{\text{real}} - D_{n_{\text{crdi}}}^n, \end{aligned} \quad (31)$$

where D_{1i}^n is the dispersion coefficient used in the prediction step and D_{2i}^n is the dispersion coefficient used in the correction step.

The modified MacCormack scheme is conditionally stable subject to the constraint in (16). The stability requirements for the scheme:

$$\begin{aligned} \lambda &= \frac{D_{\text{max}} \Delta t}{(\Delta x)^2} < \frac{1}{2}, \\ \gamma_i^n &= \frac{\widehat{U}_i^n \Delta t}{\Delta x} < 0.9, \end{aligned} \quad (32)$$

where the maximum of numerical dispersion coefficients is $D_{\text{max}} = \max\{D_{1i}^n, D_{2i}^n : 0 \leq i \leq M, 0 \leq n \leq N\}$.

5. The Accuracy of the Hydrodynamic Approximation

It is not hard to find the analytical solution $d(x, t)$ in (5) with $f(t) = \sin t$. By changing of variables, $d(x, t) = e^{it} \mathcal{D}(x)$ and $u(x, t) = e^{it} \mathcal{U}(x)$ for some $\mathcal{D}(x), \mathcal{U}(x) \in C_0^2[0, 1]$ by substituting it in (5). Using a separable variables technique, we can obtain $d(1, t)$ a solution [10]:

$$d(1, t) = \frac{\sin t \cos \beta \cosh \alpha - \cos t \sin \beta \sinh \alpha}{\cos^2 \beta \cosh^2 \alpha + \sin^2 \beta \sinh^2 \alpha}, \quad (33)$$

TABLE 1: The velocity of water flow $u(x, t)$.

t	$x = 0$	$x = 0.1$	$x = 0.2$	$x = 0.3$	$x = 0.4$	$x = 0.5$	$x = 0.6$	$x = 0.7$	$x = 0.8$	$x = 0.9$	$x = 1.0$
10	1.3125	1.2187	1.1125	0.9960	0.8704	0.7372	0.5977	0.4530	0.3041	0.1525	0.0000
20	-1.0899	-1.0355	-0.9644	-0.8782	-0.7784	-0.6670	-0.5456	-0.4162	-0.2808	-0.1414	0.0000
30	0.5200	0.5224	0.5088	0.4801	0.4380	0.3839	0.3196	0.2471	0.1683	0.0852	0.0000
40	0.2172	0.1586	0.1105	0.0723	0.0433	0.0226	0.0091	0.0014	-0.0015	-0.0015	0.0000

TABLE 2: The pollutant concentration $C(x, t)$ of traditional MacCormack scheme, $\Delta x = 0.025$ and $\Delta t = 0.00125$.

t	$x = 0$	$x = 0.1$	$x = 0.2$	$x = 0.3$	$x = 0.4$	$x = 0.5$	$x = 0.6$	$x = 0.7$	$x = 0.8$	$x = 0.9$	$x = 1.0$
10	1.000000	0.174513	0.029152	0.004634	0.000697	0.000099	0.000013	0.000002	0.000000	0.000000	0.000000
20	1.000000	0.054532	0.003068	0.000180	0.000011	0.000001	0.000000	0.000000	0.000000	0.000000	0.000000
30	1.000000	0.125937	0.015943	0.002012	0.000251	0.000031	0.000004	0.000000	0.000000	0.000000	0.000000
40	1.000000	0.105911	0.010827	0.001074	0.000104	0.000010	0.000001	0.000000	0.000000	0.000000	0.000000

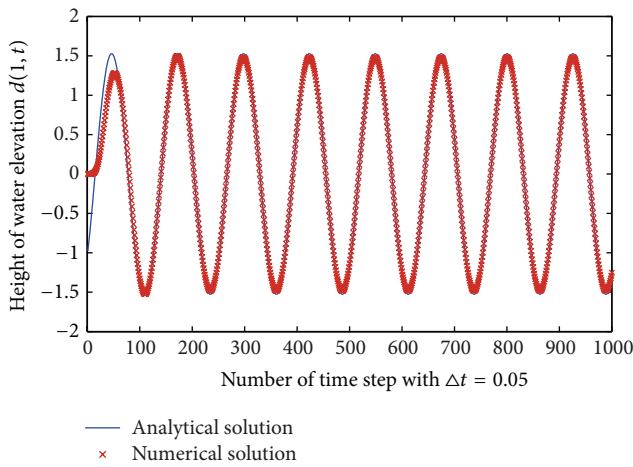
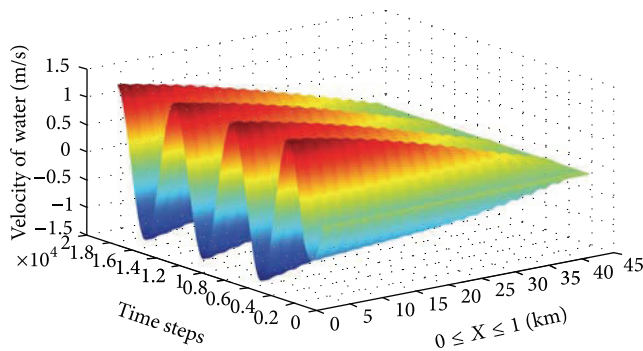
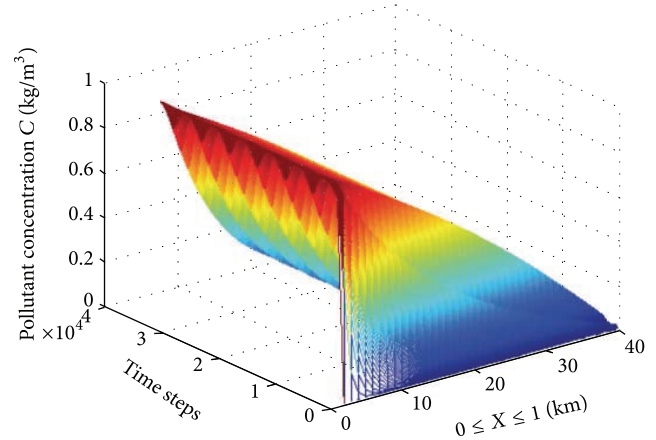
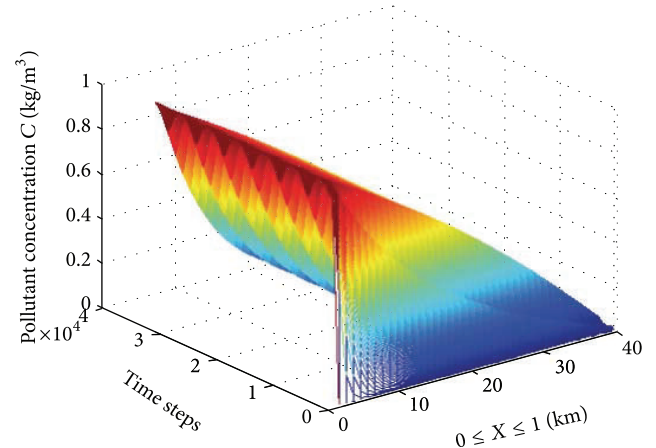


FIGURE 2: Comparison of analytical solution for height of water elevation with results obtained by numerical technique at the end point of the domain.

FIGURE 3: The water velocity $u(x, t)$ m/s.

where $\alpha = 2^{1/4} \cos(3\pi/8)$ and $\beta = 2^{1/4} \sin(3\pi/8)$. However, it is not easy to find the analytical solution $u(x, t)$ of (5). We use the solution $d(1, t)$ obtained in (33) to verify our approximate solution obtained by the Crank-Nicolson method equation (13). Actually when the Crank-Nicolson method is used, we get the approximate solution both $d(x, t)$ and $u(x, t)$. We

FIGURE 4: The pollutant concentration $C(x, t)$ (mg/L) using traditional MacCormack scheme.FIGURE 5: The pollutant concentration $C(x, t)$ (mg/L) using modified MacCormack scheme.

assume that when we get a good approximation for $d(x, t)$, this implies that the method gives a good approximation for $u(x, t)$. The verification of the approximate solution $\bar{d}(1, t)$ is shown in Figure 2.

TABLE 3: The pollutant concentration $C(x, t)$ of modified MacCormack scheme, $\Delta x = 0.025$ and $\Delta t = 0.00125$.

t	$x = 0$	$x = 0.1$	$x = 0.2$	$x = 0.3$	$x = 0.4$	$x = 0.5$	$x = 0.6$	$x = 0.7$	$x = 0.8$	$x = 0.9$	$x = 1.0$
10	1.000000	0.146939	0.021001	0.002907	0.000388	0.000050	0.000006	0.000001	0.000000	0.000000	0.000000
20	1.000000	0.059627	0.003656	0.000233	0.000015	0.000001	0.000000	0.000000	0.000000	0.000000	0.000000
30	1.000000	0.117948	0.013959	0.001648	0.000193	0.000022	0.000003	0.000000	0.000000	0.000000	0.000000
40	1.000000	0.103863	0.010501	0.001038	0.000101	0.000010	0.000001	0.000000	0.000000	0.000000	0.000000

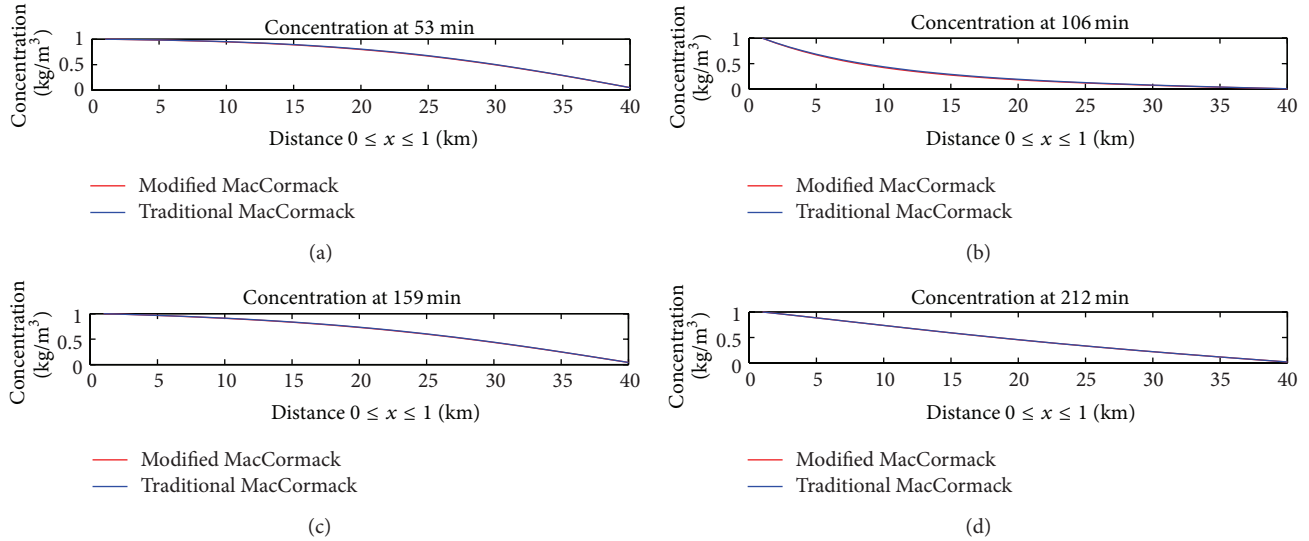


FIGURE 6: The comparison of concentration at 4 different time instants of Modified MacCormack and Traditional MacCormack methods.

Figure 2 shows the comparison between the analytical solutions $d(1, t)$ and the approximate solutions $\tilde{d}(1, t)$ only at the end of the domain.

Unfortunately, the analytical solutions of the hydrodynamic model could not be found over the entire domain [10]. This implied that the analytical solutions of the dispersion model could not be computed at any points in the domain as well.

6. Application to the Stream Water Quality Assessment Problem

Suppose that the measurement of pollutant concentration C in a nonuniform flow stream is considered. A stream is aligned with longitudinal distance, 1.0 (km) total length and 1.0 (m) depth. There is a plant which discharges waste water into the stream and the pollutant concentration at the discharge point is $C(0, t) = C_0 = 1$ (mg/L) at $x = 0$ for all $t > 0$ and $C(x, 0) = 0$ (mg/L) at $t = 0$. The elevation of water at the discharge point can be described as a function $d(0, t) = f(t) = \sin t$ (m) for all $t > 0$, and the elevation does not change at $x = 1.0$ (km). The physical parameters of the stream system are diffusion coefficient $D = 0.0125$ (m²/s) and a first-order reaction rate 10^{-5} s⁻¹. In the analysis conducted in this study, meshing the stream into 40 elements with $\Delta x = 0.025$, and the time increment is 0.4 (s) with $\Delta t = 0.00125$, characterizing a one-dimensional flow. Using the Crank-Nicolson method of [9, 10, 13], it can be

obtained the water velocity $u(x, t)$ in Table 1 and Figure 3. Next, the approximate water velocity can be plugged into the traditional MacCormack scheme in (27). We also plug the approximate water velocity into the modified MacCormack scheme (27) with numerical dispersion coefficients (31). The approximation of pollutant concentrations C of both schemes is shown in Tables 2 and 3 and Figures 4 and 5. The comparison of traditional MacCormack and modified MacCormack is shown in Figure 6.

7. Discussion and Conclusions

The approximation of the pollutant concentrations of the traditional and modified MacCormack schemes is shown in Tables 2 and 3. The real-world problems require a small amount of time interval in obtaining accurate solutions. Unfortunately, the analytical solutions of the hydrodynamic model could not be found over the entire domain. This also implies that the analytical solutions of dispersion model could not work out at any point on the entire domain as well [13].

In [13], it is revealed that the diffusion coefficients of the pollutant matter can reduce the concentration of the nonuniform stream. If sewage effluent with a low diffusion coefficient has discharged into a nonuniform flow stream, then the water quality will be lower than a discharging of high diffusion coefficients of other pollutant matters.

We propose a modified MacCormack scheme by adding a simple revision to the traditional MacCormack scheme. The numerical dispersion has been introduced because the derivative approximation during discretization is not centered. The traditional MacCormack scheme shows excessive dispersion effects for large time and space step lengths, significantly decreasing the efficiency of the traditional MacCormack scheme [3]. To eliminate the numerical dispersion effect, the modified MacCormack scheme for the nonuniform flow is proposed. Though revision shows a good agreement in accuracy with the original one, the modified MacCormack scheme becomes less efficient than the traditional MacCormack scheme.

In this paper, the hydrodynamic model and the convection-diffusion-reaction equation can be combined to approximate the pollutant concentration in a stream when the current reflecting water in the stream is not uniform. The technique developed in this paper, the response of the stream to the two different external inputs: the elevation of water and the pollutant concentration at the discharge point, can be obtained. Both of the traditional and the modified MacCormack schemes can be used in the dispersion model since the scheme is very simple to implement. By both of the traditional and the modified MacCormack finite difference formulations, we obtain that the proposed technique is applicable and economical to be used in the real-world problem due to its simplicity to program and the straightforwardness of the implementation. It is also possible to find tentative better locations and better periods of time of the different discharge points to a stream.

Conflict of Interests

The author declares that there is no conflict of interests regarding the publication of this paper.

Acknowledgments

The author greatly appreciates all valuable comments received from Prof. Chatchai Leenawong and the referees.

References

- [1] N. Pochai, S. Tangmanee, L. J. Crane, and J. J. H. Miller, "A mathematical model of water pollution control using the finite element method," *Proceedings in Applied Mathematics and Mechanics*, vol. 6, no. 1, pp. 755–756, 2006.
- [2] J. Y. Chen, C. Ko, S. Bhattacharjee, and M. Elimelech, "Role of spatial distribution of porous medium surface charge heterogeneity in colloid transport," *Colloids and Surfaces A*, vol. 191, no. 1-2, pp. 3–15, 2001.
- [3] G. Li and C. R. Jackson, "Simple, accurate, and efficient revisions to MacCormack and Saul'yev schemes: high Peclet numbers," *Applied Mathematics and Computation*, vol. 186, no. 1, pp. 610–622, 2007.
- [4] E. M. O'Loughlin and K. H. Bowmer, "Dilution and decay of aquatic herbicides in flowing channels," *Journal of Hydrology*, vol. 26, no. 3-4, pp. 217–235, 1975.
- [5] M. Dehghan, "Numerical schemes for one-dimensional parabolic equations with nonstandard initial condition," *Applied Mathematics and Computation*, vol. 147, no. 2, pp. 321–331, 2004.
- [6] A. I. Stamou, "Improving the numerical modeling of river water quality by using high order difference schemes," *Water Research*, vol. 26, no. 12, pp. 1563–1570, 1992.
- [7] P. Tabuenca, J. Vila, J. Cardona, and A. Samartin, "Finite element simulation of dispersion in the Bay of Santander," *Advances in Engineering Software*, vol. 28, no. 5, pp. 313–332, 1997.
- [8] N. Pochai, "A numerical computation of the non-dimensional form of a non-linear hydrodynamic model in a uniform reservoir," *Journal of Nonlinear Analysis: Hybrid Systems*, vol. 3, no. 4, pp. 463–466, 2009.
- [9] N. Pochai, S. Tangmanee, L. J. Crane, and J. J. H. Miller, "A water quality computation in the uniform channel," *Journal of Interdisciplinary Mathematics*, vol. 11, no. 6, pp. 803–814, 2008.
- [10] N. Pochai, "A numerical computation of a non-dimensional form of stream water quality model with hydrodynamic advection-dispersion-reaction equations," *Journal of Nonlinear Analysis: Hybrid Systems*, vol. 3, no. 4, pp. 666–673, 2009.
- [11] W. F. Ames, *Numerical Methods for Partial Differential Equations*, Academic Press, 2nd edition, 1977.
- [12] S. C. Chapra, *Surface Water-Quality Modeling*, McGraw-Hill, 1997.
- [13] N. Pochai, "A numerical treatment of nondimensional form of water quality model in a nonuniform flow stream using Saul'yev scheme," *Mathematical Problems in Engineering*, vol. 2011, Article ID 491317, 15 pages, 2011.
- [14] H. Karahan, "A third-order upwind scheme for the advection-diffusion equation using spreadsheets," *Advances in Engineering Software*, vol. 38, no. 10, pp. 688–697, 2007.
- [15] M.-S. Liou and C. J. Steffen Jr., "A new flux splitting scheme," *Applied Mathematics and Computation*, vol. 107, no. 1, pp. 23–39, 1993.
- [16] A. Mazzia, L. Bergamaschi, C. N. Dawson, and M. Putti, "Godunov mixed methods on triangular grids for advection-dispersion equations," *Computational Geosciences*, vol. 6, no. 2, pp. 123–139, 2002.
- [17] C. Dawson, "Godunov-mixed methods for advection-diffusion equations in multidimensions," *SIAM Journal on Numerical Analysis*, vol. 30, no. 5, pp. 1315–1332, 1993.
- [18] K. Alhumaizi, "Flux-limiting solution techniques for simulation of reaction-diffusion-convection system," *Communications in Nonlinear Science and Numerical Simulation*, vol. 12, no. 6, pp. 953–965, 2007.
- [19] N. Happenhofer, O. Koch, F. Kupka, and F. Zaussinger, "Total variation diminishing implicit Runge-Kutta methods for dissipative advection-diffusion problems in astrophysics," *Proceedings in Applied Mathematics and Mechanics*, vol. 11, pp. 777–778, 2011.
- [20] H. Ninomiya and K. Onishi, *Flow Analysis Using a PC*, CRC Press, 1991.
- [21] A. R. Mitchell, *Computational Methods in Partial Differential Equations*, John Wiley & Sons, 1969.
- [22] B. Bradie, *A Friendly Introduction to Numerical Analysis*, Prentice Hall, 2005.

Research Article

Eddy Heat Conduction and Nonlinear Stability of a Darcy Lapwood System Analysed by the Finite Spectral Method

Jónas Eliasson^{1,2}

¹ Earthquake Engineering Research Centre, University of Iceland, 800 Selfoss, Iceland

² Disaster Prevention Research Institute, University of Kyoto, Gokasyo, Uji, Kyoto 6110011, Japan

Correspondence should be addressed to Jónas Eliasson; jonase@hi.is

Received 23 September 2013; Accepted 11 December 2013; Published 5 February 2014

Academic Editor: Luís Godinho

Copyright © 2014 Jónas Eliasson. This is an open access article distributed under the Creative Commons Attribution License, which permits unrestricted use, distribution, and reproduction in any medium, provided the original work is properly cited.

A finite Fourier transform is used to perform both linear and nonlinear stability analyses of a Darcy-Lapwood system of convective rolls. The method shows how many modes are unstable, the wave number instability band within each mode, the maximum growth rate (most critical) wave numbers on each mode, and the nonlinear growth rates for each amplitude as a function of the porous Rayleigh number. Single amplitude controls the nonlinear growth rates and thereby the physical flow rate and fluid velocity, on each mode. They are called the flak amplitudes. A discrete Fourier transform is used for numerical simulations and here frequency combinations appear that the traditional cut-off infinite transforms do not have. The discrete show a stationary solution in the weak instability phase, but when carried past 2 unstable modes they show fluctuating motion where all amplitudes except the flak may be zero on the average. This leads to a flak amplitude scaling process of the heat conduction, producing an eddy heat conduction coefficient where a $Nu-R_{aL}$ relationship is found. It fits better to experiments than previously found solutions but is lower than experiments.

1. Introduction

Convection in porous media is intensively studied because of its many applications in science and industry. Free convection in porous media (i.e., convection without the forcing of horizontal temperature gradients) has been studied from 1948, [1–3] made the first experiments, and [4] treated the stability of 2-dimensional cellular flow (rolls). Others are investigating stability problems with increasing complexity, for example, [5]. Modal flow and the spectral method were used to simulate unsteady motion by [6].

The spectral method is used in [7] and it gives an excellent review of approximate solutions, sometimes based on earlier findings [8, 9]. In the review paper [7] the most general case, the DLFB (Darcy-Lapwood-Forchheimer-Brinkman) equation, is studied, sometimes with Coriolis force and magnetic forces being included.

In thick natural aquifers the viscous dissipation, not already included in Darcy-Lapwood (DL) systems, is unimportant in most cases and so is turbulent dissipation except

in local irregularities in the porous matrix. Porous media flows on low Reynolds numbers are therefore mostly treated without the terms of Forchheimer and Brinkman; they serve as a bridge between the turbulent and viscous and Darcy regimes. This paper is devoted to the case of simple DL systems and it is shown that turbulent-like phenomena can be encountered in such flow even though dissipation is strictly Darcy-laminar. The effect of this turbulence is on the heat flow, amplitude growth rates, and the wave length spectrum and this is studied further.

The heat flow through a porous convective layer is controlled by Nusselt's number Nu . Finding it is therefore very important in industrial applications. In [10] flow in a box with open surface is investigated numerically for Rayleigh numbers up to 300 and it is found that there may be more than one flow cell. The author finds Nusselt's numbers (Nu) in the range of $3(Ra/70) - 5(Ra/200)$ for this flow and in some cases for eddy flow. He also finds single-cell flow for $Ra < 60$ but two cells for $100 < Ra$. Multicellular flow and modal flow are also encountered in other papers on the subject [11, 12].

Stability analyses of the no-flow situation and the onset of convection give important information on the structure of the resulting flow through the composition of the eigenfunctions. They depend upon the boundary conditions; therefore a great variety of eigenfunctions have been found for the rolls of the DL equation system covering different sets of boundary conditions [12–15].

The eigenfunctions of the DL system in an infinite horizontal aquifer of constant thickness and constant temperature difference are particularly simple as they are the ordinary trigonometric functions. This makes the Fourier transform of the spectral method be an expansion of the temperature function in a series of the eigenfunctions of the Sturm-Liouville problem underlying the stability analysis [6]. This makes the identification of the different modes and their stability limits particularly easy and in this paper it is shown to give rise to a new kind of non-linear stability analysis with the starting point in an arbitrary stationary solution. From this process the Fourier amplitudes emerge that make up the average vertical temperature gradient, here called the flak amplitudes. They alone control the exponential growth rate of all amplitudes and make it possible to construct by scaling an eddy coefficient of heat conduction, very similar to eddy viscosity in ordinary turbulence. This eddy coefficient of heat conduction allows the approximated solutions described by [7] to produce realistic relationship between the porous Rayleigh number and Nusselt's number for DL systems and thus give better estimates for the heat flow through the porous layer. As the flak amplitudes appear also in DLFB systems, it may be suggested to use the scaling procedure for them also, but it is much more complicated and is not attempted in this paper. Simulation grids $NI \times NJ = 7 \times 5$ up to $t = 1.5$. $R_{aL} = 180$.

2. The Darcy-Lapwood System

Two-dimensional nonlinear thermal convection in a homogeneous horizontal aquifer, uniformly heated from below and cooled from above, is described by a differential system originally presented in [16]. In [15] it is presented in cylindrical coordinates. Here we use the notations in [10]:

$$-\frac{\partial \theta}{\partial t} + \frac{\partial^2 \theta}{\partial x^2} + \frac{\partial^2 \theta}{\partial z^2} = \frac{\partial \psi}{\partial x} \cdot \frac{\partial \theta}{\partial z} - \frac{\partial \psi}{\partial z} \cdot \frac{\partial \theta}{\partial x}, \quad (1)$$

$$\frac{\partial^2 \psi}{\partial x^2} + \frac{\partial^2 \psi}{\partial z^2} = R_{aL} \cdot \frac{\partial \theta}{\partial x}, \quad (2)$$

$\theta = T/T_0$, dimensionless temperature. T_0 is the difference of the constant temperatures of top and bottom. ψ is dimensionless stream function. x and z are dimensionless coordinates in horizontal and vertical direction. Lapwood (porous) Rayleigh number, where c is heat capacity of the porous layer (cal/(kg°K)), k is coefficient of permeability (m/s), $\Delta \rho$ is fluid density difference (kg/m³) corresponding to T_0 , H is thickness of aquifer (m), and λ is coefficient of heat conduction (cal/(m s°K)) for the porous layer.

3. The Spectral Method Using Infinite Spectrum

3.1. Equations. The boundary conditions are $\psi = \theta = 0$ at $z = 1$, $\theta = 1$, and $\psi = 0$ at $z = 0$; then the temperature distribution in a cellular flow is given by the following Fourier series:

$$\theta = 1 - z + \sum_{i,j=0,1}^{\infty,\infty} P_{ij} \cos(imx) \sin(j\pi z), \quad (3)$$

m is the basic horizontal wave number, i is horizontal wave number, and j is called the mode. Individual amplitudes must satisfy the following equations:

$$\begin{aligned} & \frac{dP(i, j)}{dt} \\ &= \omega(i, j) P(i, j) - \frac{R_{aL} m^2 \pi}{4} \end{aligned} \quad (4)$$

$$\begin{aligned} & \times \sum_{- \infty, \infty}^{\infty, \infty} D(i, j, p, q) P(|p|, |q|) P(|p - i|, |q - j|), \\ & \omega(i, j) = \frac{m^2 i^2 R_{aL} - (m^2 i^2 + \pi^2 j^2)^2}{m^2 i^2 + \pi^2 j^2}. \end{aligned} \quad (5)$$

Equation (4) indicates exponential growth in the first term; (5) shows the growth rate. The last term in (4) is a sum, that is, a quadratic form in all the temperature amplitudes in (3). This simple form emerges because the trigonometric functions in (3) are the eigenfunctions of the Sturm-Liouville problem encountered in stability analysis of the Lapwood system [6]. The quadratic form in (4) may be compared to the sums presented in [7] developed for the DLB (Darcy-Lapwood-Brinkman) system. They include the same amplitude combination in the quadratic form and the later introduced flak ($P(0, 2j)$) amplitudes may be found in [7, Equation (86)], even though their system is very different.

3.2. Linear Stability Analysis. In linear stability analysis we assume no flow to be present; this means linear temperature gradient or that all amplitudes in (3) are zero. Using the regular perturbation theory, we then assume a perturbation introduced in the form of infinitesimal amplitudes. The quadratic form in (4) will now drop out and we are left with the exponential growth terms, that is, (4) without the quadratic form. Stability requires all growth rates to be negative or zero:

$$\text{all } \omega(i, j) < 0 \implies R_{aL} < 4\pi^2 j^2 = R_{aL0j}. \quad (6)$$

R_{aL0j} is the critical Rayleigh number for the mode j (the j th eigenfunction). The classical value $R_{aL, \text{crit}} = R_{aL01} = 4\pi^2$. If $Ra > R_{aL01}$ and J is a whole number defined by

$$4\pi^2 J^2 < R_{aL0j} < 4\pi^2 (J + 1)^2, \quad (7)$$

J modes are unstable and all unstable wave numbers belonging to these modes will grow exponentially in a flow started

from rest. The unstable wave numbers are within the *wave number instability band*, between i_{01} and i_{02} in the following equation, they are the zeros of (5)

$$i_{02} - i_{01} = \frac{1}{m} \sqrt{R_{aL} - R_{aL0j}}. \quad (8)$$

Maximum growth rate wave number, sometimes called the *most critical wave number*, is

$$mi_{\max} = \sqrt{\pi j \sqrt{R_{aL}} - \frac{R_{aL0j}}{4}}, \quad (9)$$

$$\text{and then } \omega_{\max} = R_{aL} - \sqrt{R_{aL} R_{aL0j}}.$$

For $R_{aL} = R_{aL01}$ (ca. 40) we find $mi_{\max} = \pi$ and it does not become 2π until $R_{aL} = 25\pi^2$ so, in a Fourier transform with $m = \pi$, the $i = 1$ will be the fastest growing wave number in flows between the first and second critical Rayleigh numbers. This sets the width of the flow cell.

3.3. Nonlinear Stability Analysis. The elements in the coefficient tensor in (4) can be calculated from the following algorithm:

$$D(i, j, p, q) = \frac{1 + \delta(p, 0)}{1 + \delta(i, 0)} \frac{(p - i)(qi - pj)}{m^2(p - i)^2 + \pi^2(q - j)^2} \frac{|q|}{q} \frac{|q - 1|}{q - j}, \quad (10)$$

$\delta(i, j) = 1$ for $i = j$; otherwise $\delta = 0$.

We now assume that a stationary solution to the system equations (4)–(10) exists. It has to fulfil the system equations with the term $dP/dt = 0$. No matter what the value of individual amplitudes is, this system must be stable against *all* perturbations $\Delta P(i, j)$ also if a perturbation is placed on only one amplitude but the others are unperturbed. This leads to the following equation for the perturbation of the stable amplitude $P(i, j)$:

$$\frac{d\Delta P(i, j)}{dt} = \Omega(i, j) \Delta P(i, j). \quad (11)$$

This is the same equation as the linear counterpart, only with a different growth rate, which from (10) is found to be

$$\Omega(i, j) = \frac{m^2 i^2 R_{aL} (1 + \pi j P(0, 2j)) - (m^2 i^2 + \pi^2 j^2)^2}{m^2 i^2 + \pi^2 j^2}. \quad (12)$$

This is the non-linear growth rate Ω instead of the linear one ω . The only difference between the nonlinear and the linear growth rate is that we must insert in (5) a new R_{aL} :

$$\tilde{R}_{aL} = R_{aL} (1 + \pi j P(0, 2j)). \quad (13)$$

As in the linear case stability requires

$$\begin{aligned} \text{all } \Omega(i, j) \leq 0 &\implies \tilde{R}_{aL} \leq R_{aL0j} \\ &\implies P(0, 2j) \leq -\frac{1}{\pi j} \frac{R_{aL} - R_{aL0j}}{R_{aL}}, \end{aligned} \quad (14)$$

where the $=$ sign means neutral stability. It must be noted that this is a necessary condition for any solution to be stable, but it is not sufficient as all amplitudes are not perturbed.

If a stable solution turns unstable (e.g., from increasing T_0) the disturbance of one amplitude may eventually spread to all the others. Taking $P(0, 2j)$ themselves they have this equation

$$\begin{aligned} \frac{dP(0, 2j)}{dt} &= -4\pi^2 j^2 P(0, 2j) \\ &\quad - R_{aL} \pi j \sum_1^{\infty} \frac{m^2 p^2}{m^2 p^2 + \pi^2 j^2} \frac{1}{2} P^2(p, j) + \dots \end{aligned} \quad (15)$$

Here there are two opposing forces, the strong curbing effect of the negative linear growth rate and the negative sum that carries in it the total spectral energy on the j th mode. There is infinity of other quadratic terms, not shown, but these have a good chance of cancelling each other out in a time average, as they would contain the correlation coefficient between the respective amplitudes. If any amplitude on any mode gets very big the $P(0, 2j)$ will grow strongly negative with it and then pull it down as the nonlinear growth rate turns negative. Such action may clearly be seen in the following simulations and therefore we call the $P(0, 2j)$'s flak amplitudes. The amplitude combinations in the quadratic form of (4) reflect the fundamental property of the trigonometric functions that $e^{mx} e^{nx} = e^{(m+n)x}$. They are the same for all two-dimensional systems having the nonlinearities in quadratic terms only.

The flak amplitudes govern the flow pattern. They grow and diminish with the energy on the corresponding unstable mode by controlling the nonlinear growth rates Ω of all flow amplitudes. Later we see that they make up the horizontal average temperature distribution and with it the Nu. They are always negative and must not be above a certain stability value in any stationary flow that might exist. There is a single infinity of critical Rayleigh numbers; each time one is passed while the fluid is heating up, the corresponding flak amplitude has to grow to a significant value.

It may be shown that (1) and (2) have a symmetrical solution that is even; that is, all amplitudes in (4) where $i + j$ is an uneven number are zero. In [4, 7] this is used; the consequence is that, when only one stable solution exists for each R_{aL} , it is even. The physical difference of uneven and even solutions is that uneven solutions have uneven flak amplitudes $P(0, j)$ with j being an uneven number. Then the average heat flow at top and bottom is not the same and the porous layer may be heating up or cooling down as a whole. An even Fourier transform is more stable than the one where uneven amplitudes are allowed. But it seems inevitable that uneven amplitudes can participate in unsteady flow. Stability analysis of the even solution [6] indicate that this solution may be stable in the R_{aL} number range $40 < A < 160$ or between the two first critical R_{aL} numbers.

Equation (14) does not have to hold for fluctuating motion when many modes are unstable. It is however difficult to see how fluctuating motion (Figure 4) can be maintained unless the flak amplitudes do fluctuate around (14) value.

3.4. The Spectral Method Using Discrete Fourier Transform. In numerical calculations (4) cannot be truncated without introducing systematic errors. Finite Fourier transforms will be used instead and then new amplitude combinations appear in the quadratic form in (4). The new quadratic form becomes

$$\sum_{-NI, -NJ+1}^{NI, NJ-1} D(i, j, p, q) P(|p|, |q|) P(p', q'), \quad (16)$$

where

$$p' = |i - p| + NI + p - i - |NI + p - i|,$$

$$q' = |j - q| + NJ + q - j - |NJ + q - j|,$$

$$D(i, j, p, q) = \frac{p' (p' |q| s_1 + |p| q' s_2) (1 + \delta(p, 0))}{(m^2 p'^2 + \pi^2 q'^2) (1 + \delta(i, 0) + \delta(i, NI))}. \quad (17)$$

NI and NJ are the horizontal and vertical maximum wave numbers; δ is Kronecker's delta; s_1 and s_2 are sign control functions that are to be taken from Table 1 as plus or minus one.

As may be seen by comparing (10) and (17), truncation of (3) may introduce a significant error. The discrete quadratic equation (16) is evaluated for discrete values of x and z only, so it contains amplitude combinations that are not at all present in the infinite quadratic equations (4) and (10), as explained in [6]. If the truncation is done as a cutoff at constant $i + j$ these amplitude combinations are totally absent.

When an infinite transform is truncated, all the amplitudes above the cut-off frequency are considered to be zero, but discrete forms may be cut off anywhere, discrete forms may be cut off anywhere. A discrete Fourier transform is a process where any number of points is transformed into an equal number of Fourier coefficients, so the transform creates a function that goes through the entire original points exactly. Therefore, for all situations, stable or unstable, there exists a finite Fourier transform for any number of NI and NJ. It may be noted that FFT algorithm is a discrete transformation so turbulence simulations using this technique have the extra frequency combinations included.

4. Simulations Using the Discrete Fourier Transform

4.1. General Remarks. To simulate, m as well as NI and NJ has to be selected. When fluctuating motion like this is simulated using (4) with a constant value of m , one is actually simulating convection in a box. Simulations using (16) and (17) may be fired up by putting a small constant on all amplitudes (spatially distributed random noise). For low Rayleigh numbers this leads to a stable solution where all the uneven amplitudes disappear. In order to give a realistic picture of the flow, simulations need to include sufficiently many modes, so all unstable modes are controlled. $NJ - 1$ must therefore be not less than two times the number of unstable modes, at least in theory. Intuitively, one would expect too low NJ simulations to be unstable for high Rayleigh numbers, but

on the contrary they are more stable. The physical explanation of this is that using a discrete transform with low $NI \times NJ$ means that we only have $NI \times NJ$ many values for the Ψ and θ and each of these values must represent the average in the corresponding rectangle. But averaging the equations means that a new coefficient of heat conduction, similar to the eddy viscosity, appears on the scene (21). This is explained in the section on scaling.

In the very weak instability phase (R_{aL} little higher than 40), only one mode is unstable and $m = \pi$ gives the maximum growth rate of the instabilities, so in (14) the period $P(1, 1)$ will grow fastest when we use $m = \pi$. This is therefore used in all the simulations; it makes the results better comparable.

4.2. Simulations with $NI \times NJ$ Grid 2×3 . Possible number of amplitudes is 6, $((NJ - 1) \times (NI + 1))$, making 3 even amplitudes but one of them, $P(2, 2)$, turns out to be zero. The two remaining are the $P(1, 1)$ and its flak amplitude $P(0, 2)$.

This approximation has been studied by [4], who use a series expansion to find it, and [6] that uses (16) and (17). This rather crude approximation can take all R_{aL} 's and is always stable.

The formula for this solution is

$$\theta(x, z) = 1 + z + P_{11} \cos mx \sin \pi z - P_{02} \sin 2\pi z, \quad (18)$$

$$P_{11} = 4 \sqrt{\frac{R_{aL} - R_{aL01}}{R_{aL}^2}}, \quad P_{02} = -\frac{1}{\pi} \frac{R_{aL} - R_{aL01}}{R_{aL}}, \quad (19)$$

$$Nu = 1 + 2 \frac{R_{aL} - R_{aL01}}{R_{aL}}.$$

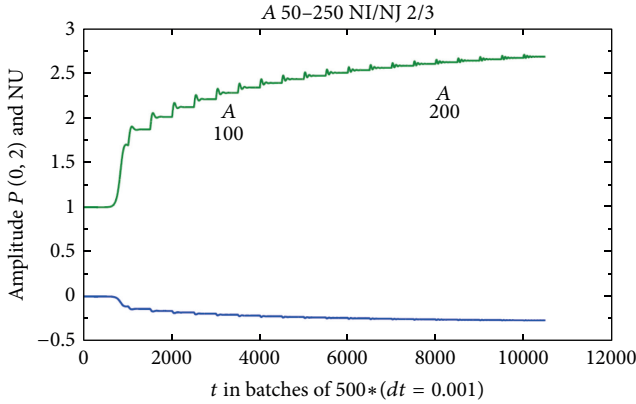
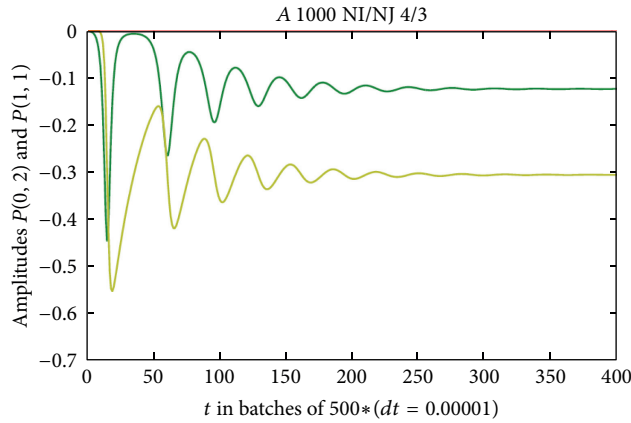
Figure 1 shows the simulation for Rayleigh numbers 50–250. All simulations with $NJ = 3$ produce the same stable result as (18) and the flak is the same as (14) with the equal sign. The maximum value of Nu that (18) can give is 3; this low value of Nu shows better than the value of the amplitudes how crude the approximation (18) is. There are in reality 5 unstable modes, but only two are in the simulation and of their amplitudes only P_{11} and P_{02} are nonzero. Increasing NI to 4 but keeping $NJ = 3$ changes very little. More unstable modes are needed, Figure 2. But a stable solution is obtained for $R_{aL} = 1000$, that is, 5 unstable modes.

4.3. Simulations with $NI \times NJ$ Grid 7×5 . Figure 3 shows $NI = 7$ and $NJ = 5$ simulation. This grid is slightly more accurate than the 2×3 . It contains 2 flak amplitudes and should therefore be able to give a realistic picture of stable stationary flows that might exist up to the third critical Rayleigh number. The possible number of amplitudes is 32 $((NJ - 1) \times (NI + 1))$ making 16 even amplitudes. Of them 9 end up with significant values to the second digit in Table 2.

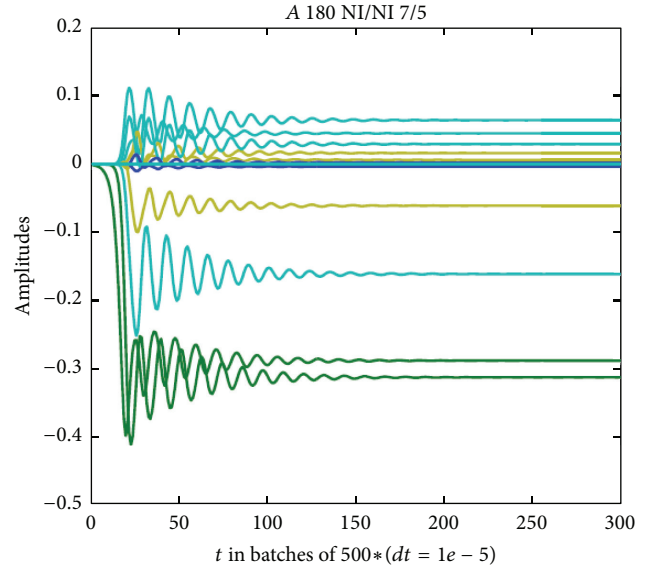
In Table 2 uneven amplitudes are in lighter shade. Runs with uneven amplitudes in the spectrum show that all uneven amplitudes diminish with time and drop out. Simulated $P(0, 2)$ is -0.31 and $Nu = 2.9$; this includes some aliasing effects from the finite transform. Equations (14) and (21) give that $P(0, 2)$ is -0.25 and $Nu = 2.8$. The results compare favourably and show how the flak amplitudes turn

TABLE 1: Sign control functions.

Range	$q < j - NJ$	$j - NJ < q < 0$	$0 < q < j$	$q > j$
$p < i - NI$	$- +$	$++$	$+ -$	$--$
$i - NI > p > 0$	$--$	$+ -$	$++$	$- +$
$0 > p > 0$	$--$	$++$	$+ -$	$--$
$p > i$	$--$	$+ -$	$++$	$- +$
Name	$s_1 s_2$	$s_1 s_2$	$s_1 s_2$	$s_1 s_2$

FIGURE 1: Simulations using $NI = 2$ and $NJ = 3$ showing oscillating approach to the stable asymptotes of Nu and $P(0, 2)$.FIGURE 2: Simulation using $NI = 4$ and $NJ = 3$. $R_{aL} = 1000$.TABLE 2: Amplitude array grid 7×5 , $R_{aL} = 180$ to $t = 1.5$.

i/j	1	2	3	4
0	0.00	-0.31	0.00	0.03
1	-0.29	0.00	0.06	0.00
2	0.00	-0.16	0.00	-0.06
3	0.05	0.00	0.02	0.00
4	0.00	0.01	0.00	0.00
5	0.00	0.00	0.00	0.00
6	0.00	0.00	0.00	0.00
7	0.00	0.00	0.00	0.00

FIGURE 3: Simulation grids $NI \times NJ = 7 \times 5$ up to $t = 1.5$. $R_{aL} = 180$.

the unstable modes into stationary motion. Figure 3 shows the time history of the simulation.

The slight increase in A from 180 to 190 changes this completely. Now we have a stable periodically fluctuating solution, Figure 4. The 7×5 grid approximation does not render stable solutions for higher Rayleigh numbers.

4.4. Simulations with $NI \times NJ$ Grid 9×7 . Here we look for how the solutions in the 7×5 grid look in a slightly more accurate grid that contains 3 flak amplitudes and examine the fluctuating motion more closely. The possible number of amplitudes is 60 making 30 even amplitudes.

Simulations in a 9×7 grid are a little more unstable than in the 7×5 grid. Fluctuating periodic flow is reached at $R_{aL} = 165$ and can be maintained until $R_{aL} = 180$; see Figure 5. The average amplitude array of $R_{aL} = 165$ is shown in Table 3, and the much larger standard deviations are in Table 4. Here we have the interesting result that the average flak amplitude is $P(0, 2) = -0.2$ while all others are practically zero; this gives $Nu = 2.3$. Equation (14) stability limit for $P(0, 2)$ is -0.2411 below the simulation value. This is to be expected as this solution is not stationary. Noting the standard deviation in Table 4 (0.08), it corresponds to a fluctuation of about 0.1 around the mean value. The value of this flak amplitude will

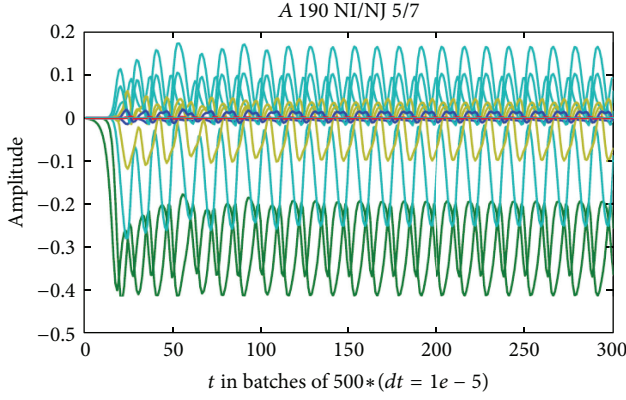


FIGURE 4: Simulation grids $NI \times NJ = 7 \times 5$. $R_{aL} = 190$, stable, periodic motion to $t = 1.5$.

TABLE 3: Average of amplitudes, $R_{aL} = 165$ grid 9×7 .

i/j	1	2	3	4	5	6
0	0.00	-0.20	0.00	0.01	0.00	0.00
1	0.00	0.00	0.00	0.00	0.00	0.00
2	0.00	-0.02	0.00	0.00	0.00	0.00
3	0.00	0.00	0.00	0.00	0.00	0.00
4	0.00	0.02	0.00	-0.01	0.00	0.00
5	0.00	0.00	0.00	0.00	0.00	0.00
6	0.00	0.00	0.00	0.00	0.00	0.00
7	0.00	0.00	0.00	0.00	0.00	0.00
8	0.00	0.00	0.00	0.00	0.00	0.00
9	0.00	0.00	0.00	0.00	0.00	0.00

TABLE 4: Standard deviation of amplitudes, in Table 2 and Figure 5.

i/j	1	2	3	4	5	6
0	0.00	0.11	0.00	0.03	0.00	0.01
1	0.18	0.00	0.06	0.00	0.02	0.00
2	0.00	0.08	0.00	0.03	0.00	0.01
3	0.08	0.00	0.04	0.00	0.01	0.00
4	0.00	0.04	0.00	0.02	0.00	0.00
5	0.01	0.00	0.01	0.00	0.00	0.00
6	0.00	0.00	0.00	0.00	0.00	0.00
7	0.00	0.00	0.00	0.00	0.00	0.00
8	0.00	0.00	0.00	0.00	0.00	0.00
9	0.00	0.00	0.00	0.00	0.00	0.00

therefore be between ca. -0.1 and -0.3 , with these values being on the unstable and stable side, respectively, of the stability limit (14). Figures 4 and 5 show this flak amplitude fluctuation clearly. Equation (21) gives $Nu = 2.5$ and we see that flak amplitudes and Nu are diminished from the stationary level but still up and active.

The simulations in the 5×7 and 9×7 grids show that stable solutions can be maintained only up to the second critical R_{aL} where periodic motion begins. Similar behaviour is observed in fluid turbulence; when the Reynolds number is increased, fluctuating motion sets in. Many vortex flow fields of this type

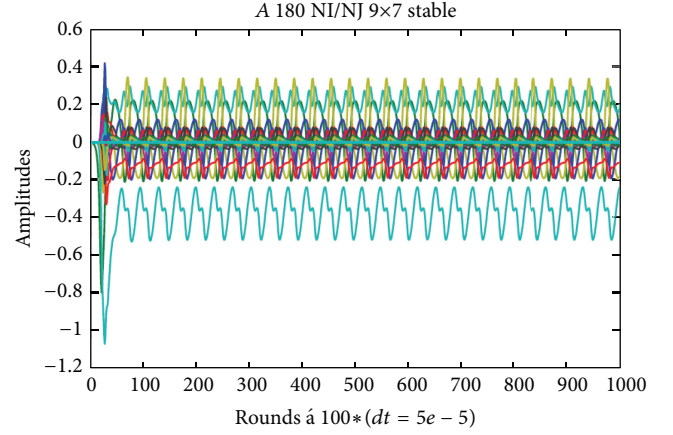


FIGURE 5: Simulation 9×7 . $R_{aL} = 180$, stable, periodic motion to $t = 5$.

are very well known in fluid mechanics (Reynolds, Taylor, Karman, and Kelvin-Helmholtz). With increasing instability these regular flows disappear and chaotic turbulence appears instead. This seems to happen here between the second and the third critical Reynolds numbers. This is in accordance with the findings in [4, 6]; stable motion is concluded to cease at the second critical Rayleigh number. Chaotic motion is found in [7] for that system at high fluid Ra numbers.

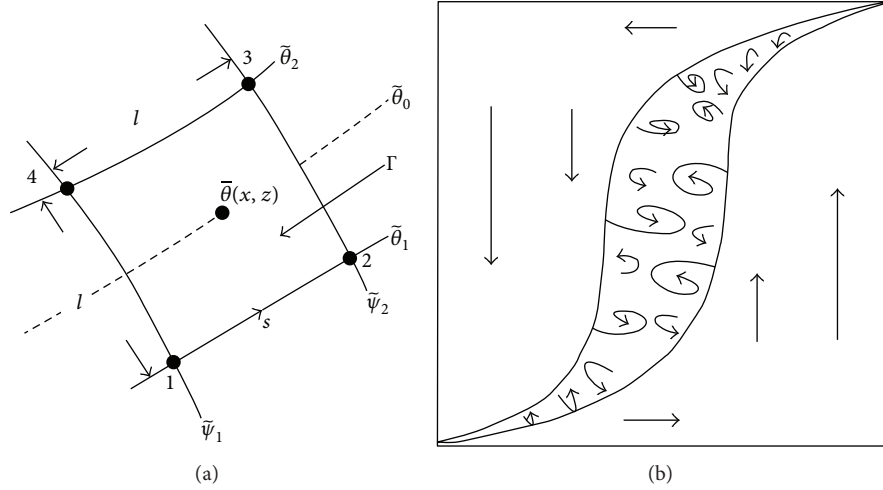
5. Scaling

The amplitudes in Tables 2 and 3 have average amplitudes and high standard deviation. The effect of this is to create a flow with “eddy heat conduction,” a phenomenon similar to eddy momentum transport in fluid turbulence.

It has been shown [17] that, when a running average is taken in the convection box (Figure 6) covering a grid area of $(l \times s)$, the nonlinear terms in (1) will produce a net transport of heat into the $l \times s$ element when the second derivative of the average temperature distribution does not vanish. This net heat flow may be represented as the divergence of an eddy heat flow vector equal to $\lambda^e(x, z) \cdot \text{grad}\theta$. This is the heat transported by fluctuations in excess of the molecular heat conduction and the convection by means of the average flow velocity. To model the flow in a coarse grid (Figure 6(a)) it is therefore necessary to include in the simulations a subgrid model that represents this heat flow, just as it is necessary to include a subgrid model to take care of the Reynolds stress tensor in macroscale models of turbulent flow.

The widely popular 2×3 grid solution is one flow cell in one single block, so the underlying assumption is $\lambda^e(x, z) = \text{constant}$. This is a crude simplification, similar to Prandtl’s mixing length theory. It is not quite correct, as λ^e would most likely take the highest values in the zone shown in Figure 6(b). We must conclude that in this solution there is active eddy heat conduction coefficient λ^e acting in excess of the normal heat conduction coefficient λ so the R_{aL} which we must use in (16) is scaled down in the following manner:

$$R_{aL}^e = \frac{\lambda}{\lambda + \lambda^e} R_{aL}. \quad (20)$$

FIGURE 6: Averaging the flow in a net of dimensions l and s .

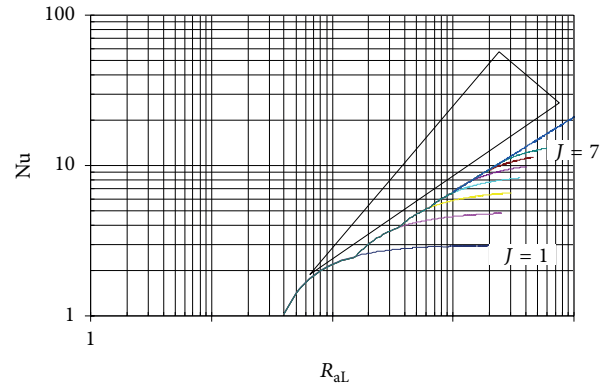
In finding λ^e we have a closure problem just as in turbulence; principally it must be found in experiments. From the simulations we learn that in stable and oscillatory solutions the flak amplitudes always have significant values. By averaging the temperature gradient given by (3) at either top or bottom and calculating the heat flow and using the equal sign in (14) for the flak we get

$$\text{Nu} = 1 + 2 \sum_{j=1}^J \frac{R_{aL} - R_{aL0j}}{R_{aL}} \quad (21)$$

$$\Rightarrow \frac{R_{aL}}{R_{aL}^e} = 2 \frac{\sqrt{R_{aL}}/\pi - \pi/\sqrt{R_{aL}}}{3} = 1 + \frac{\lambda^e}{\lambda}.$$

This result is an approximation valid for R_{aL} numbers larger than the second critical Rayleigh number. If R_{aL}^e is used instead of R_{aL} then the 2×3 grid solution (18) approximates the flow field in this region. One has to remember that the $\lambda^e + \lambda$ has to be used instead of λ when calculating the heat flow from Nu in (18); otherwise this approximation will render too low heat flow. The Nu numbers can be estimated directly by (21); for high R_{aL} , $\text{Nu} = 2\sqrt{R_{aL}}/3\pi$ is a good approximation. It should be noted that (21) means that stationary average flow can be approximated up to $R_{aL} = 27000$.

Bifurcations are known to occur in porous media [17]. The first bifurcation happens in DL systems at the first critical R_{aL} number. According to (14), the physical process in fluctuating flow is that the flak amplitudes maintain significant values to keep the nonlinear growth rates down and hinder the amplitudes they control from increasing without limit. Then there must be a new bifurcation each time R_{aL} passes a critical R_{aL} number. Equation (21) is the result of repeated bifurcation each time the Rayleigh number passes a critical value and one more mode is rendered unstable in the free convection. The result may be seen in Figure 7.

FIGURE 7: Nusselt number based on stability limits for $P(0, 2j)$ for J unstable modes. The triangle shows approximate location of Nu- R_{aL} test results reported by [1-3, 7, 18, 19].

6. Laboratory Scales

To make laboratory tests of convection in porous media one has to scale natural convection (e.g., geothermal fields) down to laboratory dimensions; in doing this, dynamic similarity may be a problem. One dimensionless parameter, for example, the Rayleigh number, can be kept constant in the model and the prototype but not more than that. Aquifer thickness, H , is typically 1000 m in geothermal reservoirs but ~ 1 m in the laboratory. To get a flow going the aquifer rock matrix has to be replaced by glass or plastic pearls with up to 1000-fold permeability and this brings the test from the DL regime of the aquifer into the DLFB regime. Acknowledging this fact [7] consequently uses Ra, not R_{aL} . This brings up the question of dispersion. This seems to be overlooked, but dispersion must play a role in laboratory experiments with a porous matrix of relatively large glass pearls. The scale effects

in the dispersion term may be estimated from the dispersion equation:

$$\frac{\partial C}{\partial t} = \frac{\partial}{\partial x_i} \left(A_{ij} \frac{\partial C}{\partial x_j} + \lambda \frac{\partial C}{\partial x_i} - C v_i \right); \quad (22)$$

$$\begin{bmatrix} v_i = (v, 0, 0) \\ x_i = (x_1, x_2, x_3) \end{bmatrix}; \quad A_{ij} = \begin{bmatrix} a_1 v & 0 & 0 \\ 0 & a_2 v & 0 \\ 0 & 0 & a_2 v \end{bmatrix}.$$

This assumes the x_1 axis in the direction of the flow. A_{ij} is the dispersion tensor. C denotes the concentration of a solute, in our case the mixing ration of hot water into cold, or the dimensionless temperature θ . The λ term is the molecular diffusion, in our case the coefficient of heat conduction as before. In natural low permeability aquifers, v is very small and the dispersion term is negligible compared to the λ term and generally left out. Estimating the dispersion/conduction ratio DCR, with respect to dynamic similitude, we see that the DCR will not be the same dimensionless number in model and prototype regardless if DL scaling (R_{aL} constant), or DLFB scaling (Ra constant) is used, the following equation shows this,

$$\begin{aligned} \text{DCR} &= \widehat{\text{DCR}} \frac{a}{H} R_{aL} \\ &= \widehat{\text{DCR}} \frac{a}{Ho^2} Ra; \quad \widehat{\text{DCR}} \text{ is dimensionless DCR.} \end{aligned} \quad (23)$$

Here $V_s = k\Delta\rho/\rho$ is used for the velocity scale in the dispersion term, σ is the porosity parameter H/\sqrt{k} [7], σ^{-2} is called the Darcy number by some, and Ra is the fluid Rayleigh number ($Ra = R_{aL}\sigma^2$). The parameter a is called the dispersivity and is usually taken as proportional to length scale; [20] suggests the order of magnitude 0.01–0.1. To use this value, both the aquifers in nature and the laboratory would have to be glass pearls which of course is not the case, but if that is overlooked, R_{aL} scaling (R_{aL} is the same in model and prototype) would give dynamic similarity. When Ra scaling is applied, the ratio $\sigma_{\text{prototype}}/\sigma_{\text{model}}$ can easily be in the range 10^3 – 10^6 ; this makes the R_{aL} values much higher in the model than in the prototype as $Ra = R_{aL}\sigma^2$. Then heat dispersion is more important than heat conduction resulting in higher Nusselt's number in the laboratory tests than in natural aquifers of large dimensions. DLFB systems can accordingly not be scaled to DL systems when the FB terms have a significant effect.

6.1. Nusselt Number Compared To Experiments. Trying to rescale laboratory results and compare computed and measured Nusselt's numbers is impossible, except possibly for the two-amplitude (one block) solution, where dispersion effects may be included in the λ^e . The 2×3 grid procedure can only produce Nu numbers up to 3 in the Lapwood system. [7] bring it up to approximately 4 in their system using a cutoff frequency of $i + j = 12$, which corresponds to the 5×7 grid solution. Nusselt's numbers in natural aquifers of large dimensions tend to be higher.

Figure 7 shows Nusselt's number based on the assumption that repeated bifurcation brings into the picture new flak

amplitudes for each new mode. The formula $Nu = 2\sqrt{R_{aL}}/3\pi$ (blue line, Figure 7) is a good approximation for $J \geq 5$. Nu values from laboratory tests are higher, but effects of eventual scaling or forcing (see next chapter) are unknown so the triangle for the results location is only approximate for pure DL systems.

6.2. Effect of Forcing. Due to (2), all horizontal temperature gradients from outside force the DL system. Forcing creates some flow, no matter how low the R_{aL} number is. Forced convection is an interesting topic with many applications; in [21] there is a review of the results in this field. When heating and cooling are between two vertical walls, stability does not have to be a problem and elegant solutions can be found both analytically and numerically [22]. The work in [23] is very interesting, showing an analytical solution of a forced system with variable permeability.

In [24] there is a treatment of the heat transfer through a box with heated sides using the DLFB system with added turbulence by a κ - ϵ subgrid model and a dispersion term included. The turbulence increases Nu significantly but the effect of changing σ^2 from 10^7 to 10^8 is even greater. They use R_{aL} but if their Figure 4 in [24] is rescaled to Ra , the lower σ^2 curve (higher Darcy number, Da in their notation) produces higher Nu numbers for the same Ra , which illustrates the scaling difficulty mentioned above and could point to the influence of dispersion. [25] studies the same problem and the conclusion is that dispersion has a significant effect.

Forcing thus makes it possible to analyze numerically and analytically situations with high heat transfers counted in Nu numbers, situations where numerical simulations of free convection with similar Nu numbers become unstable because the flow fluctuates. The effect of basic processes such as dispersion must generally have the same effect on the magnitude of heat flow in forced and free convection problems.

7. Discussion

The physical process of free convection flow in porous media suggests itself to be the following. For Rayleigh $R_{aL01} < R_{aL} < R_{aL02}$ convection sets in as a result of a bifurcation process when small disturbances of the spatial wave number $m = \pi$ become unstable and start to grow exponentially with time. For wave numbers below the second critical wave number only one mode (the first) is unstable. The entire energy spectrum of unstable wave numbers in that mode participates in making the first flak amplitude $P(0, 2)$ highly negative. Then the nonlinear growth rates of all first mode wave numbers turn negative and all the flow amplitudes on the first mode start decaying. This process repeats itself until stationary cellular flow of convective rolls is achieved (Figure 2).

If the Rayleigh number is increased slightly above the second critical Rayleigh number, a fluctuating flow sets in, but the 2×3 grid approximation does not show fluctuations at any Rayleigh number. In contrast hereto, the 5×7 and 9×7 grid discrete Fourier transforms (16) and (17) show stable

periodic motion for R_{aL} numbers just above the R_{aL02} , but it changes to fluctuating motion that resembles eddy motion in turbulent flow when the R_{aL} is slightly increased. In this fluctuating flow, the flow amplitudes shift from positive to negative indicating reversal of the flow direction in a periodic manner, but the flak amplitude stays high and fluctuates around the stability value (14). In this flow the average amplitudes are less important than the standard deviations and the correlation between amplitudes. The flak amplitudes are the only exception.

For higher Rayleigh numbers the flow becomes chaotic. Forcing will delay this considerably, so in laboratory experiments it is very important to exclude all forcing.

This flow resembles fluid turbulence in many ways. In spatially averaged equations the average amplitudes of fluctuations smaller than the grid size drop out leaving an eddy heat conduction effect. This leads to the scaling rule that makes it possible to use the 2×3 grid solution and still get realistic Nu numbers.

Turbulent fluid flow is governed by the eddy momentum transport due to the fluctuation that results from quadratic forms of the velocities in the Reynolds stress tensor. In a Darcy-Lapwood system there is eddy heat flow due to the fluctuation that results from quadratic forms of the velocities and the temperature. The flow is very slow, the nondimensional time interval from 0 to 1 can mean 30.000 years, [6] and heat conduction is faster than heat dispersion.

Systems governed by the fluid Rayleigh number Ra do not in principle scale to Lapwood systems, and there are strong indications that Ra systems (DLFB, DLB, and DL systems with added effects of turbulence or dispersion) scaled down to laboratory model size with $R_{aL} = Ra/\sigma^2$ run on higher heat flow due to dispersion in the pore matrix than the prototype.

As fluctuations dominate the flow at high R_{aL} number flows and contribute to the heat flow, stable nonfluctuating solutions, analytical as the 2×3 approximation or numerical, do need something like the eddy heat flow coefficient λ^e to render correct heat flow when the convection is free.

This investigation covers convective rolls. When strong fluctuations set in, the rolls become unstable and the flow becomes three-dimensional. The rolls are still there as a background motion, but when R_{aL} passes 3000–4000 they have probably disappeared. In [26] a scaling approximation with a boundary layer at top and bottom $\sim R_{aL}^{-1}$ is used for $R_{aL} > 1300$; it gives $Nu \sim R_{aL}$, but there is fair agreement with the results here, up to that point. To investigate three-dimensional flow, it would be interesting to perform an analysis with the finite Fourier transform of a two- or three-roll system intersecting each other. But this would still produce a quadratic form similar to what we have, so it does not have to change much. Here it is judged unlikely that it would suddenly change the $Nu \sim R_{aL}^{1/2}$ to $Nu \sim R_{aL}$, ([26], Figure 2).

8. Conclusions

In the Darcy-Lapwood system there are $J = \sqrt{R_{aL}}/2\pi$ unstable modes (J nearest lower integer).

Associated with all amplitudes, $P(i, j)$ on a fixed mode (constant j), there is a flak amplitude. It is the amplitude on the zero frequency of the mode with the double mode number $P(0, 2j)$ being the same for all horizontal wave numbers (i). The flak amplitude is always negative, independent of the sign of the amplitudes.

The flak amplitudes have a neutral stability value as shown by (14). If a stationary solution exists, it is symmetrical with all flak amplitudes not higher (less negative) than this value.

The Fourier transforms of the spectral method do have to include active modes up to double the number of unstable modes. Using discrete Fourier transform includes several frequency combinations generated by the nonlinear terms of the system (included in the Jacobian of (1)) that the truncated infinite form does not have.

Using the discrete Fourier transform makes it possible to use very coarse grids in numerical simulations, such as the 2×3 approximation, but then the flows on unstable modes not represented in the grid are aliased on the existing modes. For high R_{aL} coarse grids give too low Nusselt's numbers even though the fluid flow picture seems realistic.

Simulations above the second critical R_{aL} result in fluctuating flow. Even though the average fluctuations may have zero average amplitude and thus do not participate in the average fluid motion, they are active in transporting heat.

The assumption that all the flak amplitudes fluctuate around the stability value results in the scaling rule (17) that makes it possible to use the 2×3 solution to obtain realistic heat flow (Nu) by defining an eddy heat conduction coefficient λ^e that makes up for the missing effect of the fluctuations not present in the 2×3 approximate solution.

Assuming the flak amplitudes to stay on the neutral stability value on the average results in the approximate formula $Nu = 2\sqrt{R_{aL}}/3\pi$ for $J > 5$. Then the 2×3 approximation renders realistic Nu , when λ^e is used. Without this scaling, $Nu = 3$ is maximum in the 2×3 approximation. It gives a stable flow for all R_{aL} .

With 2 unstable modes ($R_{aL} > 160$) fluctuating motion sets in with the fluctuations more dominating in the finer grid transforms, as finer grids bring higher growth rates into the simulation.

Today's research focuses on DLFB systems as this equation system is more accurate for high permeability small scale flow systems. Studies of these systems do not automatically include the mathematically simpler DL system because of scaling problems associated with the great difference in the porosity value σ that follows the higher permeability and smaller linear scale.

Strong forcing stabilizes flows that would be otherwise unstable. But flow on the first mode does not stabilize the flow in DL systems as flak amplitudes have no effect outside their own mode. A DL system will pick up disturbances from outside that fall into the wave number instability band window, when the corresponding flak is in a downswing. Natural disturbances from outside, for example, tidal and barometric effects, will therefore start new fluctuations and the system will by time become independent of the initial condition thus forgetting its past and becoming chaotic.

Conflict of Interests

The author declares that there is no conflict of interests regarding the publication of this paper.

References

- [1] J. W. Elder, "Steady free convection in a porous medium heated from below," *Journal of Fluid Mechanics*, vol. 27, part 1, p. 29, 1967.
- [2] K. I. Schneider, "Investigations of the influence of free convection on heat transfer through granular material," in *Proceedings of the 11th International Congress on Refrigeration*, pp. 247–254, 1963.
- [3] R. A. Wooding, "Free convection of fluid in a vertical tube filled with porous material," *Journal of Fluid Mechanics*, vol. 13, pp. 129–144, 1962.
- [4] E. Palm, J. E. Weber, and O. Kvernfold, "On steady convection in a porous medium," *Journal of Fluid Mechanics*, vol. 54, part 1, p. 153, 1972.
- [5] A. A. Avramenko, A. V. Kuznetsov, B. I. Basok, and D. G. Blinov, "Investigation of stability of a laminar flow in a parallel-plate channel filled with a fluid saturated porous medium," *Physics of Fluids*, vol. 17, no. 9, Article ID 094102, pp. 1–6, 2005.
- [6] J. Eliasson, "Convective ground water flow," Series Paper 3, Institute of Hydrodynamics & Hydraulic Engineering, Technical University of Denmark, 1973.
- [7] N. Rudraiah, P. G. Siddheshwar, and T. Masuoka, "Nonlinear convection in porous media: a review," *Journal of Porous Media*, vol. 6, no. 1, pp. 1–32, 2003.
- [8] N. Rudraiah, "Turbulent convection in porous media using spectral method," in *Proceedings of the 2nd Asian Congress of Fluid Mechanics*, pp. 1015–1020, Seicha Press, Beijing, China, 1983.
- [9] N. Rudraiah and S. B. Rao, "Nonlinear cellular convection and heat transport in a porous medium," *Applied Scientific Research*, vol. 39, no. 1, pp. 21–43, 1982.
- [10] E. Holzbecher, "Free and forced convection in porous media open at the top," *Heat and Mass Transfer*, vol. 41, no. 7, pp. 606–614, 2005.
- [11] I. Sezai, "Flow patterns in a fluid-saturated porous cube heated from below," *Journal of Fluid Mechanics*, vol. 523, pp. 393–410, 2005.
- [12] D. A. S. Rees and P. A. Tyvand, "Oscillatory convection in a two-dimensional porous box with asymmetric lateral boundary conditions," *Physics of Fluids*, vol. 16, no. 10, pp. 3706–3714, 2004.
- [13] M.-H. Chang, "Thermal convection in superposed fluid and porous layers subjected to a horizontal plane Couette flow," *Physics of Fluids*, vol. 17, no. 6, Article ID 064106, 2005.
- [14] M. Mamou, "Stability analysis of thermosolutal convection in a vertical packed porous enclosure," *Physics of Fluids*, vol. 14, no. 12, pp. 4302–4314, 2002.
- [15] K. B. Haugen and P. A. Tyvand, "Onset of thermal convection in a vertical porous cylinder with conducting wall," *Physics of Fluids*, vol. 15, no. 9, pp. 2661–2667, 2003.
- [16] E. R. Lapwood, "Convection of a fluid in a porous medium," *Proceedings of the Cambridge Philosophical Society*, vol. 44, pp. 508–521, 1948.
- [17] J. Eliasson, "A note on the unsteady nonlinear convection in porous media," Progress Reports 45, Technical University of Denmark, Institute of Hydrodynamics and Hydraulic Engineering, 1978.
- [18] M. Combarous, "Natural convection in porous media and geothermal system," in *Proceedings of the 6th International Heat Transfer Conference*, vol. 6, pp. 45–59, 1978.
- [19] J. M. Straus, "Large amplitude convection in porous media," *Journal of Fluid Mechanics*, vol. 64, no. 1, pp. 51–63, 1974.
- [20] C. W. Fetter, *Contaminant Hydrogeology*, Macmillan, 1993.
- [21] I. Pop and D. B. Ingham, *Convective Heat Transfer: Mathematical and Computational Modelling of Viscous Fluids and Porous Media*, Pergamon Press, Oxford, UK, 2001.
- [22] A. Misirlioglu, A. C. Baytas, and I. Pop, "Free convection in a wavy cavity filled with a porous medium," *International Journal of Heat and Mass Transfer*, vol. 48, no. 9, pp. 1840–1850, 2005.
- [23] M. F. El-Amin, N. A. Ebrahiem, A. Salama, and S. Sun, "Radiative mixed convection over an isothermal cone embedded in a porous medium with variable permeability," *Journal of Applied Mathematics*, vol. 2011, Article ID 124590, 10 pages, 2011.
- [24] H. Beji, "Effets des non-linéarités et de la dispersion thermique sur la convection naturelle en milieu poreux confiné," *Journal de Physique III*, pp. 267–284, 1993.
- [25] E. J. Braga and M. J. S. de Lemos, "Turbulent natural convection in a porous square cavity computed with a macroscopic κ - ϵ model," *International Journal of Heat and Mass Transfer*, vol. 47, no. 26, pp. 5639–5650, 2004.
- [26] D. R. Hewitt, J. A. Neufeld, and J. R. Lister, "Ultimate regime of high Rayleigh number convection in a porous medium," *Physical Review Letters*, vol. 108, no. 22, Article ID 224503, 2012.

Review Article

An Overview of Recent Advances in the Iterative Analysis of Coupled Models for Wave Propagation

D. Soares Jr.¹ and L. Godinho²

¹ Structural Engineering Department, Federal University of Juiz de Fora, Cidade Universitária, 36036-330 Juiz de Fora, MG, Brazil

² CICC, Department of Civil Engineering, University of Coimbra, 3030-788 Coimbra, Portugal

Correspondence should be addressed to D. Soares Jr.; delfim.soares@ufjf.edu.br

Received 18 September 2013; Accepted 25 November 2013; Published 14 January 2014

Academic Editor: Daniel Dias-da-Costa

Copyright © 2014 D. Soares Jr. and L. Godinho. This is an open access article distributed under the Creative Commons Attribution License, which permits unrestricted use, distribution, and reproduction in any medium, provided the original work is properly cited.

Wave propagation problems can be solved using a variety of methods. However, in many cases, the joint use of different numerical procedures to model different parts of the problem may be advisable and strategies to perform the coupling between them must be developed. Many works have been published on this subject, addressing the case of electromagnetic, acoustic, or elastic waves and making use of different strategies to perform this coupling. Both direct and iterative approaches can be used, and they may exhibit specific advantages and disadvantages. This work focuses on the use of iterative coupling schemes for the analysis of wave propagation problems, presenting an overview of the application of iterative procedures to perform the coupling between different methods. Both frequency- and time-domain analyses are addressed, and problems involving acoustic, mechanical, and electromagnetic wave propagation problems are illustrated.

1. Introduction

The analysis of wave propagation, either involving electromagnetic, acoustic, or elastic waves, has been widely studied by researchers using different strategies and methodologies, as can be seen, for example, in [1–10], among many others. In many cases, the interaction between different types of media, such as fluid-solid or soil-structure interaction problems, poses significant challenges that can hardly be tackled by means of a single numerical method, requiring the joint use of different procedures to model different parts of the problem. Indeed, taking into consideration the specificities and particular features of distinct numerical methods, their combined use, as coupled or hybrid models, has been proposed by many authors, in order to explore the individual advantages of each technique.

In acoustic and elastodynamic problems, coupled models, including, for example, the joint use of the boundary element method (BEM) and the method of fundamental solutions (MFS) [11] or of the BEM and the meshless Kansa's method [12], have been successfully applied. Similarly, when modelling dynamic fluid-structure and soil-structure interactions, wave propagation in elastic media with heterogeneities,

or the transmission of ground-borne vibration, coupled models using the finite element method (FEM) and the BEM have been extensively documented in the literature [13–19], mostly using the FEM to model the structure and the BEM to model the hosting infinite or semiinfinite medium. Although these approaches can be quite useful in addressing many engineering problems, they mostly correspond to standard direct coupling methodologies and thus exhibit well-known limitations. Indeed, directly coupling distinct methods involves assembling a single system matrix, accounting for the contributions of each method and for the required coupling interface conditions, which frequently becomes poorly conditioned due to the different nature of the methods. Since this system is formed from the contributions of distinct methods, it is also usually not possible to make use of their individual advantages in terms of optimized solvers or memory storage (e.g., in BEM-FEM the final system will no longer be banded and symmetric, etc.). In addition to this limitation, by forming a single system of equations, a very large problem usually arises, leading to increased computational efforts and thus to a loss of performance.

All these limitations have justified the appearance of iterative algorithms to obtain accurate solutions in a more efficient

manner. Perhaps one of the first iterative techniques to be developed for general problems is the well-known Schwarz alternating strategy [20, 21], in which the domain of analysis is partitioned in overlapping subdomains, and the solution is found by successively iterating along these subdomains until convergence is reached. This classical and simple to implement algorithm has been applied to many problem types, including potential problems [22] or electromagnetic wave propagation problems [23]. However, for the case of acoustic problems or elastic wave propagation problems, formulated in the frequency domain, the special oscillatory structure of the solution leads to severe convergence problems when using such classic approaches, and more sophisticated and difficult to implement strategies must be defined.

In recent years, more elaborate iterative domain decomposition techniques have been proposed and discussed in order to analyze a wide range of problems, providing good results especially in terms of flexibility and efficiency. Mostly, these techniques have been applied to nontransient applications, and they usually consider the analysis of coupled models, taking into account the interaction of different discretization methods, physical phenomena, and so forth. In fact, for complex models, iterative domain decomposition techniques are recommended, usually providing a better approach for the analysis. Indeed, a proper numerical simulation is hardly achieved by a single numerical technique in those cases, mostly because complex and quite different phenomena interact, requiring particularized advanced expertise, and/or large scale problems are involved, demanding high computational efforts.

Nowadays, several works are available discussing iterative nonoverlapping partitioned analysis. Taking into account elliptic problems, Rice et al. [24] presented a quite complete discussion, considering several interface relaxation procedures and comparing formulations and performances. As a matter of fact, most of the publications on the topic are focused on elliptic models, few being devoted to hyperbolic problems. Taking into account computational mechanics, one of the first publications on the topic was presented by Lin et al. [25], which discussed a relaxed iterative procedure to couple the FEM and the BEM, considering linear static analyses. Similar approaches have been presented later on, considering potential and mechanical static linear analyses [26, 27]. In the works of Elleithy et al. [28, 29], concerning mechanical static and potential problems, the authors propose that the domain of the original problem is subdivided into subdomains, each of them modeled by the finite element or boundary element methods; the coupling between the different subdomains is performed using smoothing operators on the interdomain boundaries. Their strategy allows separate computations for the BEM and FEM subdomains, with successive update of the boundary conditions at the interfaces being performed until convergence is achieved. In [30–32], similar approaches for the analysis of different linear problems using domain decomposition techniques were also presented. Further developments of these strategies to nonlinear analysis in solid mechanics can also be found in the works of Elleithy et al. [33], using an interface relaxation finite element-boundary

element coupling method (FEM-BEM coupling) for elastoplastic analysis, or Jahromi et al. [34], who established a coupling procedure based on a sequential iterative Dirichlet-Neumann coupling algorithm for nonlinear soil-structure interaction. It must be noted that the described works refer to nontransient problems, either linear or nonlinear, and no application to wave propagation analysis is focused on in these works.

Taking into account time-domain wave propagation models, the first work on the topic seems to have been presented by Soares et al. [35], who described a relaxed FEM-BEM iterative coupling procedure to analyze dynamic nonlinear problems, considering different time discretizations within each sub-domain of the model. Later on, this technique has been further developed to analyze other wave propagation models, including acoustic, elastic, and electromagnetic wave propagation or solid-fluid interaction, taking into account several different numerical procedures using the FEM and the BEM [36–45] or the meshless local Petrov-Galerkin method [46]. Most of these works are focused on the iterative coupling of different numerical discretization techniques, and a review considering the iterative coupling of the FEM and the BEM, taking into account some wave propagation models in computational mechanics, has been presented in [47]. The coupling of acoustic and mechanic wave propagation models, on the other hand, has been reviewed in [48], taking into account different domain decomposition techniques and considering several numerical discretization techniques.

In the analysis of wave propagation using frequency-domain formulations, iterative coupling procedures can be found in the literature, mostly considering acoustic-acoustic and acoustic-elastodynamic coupling [49–54]. As it has been reported, frequency-domain wave propagation analyses usually give rise to ill-posed problems and, in these cases, the convergence of the iterative coupling algorithm can be either too slow or unachievable. This is the case in acoustic-acoustic, acoustic-elastodynamic, and elastodynamic-elastodynamic interacting models and, as discussed in this work, convergence can be hardly achieved if no special procedure is considered, especially if higher frequencies are focused on. As referred in the literature, in order to deal with this ill-posed problem and ensure convergence of the iterative coupling algorithm, special techniques, such as the adoption of optimal relaxation parameters, must be considered.

In this work, time- and frequency-domain analyses of wave propagation models are reviewed, taking into account relaxed iterative coupling procedures. In this context, several wave propagation models (such as electromagnetic, acoustic, mechanic) are considered, and several numerical procedures (such as the finite element method, the boundary element method, and meshless methods) are employed to discretize the model. In the iterative coupling approach, each subdomain of the global model is analyzed independently (as an uncoupled model) and a successive renewal of the variables at the common interfaces is performed, until convergence is achieved. These iterative methodologies exhibit several advantages when compared to standard coupling schemes, for instance,

- (i) different subdomains can be analysed separately, leading to smaller and better-conditioned systems of equations (different solvers, suitable for each sub-domain, may be employed);
- (ii) only interface routines are required when one wishes to use existing codes to build coupling algorithms (thus, coupled systems may be solved by separate program modules, taking full advantage of specialized features and disciplinary expertise);
- (iii) matching nodes at common interfaces are not required, greatly improving the flexibility and versatility of the coupled analyses, especially when different discretization methods are considered;
- (iv) matching time steps at common interfaces are not required (in time-domain analysis), allowing optimal temporal discretizations within each sub-domain, improving accuracy and stability aspects;
- (v) nonlinear analyses (as well as other iterative-based analyses) may be carried out in the same iterative loop of the iterative coupling, not introducing a relevant extra computational effort for the model;
- (vi) more efficient analyses can be obtained, once the global model can be reduced to several subdomains with reduced size matrices.

As a matter of fact, Gauzellino et al. [55] compared the iterative domain decomposition and global solution taking into account three-dimensional Helmholtz problems. Their numerical results show that iterative domain decomposition methods perform far better than global methods. In addition, they observed that iterative domain decomposition methods involving small subdomains work better than those with subdomains involving a large number of elements. Similar results have been obtained by Soares et al. [51], taking into account two-dimensional Helmholtz problems.

To give a detailed overview of the recent developments found in many of the referred works, the remainder of this paper will address a number of application examples concerning different phenomena and methods. First, the governing equations related to wave propagation models are generically and briefly presented. In the sequence, an efficient iterative coupling technique is described, including the mathematical derivation of the optimized relaxation methodology. Some numerical applications are finally presented, illustrating the accuracy, performance, and potentialities of the discussed procedures, taking into account different wave propagation models and discretization techniques.

2. Governing Equations

Wave propagation phenomena may be generically described by the following time/frequency-domain governing equations:

$$\begin{aligned} c_0(x, t) + c_1(x) \ddot{u}(x, t) + c_2(x) \dot{u}(x, t) \\ + c_3(x) \partial f(u(x, t)) = 0, \end{aligned} \quad (1a)$$

$$\begin{aligned} \bar{c}_0(x, \omega) - \omega^2 \bar{c}_1(x) \bar{u}(x, \omega) + i\omega \bar{c}_2(x) \bar{u}(x, \omega) \\ + \bar{c}_3(x) \partial f(\bar{u}(x, \omega)) = 0 \end{aligned} \quad (1b)$$

which can be further generalized in order to consider more complex behavior, such as time varying coefficients ($c_l(x, t)$, $l = 1, 2, 3$), nonlinearities ($c_l(x, u(x, t))$, $l = 0, 1, 2, 3$; etc.) Equation (1a) stands for the time domain governing equation, whereas (1b) stands for its frequency-domain counterpart (overbars indicate frequency-domain values). In these equations, u represents the incognita field, which can be scalar, vectorial, and so forth, according to the physical model in focus. c_i stands for a general coefficient representation, which can as well be a scalar, a tensor, and so forth. Overdots stand for time derivatives, whereas ∂f indicates a spatial derivative operator. The complex number is denoted by i and the time, frequency, and space domains are represented by t , ω , and x , respectively (in this case, $x \in \Omega$, where Ω is the spatial domain of the model).

The boundary conditions ($x \in \Gamma$, where Γ is the boundary of the model) may be generically described as (for simplicity, from this point onwards, overbars are no longer used to indicate frequency-domain values and ς stands for t or ω , according to the case of analysis)

$$f(u(x, \varsigma), v(x, \varsigma)) = c(x, \varsigma), \quad (2)$$

where, once again, c stands for known terms. In (2), f stands for a generic function, representing the combination of its arguments. The variable v , which may be considered prescribed at the boundary of the model, is a function of u , and it is usually expressed considering some normal projection (normal to the boundary) of the spatial derivatives of u (i.e., $v = \partial f_n(u)$).

To completely define the model, initial conditions (which are usually adopted null in frequency-domain analyses) must also be defined. In this case, a generic representation can be given by $f(u(x, t = 0), \dot{u}(x, t = 0)) = c(x)$, where notation analogous to that of (2) is considered.

Taking into account coupled models in which different domains interact by a common interface, interface conditions must be stated, indicating how the domains interact. This can be generically expressed as

$$f_1(u(x^-, \varsigma), v(x^-, \varsigma)) = f_2(u(x^+, \varsigma), v(x^+, \varsigma)), \quad (3)$$

where $x \in \Gamma_I$, $x^- \in \Gamma_I \cup \Omega_1$, $x^+ \in \Gamma_I \cup \Omega_2$, and Γ_I is the common interface between domains Ω_1 and Ω_2 . In (3), functions f_1 and f_2 describe how the interaction between the coupled domains takes place by relating their boundary values on the common interface.

3. Iterative Coupling Analysis

In order to enable the coupling between sectioned domains of a global model, an iterative procedure is employed here, which performs a successive renewal of the relevant variables at the common interfaces. This approach is based on the imposition of prescribed boundary conditions, properly evaluated, at the interfaces of the sectioned domains, allowing each domain of the global model to be analyzed separately.

Since the sectioned domains are analyzed separately, the relevant systems of equations are formed independently, before the iterative process starts (in the case of linear analyses), and are kept constant along the iterative process, rendering a very efficient procedure. The separate treatment of the sectioned domains allows independent discretizations to be considered on each domain, without any special requirement of matching nodes along the common interfaces. Moreover, in the case of time-domain analysis, different time-steps may also be considered for each domain. Thus, the coupling algorithm can be presented for a generic case, in which the interface nodes may not match, and the interface time instants are disconnected, allowing exploiting the benefits of the iterative coupling formulation.

To ensure and/or to speed up convergence, a relaxation parameter λ is introduced in the iterative coupling algorithm. The effectiveness of the iterative process is strongly related to the selection of this relaxation parameter, since an inappropriate selection for λ can significantly increase the number of iterations in the analysis or, even worse, make convergence unfeasible. As it has been reported [49, 51], frequency-domain analyses usually give rise to ill-posed problems and, in these cases, the convergence of simple iterative coupling algorithms can either be too slow or unachievable. In order to deal with ill-posed problems and ensure convergence of the iterative coupling algorithm, an optimal iterative procedure is adopted here, with optimal relaxation parameters being computed at each iterative step. As it is illustrated in the next section, the introduction of these optimal relaxation parameters allows the iterative coupling technique to be very effective, especially in the frequency domain, ensuring convergence at a low number of iterative steps.

3.1. Iterative Algorithm. Initially, in the k th iterative step of the coupled analysis of domains 1 and 2, the so-called domain 1 is analyzed and the variables u or v at the common interfaces of the domain are computed, taking into account prescribed values of v or u at these common interfaces. These prescribed values of v or u are provided from the previous iterative step (in the first iterative step, null or previous time-step values may be considered). Once the variables u or v are computed, they are applied to evaluate the boundary conditions that are prescribed at the common interfaces of domain 2, as described by (3). Taking into account these prescribed u or v boundary conditions, the so-called domain 2 is analyzed and the variables v or u at the common interfaces of the domain are computed. Then, the computed v or u values are applied to evaluate the boundary conditions that are prescribed at the common interfaces of domain 1, reinitiating the iterative cycle. A sketch of this cycle is depicted in Figure 1.

As previously discussed, relaxation parameters must be considered in order to ensure and/or to speed up the convergence of the iterative process. Thus, the values that are computed after the analysis of the sectioned domain may be combined with its previous iterative step counterpart, relaxing the computation of the actual iterative step value. Mathematically, this can be represented as follows:

$$y^{(k+1)} = (\lambda) y^{(k+\lambda)} + (1 - \lambda) y^{(k)}, \quad (4)$$

where λ is the adopted relaxation parameter and y stands for u or v , according to the case of analysis; one should note that $y^{(k+\lambda)}$ is the value computed at the end of the iterative step, before the application of the relaxation parameter.

A proper selection for λ at each iterative step is extremely important for the effectiveness of the iterative coupling procedure. In order to obtain an easy to implement, efficient, and effective expression for the relaxation parameter computation, optimal λ values are deduced in Section 3.2.

3.2. Optimal Relaxation Parameter. In order to evaluate an optimal relaxation parameter, the following square error functional is minimized here:

$$\varepsilon(\lambda) = \left\| \mathbf{Y}^{(k+1)}(\lambda) - \mathbf{Y}^{(k)}(\lambda) \right\|^2, \quad (5)$$

where \mathbf{Y} stands for a vector whose entries are u or v values, computed at the common interfaces.

Taking into account the relaxation of the field values for the $(k+1)$ and (k) iterations, (6a) and (6b) may be written, based on the definition in (4):

$$\mathbf{Y}^{(k+1)} = (\lambda) \mathbf{Y}^{(k+\lambda)} + (1 - \lambda) \mathbf{Y}^{(k)}, \quad (6a)$$

$$\mathbf{Y}^{(k)} = (\lambda) \mathbf{Y}^{(k+\lambda-1)} + (1 - \lambda) \mathbf{Y}^{(k-1)}. \quad (6b)$$

Substituting (6a) and (6b) into (5) yields

$$\begin{aligned} \varepsilon(\lambda) &= \left\| (\lambda) \mathbf{W}^{(k+\lambda)} + (1 - \lambda) \mathbf{W}^{(k)} \right\|^2 \\ &= (\lambda^2) \left\| \mathbf{W}^{(k+\lambda)} \right\|^2 + 2\lambda(1 - \lambda) (\mathbf{W}^{(k+\lambda)}, \mathbf{W}^{(k)}) \\ &\quad + (1 - \lambda)^2 \left\| \mathbf{W}^{(k)} \right\|^2, \end{aligned} \quad (7)$$

where the inner product definition is employed (e.g., $(\mathbf{W}, \mathbf{W}) = \|\mathbf{W}\|^2$) and new variables, as defined in the following, are considered:

$$\mathbf{W}^{(k+\lambda)} = \mathbf{Y}^{(k+\lambda)} - \mathbf{Y}^{(k+\lambda-1)} \quad (8)$$

To find the optimal λ that minimizes the functional $\varepsilon(\lambda)$, (7) is differentiated with respect to λ and the result is set to zero, described as follows:

$$\begin{aligned} (\lambda) \left\| \mathbf{W}^{(k+\lambda)} \right\|^2 + (1 - 2\lambda) (\mathbf{W}^{(k+\lambda)}, \mathbf{W}^{(k)}) \\ + (\lambda - 1) \left\| \mathbf{W}^{(k)} \right\|^2 = 0. \end{aligned} \quad (9)$$

Rearranging the terms in (9) yields

$$\lambda = \frac{(\mathbf{W}^{(k)}, \mathbf{W}^{(k)} - \mathbf{W}^{(k+\lambda)})}{\left\| \mathbf{W}^{(k)} - \mathbf{W}^{(k+\lambda)} \right\|^2} \quad (10)$$

which is an easy to implement expression that provides an optimal value for the relaxation parameter λ , at each iterative step. This expression requires a low computational cost, when compared to other alternatives that can be found in the literature (see, e.g., [28, 29]) and it provides very good results, as it has been reported taking into account different physical models and domain analyses [43, 44, 51–54]. The iterative process is relatively insensitive to the value of the relaxation parameter adopted for the first iterative step and $\lambda = 0.5$ can be considered in this case, for instance.

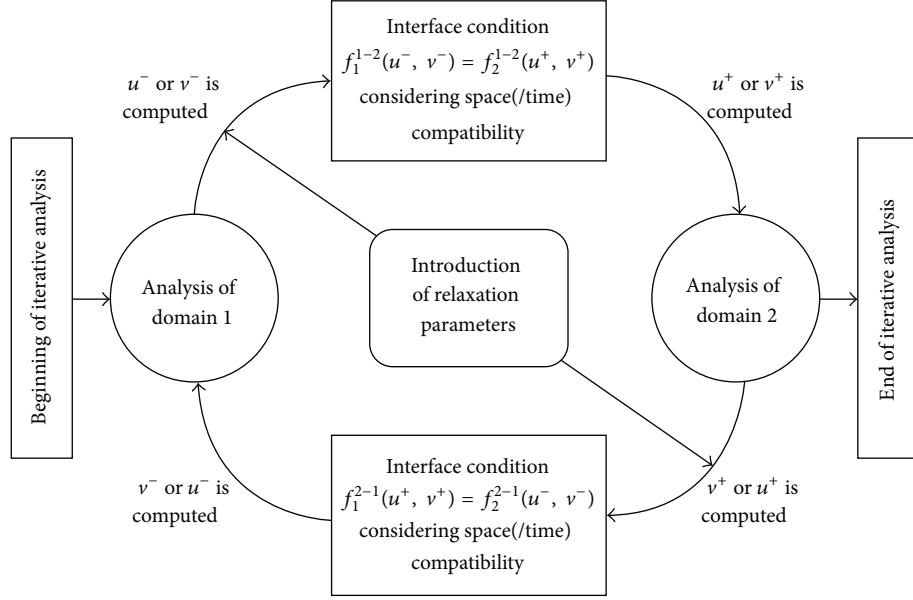


FIGURE 1: Sketch of the iterative coupling algorithm.

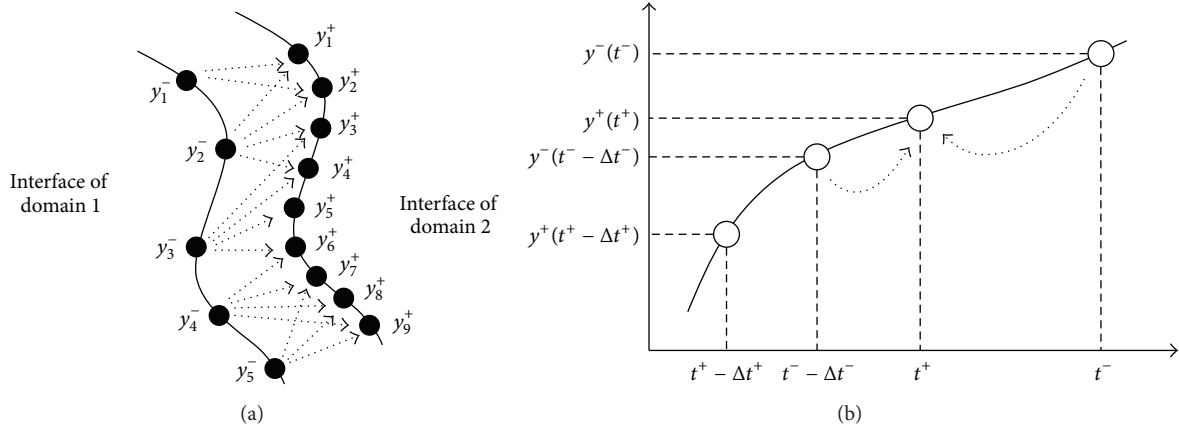


FIGURE 2: (a) Sketch for a spatial interpolation of nodal values on the interface: $y_1^+ = I(y_1^-, y_2^-)$, $y_2^+ = I(y_1^-, y_2^-)$, $y_3^+ = I(y_2^-, y_3^-)$, and so forth; (b) sketch for a temporal interpolation of time-step values on the interface: $y^+(t^+) = I(y^-(t^-), y^-(t^- - \Delta t^-))$, and so forth, where I stands for a linear interpolation function.

3.3. Interface Compatibility. As previously discussed, independent spatial (and temporal, in time-domain analysis) discretizations may be considered for each domain of the model, not requiring matching nodes (or equal time steps) at the common interfaces. Thus, special procedures must be employed to ensure the interface spatial (and temporal) compatibility. In order to do so, interpolation and extrapolation procedures are considered here. These procedures can be generically described by

$$y(x_i, \varsigma) = \sum_{j=1}^J \alpha_j y(x_j, \varsigma), \quad (11a)$$

$$y(x, t_n) = \beta_0 y(x, t_m) + \sum_{j=1}^J \beta_j y(x, (t - j\Delta t)_{m/n}), \quad (11b)$$

where (11a) stands for spatial interpolations and (11b) stands for time interpolations/extrapolations (α_j and β_j stand for spatial interpolation coefficients and time interpolation/extrapolation coefficients, respectively, where Δt represents the time step). In Figure 2, simple sketches for the spatial and temporal interpolation procedures are depicted, taking into account linear interpolations.

Although time interpolations usually can be carried out without further difficulties, time extrapolations may give rise to instabilities if not properly elaborated. Thus, extrapolations should be performed in consonance with the field approximations being adopted within each time step and with the time discretization procedures being considered in the analysis, in order to formulate a consistent procedure. Once a consistent methodology is elaborated, time interpolation/extrapolation

procedures can be employed with confidence, as referred in the literature [47, 48] and illustrated in the next section. One should notice that usually different optimal (optimal in terms of accuracy, stability and efficiency) time steps are required when taking into account different numerical methods, spatial discretizations, material properties, physical phenomena, and so forth. Thus, in some cases, considering different time steps within each domain of a coupled model is of maximal importance to allow the effectiveness of the analysis.

Using space(/time) interpolation(/extrapolation) procedures, optimal modeling of each sectioned domain may be achieved, which is very important in what concerns flexibility, efficiency, accuracy, and stability aspects.

4. Numerical Applications

In this section, the general procedures previously discussed are particularized and briefly detailed, taking into account different physical models and discretization techniques. Thus, the discussed iterative coupling methodology is applied considering a wide range of wave propagation models and numerical methods, richly illustrating its performance and potentialities.

In this context, time- and frequency-domain analyses are carried out here, and electromagnetic, acoustic, and mechanical wave propagation phenomena (as well as their interactions) are discussed in the applications that follow. Moreover, different numerical techniques (such as the finite element method, the boundary element method, and meshless methods) are applied to discretize the different domains of the model, illustrating the versatility and generality of the discussed iterative method.

4.1. Electromagnetic Waves. In electromagnetic models, vectorial wave equations describe the electric and the magnetic field evolution [56, 57]. In this case, (1a) can be rewritten as (in this subsection, time-domain analyses are focused on):

$$\nabla \times (\mu(x)^{-1} \nabla \times \mathbf{E}(x, t)) + \varepsilon(x) \ddot{\mathbf{E}}(x, t) = -\dot{\mathbf{J}}(x, t), \quad (12a)$$

$$\begin{aligned} \nabla \times (\varepsilon(x)^{-1} \nabla \times \mathbf{H}(x, t)) + \mu(x) \ddot{\mathbf{H}}(x, t) \\ = \nabla \times (\varepsilon(x)^{-1} \mathbf{J}(x, t)), \end{aligned} \quad (12b)$$

and (3) can be rewritten as

$$\mathbf{n}(x) \times (\mathbf{E}(x^+, t) - \mathbf{E}(x^-, t)) = \mathbf{0}, \quad (13a)$$

$$(\mathbf{D}(x^+, t) - \mathbf{D}(x^-, t)) \cdot \mathbf{n}(x) = \rho(x, t), \quad (13b)$$

$$(\mathbf{B}(x^+, t) - \mathbf{B}(x^-, t)) \cdot \mathbf{n}(x) = 0, \quad (13c)$$

$$\mathbf{n}(x) \times (\mathbf{H}(x^+, t) - \mathbf{H}(x^-, t)) = \mathbf{J}(x, t), \quad (13d)$$

where \mathbf{E} and \mathbf{H} are the electric and magnetic field intensity vectors, respectively; \mathbf{D} and \mathbf{B} represent the electric and magnetic flux densities, respectively; and \mathbf{J} and ρ stand for the electric current and electric charge density, respectively. The parameters ε and μ denote, respectively, the permittivity and

permeability of the medium and its wave propagation velocity is specified as $c = (\varepsilon\mu)^{-1/2}$. \mathbf{n} is the normal vector, from domain 1 to domain 2. Equations (13a) and (13b) state that the tangential component of \mathbf{E} is continuous across the interface and that the normal component of \mathbf{D} has a step of surface charge on the interface surface, respectively. Equations (13c) and (13d) state that the normal component of \mathbf{B} is continuous across the interface and that the tangential component of \mathbf{H} is continuous across the interface if there is no surface current present, respectively.

In the present application, the electromagnetic fields surrounding infinitely long wires are studied [41]. Two cases of analysis are focused here, namely, (a) case 1, where one wire is considered; (b) case 2, where two wires are employed. For both cases, the wires are carrying time-dependent currents (i.e., $I(t) = t$ or $I(t) = t^2$) and they are located along the adopted z -axis. A sketch of the model is depicted in Figure 3.

The spatial and temporal evolution of the electric field intensity vector is analyzed here taking into account a finite element method (FEM)—boundary element method (BEM) coupled formulation. In this context, the FEM is applied to model the region close to the wires, whereas the BEM simulates the remaining infinity domain. As it is well known, the BEM employs fundamental solutions which fulfill the radiation condition. Thus, this formulation is very suitable to perform infinite domain analysis, once reflected waves from infinity are avoided [58].

The adopted spatial discretization is also described in Figure 3. In this case, 2344 linear triangular finite elements and 80 linear boundary elements are employed in the analyses (see references [57, 58] for more details regarding the FEM and the BEM applied to electromagnetic analyses). The radius of the FEM-BEM interface is defined by $R = 1$ m and matching nodes are considered at the interface. For temporal discretization, the selected time step is given by $\Delta t = 5 \cdot 10^{-11}$ s for both domains. The physical properties of the medium (air) are $\mu = 1.2566 \cdot 10^{-6}$ H/m and $\varepsilon = 8.8544 \cdot 10^{-12}$ F/m.

Figure 4 shows the modulus of the electric field intensity obtained at points A and B (see Figure 3) considering the iterative coupling methodology. Analytical time histories [58] are also depicted in Figure 4, highlighting the good accuracy of the numerical results. In Figure 5, charts are displayed, indicating the percentage of occurrence of different relaxation parameter values (evaluated according to expression (10)), in each analysis. As can be observed, for all considered cases, optimal relaxation parameters are mostly in the interval $0.7 \leq \lambda \leq 0.8$. In fact, an optimal relaxation parameter selection is extremely case dependent. It is function of the physical properties of the model, geometric aspects, adopted spatial and temporal discretizations, and so forth. Equation (10) provides a simple expression to evaluate this complex parameter.

In order to illustrate the effectiveness of the methodology when considering different time discretizations for different domains, Figure 6 depicts results that are computed considering $\Delta t = 2.5 \cdot 10^{-11}$ s for the FEM and $\Delta t = 2.0 \cdot 10^{-10}$ s for the BEM (i.e., a difference of 8 times between the time steps). For simplicity, results are presented considering just the first case

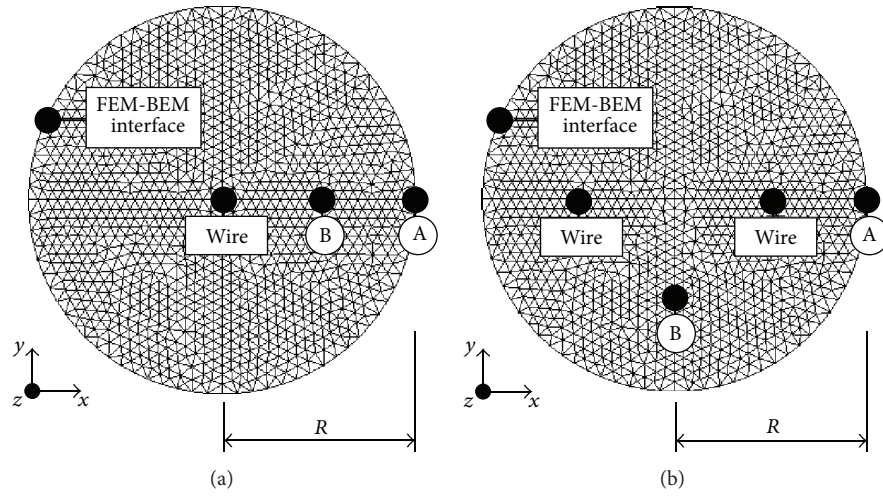


FIGURE 3: Sketch of the electromagnetic models and adopted FEM/BEM spatial discretizations: (a) case 1, one wire; (b) case 2, two wires.

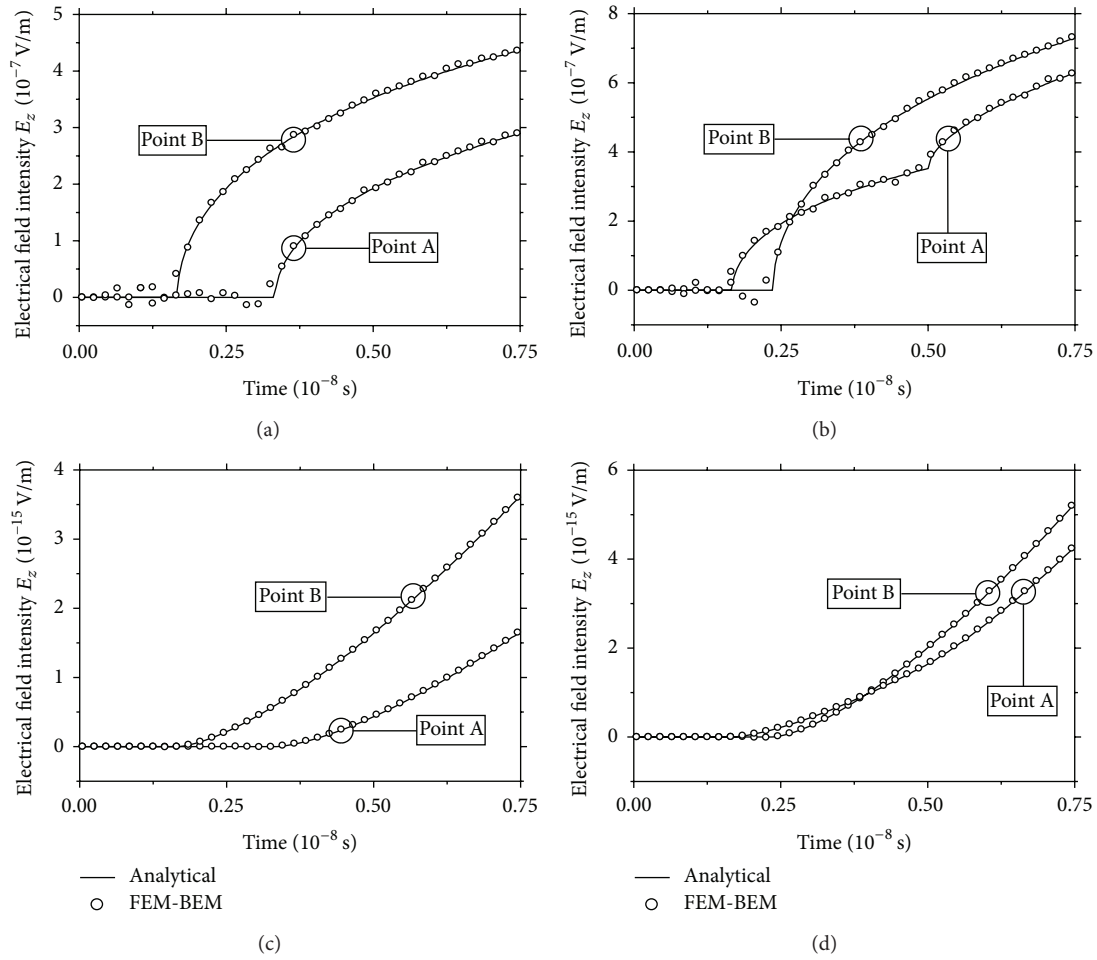


FIGURE 4: Time history results for the electric field intensity at points A and B considering $I(t) = t$ and (a) case 1 and (b) case 2; $I(t) = t^2$ and (c) case 1 and (d) case 2.

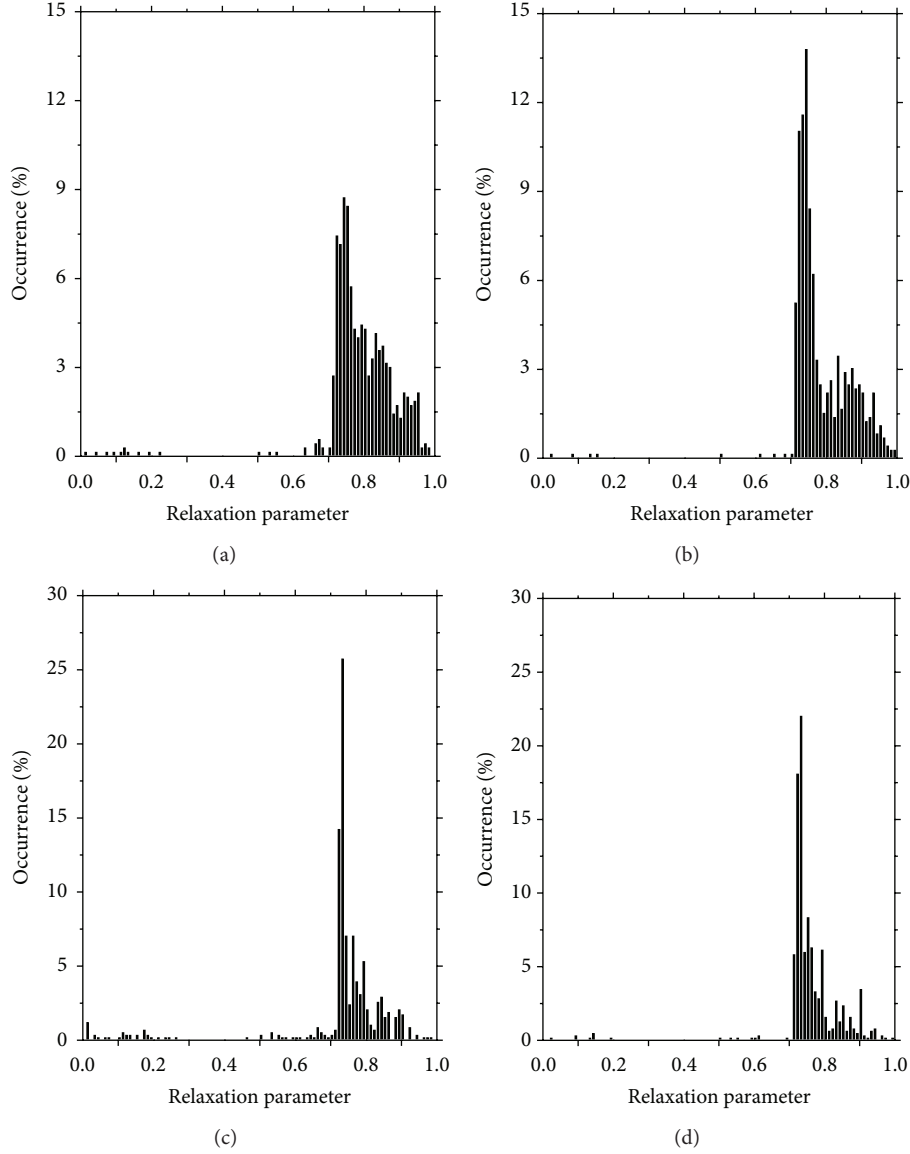


FIGURE 5: Percentage of occurrence of different relaxation parameter values during the analysis, considering $I(t) = t$ and (a) case 1 and (b) case 2; $I(t) = t^2$ and (c) case 1 and (d) case 2.

of analysis, that is, case 1 and $I(t) = t$. As one can observe in Figure 6(a), good results are still obtained taking into account the iterative formulation, in spite of the existing time disconnections at the interface. In Figure 6(b), the evolution of the relaxation parameter is depicted, taking into account this last configuration. As one can observe, in this case, optimal relaxation parameter values are between 0.7 and 1.0 and mostly concentrate on the interval (0.9, 1.0). In fact, it is expected that these values get closer to 1.0 when smaller time steps are considered. In the present analysis, an average number of 4.92 iterations per time step is obtained (taking into account 800 FEM time steps), which is a relatively low number, illustrating the good performance of the technique (it must be remarked that a tight tolerance criterion was adopted for the convergence of the iterative analysis).

4.2. Acoustic Waves. In acoustic models, a scalar wave equation describes the acoustic pressure field evolution [1]. In this case, (1b) can be rewritten as (in this subsection, frequency-domain analyses are focused)

$$\nabla \cdot (\kappa(x) \nabla p(x, \omega)) + \omega^2 \rho(x) p(x, \omega) = \gamma(x, \omega) \quad (14)$$

and (3) can be rewritten as

$$(p(x^+, \omega) - p(x^-, \omega)) = 0, \quad (15a)$$

$$(q(x^+, \omega) - q(x^-, \omega)) = g(x, \omega), \quad (15b)$$

where p is the hydrodynamic pressure and γ and g stand for domain and surface sources, respectively. The parameters ρ and κ denote, respectively, the mass density and compressibility of the medium and its wave propagation velocity

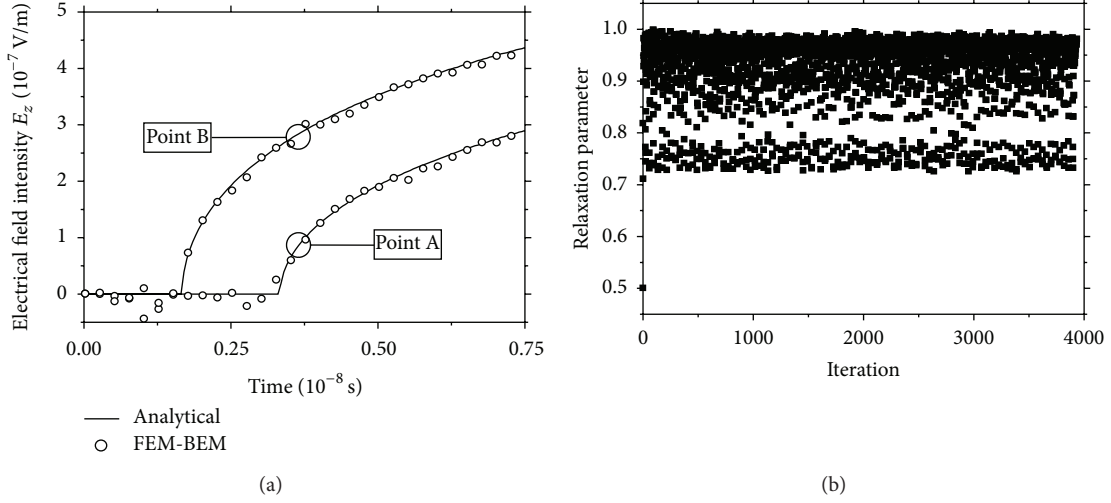


FIGURE 6: Results considering different time steps for each domain: (a) electric field intensity at points A and B; (b) optimal relaxation parameters for each iterative step.

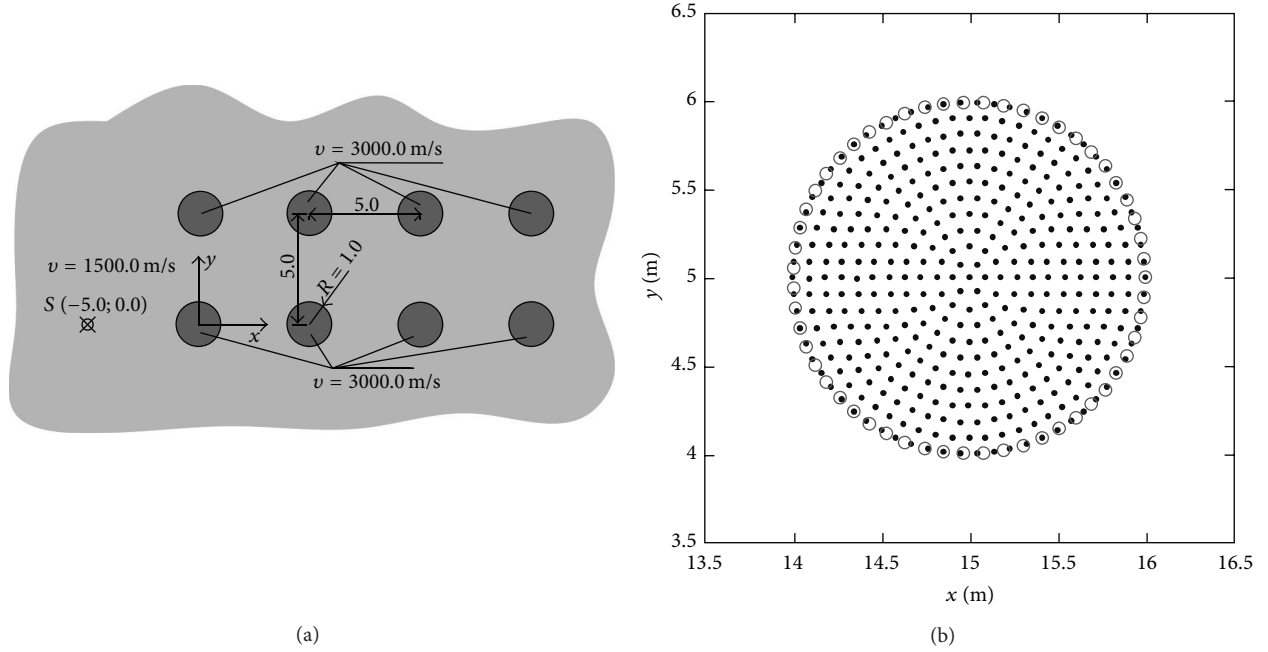


FIGURE 7: (a) Sketch for the heterogeneous medium with multiple subregions; (b) boundary and domain point distribution, considering the spatial discretization of an inclusion and adjacent fluid.

is specified as $v = (\kappa/\rho)^{1/2}$. The hydrodynamic fluxes on the interfaces are represented by q , and they are defined by $q = \kappa \nabla p \cdot \mathbf{n}$, where \mathbf{n} is the normal vector, from domain 1 to domain 2. Equation (15a) states that the pressure is continuous across the interface, whereas (15b) states that the flux is continuous across the interface if there is no surface source.

The advantages of using iterative coupling procedures are revealed when more complex configurations are analyzed. In this subsection, the case of a heterogeneous domain, composed of a homogeneous fluid incorporating multiple circular inclusions with different properties, is analyzed.

For this purpose, consider the host medium to allow the propagation of sound with a velocity of 1500 m/s, and this medium is excited by a line source located at $x_s = -5.0$ m and $y_s = 0.0$ m. Within this fluid, consider the presence of 8 circular inclusions; all of them are with unit radius and filled with a different fluid, allowing sound waves to travel at 3000 m/s, as depicted in Figure 7.

The above-described system has been analyzed taking into account the proposed iterative coupling procedure making use of the Kansa's method (KM) to model all the inclusions and of the method of fundamental solutions (MFS) to model the host fluid (see references [12, 59–61]

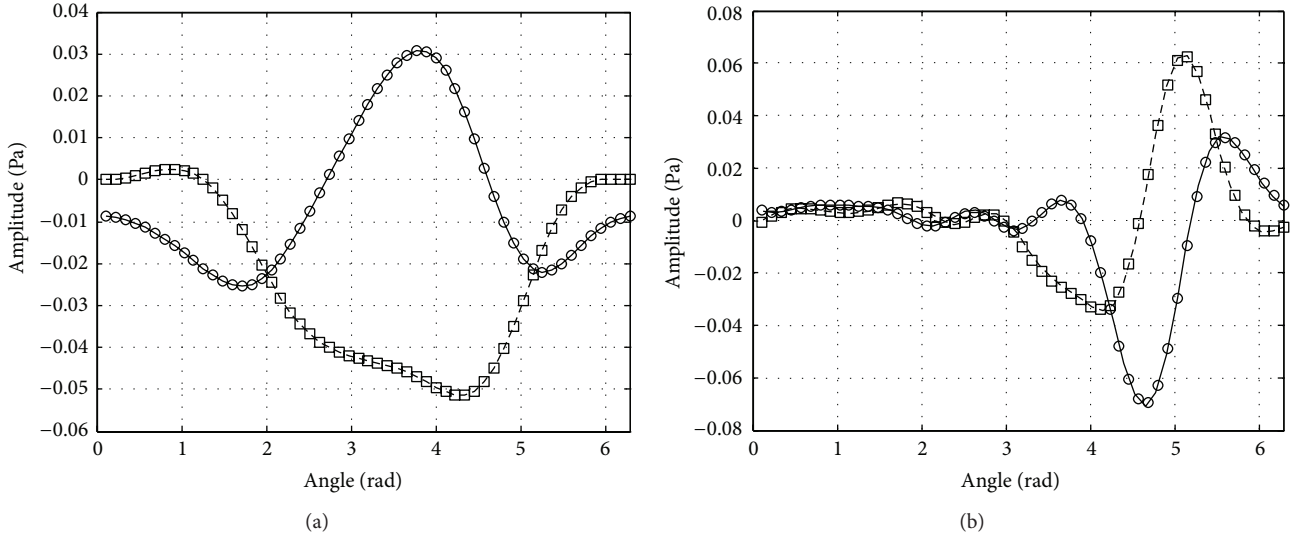


FIGURE 8: Hydrodynamic pressures along the common interface of the 8th inclusion for (a) $\omega = 400$ Hz and (b) $\omega = 1000$ Hz (—, real-iterative; ---, Imag-iterative; ○, Real-direct; □, Imag-direct).

for more details regarding the KM and the MFS applied to acoustic analyses). One should note that, since the real source is positioned at the outer region, the iterative process is initialized with the analysis of the MFS model, considering prescribed Neumann boundary conditions at the common interfaces. Once the boundary pressures for the outer region are computed, these values are transferred to the closed regions by imposing Dirichlet boundary conditions, incorporating information about the influence of each inclusion on the remaining heterogeneities. Then, each KM subregion is analysed independently and the internal boundary values (normal fluxes) are evaluated autonomously for each inclusion. The iterative procedure then goes further, including the calculation of the relaxation parameter at each iterative step, as well as the correction of boundary variables, until convergence is achieved.

To model the system, each MFS boundary is discretized by 55 points. 331 KM domain points are equally distributed within each inclusion, and 66 KM boundary points (around 31 points per wavelength) are used (see Figure 7(b)). The complexity of the model hinders the definition of a closed form solution; thus, the results are checked against a numerical model which performs the direct (i.e., noniterative) coupling between both methods. In that model, 66 boundary points are used in the MFS to define the boundary of each inclusion, and 66 and 331 KM boundary and domain points, respectively, are adopted for the discretization of each inclusion (analogously to the iterative coupling procedure). Figure 8 compares the responses computed by the iterative and the direct coupling methodologies. Results are depicted along the boundary of the 8th inclusion, for excitation frequencies of 400 Hz (Figure 8(a)) and 1000 Hz (Figure 8(b)). As can be observed in the figure, there is a perfect match between both approaches, with the iterative procedure clearly converging to the correct solution.

It is important, at this point, to highlight the differences in the computational times of the direct and of the iterative

coupling approaches. For the present model configuration, the direct coupling approach had to deal simultaneously with 528 boundary points and a total of 2648 internal points (i.e., considering a coupled matrix of dimension 3704), which is implied in 373.89 s of CPU time in a Matlab implementation (being this CPU time independent of the frequency in focus). For the iterative coupling approach, using 55 boundary points for the MFS and 66 boundary points for the KM, it was possible to obtain analogous results considering 12.06 s of CPU time for the frequency of 200 Hz and 32.32 s for the frequency of 1000 Hz (i.e., 3.23% and 8.64% of the computational cost of the direct coupling methodology, resp.). Even if the same number of boundary points is used in the iterative coupling approach for the MFS (i.e., 66 points), the final CPU time would just increase up to 35.71 s (9.55% of the computational cost of the direct coupling methodology). These results are summarized in Table 1, where the number of iterations and the CPU time are presented for the first scenarios (i.e., 55 boundary points for the MFS) and for frequencies between 50 Hz and 1000 Hz. The values described in Table 1 further confirm that the difference in calculation times between the iterative and the direct coupling approach is striking and reveal an excellent gain in performance favouring the iterative coupling technique. It is important to understand that this gain is strongly related to the possibility of dealing with smaller-sized matrices when using the iterative coupling procedure. Moreover, it is possible to invert (or triangularize, etc.) the relevant matrices only at the first iterative step and then proceed with the calculations using the inverted matrices (or forward/back substituting, etc.). As a consequence, after the first iteration, only matrix vector multiplication operations are required, and very high savings in what concerns computational time are achieved. In fact, considering that the number of operations required for matrix inversion can be assumed to be of the order of N^3 (N being the matrix size), a simple calculation allows concluding that, for the current model, the relative cost of inverting the

TABLE 1: Total number of iterations and relative CPU time (iterative/direct coupling) for the acoustic model.

Frequency (Hz)	Iterations	Relative CPU time (%)
50	14	2.09
100	18	2.43
150	29	3.19
200	31	3.23
250	26	2.78
300	40	3.86
350	31	3.13
400	32	3.20
450	30	3.02
500	49	4.49
550	48	4.40
600	45	4.18
650	68	5.94
700	34	3.28
750	39	3.66
800	110	9.20
850	98	8.28
900	78	6.75
950	104	8.83
1000	100	8.64

eight KM matrices (each one being a square matrix with 397×397 entries) and the MFS matrix (with 440×440 entries) is less than 2% of the cost of inverting a larger 3704×3704 matrix, as required for the direct coupling strategy. Similar conclusions can be obtained considering other solver procedures, such as matrix triangularizations, demonstrating that a considerably less expensive methodology is obtained if the different subdomains are analysed separately (even considering an eventual high number of iterative steps in the iterative analysis).

Analyzing the difference in computational times between the two analyzed frequencies (i.e., 200 Hz and 1000 Hz) also reveals a significant difference between them. This difference is related to the number of iterations required for convergence, which was higher when the excitation frequency of 1000 Hz was considered. The plot in Figure 9 indicates the number of iterations required for convergence along a range of frequencies between 10 Hz and 1000 Hz, using a constant number of boundary (55 for the MFS and 66 for the KM) and internal points (331 for the KM). As expected, the number of iterations increases with the frequency. It is interesting to note that the maximum necessary number of iterations occurred for a frequency of 990 Hz, requiring 170 iterations and a CPU time of 54.80 s to converge, which is less than 15% of the CPU time required by the direct coupling for the same frequency.

In Figure 10, the wavefield produced within and around the inclusions is illustrated for excitation frequencies of 600 Hz and 1000 Hz. As expected, as the frequency increases, the multiple inclusions generate progressively more complex wave fields, with the interaction between them becoming very significant for the higher frequency. Observation of

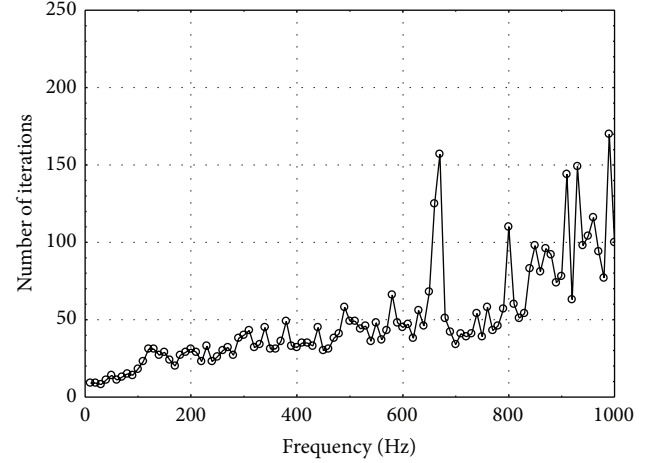


FIGURE 9: Total number of iterations considering different frequencies and 55 collocation points for the MFS and 66 boundary points for the KM, at each circular inclusion.

these results also reveals a strong shadow effect produced by the inclusions, with much lower amplitudes being registered in the region behind the inclusions placed further away from the source. This effect is even more pronounced for the higher frequency. Interestingly, for both frequencies, the space between the two lines of inclusions works as a guiding path, along which the sound energy travels with less attenuation.

4.3. Mechanical Waves. In dynamic models, a vectorial wave equation describes the displacement field evolution [1]. In this case, considering linear behaviour, (1a) can be rewritten as (in this subsection, time-domain analyses are focused)

$$\begin{aligned} \nabla \times (\mu(x) \nabla \times \mathbf{u}(x, t)) \\ - \nabla ((\eta(x) + 2\mu(x)) \nabla \cdot \mathbf{u}(x, t)) + \rho(x) \ddot{\mathbf{u}}(x, t) = \mathbf{f}(x, t), \end{aligned} \quad (16)$$

and (3) can be rewritten as:

$$(\mathbf{u}(x^+, t) - \mathbf{u}(x^-, t)) = 0, \quad (17a)$$

$$(\boldsymbol{\sigma}(x^+, t) - \boldsymbol{\sigma}(x^-, t)) \mathbf{n}(x) = \boldsymbol{\tau}(x, t), \quad (17b)$$

where \mathbf{u} is the displacement vector and \mathbf{f} and $\boldsymbol{\tau}$ stand for domain and surface forces, respectively. The terms η and μ denote the so-called Lamé parameters, and ρ is the mass density of the medium. In this case, the wave propagation velocities are specified as $c_s = (\mu/\rho)^{1/2}$ (shear wave) and $c_d = ((\eta + 2\mu)/\rho)^{1/2}$ (dilatational wave). The stress tensor is denoted by $\boldsymbol{\sigma}$ and \mathbf{n} is the normal vector, from domain 1 to domain 2. Equation (17a) states that the displacements are continuous across the interface, whereas (17b) states that the tractions are continuous across the interface if there are no surface forces on it.

One main advantage of the discussed coupling algorithm is that other iterative processes can be carried out in the same

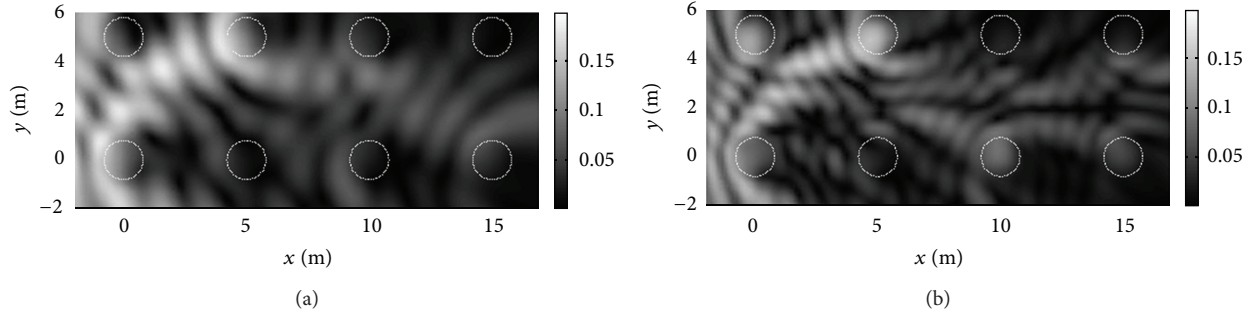


FIGURE 10: 3D plots of the sound field for frequencies of (a) 600 Hz and (b) 1000 Hz.

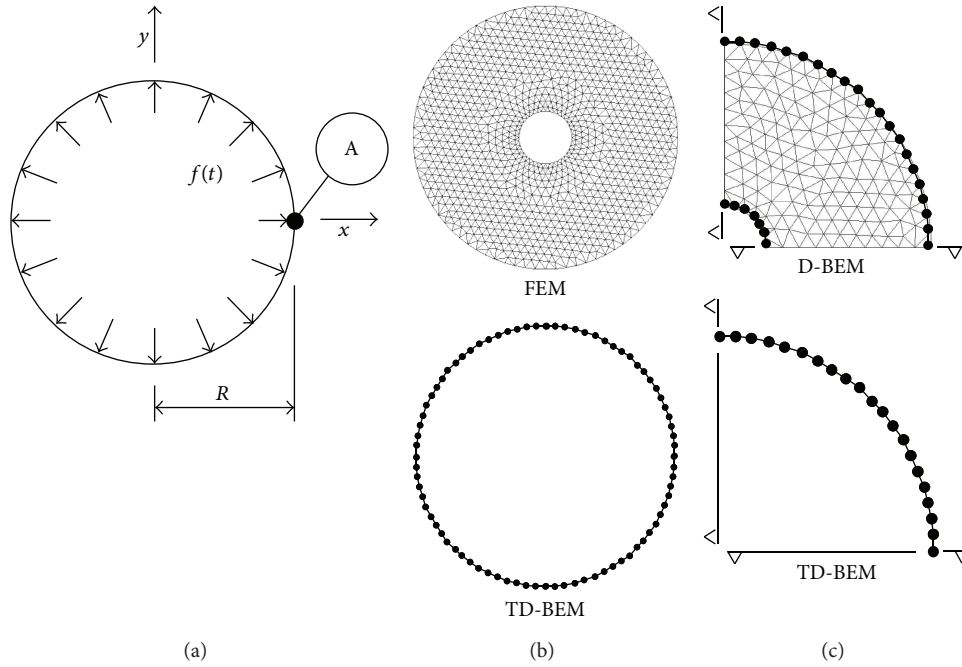


FIGURE 11: (a) Sketch of the circular cavity; (b) FEM-BEM discretization; (c) BEM-BEM discretization.

iterative loop needed for the coupling. Thus, consideration of coupled nonlinear models, as for example, may not demand a superior amount of computational effort, which is very beneficial.

In the present application, a nonlinear model is considered and elastoplastic analyses are carried out (for details about elastoplastic analyses, one is referred to [33–35, 62–64]). Moreover, two discretization approaches are employed here, one taking into account FEM-BEM coupling procedures, and another considering BEM-BEM coupled techniques (for more details about these coupled models, one is referred to [37, 43]). In this context, a nonlinear infinity domain is analyzed here, in which a circular cavity is loaded. The region expected to develop plastic strains is discretized by the finite element method, in the case of the FEM-BEM coupled analysis, or by the domain boundary element method (D-BEM), in the case of the BEM-BEM coupled analysis. The remainder of the infinity domain is discretized by the time-domain boundary element method (TD-BEM). A sketch of

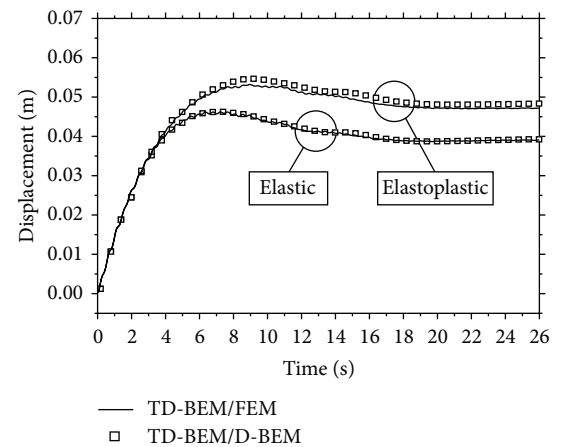


FIGURE 12: Radial displacement considering coupled TD-BEM/D-BEM and coupled TD-BEM/FEM analyses: linear and nonlinear results at point A.

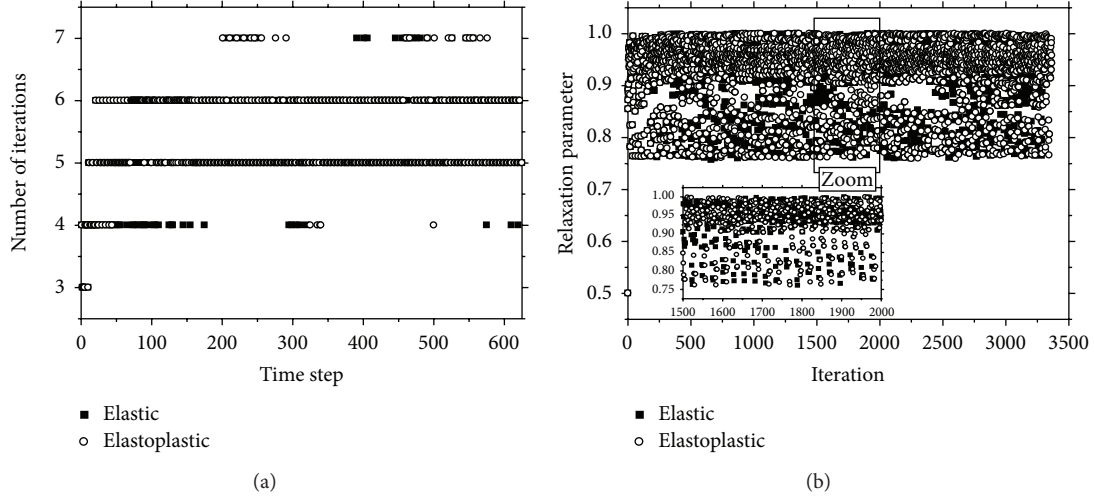


FIGURE 13: TD-BEM/FEM analyses: (a) number of iterations per time step considering optimal relaxation parameters; (b) optimal relaxation parameters for each iterative step.

the model is depicted in Figure 11, as well as the adopted discretizations. The FEM-BEM discretization is depicted in Figure 11(b). In this case, 1944 linear triangular finite elements and 80 linear boundary elements are employed in the coupled analysis. The BEM-BEM discretization is depicted in Figure 11(c). In this case, 46 linear boundary elements are employed in the BEM-BEM coupled analysis (20 linear boundary elements for the TD-BEM and 26 linear boundary elements for the D-BEM), as well as 270 linear triangular cells (D-BEM formulation). In the BEM-BEM coupled analysis, the double symmetry of the problem is taken into account. An interesting feature of the boundary element formulation is that symmetric bodies under symmetric loads can be analysed without discretization of the symmetry axes. This can be accomplished by an automatic condensation process, which integrates over reflected elements and performs the assemblage of the final matrices in reduced size [64]. The time discretization adopted is given by $\Delta t = 0.04$ s for the FEM and $\Delta t = 0.20$ s for the D-BEM and the TD-BEM.

The physical properties of the model are $\mu = 2.652 \cdot 10^8$ N/m², $\eta = 2.274 \cdot 10^8$ N/m², and $\rho = 1.804 \cdot 10^3$ kg/m³. A perfectly plastic material obeying the Mohr-Coulomb yield criterion is assumed, where $c_0 = 4.8263 \cdot 10^6$ N/m² (cohesion) and $\phi = 30^\circ$ (internal friction angle). The geometry of the problem is defined by $R = 3.048$ m (the radius of the TD-BEM circular mesh is given by $5R$).

In Figure 12, the displacement time history at point A is depicted, considering linear and nonlinear analyses. As one can notice, good agreement is observed between the FEM-BEM and BEM-BEM results. It is important to highlight that, for the FEM-BEM analyses, a difference of 5 times between the FEM and BEM time steps is considered, illustrating the effectiveness of the time interpolation/extrapolation procedures adopted in the analyses.

The number of iterations per time step and the optimal relaxation parameters, evaluated at each iterative step, are depicted in Figure 13, taking into account the FEM-BEM coupled analyses. As one may observe, basically the same

TABLE 2: Total number of iterations (considering all time steps) for the dynamic model.

Relaxation parameter	Elastic analysis	Elastoplastic analysis
1.00	3730	3740
0.90	3392	3443
0.80	3973	3993
0.70	4772	4777
Optimal	3287	3346

computational effort (i.e., number of iterative steps) is necessary for both linear and nonlinear analyses, highlighting the efficiency of the proposed methodology for complex phenomena modeling. It is also important to remark the low number of iterative steps necessary for convergence, with a maximum of 7 iterations being necessary, within a time step, taking into account the entire linear and non-linear analyses. For the focused configurations, the optimal relaxation parameters are intricately distributed within the interval (0.75; 1.00), as depicted in Figure 13(b).

In Table 2, the total number of iterations is presented, considering analyses with optimal relaxation parameters and with some constant preselected λ values. As one may observe, an inappropriate selection for the relaxation parameter can considerably increase the associated computational effort. Thus, the optimization technique is extremely important in order to provide a robust and efficient iterative coupling formulation. In Figure 14, the computed σ_{xy} stresses are depicted, considering the BEM-BEM elastoplastic analysis. An advantage of the D-BEM is that it employs nodal stress equations [37], allowing computing continuous stress fields, in counterpart to the FEM, which computes stresses based on displacement derivatives, obtaining discontinuous stress fields at element interfaces.

4.4. Coupled Acoustic-Mechanical Waves. In this case, different wave equations, as indicated in Sections 4.2 and 4.3 (see

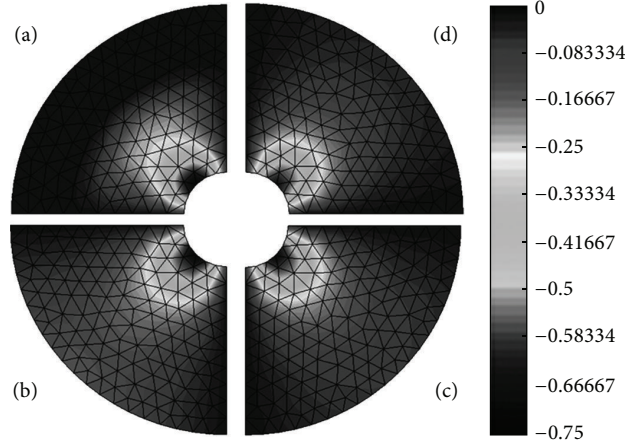


FIGURE 14: Spatial and temporal evolution of σ_{xy} considering elastoplastic analysis (scale factor: $6.8947 \cdot 10^6 \text{ N/m}^2$); (a) $t = 4 \text{ s}$; (b) $t = 8 \text{ s}$; (c) $t = 12 \text{ s}$; (d) $t = 16 \text{ s}$.

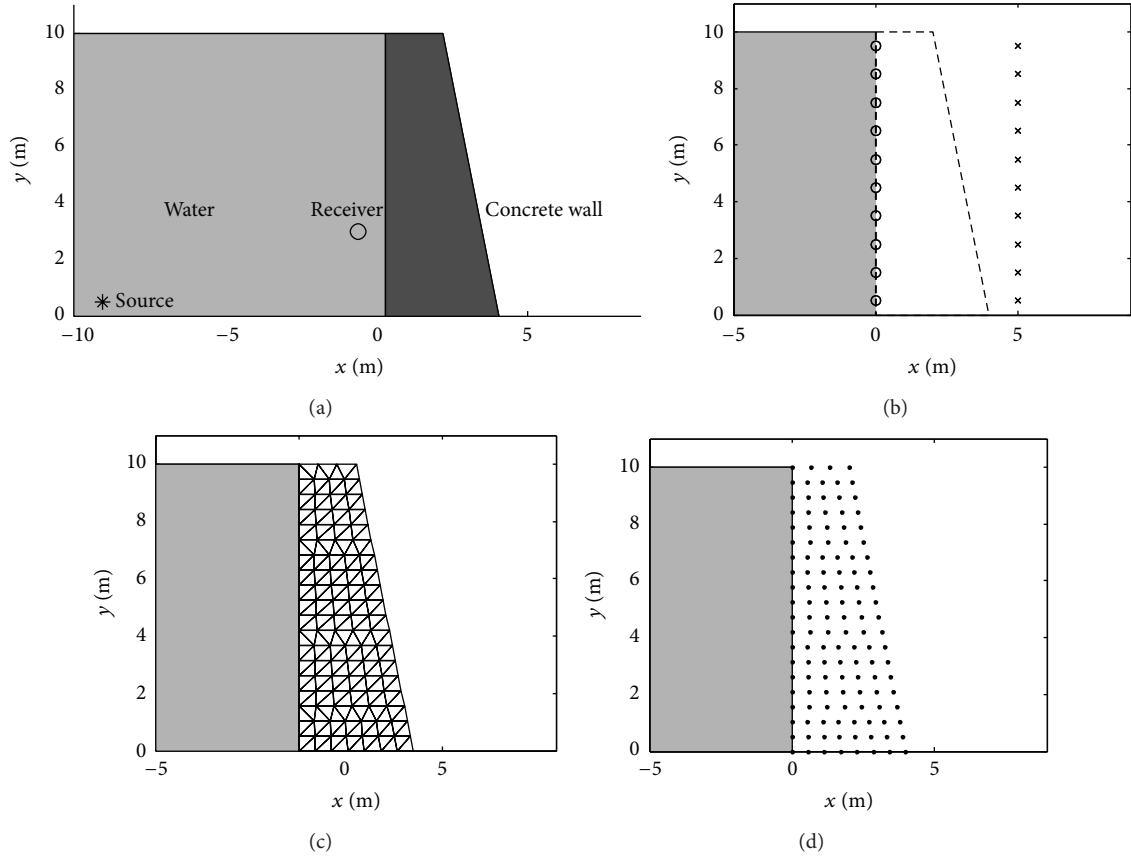


FIGURE 15: (a) Sketch of the coupled acoustic-dynamic model; (b) MFS collocation points (o) and virtual sources (x); (c) FEM mesh when 20 nodes are used along the solid-fluid interface; (d) node distribution for the meshless methods when 20 nodes are used along the solid-fluid interface.

(14) and (16)), describe different domains of the global model. The interface conditions for the acoustic-dynamic coupling (3) can then be written as (in this subsection, frequency-domain analyses are focused)

$$(\mathbf{n}(x) \cdot \boldsymbol{\sigma}(x^+, \omega) \mathbf{n}(x) - p(x^-, \omega)) = 0, \quad (18a)$$

$$(-\omega^2 \mathbf{n}(x) \cdot \mathbf{u}(x^+, \omega) - v(x^-)^2 q(x^-, \omega)) = 0, \quad (18b)$$

where \mathbf{u} is the displacement vector and $\boldsymbol{\sigma}$ is the stress tensor of the dynamic model (domain 1). p is the hydrodynamic pressure and q is the hydrodynamic flux of the acoustic model (domain 2). \mathbf{n} is the normal vector, from domain 1 to domain 2. The acoustic wave propagation velocity is denoted by v . Equation (18a) states that the normal components of the dynamic tractions are equal to the acoustic pressures

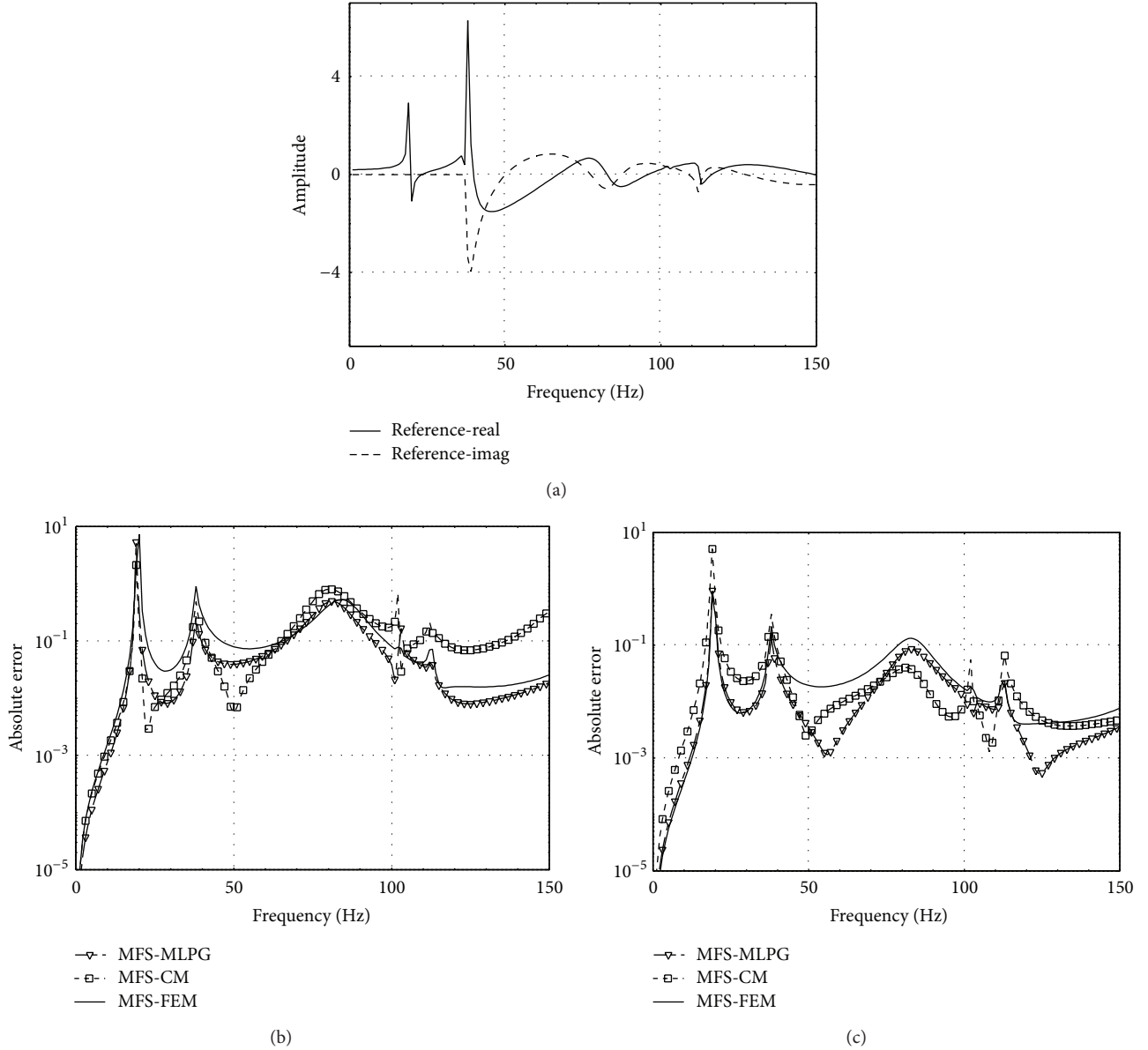


FIGURE 16: (a) Reference pressure result; absolute error considering (b) 20 and (c) 40 boundary nodes in the solid, along the solid-fluid interface.

and (18b) relates the normal components of the dynamic accelerations to the acoustic fluxes.

In the present application, a model in which a concrete wall of 10.0 m high is coupled to a fluid waveguide, filled with water, is analyzed. A sketch of the model is depicted in Figure 15(a). For this case, a pressure source is positioned in the waveguide, at $(-10.0; 0.5)$, illuminating the system. The concrete structure corresponds to a wall with variable cross-section, exhibiting thicknesses of 4.0 m at its basis and of 2.0 m at its top.

To simulate this coupled system, several approaches are employed. For the fluid medium, the MFS is used in all cases, allowing the use of the Green's function for a waveguide (see [61] for details concerning this function). This Green's function is written as a summation of modes, and its convergence is very difficult when the source and the receiver

are positioned along the same vertical line, thus posing severe difficulties for its use together with a BEM formulation. The structure is modelled using three different methods, namely, the FEM, a local collocation method (CM) (see [65] for details about this procedure), and a meshless local Petrov-Galerkin technique (MLPG) (see [65, 66] for details about this procedure). Representations of the node distribution for each one of the methods can be found in Figures 15(b)–15(d).

Since no analytical solution can be found in the literature for the present case, a numerical solution making use of a full BEM model ensuring the correct coupling between the solid and the fluid is used. For this case, the rigid bottom of the waveguide is accounted for using an image-source Green's function, while the free surface is fully discretized up to a distance of 60.0 m from the concrete wall; after this, an anechoic termination is considered, imposing adequate Robin

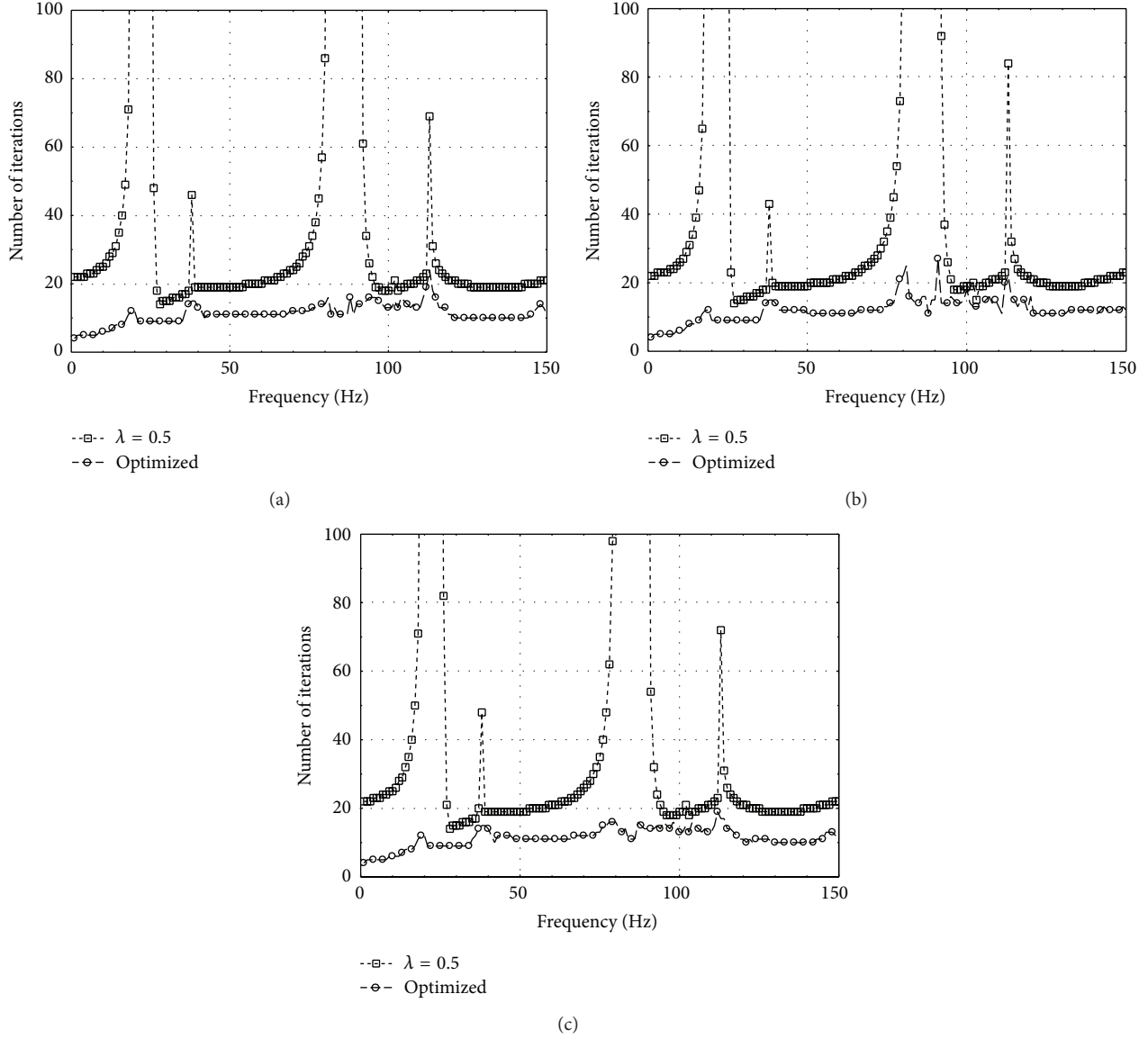


FIGURE 17: Number of iterations required for convergence: (a) MFS-FEM; (b) MFS-CM; (c) MFS-MLPG.

boundary conditions. For the solid, full-space Green's functions are adopted, and 60 nodal points are used along the solid-fluid interface, ensuring that accurate results can be obtained. A total of 796 boundary elements are used to build this model. Details on the mathematical formulation of this technique can be found in the works of Tadeu and Godinho [7].

Figure 16(a) illustrates the reference response in terms of real and imaginary components of the acoustic pressure at a receiver located at $(-1.0; 3.0)$, for frequencies between 1 Hz and 150 Hz. This position is chosen so that the effect of the vibration of the concrete wall and thus of the solid-fluid coupling can be evident in the responses. As can be seen in the figure, two peaks with significant amplitude can be observed, corresponding to vibration modes of the wall coupled to the fluid; after these peaks, the response exhibits a smoother form. Figures 16(b) and 16(c) illustrate

the absolute difference, to the reference solution, calculated for the three different approaches, namely, the MFS-FEM, the MFS-CM, and the MFS-MLPG. For the fluid, 10 nodes are positioned along the interface, while for the solid, results are presented for 20 (Figure 16(b)) and 40 nodes (Figure 16(c)). When 20 nodes are used, the responses provided by the three approaches are very similar, with the two meshless methods exhibiting a lower error level at the lower frequencies, and with a worse behaviour of the CM being observable in the higher frequencies. Observing the figure, it is apparent that the MLPG is providing a more accurate response throughout the analysed frequency range, exhibiting a lower error than the FEM even at high frequencies. When more nodes are used (Figure 16(c)), the error levels provided by all methods improve, although the MLPG still exhibits a better overall behaviour than the remaining methods.

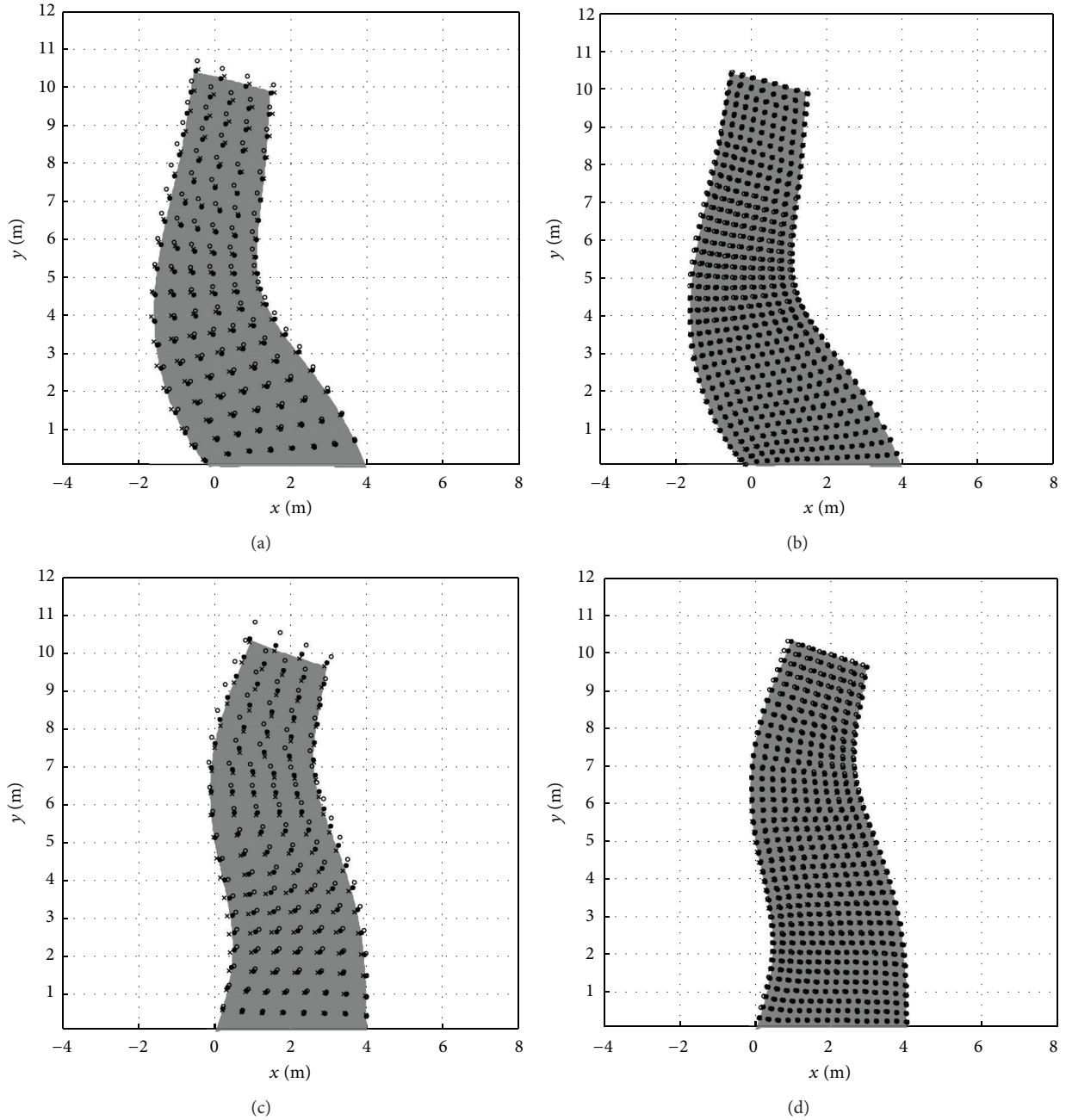


FIGURE 18: Real ((a) and (b)) and imaginary ((c) and (d)) parts of the deformation of the solid structure (amplified) when the excitation frequency is 125 Hz. Results are shown for 20 ((a) and (c)) and 40 ((b) and (d)) boundary nodes in the solid, along the fluid-solid interface, when using the FEM (\times), CM (\circ), and MLPG (\bullet).

It is important to notice that, although different error levels are observed for each method, the iterative coupling algorithm always quickly converges even for frequencies in the vicinity of the response peaks referred to before. Figure 17 illustrates the number of iterations required for convergence, for the three approaches, considering 40 nodes along the interface to model the solid. Clearly, all three approaches exhibit very similar curves, requiring similar numbers of iterations for the iterative process to reach convergence at each frequency. It is also very clear that, for this case, the

number of iterations is always small, slightly exceeding 20 iterations only at a few specific frequencies. For the remaining frequencies, only about 10 to 15 iterations are necessary to attain convergence. In the same figure, the number of iterations required, when a fixed relaxation parameter is used (i.e., $\lambda = 0.5$), is also depicted. Comparison between the curves calculated with optimal and fixed parameters reveals a striking difference, with the optimal parameter always leading to significantly less iterations and ensuring convergence for all frequencies. When the relaxation parameter is fixed,

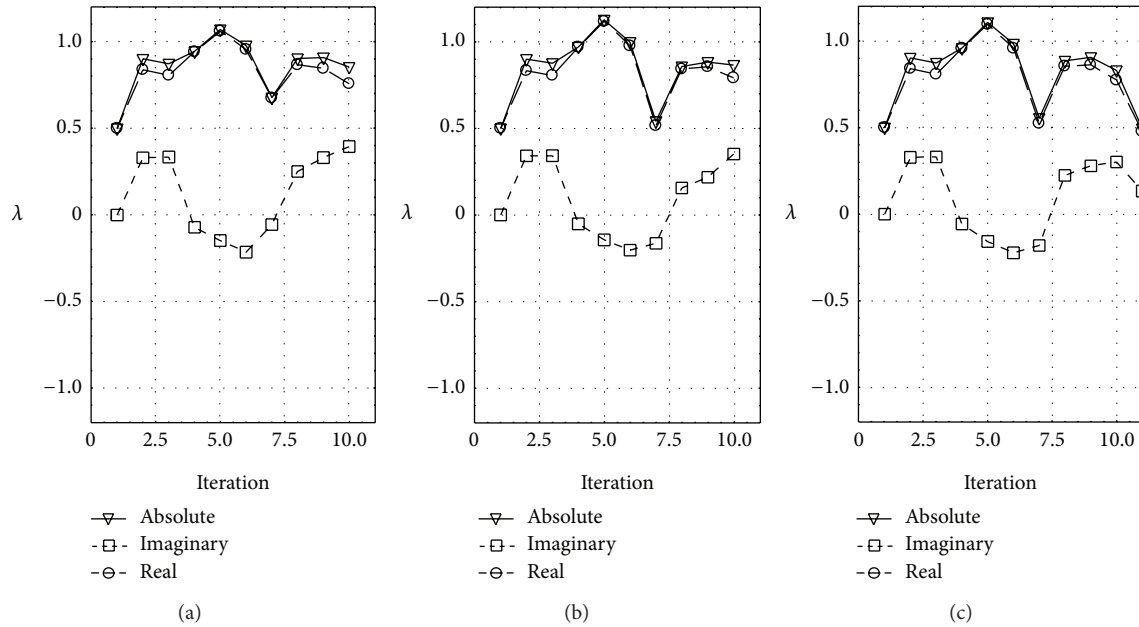


FIGURE 19: Variation of the complex relaxation parameter throughout the iterative process: (a) MFS-FEM; (b) MFS-CM; (c) MFS-MLPG.

convergence cannot be reached at two sets of frequencies, associated with specific dynamic behaviours of the system. These results once again illustrate the importance of using a well-chosen relaxation parameter to ensure that effective analyses are obtained.

The set of plots shown in Figure 18 illustrates the deformation of the structure at frequency 125 Hz. In the plotted results, a grey patch is used to identify the reference response, while marks are used to depict the (amplified) deformed shape of the structure when analysed by the three iteratively coupled approaches. The left column reveals the response for 20 nodes positioned in the solid along the interface, whereas the right column shows the equivalent result computed for 40 nodes. It can be observed that, for all approaches, the response improves significantly when more nodes are used, indicating that the convergent behaviour of the methods can be observed. The computed responses reveal very similar shape and displacement amplitudes when compared to the reference solution, with the response provided by the MFS-CM approach being somewhat worse than the remaining two. In fact, the MFS-MLPG and the MFS-FEM exhibit very similar behaviours, with lower discrepancies being registered for the meshless method. Finally, Figure 19 illustrates the variation of the complex relaxation parameter throughout the iterative process, showing its real and imaginary components, together with its absolute value. Those plots reveal a very similar evolution of the parameter for all combinations of methods; again, this indicates that the discussed iterative procedure is quite independent of the discretization methods involved in the analyses.

5. Conclusions

This paper presents an overview of the application of iterative coupling strategies to the analysis of wave propagation problems. Different methods were considered, including

mesh-based and meshless methods, ranging from the more classic BEM and FEM to the less usual MLPG, collocation methods, or MFS. Several examples of the iterative coupling technique were presented in Section 4, including the application of the scheme to electromagnetic, acoustic, elastic/elastoplastic, and acoustic-elastic interaction problems. The generality and flexibility of the iterative scheme allowed an efficient analysis of these problems, either using time or frequency domain models. The use of an optimized relaxation parameter (which is the basis of this scheme) proved to be quite important, clearly accelerating (or in some cases ensuring) convergence; for all tested cases, this parameter was shown to unpredictably vary throughout the iterative process, and thus its appropriate recalculation at each iterative step becomes important. The illustrated analyses clearly indicated that the strategy can be effectively used for different methods and that the performance of the iterative technique is quite insensitive to the discretization methods employed in the analyses.

It should be highlighted that the coupling technique presented here is based on previous experience and works of the authors and, although the paper is focused in wave propagation problems, the iterative strategy presently discussed can be regarded as a quite generic framework to perform the coupling between different methods in many types of applications.

Conflict of Interests

The authors declare that there is no conflict of interests regarding the publication of this paper.

Acknowledgments

The financial support by CNPq (Conselho Nacional de Desenvolvimento Científico e Tecnológico) and FAPEMIG

(Fundação de Amparo à Pesquisa do Estado de Minas Gerais) is greatly acknowledged.

References

- [1] Y. H. Pao and C. C. Mow, *Diffraction of Elastic Waves and Dynamic Stress Concentrations*, Crane, Russak & Company, New York, NY, USA, 1973.
- [2] J. D. Achenbach, W. Lin, and L. M. Keer, "Mathematical modelling of ultrasonic wave scattering by sub-surface cracks," *Ultrasonics*, vol. 24, no. 4, pp. 207–215, 1986.
- [3] R. A. Stephen, "A review of finite difference methods for seismo-acoustics problems at the seafloor," *Reviews of Geophysics*, vol. 26, no. 3, pp. 445–458, 1988.
- [4] J. Dominguez, *Boundary Elements in Dynamics*, Southampton: Computational Mechanics Publications, 1993.
- [5] A. Karlsson and K. Kreider, "Transient electromagnetic wave propagation in transverse periodic media," *Wave Motion*, vol. 23, no. 3, pp. 259–277, 1996.
- [6] D. Clouteau, G. Degrande, and G. Lombaert, "Numerical modelling of traffic induced vibrations," *Meccanica*, vol. 36, no. 4, pp. 401–420, 2001.
- [7] A. Tadeu and L. Godinho, "Scattering of acoustic waves by movable lightweight elastic screens," *Engineering Analysis with Boundary Elements*, vol. 27, no. 3, pp. 215–226, 2003.
- [8] J. L. Wegner, M. M. Yao, and X. Zhang, "Dynamic wave-soil-structure interaction analysis in the time domain," *Computers & Structures*, vol. 83, no. 27, pp. 2206–2214, 2005.
- [9] Y. B. Yang and L. C. Hsu, "A review of researches on ground-borne vibrations due to moving trains via underground tunnels," *Advances in Structural Engineering*, vol. 9, no. 3, pp. 377–392, 2006.
- [10] Y. B. Yang and H. H. Hung, *Wave Propagation for Train-Induced Vibrations. A Finite/Infinite Element Approach*, World Scientific, 2009.
- [11] I. Castro and A. Tadeu, "Coupling of the BEM with the MFS for the numerical simulation of frequency domain 2-D elastic wave propagation in the presence of elastic inclusions and cracks," *Engineering Analysis with Boundary Elements*, vol. 36, no. 2, pp. 169–180, 2012.
- [12] L. Godinho and A. Tadeu, "Acoustic analysis of heterogeneous domains coupling the BEM with Kansas method," *Engineering Analysis with Boundary Elements*, vol. 36, no. 6, pp. 1014–1026, 2012.
- [13] O. C. Zienkiewicz, D. W. Kelly, and P. Bettess, "The coupling of the finite element method and boundary solution procedures," *International Journal for Numerical Methods in Engineering*, vol. 11, no. 2, pp. 355–375, 1977.
- [14] O. von Estorff and M. J. Prabucki, "Dynamic response in the time domain by coupled boundary and finite elements," *Computational Mechanics*, vol. 6, no. 1, pp. 35–46, 1990.
- [15] G. Kergourlay, E. Balmès, and D. Clouteau, "Model reduction for efficient FEM/BEM coupling," in *Proceedings of the 25th International Conference on Noise and Vibration Engineering (ISMA '00)*, vol. 25, pp. 1189–1196, September 2000.
- [16] E. Savin and D. Clouteau, "Elastic wave propagation in a 3-D unbounded random heterogeneous medium coupled with a bounded medium. Application to seismic soil-structure interaction (SSSI)," *International Journal for Numerical Methods in Engineering*, vol. 54, no. 4, pp. 607–630, 2002.
- [17] C. C. Spyarakos and C. Xu, "Dynamic analysis of flexible massive strip-foundations embedded in layered soils by hybrid BEM-FEM," *Computers & Structures*, vol. 82, no. 29–30, pp. 2541–2550, 2004.
- [18] M. Adam and O. von Estorff, "Reduction of train-induced building vibrations by using open and filled trenches," *Computers & Structures*, vol. 83, no. 1, pp. 11–24, 2005.
- [19] L. Andersen and C. J. C. Jones, "Coupled boundary and finite element analysis of vibration from railway tunnels—a comparison of two- and three-dimensional models," *Journal of Sound and Vibration*, vol. 293, no. 3, pp. 611–625, 2006.
- [20] H. A. Schwarz, "Ueber einige Abbildungsaufgaben," *Journal für die Reine und Angewandte Mathematik*, vol. 70, pp. 105–120, 1869.
- [21] M. J. Gander, "Schwarz methods over the course of time," *Electronic Transactions on Numerical Analysis*, vol. 31, pp. 228–255, 2008.
- [22] L. Ling and E. J. Kansa, "Preconditioning for radial basis functions with domain decomposition methods," *Mathematical and Computer Modelling*, vol. 40, no. 13, pp. 1413–1427, 2004.
- [23] V. Dolean, M. El Bouajaji, M. J. Gander, S. Lanteri, and R. Perrussel, "Domain decomposition methods for electromagnetic wave propagation problems in heterogeneous media and complex domains," in *Domain Decomposition Methods in Science and Engineering*, pp. 15–26, Springer, Berlin, Germany, 2011.
- [24] J. R. Rice, P. Tsompanopoulou, and E. Vavalis, "Interface relaxation methods for elliptic differential equations," *Applied Numerical Mathematics*, vol. 32, no. 2, pp. 219–245, 2000.
- [25] C.-C. Lin, E. C. Lawton, J. A. Caliendo, and L. R. Anderson, "An iterative finite element-boundary element algorithm," *Computers & Structures*, vol. 59, no. 5, pp. 899–909, 1996.
- [26] Q. Deng, "An analysis for a nonoverlapping domain decomposition iterative procedure," *SIAM Journal on Scientific Computing*, vol. 18, no. 5, pp. 1517–1525, 1997.
- [27] D. Yang, "A parallel iterative nonoverlapping domain decomposition procedure for elliptic problems," *IMA Journal of Numerical Analysis*, vol. 16, no. 1, pp. 75–91, 1996.
- [28] W. M. Elleithy, H. J. Al-Gahtani, and M. El-Gebeily, "Iterative coupling of BE and FE methods in elastostatics," *Engineering Analysis with Boundary Elements*, vol. 25, no. 8, pp. 685–695, 2001.
- [29] W. M. Elleithy and M. Tanaka, "Interface relaxation algorithms for BEM-BEM coupling and FEM-BEM coupling," *Computer Methods in Applied Mechanics and Engineering*, vol. 192, no. 26–27, pp. 2977–2992, 2003.
- [30] B. Yan, J. Du, N. Hu, and H. Sekine, "Domain decomposition algorithm with finite element-boundary element coupling," *Applied Mathematics and Mechanics*, vol. 27, no. 4, pp. 519–525, 2006.
- [31] Y. Boubendir, A. Bendali, and M. B. Fares, "Coupling of a non-overlapping domain decomposition method for a nodal finite element method with a boundary element method," *International Journal for Numerical Methods in Engineering*, vol. 73, no. 11, pp. 1624–1650, 2008.
- [32] G. H. Miller and E. G. Puckett, "A Neumann-Neumann preconditioned iterative substructuring approach for computing solutions to Poisson's equation with prescribed jumps on an embedded boundary," *Journal of Computational Physics*, vol. 235, pp. 683–700, 2013.

- [33] W. M. Elleithy, M. Tanaka, and A. Guzik, "Interface relaxation FEM-BEM coupling method for elasto-plastic analysis," *Engineering Analysis with Boundary Elements*, vol. 28, no. 7, pp. 849–857, 2004.
- [34] H. Z. Jahromi, B. A. Izzuddin, and L. Zdravkovic, "A domain decomposition approach for coupled modelling of nonlinear soil-structure interaction," *Computer Methods in Applied Mechanics and Engineering*, vol. 198, no. 33, pp. 2738–2749, 2009.
- [35] D. Soares Jr., O. von Estorff, and W. J. Mansur, "Iterative coupling of BEM and FEM for nonlinear dynamic analyses," *Computational Mechanics*, vol. 34, no. 1, pp. 67–73, 2004.
- [36] J. Soares, O. von Estorff, and W. J. Mansur, "Efficient non-linear solid-fluid interaction analysis by an iterative BEM/FEM coupling," *International Journal for Numerical Methods in Engineering*, vol. 64, no. 11, pp. 1416–1431, 2005.
- [37] D. Soares Jr., J. A. M. Carrer, and W. J. Mansur, "Non-linear elastodynamic analysis by the BEM: an approach based on the iterative coupling of the D-BEM and TD-BEM formulations," *Engineering Analysis with Boundary Elements*, vol. 29, no. 8, pp. 761–774, 2005.
- [38] O. von Estorff and C. Hagen, "Iterative coupling of FEM and BEM in 3D transient elastodynamics," *Engineering Analysis with Boundary Elements*, vol. 29, no. 8, pp. 775–787, 2005.
- [39] D. Soares Jr. and W. J. Mansur, "Dynamic analysis of fluid-soil-structure interaction problems by the boundary element method," *Journal of Computational Physics*, vol. 219, no. 2, pp. 498–512, 2006.
- [40] D. Soares Jr., "Numerical modelling of acoustic-elastodynamic coupled problems by stabilized boundary element techniques," *Computational Mechanics*, vol. 42, no. 6, pp. 787–802, 2008.
- [41] D. Soares Jr., "A time-domain FEM-BEM iterative coupling algorithm to numerically model the propagation of electromagnetic waves," *Computer Modeling in Engineering and Sciences*, vol. 32, no. 2, pp. 57–68, 2008.
- [42] A. Warszawski, D. Soares Jr., and W. J. Mansur, "A FEM-BEM coupling procedure to model the propagation of interacting acoustic-acoustic/acoustic-elastic waves through axisymmetric media," *Computer Methods in Applied Mechanics and Engineering*, vol. 197, no. 45, pp. 3828–3835, 2008.
- [43] D. Soares Jr., "An optimised FEM-BEM time-domain iterative coupling algorithm for dynamic analyses," *Computers & Structures*, vol. 86, no. 19–20, pp. 1839–1844, 2008.
- [44] D. Soares Jr., "Fluid-structure interaction analysis by optimised boundary element-finite element coupling procedures," *Journal of Sound and Vibration*, vol. 322, no. 1–2, pp. 184–195, 2009.
- [45] D. Soares Jr., "Acoustic modelling by BEM-FEM coupling procedures taking into account explicit and implicit multi-domain decomposition techniques," *International Journal for Numerical Methods in Engineering*, vol. 78, no. 9, pp. 1076–1093, 2009.
- [46] D. Soares Jr., "An iterative time-domain algorithm for acoustic-elastodynamic coupled analysis considering meshless local Petrov-Galerkin formulations," *Computer Modeling in Engineering and Sciences*, vol. 54, no. 2, pp. 201–221, 2009.
- [47] D. Soares, "FEM-BEM iterative coupling procedures to analyze interacting wave propagation models: fluid-fluid, solid-solid and fluid-solid analyses," *Coupled Systems Mechanics*, vol. 1, pp. 19–37, 2012.
- [48] D. Soares Jr., "Coupled numerical methods to analyze interacting acoustic-dynamic models by multidomain decomposition techniques," *Mathematical Problems in Engineering*, vol. 2011, Article ID 245170, 28 pages, 2011.
- [49] J.-D. Benamou and B. Desprès, "A domain decomposition method for the Helmholtz equation and related optimal control problems," *Journal of Computational Physics*, vol. 136, no. 1, pp. 68–82, 1997.
- [50] A. Bendali, Y. Boubendir, and M. Fares, "A FETI-like domain decomposition method for coupling finite elements and boundary elements in large-size problems of acoustic scattering," *Computers & Structures*, vol. 85, no. 9, pp. 526–535, 2007.
- [51] D. Soares Jr., L. Godinho, A. Pereira, and C. Dors, "Frequency domain analysis of acoustic wave propagation in heterogeneous media considering iterative coupling procedures between the method of fundamental solutions and Kansa's method," *International Journal for Numerical Methods in Engineering*, vol. 89, no. 7, pp. 914–938, 2012.
- [52] D. Soares and L. Godinho, "An optimized BEM-FEM iterative coupling algorithm for acoustic-elastodynamic interaction analyses in the frequency domain," *Computers & Structures*, vol. 106–107, pp. 68–80, 2012.
- [53] L. Godinho and D. Soares, "Frequency domain analysis of fluid-solid interaction problems by means of iteratively coupled meshless approaches," *Computer Modeling in Engineering & Sciences*, vol. 87, no. 4, pp. 327–354, 2012.
- [54] L. Godinho and D. Soares, "Frequency domain analysis of interacting acoustic-elastodynamic models taking into account optimized iterative coupling of different numerical methods," *Engineering Analysis with Boundary Elements*, vol. 37, no. 7, pp. 1074–1088, 2013.
- [55] P. M. Gauzellino, F. I. Zyserman, and J. E. Santos, "Nonconforming finite element methods for the three-dimensional helmholtz equation: terative domain decomposition or global solution?" *Journal of Computational Acoustics*, vol. 17, no. 2, pp. 159–173, 2009.
- [56] J. P. A. Bastos and N. Ida, *Electromagnetics and Calculation of Fields*, Springer, New York, NY, USA, 1997.
- [57] J. M. Jin, J. Jin, and J. M. Jin, *The Finite Element Method in Electromagnetics*, Wiley, New York, NY, USA, 2002.
- [58] D. Soares Jr. and M. P. Vinagre, "Numerical computation of electromagnetic fields by the time-domain boundary element method and the complex variable method," *Computer Modeling in Engineering and Sciences*, vol. 25, no. 1, pp. 1–8, 2008.
- [59] L. Godinho, A. Tadeu, and P. Amado Mendes, "Wave propagation around thin structures using the MFS," *Computers, Materials and Continua*, vol. 5, no. 2, pp. 117–127, 2007.
- [60] L. Godinho, E. Costa, A. Pereira, and J. Santiago, "Some observations on the behavior of the method of fundamental solutions in 3d acoustic problems," *International Journal of Computational Methods*, vol. 9, no. 4, Article ID 1250049, 2012.
- [61] E. G. A. Costa, L. Godinho, J. A. F. Santiago, A. Pereira, and C. Dors, "Efficient numerical models for the prediction of acoustic wave propagation in the vicinity of a wedge coastal region," *Engineering Analysis with Boundary Elements*, vol. 35, no. 6, pp. 855–867, 2011.
- [62] W. F. Chen and D. J. Han, *Plasticity for Structural Engineers*, Spring, New York, NY, USA, 1988.
- [63] A. S. Khan and S. Huang, *Continuum Theory of Plasticity*, John Wiley & Sons, New York, NY, USA, 1995.
- [64] J. C. F. Telles, *The Boundary Element Method Applied to Inelastic Problems*, Spring, Berlin, Germany, 1983.
- [65] S. N. Atluri, *The Meshless Method (MLPG) for Domain & BIE Discretizations*, vol. 677, Tech Science Press, Forsyth, Ga, USA, 2004.

- [66] J. R. Xiao and M. A. McCarthy, "A local heaviside weighted meshless method for two-dimensional solids using radial basis functions," *Computational Mechanics*, vol. 31, no. 3-4, pp. 301–315, 2003.

Research Article

Experiment and Application of Market-Based Control for Engineering Structures

Gang Li,^{1,2} Wen Wang,¹ and Hong-Nan Li¹

¹ Faculty of Infrastructure Engineering, Dalian University of Technology, Dalian 116023, China

² Faculty of Infrastructure Engineering, Dalian University of Technology, Institute of Earthquake Engineering, 2 Linggong Road, Dalian, Liaoning 116024, China

Correspondence should be addressed to Gang Li; gli@dlut.edu.cn

Received 5 September 2013; Accepted 24 October 2013

Academic Editor: Delfim Soares Jr.

Copyright © 2013 Gang Li et al. This is an open access article distributed under the Creative Commons Attribution License, which permits unrestricted use, distribution, and reproduction in any medium, provided the original work is properly cited.

An experimental study on the vibration control of a single-degree-of-freedom model is carried out to verify market-based control (MBC) strategy effect. Results show that the MBC strategy can reduce both displacement and acceleration responses. Additionally, the MBC strategy is applied to a long-span bridge considering the travelling wave effect. Numerical simulations indicate that the displacement and acceleration responses of the long-span bridge with the travelling wave effect are smaller than those without, and the larger the velocity of travelling wave is, the better the control effect of MBC is. Based on the MBC theory and multimarket-based control (MMBC) presented here it is further applied to a large-space structure considering multiple dimensional features of structural model and ground motions. It is concluded that the MMBC strategy reduces the displacement response of the large-space structure, especially on vertical displacements, but has limited control effects on accelerations.

1. Introduction

The concept of structural control in civil engineering was first proposed in 1970s [1]. Since then, this technology has been developed greatly. According to the energy source (external or internal), structural control systems can be classified as passive, active, semiactive, or mixed control strategies. For active and semiactive control techniques, the control force is often determined by the control laws. Some typical control laws, that is, linear quadratic regulator (LQR), modal control, smart control, H_2 and H_∞ , and so forth, have become hot research topics rapidly in recent years [2–5]. For general structures, these control laws usually use a central computer responsible for the control of the entire system, but they exhibit limitation for large complex structures due to numerous degrees of freedom of the large complex structure. The market-based control (MBC) as a special control theory introduces the price mechanism of free market economy into the field of structural control in civil engineering. The MBC is developed based on an analogy between the relations of

control force-energy sources and those of supply-demand in the market economy. The optimal problem of control force from actuator is transformed to that of allocation resources in the market.

The MBC concept was proposed by Clearwater [6]. It was applied to solve the optimal decentralized control problem of complex dynamic systems, allocate and coordinate the actions of different mechatronic systems, and develop a multi-agent system for realizing the traffic intelligent control [7–9]. In addition, some prior research works about MBC used in various fields were carried out, such as the telecommunication, mechanism, and mission plan [10–12]. Application of the MBC in civil engineering to reduce the structural response under environmental loads has been carried out after the twenty first century [13–17].

However, previous researches mainly focused on ordinary structures, and few emphasized on applications of MBC in long-span and large-space structures. There are still existing problems in applications for these kinds of structures, such as travelling wave effect and multiple dimensions of

ground motion. The structural control technology in long-span structure have drawn many researchers' attention [18–21]. Because an earthquake excitation consists of superposition of a large number of waves carrying different characteristics, the different positions along a long-span structure are generally with different motions. Bridges as typical long-span structures; their control techniques considering multi-support and travelling seismic wave effects have been carried out by various researchers [22, 23]. These research results showed that control effect had an obvious distinction between uniform ground motion and differential ground motions. Large-space structures generally have thousands of degrees of freedoms and outstanding spatial characteristics; hence, multiple dimensional features, such as the spatial model and inputted ground motions, should be taken into account together. Additionally, theoretical researches have verified that the MBC is an effective control strategy, but experiments with the approach for model or actual structure have not been reported till now. Based on the above reason, a model test is carried out to validate the effectiveness of MBC in this paper, and the MBC strategy is applied to a long-span bridge considering the travelling wave effect and to a large-space structure considering multiple dimensional ground motion inputs, respectively.

2. Fundamental and Experiment

2.1. Basic Theory. The main objective of this study is to solve problems in structural control by the usage of MBC. In the MBC, power sources and controlled devices in a control system are abstracted to sellers and buyers in a free market. The relationship between the energy demand and supply in a control system corresponds to the supply-demand relation in the free market. The supply-demand relation is influenced by the equilibrium price, and the equilibrium price is certainly affected by the supply-demand relation in return. Take a virtual free market and single-degree-of-freedom system as an illustration to show the application of the MBC in structural control area.

The governing equation of motion for a SDOF system with controller can be expressed as

$$m\ddot{x}(t) + c\dot{x}(t) + kx(t) = -F(t) + U(t), \quad (1)$$

where $x(t)$, $\dot{x}(t)$, and $\ddot{x}(t)$ represent the displacement, velocity, and acceleration of the SDOF system, respectively; m and k are the system mass and stiffness, respectively; c denotes the viscous damping coefficient; $U(t)$ is the controlling force from the actuator; $F(t)$ is the environmental load.

The demand function J_D is determined by its energy consumption Q_D , energy price p , and responses of the dynamic system $Y(t)$; the sellers' supply function J_S is determined by its own original energy Q_S and energy price p . Buyers and sellers both pursue their maximum interests at any time. This process has to be restricted by commodity quantities Q_{\max} and virtual wealth W_{\max} . The relation is shown as follows:

$$\begin{aligned} \max J_S(Q_S, p) \quad & Q_S \leq Q_{\max}, \\ \max J_D(Q_{D1}, p, Y(t)) \quad & p \cdot Q_D \leq W_{\max}. \end{aligned} \quad (2)$$

In the free market, there is a general equilibrium rule between the supply and demand. The rule can be expressed as

$$Q_S = Q_D. \quad (3)$$

Actually, the supply-demand relation is a core of the overall MBC theory. There have been several mathematical models reflecting the supply-demand relation by now, such as linear-supply and linear-demand model [14], linear-supply and power-demand model [16], advanced linear-supply and power-demand model, and linear-supply and exponential-demand model [16]. Detailed introductions of these supply-demand models can be found in corresponding references. A simple relation of the supply function and price, linear model, is used here as

$$Q_S = \eta \cdot p(t). \quad (4)$$

And the advanced linear-supply and power-demand model (ALPM) demand function is chosen to depict the relation of the demand and price as

$$Q_D = \frac{W(t) |\alpha x(t) + \beta \dot{x}(t)|}{p(t)}, \quad (5)$$

where η is the parameter that reflects the energy supply, x and \dot{x} are the story-displacement and story-velocity of the structural system and α and β are the weighting coefficients.

Substituting (4) and (5) into (3), an equilibrium price is obtained through solving (3) at any time step. The distribution of scarce resources reaches maximized benefits under the equilibrium price. The solution of (3) is called the Pareto optimal solution in economics [13]. Then, the control force is written as

$$U(t) = -K \cdot \frac{W(t) \cdot (\alpha x(t) + \beta \dot{x}(t))}{p(t)}, \quad (6)$$

where K is the gain coefficient related to the actuator.

Substitute (6) into (1); the MBC is implemented in the structural vibration control.

2.2. Experiment. A single-degree-of-freedom of structural model is made of steel and organic glass plates. The organic glass plate is chosen to model the floor of structure, and steel plates are as structural elements for resisting lateral force. Two piezoelectric ceramic thin plates are affixed on the surface of steel plates, one of which named the PZT-1 is an exciting device at the beginning of experiment, and it becomes an actuator to control the structural response after the excitation and another of which named the PZT-2 is a collecting sensor for the structural response. The structural model and piezoelectric ceramic thin plates are shown in Figure 1 and their parameters are listed in Tables 1 and 2.

The model vibrates under the excitation by the PZT-1 at the beginning and the vibration makes the PZT-2 deformed and results in electric signals change. The response of structural model is obtained from collecting and processing the electric signals. The PZT-1 is an actuator during structural

TABLE 1: Parameters of the structural model.

Component	Mass (kg)	Size (mm)	Elastic modulus (Pa)	Number
Organic glass	0.496	$350 \times 120 \times 10$	—	2
Steel	0.471	$500 \times 120 \times 1$	2.06×10^{11}	2

TABLE 2: Parameters of the piezoelectric.

Piezoelectric ceramic	Size (mm)	Relative freedom dielectric constant		Piezoelectric constant (10^{-12}C/N)		
		ϵ_{T13}	ϵ_{T11}	D_{31}	D_{33}	D_{15}
PZT-1	$30 \times 40 \times 0.4$	1400	1550	160	350	500
PZT-2	$15 \times 15 \times 0.4$					

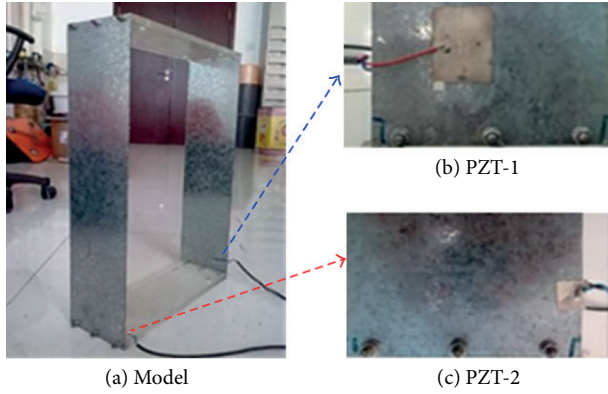


FIGURE 1: Structural model in test.

model vibration. The value of control force from the PZT-1 is calculated by the MBC strategy based on the structural response status from the PZT-2. The whole control process is shown in Figure 2.

Experimental devices include a PC with the MBC strategy, input and out control board, and piezoelectric driving device. All these devices are shown in Figures 3, 4, and 5.

The natural vibration frequency of model is 18.1 Hz through the swept-frequency method. When the frequency of the environmental load equals natural frequency of the model, the vibration response of the structural model reaches maximum value. Therefore, the exciting load is defined as

$$P(t) = \sin(18.1t). \quad (7)$$

Figures 6 and 7 show proportional acceleration and displacement responses of the structural model, respectively. The proportional acceleration is a signal measured directly from the PZT-2. It can be transferred to an absolute acceleration through multiplying a parameter related to the piezoelectric. In this study, the main objective of this experiment is focused on comparing the effectiveness of the MBC. Therefore, the proportional response is used here directly. It can be seen that the response of model controlled by the MBC has an obvious reduction than that of model with free vibration (FRE).

Figure 8 shows the relation of theoretical control force and time, which is equal to the ratio of actual force to gain coefficient. Figure 9 illustrates that the price has the same

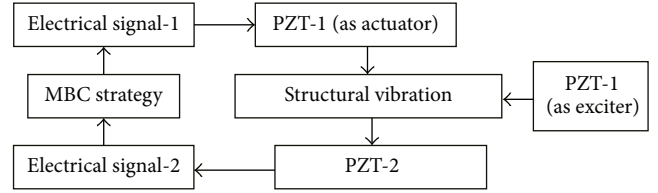


FIGURE 2: Experimental program.



FIGURE 3: Computer of control system.

changing trend as the theoretical control force in time history. The change regularity of price in the market is consistent with that of control force from actuator illustrated efficiency of the MBC algorithm.

3. Application of the MBC in Long-Span Bridges

3.1. Governing Equation considering the Multiple Support. The equation of motion for the bridge considering multi-support is written as

$$\begin{bmatrix} \mathbf{M}_{ss} & \mathbf{M}_{sb} \\ \mathbf{M}_{bs} & \mathbf{M}_{bb} \end{bmatrix} \begin{Bmatrix} \ddot{\mathbf{X}}_s \\ \ddot{\mathbf{X}}_b \end{Bmatrix} + \begin{bmatrix} \mathbf{C}_{ss} & \mathbf{C}_{sb} \\ \mathbf{C}_{bs} & \mathbf{C}_{bb} \end{bmatrix} \begin{Bmatrix} \dot{\mathbf{X}}_s \\ \dot{\mathbf{X}}_b \end{Bmatrix} + \begin{bmatrix} \mathbf{K}_{ss} & \mathbf{K}_{sb} \\ \mathbf{K}_{bs} & \mathbf{K}_{bb} \end{bmatrix} \begin{Bmatrix} \mathbf{X}_s \\ \mathbf{X}_b \end{Bmatrix} + \begin{Bmatrix} \mathbf{U}_s \\ \mathbf{U}_b \end{Bmatrix} = \begin{Bmatrix} \mathbf{P}_s \\ \mathbf{P}_b \end{Bmatrix}, \quad (8)$$



FIGURE 4: I/O interface board.



FIGURE 5: Piezoelectric driving power.

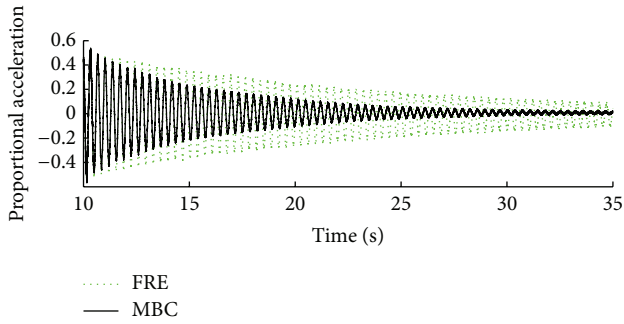


FIGURE 6: Acceleration time-history response curve.

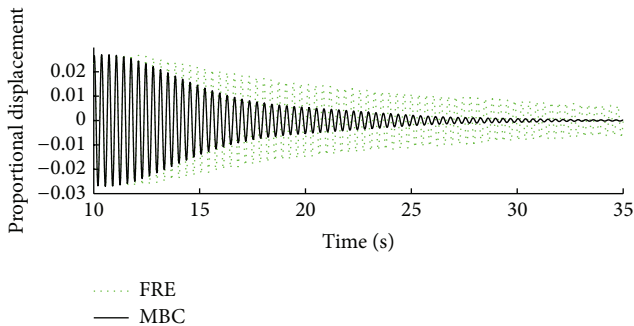


FIGURE 7: Displacement time-history response curve.

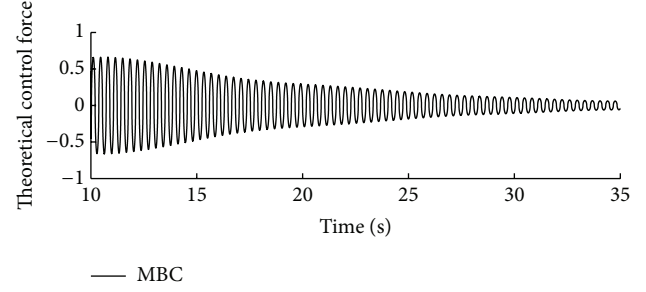


FIGURE 8: Control force time-history response curve.

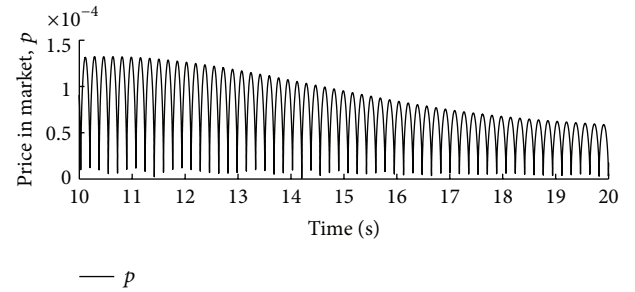


FIGURE 9: Price time-history response curve.

where \mathbf{M} , \mathbf{C} , and \mathbf{K} are the mass, damping, and stiffness matrices, respectively; \mathbf{U} and \mathbf{P} are the control force vectors from actuator and environmental force; $\ddot{\mathbf{X}}$, $\dot{\mathbf{X}}$, and \mathbf{X} are the absolute acceleration, velocity, and displacement response vectors, respectively. Subscripts s and b stand for the structure and the support. Equation (8) can be rearranged as

$$\mathbf{M}_{ss}\ddot{\mathbf{X}}_s + \mathbf{C}_{ss}\dot{\mathbf{X}}_s + \mathbf{K}_{ss}\mathbf{X}_s = \mathbf{P}_s - \mathbf{U}_s - \mathbf{M}_{sb}\ddot{\mathbf{X}}_b - \mathbf{C}_{sb}\dot{\mathbf{X}}_b - \mathbf{K}_{sb}\mathbf{X}_b. \quad (9)$$

The displacement \mathbf{X}_s is expressed by

$$\mathbf{X}_s = \mathbf{X}_{ds} + \mathbf{X}_{ss}, \quad (10)$$

where \mathbf{X}_{ds} and \mathbf{X}_{ss} are the dynamic response and the pseudostatic response. Additionally, for the pseudostatic response of the structure, there is the following relation:

$$\mathbf{X}_{ss} = -\mathbf{K}_{ss}^{-1}\mathbf{K}_{sb}\mathbf{X}_b = -\mathbf{R}\mathbf{X}_b, \quad (11)$$

where $\mathbf{R} = -\mathbf{K}_{ss}^{-1}\mathbf{K}_{sb}$. Substituting (10) and (11) to (9), there is

$$\begin{aligned} \mathbf{M}_{ss}\ddot{\mathbf{X}}_{ds} + \mathbf{C}_{ss}\dot{\mathbf{X}}_{ds} + \mathbf{K}_{ss}\mathbf{X}_{ds} \\ = \mathbf{P}_s - \mathbf{U}_s - (\mathbf{M}_{ss}\mathbf{R} + \mathbf{M}_{sb})\ddot{\mathbf{X}}_b - (\mathbf{C}_{ss}\mathbf{R} + \mathbf{C}_{sb})\dot{\mathbf{X}}_b. \end{aligned} \quad (12)$$

The damping item $(\mathbf{C}_{ss}\mathbf{R} + \mathbf{C}_{sb})\dot{\mathbf{X}}_b$ has little influence on structural responses and can be neglected. Equation (12) is then simplified to

$$\mathbf{M}_{ss}\ddot{\mathbf{X}}_{ds} + \mathbf{C}_{ss}\dot{\mathbf{X}}_{ds} + \mathbf{K}_{ss}\mathbf{X}_{ds} = \mathbf{P}_s - \mathbf{U}_s - (\mathbf{M}_{ss}\mathbf{R}_s + \mathbf{M}_{sb})\ddot{\mathbf{X}}_b. \quad (13)$$

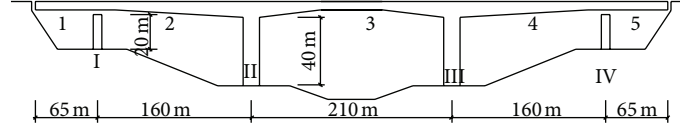


FIGURE 10: Schematic diagram of the long-span bridge.

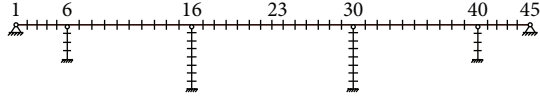


FIGURE 11: Finite element model of bridge.

TABLE 3: Parameters of MRD.

D (mm)	L (mm)	d (mm)	h (mm)	γ (Pa·s)	τ_{\max} (Pa)
250	500	100	2	1	50

3.2. Supply-Demand Relation Model. In this section, linear-supply and exponent model [16] was used as control function. The supply function is written as

$$Q_{S,i} = \eta_i \cdot p. \quad (14)$$

The demand function is expressed by

$$Q_{D,i} = W_i |\alpha_i x_{d,i} + \beta_i \dot{x}_{d,i}| \cdot e^{-c p}, \quad (15)$$

where η_i is the parameter that reflects the energy supply of i th actuator, \dot{x} and \ddot{x} are the relative displacement and velocity at ends of the i th actuator, α_i and β_i are the weighting coefficients, W_i is the initial wealth of the i th buyer, and p_j is the equivalent price of the i th actuator.

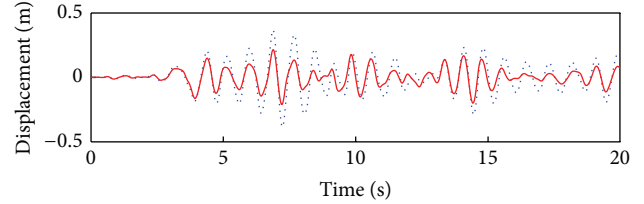
The equilibrium price p is solved through defining (14) and (15) equal. Then, control force of the i th actuator is expressed based on the price as follows:

$$U_i = \eta_i \cdot p. \quad (16)$$

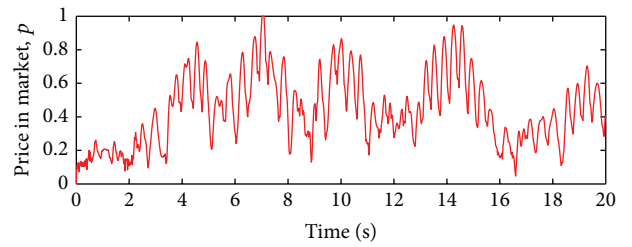
3.3. Numerical Example. A long-span bridge shown in Figure 10 has 660 meters length. Bidirectional sliding bearings are set on the abutments and continuous piers. In order to analyze the control effect of the long-span bridge under the earthquake using the MBC strategy, The Taft earthquake record (July 21, 1951, the acceleration peak value is adjusted to 400 gal) is selected as an environmental load.

Planar beam elements are used to simulate piers and beams of the bridge. The long-span bridge is modeled with 70 finite elements and 197 freedoms. Figure 11 shows finite element divisions and some typical nodes numbers for convenient expression.

32 Magnetorheological dampers (MRDs) are installed on the abutments, I and IV piers. The modified boundary Hrovat algorithm [21] is used here for numerical simulations. The maximum force from a MRD is 2000 kN. Table 3 shows parameters of these MRDs, where D is the cylinder



(a)



(b)

FIGURE 12: Displacement and price time history of no. 6 node.

diameter, L is the effective length of the piston, d is the diameter of the piston, h is the gap spacing, γ is the apparent viscosity of the liquid, and τ_{\max} is the maximum yield stress of the liquid.

The traveling wave speed as the known parameter is given during the dynamical time history analysis of the long-span bridge considering multiple supports. In order to find the rule of the response influenced by traveling wave, the velocities of traveling wave v_a are set at 400 ms^{-1} , 1000 ms^{-1} , 3000 ms^{-1} , and infinity.

Figure 12 shows the price and displacement time history of the no. 6 node with the travelling wave speed at 3000 ms^{-1} . It can be seen from these figures that (a) the MBC strategy reduces displacement responses; (b) the displacement changing trend is consistent with the price response in whole time phase. The phenomena of the energy demand increasing by the displacement and velocity are also inflected from (4). It also means that the energy supply also increases by the displacement because of energy demand equaling to energy supply. In addition, it can be drawn from (6) that energy supply is proportional to the equivalent price. Therefore, both the displacement and equivalent price have the same changing trend.

Figures 13 and 14 indicate that forces of MRDs are dependent on not only the displacement but also velocity.

In order to validate the effectiveness of the MBC with various travelling wave speed, the reduction rate is defined as

$$\gamma = \frac{x_0 - x}{x_0} \times 100\%, \quad (17)$$

where x_0 and x are responses of the bridge without and with actuators, respectively.

Figures 15 and 16 illustrate maximum displacement and acceleration comparisons of typical nodes with various traveling wave speeds. It is found that there are significant differences of the responses of bridge among these travelling wave speeds. For the bridge without control, the displacement and acceleration responses at these nodes grow with the increase of travelling waves speeds. The greater the travelling wave speed is, the larger the reduction rate becomes. Therefore, effectiveness of the structural control using the MBC without considering the travelling wave effect is superior to that with consideration.

4. Application of the MBC in Large Space Structures

4.1. Basic Theory. A free market, which is a large unity, usually consists of many submarkets. The equilibrium price of commodity in each submarket is formed depending on its own supply-demand relation. However, the price tendency of each submarket is toward the whole equilibrium price. Thus, the price of whole market is a dynamic “cobweb” model, and price of each submarket has more or less influence on the price of the whole market. This theory based on multiple submarkets is called the multiple market-based control (MMBC). The advantage of MMBC can realize the decentralized vibration control in the structural control area through the similarity between the submarket and substructure. In each substructure, the controlling force only depends on its own supply-demand relation. Only the supply and demand functions for the MMBC are introduced here, because the framework of MMBC is similar to that of the MBC.

The supply function of the k th seller in the j th submarket is expressed by

$$Q_{S,k,j} = \eta_{k,j} p_j. \quad (18)$$

The demand function of the i th buyer in the j th submarket can be written as

$$Q_{D,i,j} = \frac{W_{i,j} c_{i,j} |\alpha_{i,j} x_{d,i,j} + \beta_{i,j} \dot{x}_{d,i,j}|}{p_j}, \quad (19)$$

where $x_{d,i,j}$ and $\dot{x}_{d,i,j}$ are relative displacement and velocity of the i th seller in the j th substructure, respectively; $W_{i,j}$, $c_{i,j}$, $\alpha_{i,j}$, and $\beta_{i,j}$ are the initial wealth, demand coefficient, and weighting coefficients of the i th buyer in the j th submarket; p_j is the price in the j th submarket; $\eta_{k,j}$ is the parameter that reflects the k th seller in the j th submarket.

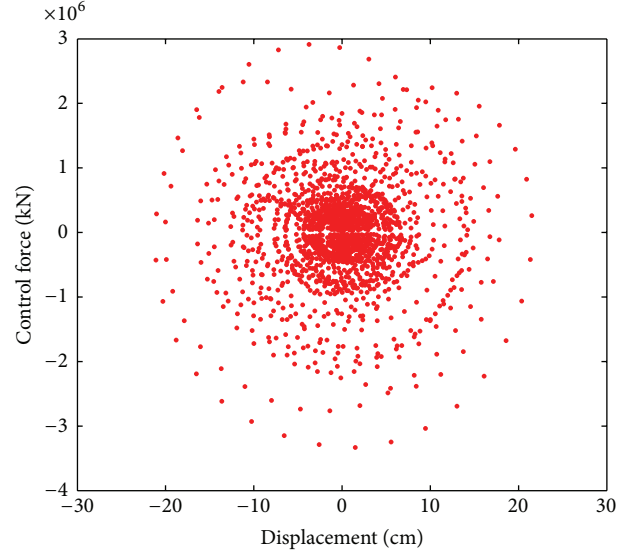


FIGURE 13: Control force versus displacement.

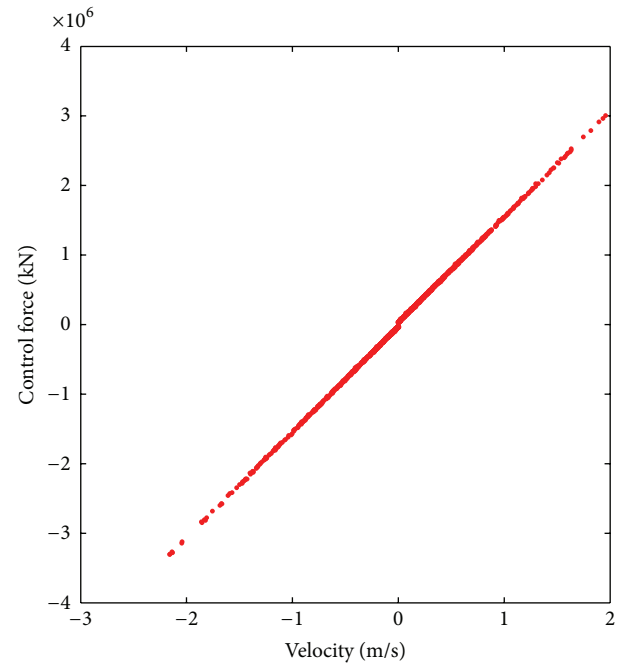


FIGURE 14: Control force versus velocity.

Then, supply-demand relationship of whole market can be written as

$$\sum_{j=1}^w \sum_{i=1}^r Q_{D,i,j} = \sum_{j=1}^w \sum_{k=1}^n Q_{S,k,j}, \quad (20)$$

where r is the number of the actuators, n is the number of energy demand sources, and w is the number of submarkets. The equilibrium price p_j is solved from (20) through iterations. The controlling force U_i is proportional to the energy

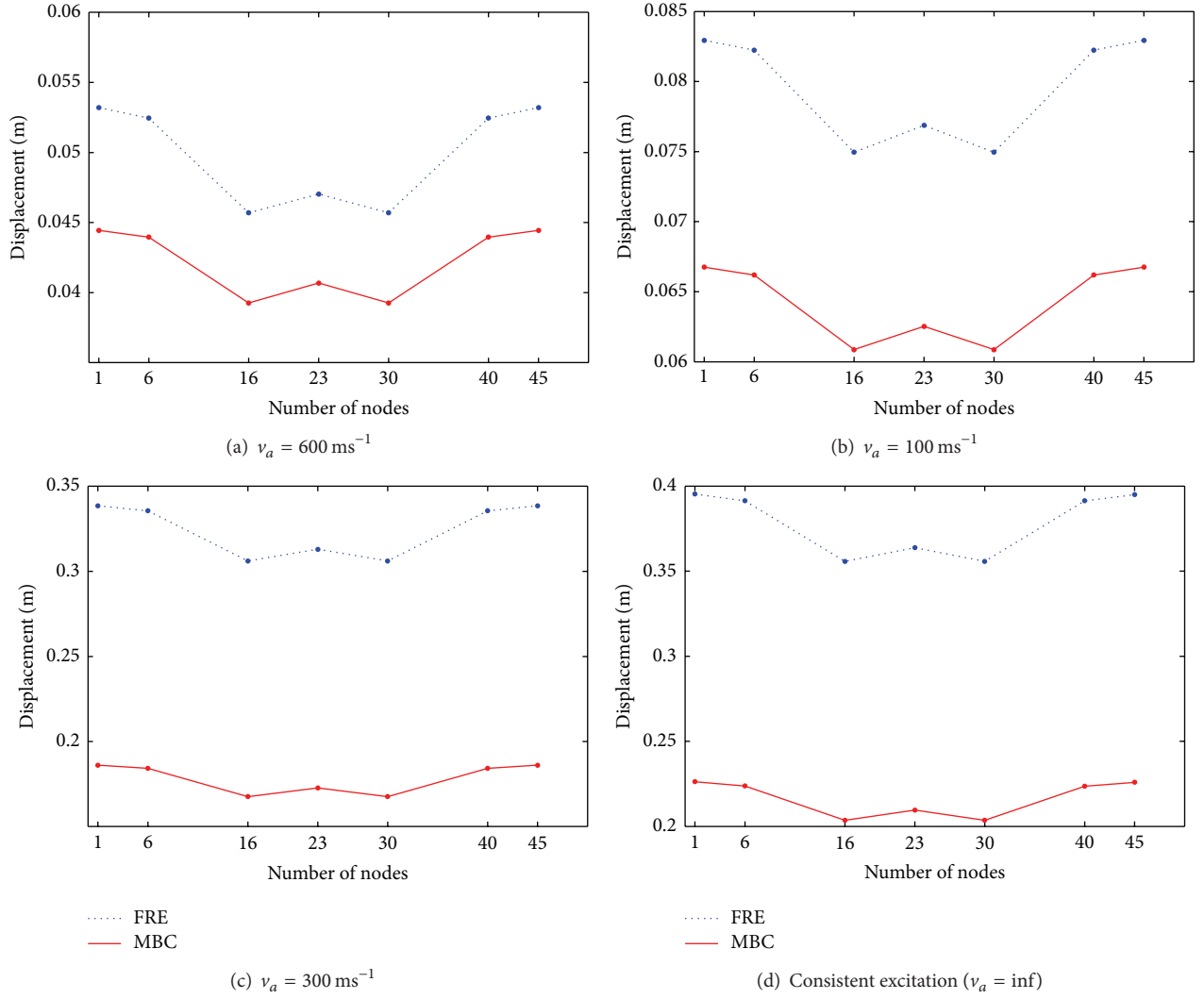


FIGURE 15: Displacement response with and without control at various velocities of travelling waves.

supply at the price p_j . The force from actuator can be drawn as

$$U_i = -K_{i,j} \frac{W_{i,j} c_{i,j} |\alpha_{i,j} x_{d,i,j} + \beta_{i,j} \dot{x}_{d,i,j}|}{p_j}, \quad (21)$$

where $K_{i,j}$ means the gain coefficient of controlling force from the i th actuator of j th substructure. Substituting (21) into the structure dynamic equation, application of the MMBC to structure may be realized.

4.2. Numerical Example. A reticulated shell structure (RSS) with 40 m span, 8 m high and 5 span-height ratio is shown in Figure 17. It has four support positions at node Number 127, 140, 151, and 163. The RSS consists of two kinds of circular 4 mm thick steel tubes: one is 133 mm in diameter; another is 140 mm in diameter. The first one is used for string bar elements of RSS and the second is adopted for support bars. In order to validate the effectiveness of MMBC for the large-space structure in three dimensions, a 3-dimensional finite

element model is established and the El Centro earthquake record (NS, May 18, 1940, the acceleration peak value is adjusted to 400 gal) is inputted in the RSS along X, Y, and Z directions. The MRDs are installed at node Number 133, 145, 157, and 169 shown in Figure 17. There are three MRDs, each is aligned with X, Y, and Z directions at each nodal position. The RSS is distributed into three substructures named as the *substructure-X*, *substructure-Y*, and *substructure-Z* for the MMBC strategy application.

Figures 18 and 19 illustrate displacement and acceleration time history responses of the RSS with and without control. Tables 4 and 5 show the maximum response and reduction rate of typical nodes. It is obviously found from the above figures and tables that the displacement response can be controlled effectively, especially on the displacement in Z direction. However, the effectiveness of the acceleration controlling is limited. The reason is that the deformation of the RSS in Z direction is larger than that in X and Y directions, and the acceleration response is not sensitive to such flexible RSS.

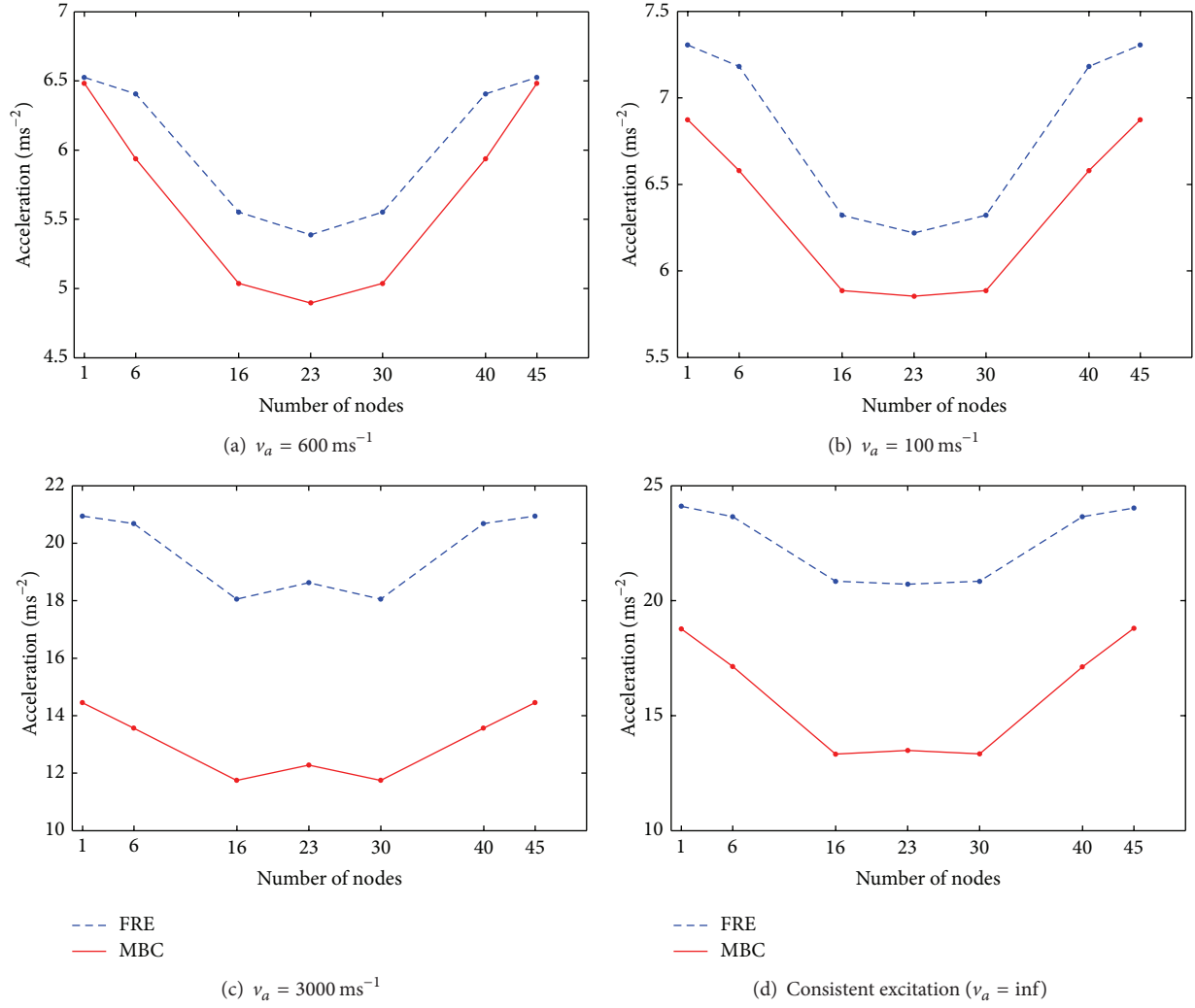


FIGURE 16: Acceleration response with and without control at various velocities of travelling waves.

TABLE 4: Maximum displacement response and reduction of typical nodes.

Nodes	Displacement (mm)			Reduction γ_d (%)		
	X	Y	Z	X	Y	Z
1	2.16/1.88	1.53/1.28	5.50/3.72	12.9	15.9	32.3
9	2.14/1.86	1.41/1.19	5.94/4.15	12.9	15.8	30.1
25	2.01/1.77	1.22/1.04	7.68/5.91	12.1	15.2	23.1
27	2.03/1.86	1.45/1.19	5.67/4.42	8.8	18.3	22.1
52	2.98/2.36	2.26/1.84	4.26/3.67	20.9	18.5	13.9
85	4.39/3.74	4.95/3.71	7.59/7.11	14.8	25.1	6.4
127	6.61/6.07	6.36/5.96	10.3/9.53	8.2	6.4	7.7

Figures 20 and 21 show the price and control force time history of three various substructures. Since the price p is a function of supply-demand model and responses of the RSS, it varies from different submarkets. In addition, the same regularity and changing trend between displacement and price in each substructure also is observed from these figures.

5. Concluding Remarks

In this paper, a vibration control experiment is carried out to validate the MBC effectiveness. The MBC is then applied to a long-span bridge considering the travelling wave effect. On the basis of MBC theory, the MMBC is presented here and applied to a large-space structure, taking into account

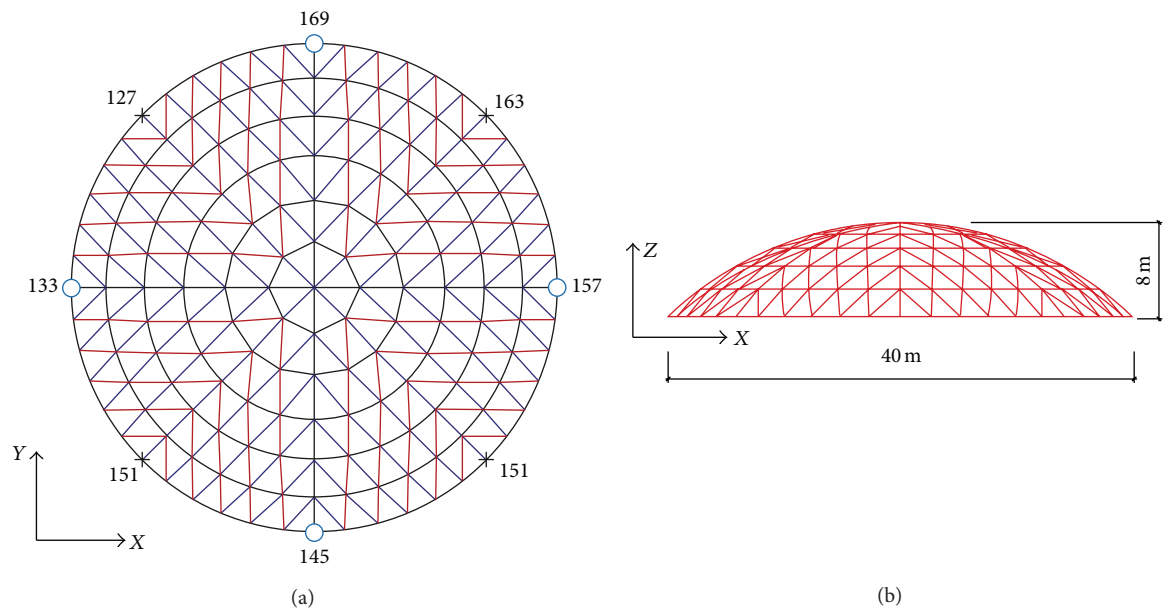


FIGURE 17: Reticulated shell structure model.

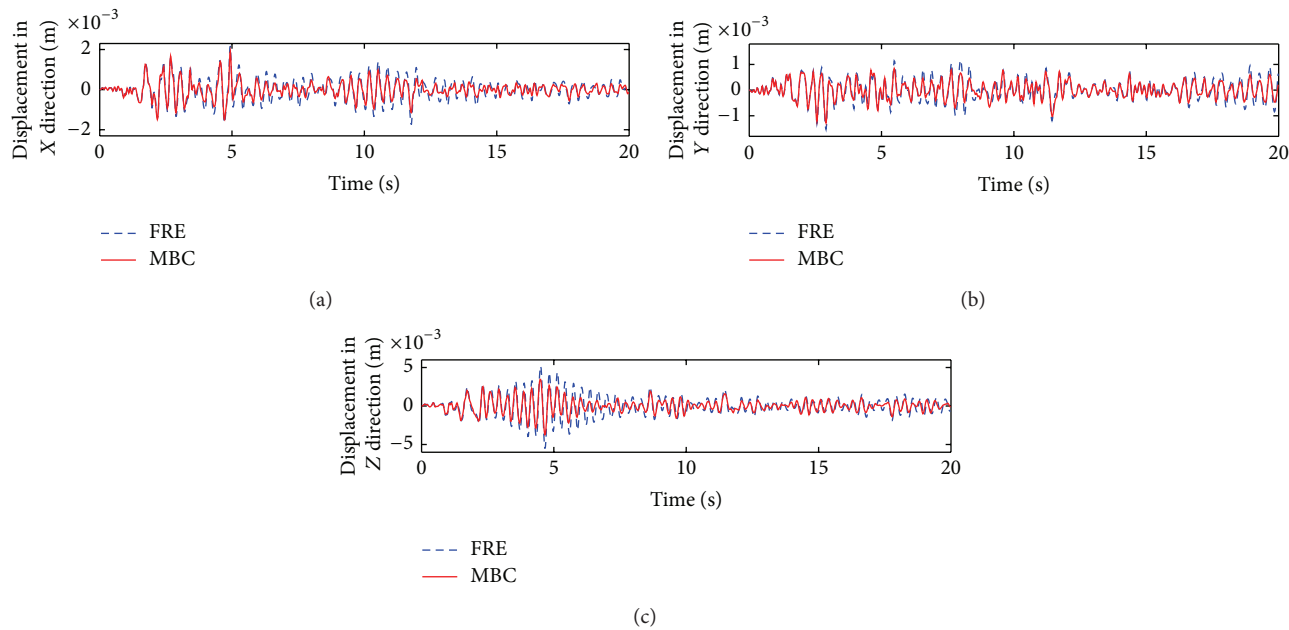


FIGURE 18: Displacement time history.

TABLE 5: Maximum acceleration response and reduction of typical nodes.

Nodes	Displacement (ms^{-2})			Reduction γ_a (%)		
	X	Y	Z	X	Y	Z
1	4.95/4.90	5.19/5.21	4.56/4.38	0.9	-0.3	3.9
9	4.99/4.30	5.23/5.26	5.09/4.89	1.1	-0.4	3.8
25	5.11/5.06	5.17/5.18	5.95/5.71	1.1	-0.3	4.0
27	5.29/5.23	5.09/5.11	5.03/4.84	1.0	-0.2	3.6
52	5.46/5.46	4.95/4.90	5.65/5.56	0.0	0.9	1.5
85	5.26/5.20	4.92/4.97	9.42/6.97	1.2	-1.1	4.8
127	6.31/5.86	7.08/6.61	10.2/9.32	7.1	6.6	8.3

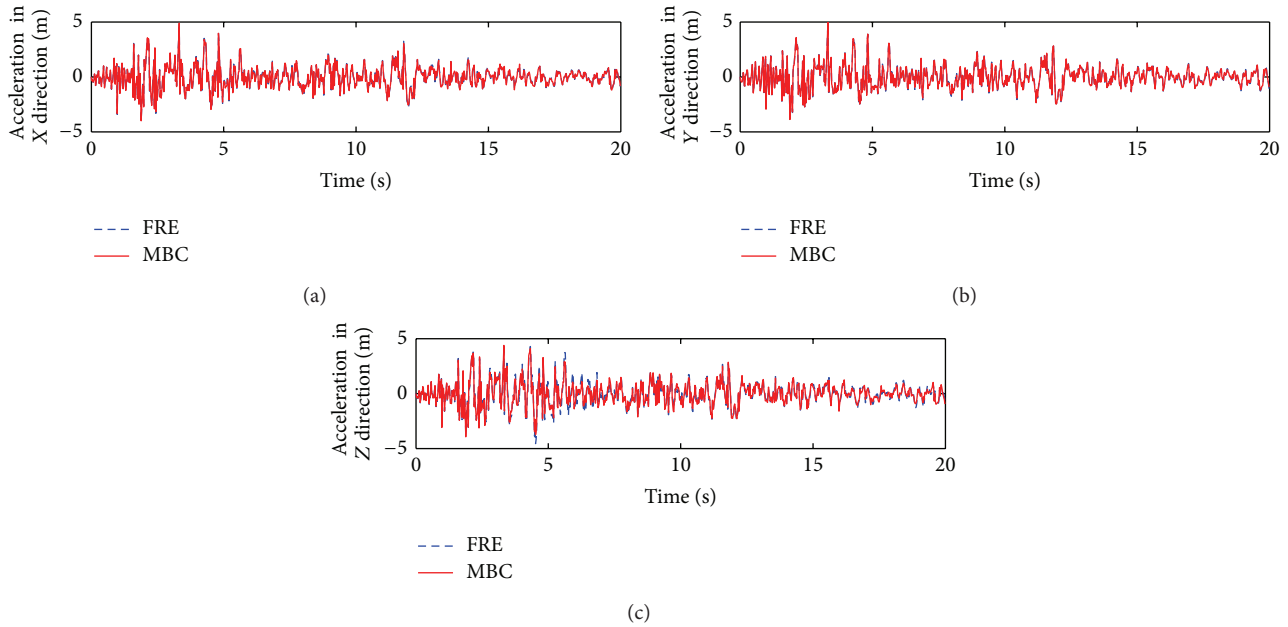


FIGURE 19: Acceleration time history.

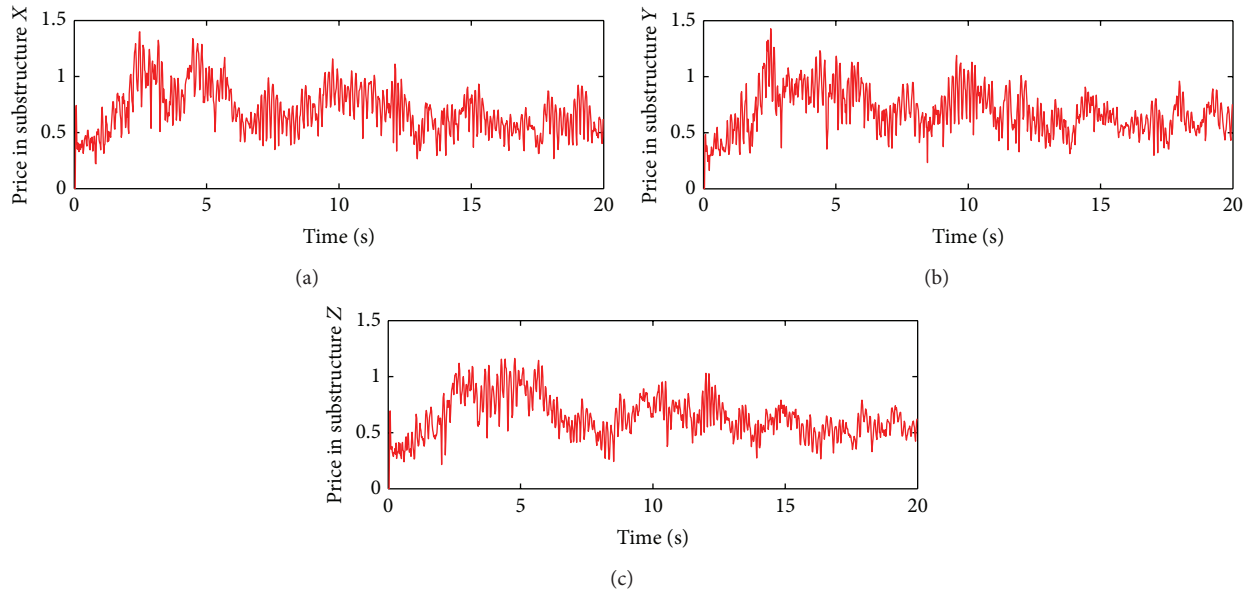


FIGURE 20: Price time history of substructure.

the multiple dimensions of ground motions. The following conclusions are drawn in this study.

- (1) The experiment validates that the MBC is an effective control strategy offering significant controlling force and value to be applied in actual structures.
- (2) The travelling wave effect has a distinct influence on responses of the long-span bridge. The MBC strategy can reduce displacement and acceleration responses of the bridge both with and without the travelling wave effects. The greater the velocity of travelling wave of ground motion is, the larger the response of

bridge is and the better the control effect is. Therefore, it is necessary to take the travelling wave effect into consideration during the analysis of vibration control of long-span structure using the MBC.

- (3) As the large-space structure is commonly flexible, especially in the vertical direction, the multiple dimensional responses and control effect of this kind of structure have to be considered. Numerical results have indicated that the displacement response of the large-space structure in the vertical direction are usually larger than those in horizontal directions, and

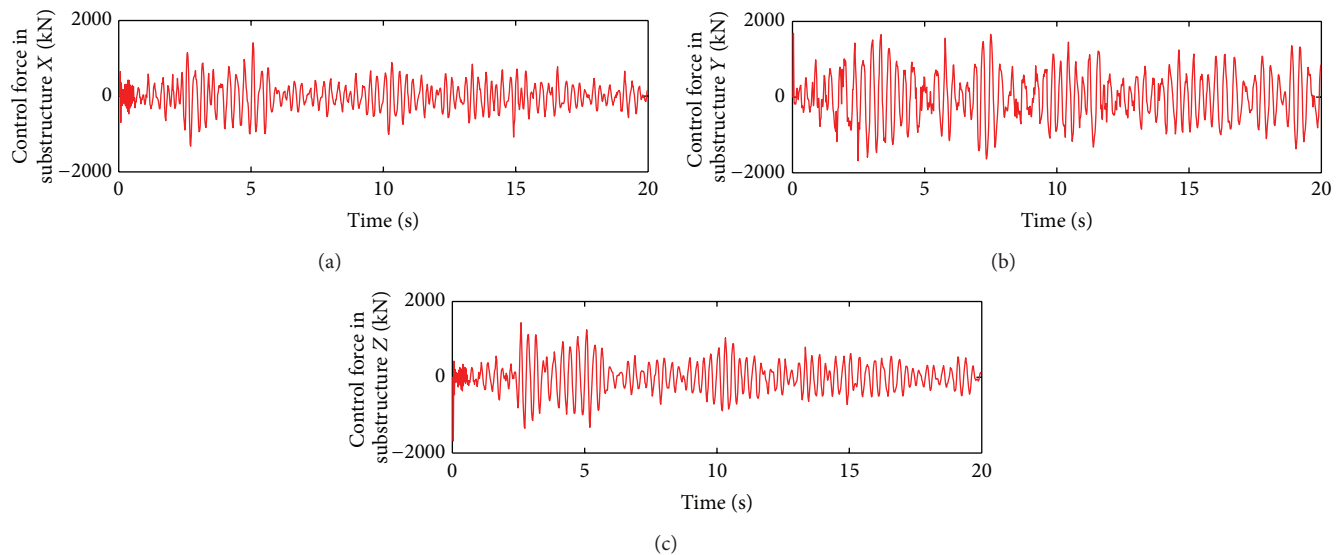


FIGURE 21: Control force time history of substructures.

the MMBC has better control effect on the displacement response than the acceleration response.

Conflict of Interests

The authors declare that there is no conflict of interests regarding the publication of this paper.

Acknowledgments

This research work was jointly supported by the Natural Science Foundation of China (Grants no. 50808036, 91215302) and the Science Fund for Creative Research Groups of the National Natural Science Foundation of China (Grant no. 51121005).

References

- [1] J. T. P. Yao, "Concept of structural control," *ASCE Journal of the Structural Division*, vol. 98, no. 7, pp. 1567–1574, 1972.
- [2] T. T. Soong, *Active Structure Control Theory and Practice*, Longman Scientific & Technical, New York, NY, USA, 1990.
- [3] J. N. Yang, J. C. Wu, and A. K. Agrawal, "Sliding Model control for nonlinear and hysteretic structures," *ASCE Journal of Engineering Mechanics*, vol. 121, no. 12, pp. 1330–1339, 1995.
- [4] L. Huo, G. Song, H. Li, and K. Grigoriadis, " H_∞ robust control design of active structural vibration suppression using an active mass damper," *Smart Materials and Structures*, vol. 17, no. 1, Article ID 015021, pp. 15–21, 2008.
- [5] A. S. Ahlawat and A. Ramaswamy, "Multiobjective optimal structural vibration control using fuzzy logic control system," *ASCE Journal of Structural Engineering*, vol. 127, no. 11, pp. 1330–1337, 2001.
- [6] S. Clearwater, *Market-Based Control: A Paradigm for Distributed Resource Allocation*, World Scientific Publishing, Singapore, 1996.
- [7] H. Voos, "Market-based algorithms for optimal decentralized control of complex dynamic systems," in *Proceedings of the 38th IEEE Conference on Decision and Control (CDC '99)*, pp. 3295–3296, Phoenix, Ariz, USA, December 1999.
- [8] W. B. Jackson, C. Mochon, S. K. Van et al., "Distributed allocation using analog market wire computation and communication," in *Proceedings of the 7th Mechatronics Forum International Conference*, Atlanta, Ga, USA, September 2000.
- [9] K. Prouskas, A. Patel, J. Pitt, and J. Barria, "A multi-agent for intelligent network load control using a market-based approach," in *Proceedings of the 4th International Conference on Multi-Agent Systems (ICMAS '00)*, pp. 231–238, IEEE Computer Society, Boston, Mass, USA, July 2000.
- [10] T. Alpcan, T. Başar, R. Srikant, and E. Altman, "CDMA uplink power control as a noncooperative game," in *Proceedings of the 40th IEEE Conference on Decision and Control (CDC '01)*, pp. 197–202, Orlando, Fla, USA, December 2001.
- [11] J. E. Hilland, R. R. Wessen, D. Porter, and R. S. Austin, "A market-based conflict resolution approach for satellite mission planning," *IEEE Transactions on Engineering Management*, vol. 48, no. 3, pp. 272–281, 2001.
- [12] M. Bernardine and A. Stents, "Comparative study between centralized, market-based, and behavioral multi-robot coordination," in *Proceedings of the 2003 IEEE/RSL International Conference on Intelligent Robots and Systems*, pp. 2297–2303, Las Vegas, Nev, USA, October 2003.
- [13] J. P. Lynch and K. H. Law, "Market-based control of linear structural systems," *Earthquake Engineering and Structural Dynamics*, vol. 31, no. 10, pp. 1855–1877, 2002.
- [14] J. P. Lynch and K. H. Law, "Energy market-based control of linear civil structures," in *Proceedings of the US-Korea Workshop on Smart Structural Systems*, Pusan, Korea, 2002.
- [15] L. Huo and H. Li, "Control law for market-based semi-active timed liquid column dampers," *Chinese Journal of Applied Mechanics*, vol. 22, no. 1, pp. 71–75, 2005.
- [16] Y. Li, *Structural vibration control using MBC strategy [M.S. thesis]*, Dalian University of Technology, 2007.

- [17] G. Li, Q. Liu, and H. Li, "Inelastic structural control based on MBC and FAM," *Mathematical Problems in Engineering*, vol. 2011, Article ID 460731, 18 pages, 2011.
- [18] H. J. Jung, B. F. Spencer Jr., and I. W. Lee, "Control of seismically excited cable-stayed bridge employing magnetorheological fluid dampers," *ASCE Journal of Structural Engineering*, vol. 129, no. 7, pp. 873–883, 2003.
- [19] M. D. Symans and S. W. Kelly, "Fuzzy logic control of bridge structures using intelligent semi-active seismic isolation systems," *Earthquake Engineering & Structural Dynamics*, vol. 28, no. 1, pp. 37–60, 1999.
- [20] S. J. Moon, L. A. Bergman, and P. G. Voulgaris, "Sliding mode control of cable-stayed bridge subjected to seismic excitation," *Journal of Engineering Mechanics*, vol. 129, no. 1, pp. 71–78, 2003.
- [21] J. P. Ou, *Structural Vibration Control-Active, Semi-Active and Smart Control*, Science Press, Beijing, China, 2003.
- [22] S. M. Allam and T. K. Datta, "Seismic behaviour of cable-stayed bridges under multi-component random ground motion," *Engineering Structures*, vol. 21, no. 1, pp. 62–74, 1999.
- [23] K. Soylik, "Comparison of random vibration methods for multi-support seismic excitation analysis of long-span bridges," *Engineering Structures*, vol. 26, no. 11, pp. 1573–1583, 2004.

Research Article

The Numerical Solution of Linear Sixth Order Boundary Value Problems with Quartic B-Splines

Mingzhu Li,^{1,2} Lijuan Chen,¹ and Qiang Ma²

¹ School of Science, Qingdao Technological University, Qingdao 266033, China

² Department of Mathematics, Harbin Institute of Technology at Weihai, Weihai 264209, China

Correspondence should be addressed to Qiang Ma; hitmaqiang@hotmail.com

Received 8 September 2013; Accepted 16 November 2013

Academic Editor: Luís Godinho

Copyright © 2013 Mingzhu Li et al. This is an open access article distributed under the Creative Commons Attribution License, which permits unrestricted use, distribution, and reproduction in any medium, provided the original work is properly cited.

A quartic B-spline method is proposed for solving the linear sixth order boundary value problems. The method converts the boundary problem to solve a system of linear equations and obtains coefficients of the corresponding B-spline functions. The method has the convergence of two order. It develops not only the quartic spline approximate solution but also the higher order approximate derivatives. Two numerical examples are presented to verify the theoretical analysis and show the validity and applicability of the method. Compared with other existing recent methods, the quartic B-spline method is a more efficient and effective tool.

1. Introduction

In the paper, we consider the linear sixth order boundary value problems (6BVP) of the form:

$$y^{(6)}(x) + f(x)y(x) = g(x), \quad (1)$$

subject to the conditions

$$\begin{aligned} y(a) &= A_0, & y'(a) &= A_1, & y''(a) &= A_2, \\ y(b) &= B_0, & y'(b) &= B_1, & y''(b) &= B_2, \end{aligned} \quad (2)$$

where $f(x)$ and $g(x)$ are continuous functions on $[a, b]$, and A_i ($i = 0, 1, 2$) and B_i ($i = 0, 1, 2$) are given finite real constants. Many mathematical models arising in various applications can be written as boundary value problems. One such problem is the sixth boundary value problem which plays an important role in astrophysics and the narrow convecting layers bounded by stable layers [1–4]. Further discussion of sixth order boundary value problems is given in [5, 6] and in a book by Chandrasekhar [7]. Theorems that list conditions for the existence and uniqueness of solution of such type of boundary value problems can be found in the book written by Agarwal [8]. However, it is

difficult to obtain the analytic solutions of (1)-(2). Therefore, the availability of numerical method for this problem is of practical importance.

Over the years, there are several authors who worked on this type of boundary value problems by using different methods. For example, finite difference method was developed by Boutayeb and Twizell [2, 3, 9]. A modified form of the decomposition method was established by Wazwaz [10] and used to solve such BVPs [11]. Sinc-Galerkin method, variational iteration method, and homotopy perturbation method were developed to study the same problem [12–14]. Spline functions have been also used to construct efficient and accurate numerical methods for solving boundary value problems. For example, Siddiqi and Akram solved the same boundary value problems by using different splines such as quintic splines, septic splines, and nonpolynomial splines [15–17]. Loghmani and Viswanadham used sixth and septic B-spline functions to solve sixth order boundary value problems [18, 19]. Instead of the above two ways, other differential spline collocation methods can also be used [20–22].

It is well known that the quartic B-spline has been widely applied for the approximation solution of boundary value problems. Caglar used quartic B-spline to solve the linear cubic order boundary value problem [23]. Besides, quartic

B-spline was also used to solve fifth order boundary value problems and the obstacle problems [24, 25]. Our method is based on quartic B-spline interpolation. It is second order convergent and with lower computational cost. Moreover, we also can get the approximate derivative values of $y^{(k)}(x)$ ($k = 1, 2, 3, 4, 5$) at the knots. This is another advantage of our method, since some methods cannot obtain those results.

This paper is arranged as follows. In Section 2, the definition of quintic B-splines has been described and some preliminary results of quartic B-spline interpolation have been presented. In Section 3, we mainly give the quartic B-spline solution of linear sixth-order boundary value problems based on the results. In Section 4, the convergence of the method has been demonstrated. In Section 5, numerical examples of linear boundary value problems are presented, which illustrate the performance of this method.

2. Quartic B-Spline

2.1. Definition of Quartic B-Spline. For an interval $[a, b] \subset \mathbb{R}$, we introduce a set of equally spaced knots of partition $\Omega = \{x_0, x_1, \dots, x_n\}$, and we assume that $n \geq 5$, $x_i = a + ih$ ($i = 0, 1, \dots, n$), $x_0 = a$, $x_n = b$.

Let $S_4[\pi]$ be the space of continuously differentiable, piecewise, quartic-degree polynomials on π . Consider the B-splines basis in $S_4[\pi]$. A detailed description of B-spline functions generated by subdivision can be founded in [26].

The zero degree B-spline is defined as

$$N_{i,0}(x) = \begin{cases} 1, & x \in [x_i, x_{i+1}], \\ 0, & \text{otherwise,} \end{cases} \quad (3)$$

and for positive constant p , it is defined in the following recursive form:

$$N_{i,p}(x) = \frac{x - x_i}{x_{i+p} - x_i} N_{i,p-1}(x) + \frac{x_{i+p+1} - x}{x_{i+p+1} - x_{i+1}} N_{i+1,p-1}, \quad (4)$$

$$p \geq 2.$$

We apply this recursion to get the quartic B-spline $N_{i,4}(x)$ ($i = -2, -1, \dots, n+1$); it is defined in $S_4[\pi]$ as follows:

$$N_{i,4}(x) = \frac{1}{24h^4} \begin{cases} (x - x_{i-2})^4, & x \in [x_{i-2}, x_{i-1}], \\ (x - x_{i-2})^4 - 5(x - x_{i-1})^4, & x \in [x_{i-1}, x_i], \\ (x - x_{i-2})^4 - 5(x - x_{i-1})^4 + 10(x - x_i)^4, & x \in [x_i, x_{i+1}], \\ (x - x_{i+3})^4 - 5(x - x_{i+2})^4, & x \in [x_{i+1}, x_{i+2}], \\ (x - x_{i+3})^4, & x \in [x_{i+2}, x_{i+3}], \\ 0, & \text{otherwise.} \end{cases} \quad (5)$$

The properties of quartic B-spline functions:

(1) compact supported:

$$N_{i,4}(x) = \begin{cases} \geq 0, & x \in [x_{i-2}, x_{i+3}], \\ 0, & \text{otherwise.} \end{cases} \quad (6)$$

TABLE 1: The values of $N_{i,4}^{(k)}(x)$ at the knots.

	x_{i-1}	x_i	x_{i+1}	x_{i+2}	Otherwise
$N_{i,4}(x)$	1/24	11/24	11/24	1/24	0
$N'_{i,4}(x)$	1/6h	3/6h	-3/6h	-1/6h	0
$N''_{i,4}(x)$	1/2h ²	-1/2h ²	-1/2h ²	1/2h ²	0
$N'''_{i,4}(x)$	1/h ³	-3/h ³	3/h ³	-1/h ³	0

(2) Normalization: $\sum_{i=-2}^{n+1} N_{i,4}(x) = 1$.

(3) Translation invariance: $N_{i,4}(x) = N_{0,4}(x - (i-1)h)$ ($i = -2, -1, \dots, n+1$).

(4) Derivation formula: $N_{i,4}^{(k)}(x) = (4!/(4-k)!) \sum_{j=1}^n \alpha_{k,j} N_{i+j,4-k}$, where

$$\alpha_{0,0} = 1,$$

$$\alpha_{k,0} = \frac{\alpha_{k-1,0}}{x_{i+3-k} - x_i}, \quad (7)$$

$$\alpha_{k,k} = \frac{-\alpha_{k-1,k-1}}{x_{i+5} - x_{i+k}},$$

$$\alpha_{k,j} = \frac{\alpha_{k-j,j} - \alpha_{k-1,j-1}}{x_{i+j+5-k} - x_{i+j}}.$$

By some trivial computations, we can obtain the value of $N_{i,4}^{(k)}(x)$ ($i = -2, -1, \dots, n+1$, $k = 0, 1, 2, 3$) at the knots, which are listed in Table 1.

2.2. Quartic B-Spline Interpolation. For a given function $y(x)$ (assuming to be sufficiently smooth), there exists a unique quartic B-spline $s(x) = \sum_{i=-2}^{n+1} c_i N_{i,4}(x)$ satisfying the interpolation conditions

$$s(x_i) = y(x_i), \quad (i = 0, 1, \dots, n),$$

$$s'(a) = y'(a), \quad s''(a) = y''(a), \quad (8)$$

$$s'(b) = y'(b), \quad s''(b) = y''(b).$$

For $j = 0, 1, \dots, n$, let $y_j = s(x_j) = y(x_j)$, $P_j = s'(x_j)$, $Q_j = s''(x_j)$, and $R_j = s^{(3)}(x_j)$ for short. Through a simple calculation by Table 1, we have

$$y_j = \sum_{i=-2}^{n+1} c_i N_{i,4}(x_j) = \frac{1}{24} (c_{j-2} + 11c_{j-1} + 11c_j + c_{j+1}), \quad (9)$$

$$P_j = \sum_{i=-2}^{n+1} c_i N'_{i,4}(x_j) = \frac{1}{6h} (-c_{j-2} - 3c_{j-1} + 3c_j + c_{j+1}), \quad (10)$$

$$Q_j = \sum_{i=-2}^{n+1} c_i N''_{i,4}(x_j) = \frac{1}{2h^2} (c_{j-2} - c_{j-1} - c_j + c_{j+1}), \quad (11)$$

$$R_j = \sum_{i=-2}^{n+1} c_i N'''_{i,4}(x_j) = \frac{1}{h^3} (-c_{j-2} + 3c_{j-1} - 3c_j + c_{j+1}). \quad (12)$$

So, we get

$$\begin{aligned} & \frac{h}{4} (P_{j-2} + 11P_{j-1} + 11P_j + P_{j+1}) \\ &= -y_{j-2} - 3y_{j-1} + 3y_j + y_{j+1}, \\ & \frac{h^2}{12} (Q_{j-1} + 10Q_j + Q_{j+1}) = y_{j-1} - 2y_j + y_{j+1}, \\ & \frac{h^3}{24} (R_{j-2} + 11R_{j-1} + 11R_j + R_{j+1}) \\ &= -y_{j-2} + 3y_{j-1} - 3y_j + y_{j+1}. \end{aligned} \quad (13)$$

Using operator notation in [27, 28], we obtain

$$\begin{aligned} P_j &= \frac{4}{h} \left(\frac{-E^{-2} - 3E^{-1} + 3I + E}{E^{-2} + 11E^{-1} + 11I + E} \right) y_j, \\ Q_j &= \frac{12}{h^2} \left(\frac{E^{-1} - 2I + E}{E^{-1} + 10I + E} \right) y_j, \\ R_j &= \frac{24}{h^3} \left(\frac{-E^{-2} + 3E^{-1} - 3I + E}{E^{-2} + 11E^{-1} + 11I + E} \right) y_j, \end{aligned} \quad (14)$$

where the operators are defined $Ey(x) = y(x+h)$, $Dy(x) = y'(x)$, and $Iy(x) = y(x)$. Let $E = \exp(hD)$ and expand them in powers of hD ; we get

$$\begin{aligned} y'(x_j) &= P_j - \frac{1}{720} h^4 y^{(5)}(x_j) + O(h^6), \\ y''(x_j) &= Q_j + \frac{1}{240} h^4 y^{(6)}(x_j) + O(h^6), \\ y'''(x_j) &= R_j - \frac{1}{12} h^2 y^{(5)}(x_j) + \frac{1}{240} h^4 y^{(7)}(x_j) + O(h^6). \end{aligned} \quad (15)$$

We can use R_j to construct numerical difference formula for $y^{(4)}(x_j)$, $y^{(5)}(x_j)$, and $y^{(6)}(x_j)$ ($j = 1, 2, \dots, n-1$) by the Taylor series expansion as follows:

$$y^{(4)}(x_j) = \frac{R_{j+1} - R_{j-1}}{2h} + O(h^2), \quad (16)$$

$$y^{(5)}(x_j) = \frac{R_{j+1} - 2R_j + R_{j-1}}{h^2} + O(h^2), \quad (17)$$

$$\begin{aligned} y^{(6)}(x_j) &= \left(\left(\frac{R_{j+2} - R_j}{2h} - 2 \frac{R_{j+1} - R_{j-1}}{2h} \right. \right. \\ &\quad \left. \left. + \frac{R_j - R_{j-2}}{2h} \right) \times (h^2)^{-1} \right) + O(h^2), \\ &= \frac{R_{j+2} - 2R_{j+1} + 2R_{j-1} - R_{j-2}}{2h^3} + O(h^2). \end{aligned} \quad (18)$$

Substituting (9)–(12) into (15)–(18) yields

$$\begin{aligned} y'(x_j) &= \frac{1}{6h} (-c_{j-2} - 3c_{j-1} + 3c_j + c_{j+1}) + O(h^4), \\ y''(x_j) &= \frac{1}{2h^2} (c_{j-2} - c_{j-1} - c_j + c_{j+1}) + O(h^4), \\ y'''(x_j) &= \frac{1}{h^3} (-c_{j-2} + 3c_{j-1} - 3c_j + c_{j+1}) + O(h^2), \\ y^{(4)}(x_j) &= \frac{1}{2h^4} (c_{j-3} - 3c_{j-2} + 2c_{j-1} + 2c_j \\ &\quad - 3c_{j+1} + c_{j+2}) + O(h^2), \\ y^{(5)}(x_j) &= \frac{1}{h^5} (-c_{j-3} + 5c_{j-2} - 10c_{j-1} + 10c_j \\ &\quad - 5c_{j+1} + c_{j+2}) + O(h^4), \\ y^{(6)}(x_j) &= \frac{1}{2h^6} (c_{j-4} - 5c_{j-3} + 9c_{j-2} - 5c_{j-1} - 5c_j \\ &\quad + 9c_{j+1} - 5c_{j+2} + c_{j+3}) + O(h^2). \end{aligned} \quad (19)$$

3. Description of Numerical Method

In the section, we give the quartic B-spline method for the linear sixth order boundary value problem. Let $s(x) = \sum_{i=-2}^{n+1} c_i N_{i,4}(x)$ be the approximate solution of 6BVP (1)–(2) and $\tilde{s}(x) = \sum_{i=-2}^{n+1} \tilde{c}_i N_{i,4}(x)$ the approximate spline of $s(x)$. Discretize (1) at the knots x_i ($i = 2, 3, \dots, n-2$), we get

$$y^{(6)}(x_i) + f(x_i) y(x_i) = g(x_i). \quad (20)$$

By (9) and (18), we turn (20) into

$$\begin{aligned} & \frac{1}{2h^6} (c_{i-4} - 5c_{i-3} + 9c_{i-2} - 5c_{i-1} \\ & \quad - 5c_i + 9c_{i+1} - 5c_{i+2} + c_{i+3}) + \frac{f(x_i)}{24} \\ & \quad \times (c_{i-2} + 11c_{i-1} + 11c_i + c_{i+1}) = g(x_i) + O(h^2), \end{aligned} \quad (21)$$

where $f(x_i)$ and $g(x_i)$ are the value of $f(x)$ and $g(x)$ at the knots x_i ($i = 2, 3, \dots, n-2$) for short. Change (21) equivalently, we yield

$$\begin{aligned} & 12(c_{i-4} - 5c_{i-3} + 9c_{i-2} - 5c_{i-1} - 5c_i \\ & \quad + 9c_{i+1} - 5c_{i+2} + c_{i+3}) + f(x_i) \\ & \quad \times (c_{i-2} + 11c_{i-1} + 11c_i + c_{i+1}) h^6 \\ &= 24h^6 g(x_i) + O(h^8). \end{aligned} \quad (22)$$

Dropping the term $O(h^8)$ from (22), we get a linear system with $n - 3$ linear equations in $n + 4$ unknowns c_i ($i = -2, -1, \dots, n + 1$)

$$\begin{aligned} & 12(c_{i-4} - 5c_{i-3} + 9c_{i-2} - 5c_{i-1} - 5c_i \\ & + 9c_{i+1} - 5c_{i+2} + c_{i+3}) + f(x_i) \\ & \times (c_{i-2} + 11c_{i-1} + 11c_i + c_{i+1})h^6 \\ & = 24h^6 g(x_i) \quad (i = 2, 3, \dots, n-2), \end{aligned} \quad (23)$$

so seven more equations are needed.

By the boundary conditions at $x = a$

$$\begin{aligned} y(a) &= A_0, \\ y'(a) &= A_1, \\ y''(a) &= A_2, \end{aligned} \quad (24)$$

we have

$$\begin{aligned} c_{-2} + 11c_{-1} + 11c_0 + c_1 &= 24A_0, \\ -c_{-2} - 3c_{-1} + 3c_0 + c_1 &= 6hA_1, \\ c_{-2} - c_{-1} - c_0 + c_1 &= 2h^2A_2. \end{aligned} \quad (25)$$

By the boundary conditions at $x = b$

$$\begin{aligned} y(b) &= B_0, \\ y'(b) &= B_1, \\ y''(b) &= B_2, \end{aligned} \quad (26)$$

we get

$$\begin{aligned} c_{n-2} + 11c_{n-1} + 11c_n + c_{n+1} &= 24B_0, \\ -c_{n-2} - 3c_{n-1} + 3c_n + c_{n+1} &= 6hB_1, \\ c_{n-2} - c_{n-1} - c_n + c_{n+1} &= 2h^2B_2. \end{aligned} \quad (27)$$

We can construct an approximate formula as follows:

$$y^{(6)}(a) = \frac{-5R_0 + 18R_1 - 24R_2 + 14R_3 - 3R_4}{24h^3} + O(h^2), \quad (28)$$

where the coefficients are determined by maximizing the error order.

Substituting (12) into (28), we have

$$\begin{aligned} & 5c_{-2} - 33c_{-1} + 93c_0 - 145c_1 + 135c_2 \\ & - 75c_3 + 23c_4 - 3c_5 = 24h^6 y^{(6)}(a) + O(h^5). \end{aligned} \quad (29)$$

Dropping the term $O(h^5)$ from (29), we can get

$$\begin{aligned} & 5c_{-2} - 33c_{-1} + 93c_0 - 145c_1 + 135c_2 - 75c_3 \\ & + 23c_4 - 3c_5 = 24h^6 y^{(6)}(a). \end{aligned} \quad (30)$$

Take (22), (25), (27), and (29) together, we get $n + 4$ linear equation with c_i ($i = -2, -1, \dots, n + 1$) as unknowns. The linear system can be written in matrix notations

$$(A + h^6 FB)C = D + E. \quad (31)$$

Take (23), (25), (27), and (30) together, we get $n + 4$ linear equation with \tilde{c}_i ($i = -2, -1, \dots, n + 1$) as unknowns. The linear system can be written in matrix notations

$$(A + h^6 FB)\tilde{C} = D, \quad (32)$$

where

$$C = (c_{-2}, c_{-1}, c_0, \dots, c_{n+1})^T,$$

$$\tilde{C} = (\tilde{c}_{-2}, \tilde{c}_{-1}, \tilde{c}_0, \dots, \tilde{c}_{n+1})^T,$$

$$D = (24h^6 y^{(6)}(a), 24A_0, 6hA_1, 2h^2A_2, 24h^6 g(x_2), \dots,$$

$$24h^6 g(x_{n-1}), 24B_0, 6hB_1, 2h^2B_2)^T,$$

$$E = (e_{-2}, e_{-1}, \dots, e_{n+1})^T,$$

$$e_{-1} = e_0 = e_1 = e_{n-1} = e_n = e_{n+1} = 0,$$

$$e_{-2} = O(h^5), \quad e_i = O(h^8) \quad (i = 2, \dots, n-2),$$

A

$$= \begin{pmatrix} 5 & -33 & 93 & -145 & 135 & -75 & 23 & -3 \\ 1 & 11 & 11 & 1 & & & & \\ -1 & -3 & 3 & 1 & & & & \\ 1 & -1 & -1 & 1 & & & & \\ 12 & -60 & 108 & -60 & -60 & 108 & -60 & 12 \\ & \ddots & \ddots & \ddots & \ddots & \ddots & \ddots & \ddots \\ & & 12 & -60 & 108 & -60 & -60 & 108 & -60 & 12 \\ & & & & & & 1 & 11 & 11 & 1 \\ & & & & & & -1 & -3 & 3 & 1 \\ & & & & & & 1 & -1 & -1 & 1 \end{pmatrix},$$

F

$$= \begin{pmatrix} 0 & & & & & & & \\ & 0 & & & & & & \\ & & 0 & & & & & \\ & & & f(x_2) & & & & \\ & & & & \ddots & & & \\ & & & & & f(x_{n-1}) & & \\ & & & & & & 0 & \\ & & & & & & & 0 & \\ & & & & & & & & 0 \end{pmatrix},$$

TABLE 2: Max $[y^{(v)}(x_i)]$ of quartic B-spline method for Example 1.

n	$\max[y(x_i)]$	$\max[y'(x_i)]$	$\max[y''(x_i)]$	$\max[y'''(x_i)]$	$\max[y^{(4)}(x_i)]$	$\max[y^{(5)}(x_i)]$
10	$3.2599e-6$	$1.3642e-5$	$1.9072e-4$	$6.1038e-3$	$1.1021e-2$	$8.444e-1$
20	$1.3846e-7$	$5.1383e-7$	$6.7388e-6$	$1.2107e-5$	$2.1304e-4$	$4.2045e-2$
40	$2.8847e-8$	$1.5453e-7$	$1.3402e-6$	$2.8482e-5$	$7.4701e-4$	$2.1074e-2$
80	$1.3493e-8$	$7.8389e-8$	$6.657e-7$	$7.5303e-5$	$3.1822e-4$	$1.602e-2$

B

$$= \begin{pmatrix} 0 & 0 & 0 & & & & & & \\ 0 & 0 & 0 & & & & & & \\ 0 & 0 & 0 & & & & & & \\ 1 & 11 & 11 & 1 & 0 & 0 & 0 & & \\ & \ddots & \ddots & \ddots & \ddots & \ddots & \ddots & \ddots & \\ & & 0 & 0 & 0 & 1 & 11 & 11 & 1 \\ & & & & & & 0 & 0 & 0 \\ & & & & & & 0 & 0 & 0 \\ & & & & & & 0 & 0 & 0 \end{pmatrix}. \quad (33)$$

After solving the linear system (32), we obtain the quartic spline approximate solution $y(x) \approx \tilde{s}(x) = \sum_{i=-2}^{n+1} \tilde{c}_i N_{i,4}(x)$. Furthermore, we can take $\tilde{s}^{(k)}(x)$ ($k = 1, 2, 3, 4, 5$) as the approximation of $y^{(k)}(x)$ ($k = 1, 2, 3, 4, 5$).

4. Convergence Analysis

By (31) and (32), we have

$$(A + h^6 FB)(C - \tilde{C}) = E. \quad (34)$$

A is invertible, and if we assume that

$$h^6 \|A^{-1}\|_{\infty} \|F\|_{\infty} \|B\|_{\infty} < 1, \quad (35)$$

then $(I + h^8 A^{-1} FB)$ is also invertible.

Hence, we get

$$C - \tilde{C} = (I + h^6 A^{-1} FB)^{-1} A^{-1} E. \quad (36)$$

By (35) and (36) and note $\|E\|_{\infty} \leq kh^8$, we have

$$\begin{aligned} \|C - \tilde{C}\|_{\infty} &\leq \frac{\|A^{-1}\|_{\infty} \|E\|_{\infty}}{1 - h^6 \|A^{-1}\|_{\infty} \|F\|_{\infty} \|B\|_{\infty}} \\ &\leq \frac{kh^6 \|A^{-1}\|_{\infty}}{1 - h^6 \|A^{-1}\|_{\infty} \|B\|_{\infty} \|F\|_{\infty}} h^2 \\ &\leq \frac{k}{\|B\|_{\infty} \|F\|_{\infty}} h^2 = O(h^2). \end{aligned} \quad (37)$$

Hence,

$$\begin{aligned} \|s - \tilde{s}\|_{\infty} &\leq \|C - \tilde{C}\|_{\infty} \sum_{i=1}^n N_{i,4}(x) \\ &= \|C - \tilde{C}\|_{\infty} = O(h^2). \end{aligned} \quad (38)$$

Generally, we get

$$\begin{aligned} \|y - \tilde{s}\|_{\infty} &\leq \|y - \tilde{s}\|_{\infty} + \|s - \tilde{s}\|_{\infty} \\ &= O(h^2) + O(h^2) = O(h^2). \end{aligned} \quad (39)$$

5. Numerical Results

In the section, we give some computational results of numerical experiments with method based on previous sections to support our theoretical discussion. We use double precision arithmetic in order to reduce the round-off errors to a minimum.

Example 1. We consider the following equation:

$$y^{(6)}(x) + y(x) = 6 \cos x, \quad 0 \leq x \leq 1,$$

$$y(0) = 0, \quad y'(0) = -1, \quad y''(0) = 2, \quad (40)$$

$$y(1) = 0, \quad y'(1) = \sin 1, \quad y''(1) = 2 \cos 1.$$

The exact solution is given by $y(x) = (x - 1) \sin x$.

The results of maximum absolute errors $\max[y^{(v)}(x_i)] = \max_{1 \leq i \leq n} |y^{(v)}(x_i) - s^{(v)}(x_i)|$ ($v = 0, 1, 2, 3, 4, 5$) for this problem are tabulated in Table 2.

Next, we compare our method with the other spline method. Consider another sixth order boundary value problem.

Example 2. Consider the boundary value problem

$$y^{(6)}(x) - y(x) = -6e^x, \quad 0 \leq x \leq 1,$$

$$y(0) = 1, \quad y'(0) = 0, \quad y''(0) = -1, \quad (41)$$

$$y(1) = 0, \quad y'(1) = -e, \quad y''(1) = -2e,$$

which has the exact solution $y(x) = (1 - x)e^x$.

The example has been solved by the collocation method based on the sixth B-spline [18], and the numerical results are stated in Table 3. Also, the system of differential equation along with the given boundary conditions was solved by Wazwaz using Adomian decomposition method [10] and Noor using variational iteration method [13]. The respective maximum absolute errors are given in Table 3. Obviously, the results of our method are very encouraging.

TABLE 3: $\text{Max}[y(x_i)]$ of different methods for Example 2.

x	Exact solution	[18]	[13]	[10]	Our method
0.1	0.99465383	$1.2159e-5$	$4.0933e-4$	$4.0933e-4$	$4.5092e-6$
0.2	0.97712221	$2.7418e-5$	$7.7820e-4$	$7.7820e-4$	$1.2619e-5$
0.3	0.94490117	$2.2053e-6$	$1.0704e-3$	$1.0704e-3$	$1.9154e-5$
0.4	0.89509482	$2.5033e-6$	$1.2578e-3$	$1.2578e-3$	$2.1632e-5$
0.5	0.82436064	$5.4836e-6$	$1.3223e-3$	$1.3223e-3$	$1.9704e-5$
0.6	0.72884752	$1.6212e-5$	$1.2578e-3$	$1.2578e-3$	$1.4548e-5$
0.7	0.60412581	$2.0682e-5$	$1.0704e-3$	$1.0704e-3$	$8.2238e-6$
0.8	0.44510819	$2.2619e-5$	$7.7820e-4$	$7.7820e-4$	$2.9420e-6$
0.9	0.24596031	$1.9460e-5$	$4.0933e-4$	$4.0933e-4$	$2.3610e-7$

6. Conclusion

In the section, we employ the quartic B-spline for solving the sixth order boundary value problems. Properties of the B-spline function are utilized to reduce the computation of this problem to some algebraic equations. The method is computationally attractive and applications are demonstrated through illustrative examples. The obtained results showed that this approach can solve the problem effectively, and the comparison shows that the proposed technique is in good agreement with the existing results in the literature.

References

- [1] J. Toomre, J. R. Zahn, and J. Latour, "Stellar convection theory II: single-model study of the second convection zone in A-type stars," *Astrophysical Journal*, vol. 207, pp. 545–563, 1976.
- [2] A. Boutayeb and E. H. Twizell, "Numerical methods for the solution of special sixth-order boundary value problems," *International Journal of Computer Mathematics*, vol. 45, no. 3-4, pp. 207–223, 1992.
- [3] E. H. Twizell and A. Boutayeb, "Numerical methods for the solution of special and general sixth order boundary value problems, with applications to Bénard layer eigenvalue problems," *Proceedings the Royal of Society A*, vol. 431, no. 1883, pp. 433–450, 1990.
- [4] S. S. Siddiqi and E. H. Twizell, "Spline solutions of linear sixth-order boundary-value problems," *International Journal of Computer Mathematics*, vol. 60, no. 3-4, pp. 295–304, 1996.
- [5] P. Bladwin, "Asymptotic estimates of the eigenvalues of a sixth order boundary value problem obtained by using global phase-integral methods," *Proceedings the Royal of Society A*, vol. 322, no. 1566, pp. 281–305, 1987.
- [6] P. Baldwin, "Localised instability in a Bénard layer," *Applicable Analysis*, vol. 24, no. 1-2, pp. 117–156, 1987.
- [7] S. Chandrasekhar, *Hydrodynamics and Hydromagnetic Stability*, New York, NY, USA, Dover edition, 1981.
- [8] R. Agarwal, *Boundary Value Problems for Higher Ordinary Differential Equations*, World Scientific, Singapore, 1997.
- [9] E. H. Twizell, *Numerical Methods for Sixth-Order Boundary Value Problems*, International Series of Numerical Mathematics, Numerical mathematics, Singapore, 1988.
- [10] A. M. Wazwaz, "A reliable modification of Adomian decomposition method," *Applied Mathematics and Computation*, vol. 102, no. 1, pp. 77–86, 1999.
- [11] A. M. Wazwaz, "The numerical solution of sixth-order boundary value problems by the modified decomposition method," *Applied Mathematics and Computation*, vol. 118, no. 2-3, pp. 311–325, 2001.
- [12] M. El-Gamel, J. R. Cannon, and A. I. Zayed, "Sinc-Galerkin method for solving linear sixth-order boundary-value problems," *Mathematics of Computation*, vol. 73, no. 247, pp. 1325–1343, 2004.
- [13] M. A. Noor, K. I. Noor, and S. T. Mohyud-Din, "Variational iteration method for solving sixth-order boundary value problems," *Communications in Nonlinear Science and Numerical Simulation*, vol. 14, no. 6, pp. 2571–2580, 2009.
- [14] M. A. Noor and S. T. Mohyud-Din, "Homotopy perturbation method for solving sixth-order boundary value problems," *Computers and Mathematics with Applications*, vol. 55, no. 12, pp. 2953–2972, 2008.
- [15] S. S. Siddiqi, G. Akram, and S. Nazeer, "Quintic spline solution of linear sixth-order boundary value problems," *Applied Mathematics and Computation*, vol. 189, no. 1, pp. 887–892, 2007.
- [16] S. S. Siddiqi and G. Akram, "Septic spline solutions of sixth-order boundary value problems," *Journal of Computational and Applied Mathematics*, vol. 215, no. 1, pp. 288–301, 2008.
- [17] G. Akram and S. S. Siddiqi, "Solution of sixth order boundary value problems using non-polynomial spline technique," *Applied Mathematics and Computation*, vol. 181, no. 1, pp. 708–720, 2006.
- [18] G. B. Lohmani and M. Ahmadinia, "Numerical solution of sixth order boundary value problems with sixth degree B-spline functions," *Applied Mathematics and Computation*, vol. 186, no. 2, pp. 992–999, 2007.
- [19] K. S. K. Kasi Viswanadham and P. Murali Krishna, "Septic B-spline collocation method for sixth order boundary value problem," *ARPN Journal of Engineering and Applied Sciences*, vol. 5, no. 7, pp. 36–40, 2010.
- [20] S. Siraj-ul-Islam, I. A. Tirmizi, F. Fazal-i-Haq, and M. A. Khan, "Non-polynomial splines approach to the solution of sixth-order boundary-value problems," *Applied Mathematics and Computation*, vol. 195, no. 1, pp. 270–284, 2008.
- [21] M. A. Ramadan, I. F. Lashien, and W. K. Zahra, "A class of methods based on a septic non-polynomial spline function for the solution of sixth-order two-point boundary value problems," *International Journal of Computer Mathematics*, vol. 85, no. 5, pp. 759–770, 2008.

- [22] A. Lamnii, H. Mraoui, D. Sbibi, A. Tijini, and A. Zidna, "Spline collocation method for solving linear sixth-order boundary-value problems," *International Journal of Computer Mathematics*, vol. 85, no. 11, pp. 1673–1684, 2008.
- [23] H. N. Caglar, S. H. Caglar, and E. H. Twizell, "Numerical solution of third-order boundary-value problems with fourth-degree B-spline functions," *International Journal of Computer Mathematics*, vol. 71, no. 3, pp. 373–381, 1999.
- [24] F. G. Lang and X. P. Xu, "Quartic B-spline collocation method for fifth order boundary value problems," *Computing*, vol. 92, no. 4, pp. 365–378, 2011.
- [25] F. Gao and C. Chi, "Solving third-order obstacle problems with quartic B-splines," *Applied Mathematics and Computation*, vol. 180, no. 1, pp. 270–274, 2006.
- [26] C. De Boor, *A Practice Guide Spline*, Springer, New York, NY, USA, 1978.
- [27] D. J. Fyfe, "The use of cubic splines in the solution of two-point boundary value problems," *The Computer Journal*, vol. 12, no. 2, pp. 188–192, 1969.
- [28] T. R. Lucas, "Error bounds for interpolating cubic splines under various end conditions," *SIAM Journal on Numerical Analysis*, vol. 11, no. 3, pp. 569–584, 1974.

Research Article

A Conjugate Gradient Method with Global Convergence for Large-Scale Unconstrained Optimization Problems

Shengwei Yao,^{1,2} Xiwen Lu,¹ and Zengxin Wei³

¹ School of Science, East China University of Science and Technology, Shanghai 200237, China

² School of Information and Statistics, Guangxi University of Finance and Economics, Nanning 530003, China

³ College of Mathematics and Information Science, Guangxi University, Nanning 530004, China

Correspondence should be addressed to Shengwei Yao; idhot@163.com

Received 26 August 2013; Accepted 22 October 2013

Academic Editor: Delfim Soares Jr.

Copyright © 2013 Shengwei Yao et al. This is an open access article distributed under the Creative Commons Attribution License, which permits unrestricted use, distribution, and reproduction in any medium, provided the original work is properly cited.

The conjugate gradient (CG) method has played a special role in solving large-scale nonlinear optimization problems due to the simplicity of their very low memory requirements. This paper proposes a conjugate gradient method which is similar to Dai-Liao conjugate gradient method (Dai and Liao, 2001) but has stronger convergence properties. The given method possesses the sufficient descent condition, and is globally convergent under strong Wolfe-Powell (SWP) line search for general function. Our numerical results show that the proposed method is very efficient for the test problems.

1. Introduction

The conjugate gradient (CG) method has played a special role in solving large-scale nonlinear optimization due to the simplicity of their iterations and their very low memory requirements. In fact, the CG method is not among the fastest or most robust optimization algorithms for nonlinear problems available today, but it remains very popular for engineers and mathematicians who are interested in solving large problems. The conjugate gradient method is designed to solve the following unconstrained optimization problem:

$$\min \{f(x) \mid x \in R^n\}, \quad (1)$$

where $f(x) : R^n \rightarrow R$ is a smooth, nonlinear function whose gradient will be denoted by $g(x)$. The iterative formula of the conjugate gradient method is given by

$$x_{k+1} = x_k + s_k, \quad s_k = \alpha_k d_k, \quad (2)$$

where α_k is a step length which is computed by carrying out a line search, and d_k is the search direction defined by

$$d_k = \begin{cases} -g_k & \text{if } k = 1, \\ -g_k + \beta_k d_{k-1} & \text{if } k \geq 2, \end{cases} \quad (3)$$

where β_k is a scalar and g_k denotes the gradient $\nabla f(x_k)$. If f is a strictly convex quadratic function, namely,

$$f(x) = \frac{1}{2} x^T H x + b^T x, \quad (4)$$

where H is a positive definite matrix and if α_k is the exact one-dimensional minimizer along the direction d_k , then the method with (2) and (3) are called the linear conjugate gradient method. Otherwise, (2) and (3) is called the nonlinear conjugate gradient method. The most important feature of linear conjugate gradient method is that the search directions satisfy the following conjugacy condition:

$$d_i^T H d_j = 0, \quad i \neq j. \quad (5)$$

For nonlinear conjugate gradient methods, for general objective functions, (5) does not hold, since the Hessian $\nabla^2 f(x)$ changes at different points.

Some well-known formulas for β_k are the Fletcher-Reeves (FR), Polak-Ribière (PR), Hestense-Stiefel (HS), and Dai-Yuan (DY) methods which are given, respectively, by

$$\beta_k^{\text{FR}} = \frac{\|g_k\|^2}{\|g_{k-1}\|^2}, \quad (6)$$

$$\beta_k^{\text{PR}} = \frac{g_k^T (g_k - g_{k-1})}{\|g_{k-1}\|^2}, \quad (7)$$

$$\beta_k^{\text{HS}} = \frac{g_k^T (g_k - g_{k-1})}{(g_k - g_{k-1})^T d_{k-1}}, \quad (8)$$

$$\beta_k^{\text{DY}} = \frac{\|g_k\|^2}{(g_k - g_{k-1})^T d_{k-1}}, \quad (9)$$

where $\|\cdot\|$ denotes the Euclidean norm. Their corresponding conjugate methods are abbreviated as FR, PR, HS, and DY methods. Although all these method are equivalent in the linear case, namely, when f is a strictly convex quadratic function and α_k are determined by exact line search, their behaviors for general objective functions may be far different.

For general functions, Zoutendijk [1] proved the global convergence of FR methods with exact line search (here and throughout this paper, for global convergence, we mean that the sequence generated by the corresponding methods will either terminate after finite steps or contain a subsequence such that it converges to a stationary point of the objective function from a given initial point). Although one would be satisfied with its global convergence properties, the FR method performs much worse than the PR (HS) method in real computations. Powell [2] analyzed a major numerical drawback of the FR method; namely, if a small step is generated away from the solution point, the subsequent steps may be also very short. On the other hand, in practical computation, the HS method resembles the PR method, and both methods are generally believed to be the most efficient conjugate gradient methods since these two methods essentially perform a restart if a bad direction occurs. However, Powell [3] constructed a counterexample and showed that the PR method and HS method can cycle infinitely without approaching the solution. This example suggests that these two methods have a drawback that they are not globally convergent for general functions. Therefore, in the past two decades, much effort has been exceterd to find out new formulas for conjugate methods such that not only they are globally convergent for general functions but also they have good numerical performance.

Recently, using a new conjugacy condition, Dai and Liao [4] proposed two new methods. Interestingly, one of their methods is not only globally convergent for general functions but also performs better than HS and PR methods. In this paper, similar to Dai and Liao's approach, we propose another formula for β_k , analyze the convergence properties for the given method, and also carry the numerical experiment which shows that the given method is robust and efficient.

The remainder of this paper is organized as follows. In Section 2, we firstly state the corresponding formula which

is proposed by Dai and Liao [4] and the motivations of this paper, and then we propose the new nonlinear conjugate gradient method. In Section 3, convergence analysis for the given method is presented. Numerical results are reported in Section 4. Finally, some conclusions are given in Section 5.

2. Motivations and New Nonlinear Conjugate Gradient Method

2.1. Dai-Liao's Methods. It is well known that the linear conjugate gradient methods generate a sequence of search directions d_k such that the conjugacy condition (5) holds. Denote y_{k-1} to be the gradient change, which means that

$$y_{k-1} = g_k - g_{k-1}. \quad (10)$$

For a general nonlinear function f , we know by the mean value theorem that there exists some $t \in (0, 1)$ such that

$$y_{k-1}^T d_k = \alpha_{k-1} d_k^T \nabla^2 f(x_{k-1} + t\alpha_{k-1} d_{k-1}) d_{k-1}. \quad (11)$$

Therefore, it is reasonable to replace (5) with the following conjugacy condition:

$$y_{k-1}^T d_k = 0. \quad (12)$$

Recently, extension of (12) has been studied by Dai and Liao in [4]. Their approach is based on the Quasi-Newton techniques. Recall that, in the Quasi-Newton method, an approximation matrix H_{k-1} of the Hessian $\nabla^2 f(x_{k-1})$ is updated such that the new matrix H_k satisfies the following Quasi-Newton equation:

$$H_k s_{k-1} = y_{k-1}. \quad (13)$$

The search direction d_k in Quasi-Newton method is calculated by

$$d_k = -H_k^{-1} g_k. \quad (14)$$

Combining these two equations, we obtain

$$d_k^T y_{k-1} = d_k^T (H_k s_{k-1}) = -g_k^T s_{k-1}. \quad (15)$$

The previous relation implies that (12) holds if the line search is exact since in this case $g_k^T d_{k-1} = 0$. However, practical numerical algorithms normally adopt inexact line searches instead of exact line searches. For this reason, it seems more reasonable to replace the conjugacy condition (12) with the condition

$$d_k^T y_{k-1} = -t g_k^T s_{k-1}, \quad t \geq 0, \quad (16)$$

where $t \geq 0$ is a scalar.

To ensure that the search direction d_k satisfies the conjugate condition (16), one only needs to multiply (3) with y_{k-1} and use (16), yielding

$$\beta_k^{\text{DL1}} = \frac{g_k^T (y_{k-1} - t s_{k-1})}{d_{k-1}^T y_{k-1}}. \quad (17)$$

It is obvious that

$$\beta_k^{\text{DL1}} = \beta_k^{\text{HS}} - t \frac{g_k^T s_{k-1}}{d_{k-1}^T y_{k-1}}. \quad (18)$$

For simplicity, we call the method with (2), (3), and (17) as DL1 method. Dai and Liao also prove that the conjugate gradient method with DL1 is globally convergent for uniformly convex functions. For general functions, Powell [3] constructed an example showing that the PR method may cycle without approaching any solution point if the step length α_k is chosen to be the first local minimizer along d_k . Since the DL1 method reduces to the PR method in the case that $g_k^T d_{k-1} = 0$ holds, this implies that the method with (17) need not converge for general functions. To get the global convergence, like Gilbert and Nocedal [5], who have proved the global convergence of the PR method with the restriction that $\beta_k^{\text{PR}} \geq 0$, Dai and Liao replaced (17) by

$$\begin{aligned} \beta_k^{\text{DL}} &= \max \left\{ \frac{g_k^T y_{k-1}}{d_{k-1}^T y_{k-1}}, 0 \right\} - t \frac{g_k^T s_{k-1}}{d_{k-1}^T y_{k-1}} \\ &= \max \{ \beta_k^{\text{HS}}, 0 \} - t \frac{g_k^T s_{k-1}}{d_{k-1}^T y_{k-1}}. \end{aligned} \quad (19)$$

We also call the method with (2), (3), and (19) as DL method. Dai and Liao show that DL method is globally convergent for general functions under the sufficient descent condition (21) and some suitable conditions. Besides, some numerical experiments in [4] indicate the efficiency of this method.

Similar to Dai and Liao's approach, Li et al. [6] proposed another conjugate condition and related conjugate gradient methods, and they also prove that the proposed methods are globally convergent under some assumptions.

2.2. Motivations. From the above discussions, Dai and Liao's approach is effective; the main reason is that the search directions d_k generated by DL1 method or DL method not only contain the gradient information but also contain some Hessian $\nabla^2 f(x)$ information. From (18) and (19), β_k^{DL1} and β_k^{DL} are formed by two parts; the first part is β_k^{HS} , and the second part is $-t(g_k^T s_{k-1}/d_{k-1}^T y_{k-1})$. So, we also can consider DL1 and DL methods as some modified forms of the HS method by adding some information of Hessian $\nabla^2 f(x)$ which is contained in the second part. The convergence properties of the HS method are similar to PR method; it does not converge for general functions even if the line search is exact. In order to get the convergence, one also needs the nonnegative restriction $\beta_k = \max\{\beta_k^{\text{HS}}, 0\}$ and the sufficient descent assumption (21). From the above discussion, the descent condition or sufficient descent condition and nonnegative property of β_k play important roles in the convergence analysis. We say that the descent condition holds if for each search directions d_k

$$g_k^T d_k < 0, \quad \forall k \geq 1. \quad (20)$$

In addition, we say that the sufficient descent condition holds if there exists a constant $c > 0$ such that for each search direction d_k , we have

$$g_k^T d_k \leq -c \|g_k\|^2, \quad \forall k \geq 1. \quad (21)$$

Motivated by the above ideal, in this paper, we focus on finding the new conjugate gradient method which possesses the following properties:

- (1) nonnegative property $\beta_k \geq 0$;
- (2) the new formula contains not only the gradient information but also some Hessian information;
- (3) the search directions d_k generated by the proposed method satisfy the sufficient descent conditions (21).

2.3. The New Conjugate Gradient Method. From the structure of (6), (7), (8), and (9), the PR and HS methods have the common numerator $g_k^T y_{k-1}$, and the FR and DY methods have the common numerator $\|g_k\|^2$; and this different choice makes them have different properties. Generally speaking, FR and DY methods have better convergence properties, and PR and HS methods have better numerical experiments. Powell [3] pointed out that the FR method, with exact line search, was susceptible to jamming. That is, the algorithm could take many short steps without making significant progress to the minimum. If the line search is exact, that means $g_k^T d_{k-1} = 0$, in this case, DY method will turn out to be FR method. So, these two methods have the same disadvantage. The PR and HS methods which share the common numerator $g_k^T y_{k-1}$ possess a built-in restart feature to avoid the jamming problem: when the step $x_k - x_{k-1}$ is small, the factor y_{k-1} in the numerator of β_k tends to zero. Hence, the next search direction d_k is essentially the steepest descent direction $-g_k$. So, the numerical performance of these methods is better than the performance of the methods with $\|g_k\|^2$ in numerator of β_k .

Just as above discussions, great attentions were given to find the methods which not only have global convergent properties but also have nice numerical experiments.

Recently, Wei et al. [7] proposed a new formula

$$\beta_k^{\text{WYL}} = \frac{g_k^T y_{k-1}^*}{\|g_{k-1}\|^2}, \quad y_{k-1}^* = g_k - \frac{\|g_k\|}{\|g_{k-1}\|} g_{k-1}. \quad (22)$$

The method with formula β_k^{WYL} not only has nice numerical results but also possesses the sufficient descent condition and global convergence properties under the strong Wolfe-Powell line search. From the structure of β_k^{WYL} , we know that the method with β_k^{WYL} can also avoid jamming: when the step $x_k - x_{k-1}$ is small, $\|g_k\|/\|g_{k-1}\|$ tends to 1 and the next search direction tends to the steepest descent direction which is similar to PR method. But WYL method has some advantages, such as under strong Wolfe-Powell line search, $\beta_k^{\text{WYL}} \geq 0$, and if the parameter $\sigma \leq 1/4$ in SWP, WYL method possesses the sufficient descent condition which deduces the global convergence of the WYL method.

In [8, 9], Shengwei et al. extended such modification to HS method as follows:

$$\beta_k^{\text{MHS}} = \frac{g_k^T y_{k-1}^*}{d_{k-1}^T y_{k-1}}, \quad y_{k-1}^* = g_k - \frac{\|g_k\|}{\|g_{k-1}\|} g_{k-1}. \quad (23)$$

The previous formulae β_k^{WYL} and β_k^{MHS} can be considered as the modification forms of β_k^{PR} and β_k^{HS} by using y_{k-1}^* to replace y_{k-1} , respectively. In [8, 9], the corresponding methods are proved to be globally convergent for general functions under the strong Wolfe-Powell line search and Grippo-Lucidi line search. Based on the same approach, some authors give other discussions and modifications in [10–12]. In fact, y_{k-1}^* is not our point at the beginning, our purpose is involving the information of the angle between g_k and g_{k-1} . From this point of view, β_k^{WYL} has the following form:

$$\beta_k^{\text{WYL}} = \beta_k^{\text{FR}} (1 - \cos(\bar{\theta}_k)), \quad (24)$$

where $\bar{\theta}_k$ is the angle between g_k and g_{k-1} . By multiplying β_k^{FR} with $1 - \cos \bar{\theta}_k$, the method not only has similar convergence properties with FR method, but also avoids jamming which is similar to PR method.

The above analysis motivates us to propose the following formula to compute β_k :

$$\beta_k^{\text{MDL1}} = \max \left\{ \frac{g_k^T y_{k-1}^*}{d_{k-1}^T y_{k-1}}, 0 \right\} - t \frac{g_k^T s_{k-1}}{d_{k-1}^T y_{k-1}}, \quad (25)$$

where $y_{k-1}^* = g_k - (\|g_k\|/\|g_{k-1}\|)g_{k-1}$. Since the β_k^{MHS} are nonnegative under the strong Wolfe-Powell line search, we omit the nonnegative restriction and propose the following formula:

$$\beta_k^{\text{MDL}} = \frac{g_k^T y_{k-1}^*}{d_{k-1}^T y_{k-1}} - t \frac{g_k^T s_{k-1}}{d_{k-1}^T y_{k-1}} = \beta_k^{\text{MHS}} - t \frac{g_k^T s_{k-1}}{d_{k-1}^T y_{k-1}}. \quad (26)$$

From (25) and (26), we know that we only substitute y_{k-1} in the first part of the numerator of β_k^{DL1} or β_k^{DL} by y_{k-1}^* . The reason is that we hope the formulae (25) and (26) contain the angle information between g_k and g_{k-1} . In fact, β_k^{MDL} can be expressed as

$$\begin{aligned} \beta_k^{\text{MDL}} &= \frac{\|g_k\|^2}{d_{k-1}^T y_{k-1}} (1 - \cos \bar{\theta}_k) - t \frac{g_k^T s_{k-1}}{d_{k-1}^T y_{k-1}} \\ &= \beta_k^{\text{DY}} (1 - \cos \bar{\theta}_k) - t \frac{g_k^T s_{k-1}}{d_{k-1}^T y_{k-1}}. \end{aligned} \quad (27)$$

For simplicity, we call the method generated by (2), (3), and (26) as MDL method and give the algorithm as follows.

Algorithm 1 (MDL).

Step 1. Given $x_1 \in R^n$, $\varepsilon \geq 0$, set $d_1 = -g_1$, $k = 1$; if $\|g_1\| \leq \varepsilon$, then stop.

Step 2. Compute t_k by some line searches.

Step 3. Let $x_{k+1} = x_k + \alpha_k d_k$, and let $g_{k+1} = g(x_{k+1})$; if $\|g_k\| \leq \varepsilon$, then stop.

Step 4. Compute β_k by (26) and generate d_{k+1} by (3).

Step 5. Set $k := k + 1$ and go to Step 2.

We make the following basic assumptions on the objective functions.

Assumption A. (i) The level set $\Gamma = \{x \in R^n : f(x) \leq f(x_1)\}$ is bounded; namely, there exists a constant $B > 0$ such that

$$\|x\| \leq B, \quad \forall x \in \Gamma. \quad (28)$$

(ii) In some neighborhood N of Γ , f is continuously differentiable, and its gradient is Lipschitz continuous; namely, there exists a constant $L > 0$ such that

$$\|g(x) - g(y)\| \leq L \|x - y\|, \quad \forall x, y \in N. \quad (29)$$

Under the above assumptions of f , there exists a constant $\bar{\gamma} \geq 0$ such that

$$\|\nabla f(x)\| \leq \bar{\gamma}, \quad \forall x \in \Gamma. \quad (30)$$

The step length α_k in Algorithm 1 (MDL) is obtained by some line search scheme. In conjugate gradient methods, the strong Wolfe-Powell conditions; namely,

$$f(x_k + \alpha_k d_k) - f(x_k) \leq \delta \alpha_k g_k^T d_k, \quad (31)$$

$$|g(x_k + \alpha_k d_k)^T d_k| \leq -\sigma g_k^T d_k, \quad (32)$$

where $0 < \delta < \sigma < 1$, are often imposed on the line search (SWP).

3. Convergence Analysis

Under Assumption A, based on the Zoutendijk condition in [1], for any conjugate gradient method with the strong Wolfe-Powell line search, Dai et al. in [13] proved the following general result.

Lemma 2. Suppose that Assumption A holds. Consider any conjugate gradient method in the form (2)-(3), where d_k is a descent direction and α_k is obtained by the strong Wolfe-Powell line search. If

$$\sum_{k \geq 1} \frac{1}{\|d_k\|^2} = \infty. \quad (33)$$

One has that

$$\liminf_{k \rightarrow \infty} \|g_k\| = 0. \quad (34)$$

If the objective functions are uniformly convex, we can prove that the norm of d_k generated by Algorithm 1 (MDL) is bounded previously. Thus, by Lemma 2 one immediately has the following result.

Theorem 3. Suppose that Assumption A holds. Consider MDL method, where d_k is a descent direction and α_k is obtained by the strong Wolfe-Powell line search. If the objective functions are uniformly convex, namely, there exists a constant $\mu > 0$ such that

$$(\nabla f(x) - \nabla f(y))^T(x - y) \geq \mu \|x - y\|^2, \quad \forall x, y \in \Gamma. \quad (35)$$

One has that

$$\lim_{k \rightarrow \infty} \|g_k\| = 0. \quad (36)$$

Proof. It follows from (35) that

$$d_{k-1}^T y_{k-1} \geq \mu \alpha_{k-1} \|d_{k-1}\|^2. \quad (37)$$

By (3), (26), (29), (30), and (37), we have

$$\begin{aligned} & \|d_k\| \\ & \leq \|g_k\| + |\beta_k^{\text{MDL}}| \|d_{k-1}\| \\ & \leq \|g_k\| + \frac{g_k^T (g_k - (\|g_k\| / \|g_{k-1}\|) g_{k-1} - t s_{k-1})}{\mu \alpha_{k-1} \|d_{k-1}\|^2} \|d_{k-1}\| \\ & = \|g_k\| \\ & \quad + \frac{g_k^T (g_k - g_{k-1} + g_{k-1} - (\|g_k\| / \|g_{k-1}\|) g_{k-1} - t s_{k-1})}{\mu \alpha_{k-1} \|d_{k-1}\|^2} \\ & \quad \times \|d_{k-1}\| \\ & \leq \|g_k\| \\ & \quad + \frac{\|g_k\| (\|g_k - g_{k-1}\| + \|g_{k-1}\| (1 - \|g_k\| / \|g_{k-1}\|) + t \|s_{k-1}\|)}{\mu \alpha_{k-1} \|d_{k-1}\|^2} \\ & \quad \times \|d_{k-1}\| \\ & \leq \|g_k\| \\ & \quad + \frac{\|g_k\| (\|g_k - g_{k-1}\| + \|g_{k-1}\| - \|g_k\| + t \|s_{k-1}\|)}{\mu \alpha_{k-1} \|d_{k-1}\|^2} \|d_{k-1}\| \\ & \leq \|g_k\| + \frac{\|g_k\| (2L \|s_{k-1}\| + t \|s_{k-1}\|)}{\mu \alpha_{k-1} \|d_{k-1}\|^2} \|d_{k-1}\| \\ & \leq \bar{\gamma} \left(1 + \frac{2L + t}{\mu} \right) = \bar{\gamma} \mu^{-1} (\mu + 2L + t), \end{aligned} \quad (38)$$

which implies the truth of (33). Therefore, by Lemma 2 we have (34), which is equivalent to (36) for uniformly convex functions. The proof is completed. \square

In order to prove the convergence of the MDL method, we need to state some properties of β_k^{MHS} .

Lemma 4. In any conjugate gradient methods, if the parameter β_k is computed by (23), namely, $\beta_k = \beta_k^{\text{MHS}}$, and α_k is determined by strong Wolfe-Powell line search of (31) and (32), then

$$\beta_k^{\text{MHS}} \geq 0. \quad (39)$$

Proof. By SWP condition (32), we have $d_{k-1}^T y_{k-1} \geq \sigma g_{k-1}^T d_{k-1} - g_{k-1}^T d_{k-1} \geq 0$, since $\sigma < 1$ and $g_1^T d_1 = -\|g_1\|^2 < 0$. So we have

$$\begin{aligned} \beta_k^{\text{MHS}} &= \frac{g_k^T (g_k - (\|g_k\| / \|g_{k-1}\|) g_{k-1})}{d_{k-1}^T y_{k-1}} \\ &= \frac{\|g_k\|^2}{d_{k-1}^T y_{k-1}} (1 - \cos \bar{\theta}_k) \geq 0. \end{aligned} \quad (40)$$

The proof is completed. \square

In addition, we can also prove that, in conjugate gradient method of forms (2)-(3), if β_k is computed by β_k^{MDL} (26) and α_k is determined by strong Wolfe-Powell line search, then the search direction d_k satisfies the sufficient descent condition (21).

Theorem 5. In any conjugate gradient methods, in which the parameter β_k is computed by (26), namely, $\beta_k = \beta_k^{\text{MDL}}$, and α_k is determined by strong Wolfe-Powell line search of (31) and (32), if $\sigma < 1/3$, then the search direction d_k satisfied the sufficient descent condition (21).

Proof. We prove this theorem by induction. Firstly, we prove the descent condition $d_k^T g_k < 0$ as follow.

Since $g_1^T d_1 = -\|g_1\|^2 < 0$, supposing that $g_i^T d_i < 0$ holds for $i \leq k-1$, we deduce that the descent condition holds by proving that $g_i^T d_i < 0$ holds for $i = k$ as follow.

By SWP condition (32), we have $d_{k-1}^T y_{k-1} \geq (\sigma - 1) g_{k-1}^T d_{k-1} > 0$. Combining (3) and (26), we have

$$\begin{aligned} \frac{g_k^T d_k}{\|g_k\|^2} &= -1 + \frac{(1 - \cos \bar{\theta}_k)}{d_{k-1}^T y_{k-1}} g_k^T d_{k-1} \\ &\quad - t * \frac{(g_k^T d_{k-1})^2 \alpha_{k-1}}{(d_{k-1}^T y_{k-1}) \|g_k\|^2} \\ &\leq -1 + 2 \frac{-\sigma g_{k-1}^T d_{k-1}}{d_{k-1}^T y_{k-1}} \\ &\leq -1 + 2 \frac{-\sigma g_{k-1}^T d_{k-1}}{(\sigma - 1) g_{k-1}^T d_{k-1}} \\ &\leq \frac{-1 + 3\sigma}{1 - \sigma} < 0. \end{aligned} \quad (41)$$

Equation (41) means that descent condition holds.

Secondly, we prove the following sufficient descent condition.

Set $c = 1 - 2\sigma/(1 - \sigma)$; since the restriction $\sigma < 1/3$, we have $0 < c < 1$. Combining $g_1^T d_1 = -\|g_1\|^2$ and (41), the sufficient descent condition (21) holds immediately. \square

By Theorem 5, we can prove the following Lemma 6.

Lemma 6. Suppose that Assumption A holds. Consider MDL method, where α_k is obtained by strong Wolfe-Powell line search with $\sigma < 1/3$. If there exists a constant $\gamma > 0$ such that

$$\|g_k\| \geq \gamma, \quad \forall k \geq 1, \quad (42)$$

then $d_k \neq 0$ and

$$\sum_{k \geq 2} \|u_k - u_{k-1}\|^2 < \infty, \quad (43)$$

where $u_k = d_k / \|d_k\|$.

Proof. Firstly, note that $d_k \neq 0$; otherwise, (21) is false. Therefore, u_k is well defined. In addition, by relation (42) and Lemma 2, we have

$$\sum_{k \geq 1} \frac{1}{\|d_k\|^2} < \infty. \quad (44)$$

Now, we divide formula β_k^{MDL} into two parts as follows:

$$\beta_k^1 = \frac{g_k^T y_{k-1}^*}{d_{k-1}^T y_{k-1}}, \quad \beta_k^2 = -t \frac{g_k^T s_{k-1}}{d_{k-1}^T y_{k-1}}, \quad (45)$$

and define

$$r_k := \frac{\vartheta_k}{\|d_k\|}, \quad \delta_k := \beta_k^1 \frac{\|d_{k-1}\|}{\|d_k\|}, \quad (46)$$

where $\vartheta_k = -g_k + \beta_k^2 d_{k-1}$.

Then by (3) we have for all $k \geq 2$,

$$u_k = r_k + \delta_k u_{k-1}. \quad (47)$$

Using the identity $\|u_k\| = \|u_{k-1}\| = 1$ and (47) we can obtain

$$\|r_k\| = \|u_k - \delta_k u_{k-1}\| = \|\delta_k u_k - u_{k-1}\|, \quad (48)$$

using the condition $\delta_k = \beta_k^{\text{MHS}}(\|d_{k-1}\|/\|d_k\|) \geq 0$, the triangle inequality, and (48), it follows that

$$\begin{aligned} \|u_k - u_{k-1}\| &\leq \|(1 + \delta) u_k - (1 + \delta) u_{k-1}\| \\ &\leq \|u_k - \delta_k u_{k-1}\| + \|\delta_k u_k - u_{k-1}\| \\ &= 2 \|r_k\|. \end{aligned} \quad (49)$$

On the other hand, the line search condition (32) gives

$$y_{k-1}^T d_{k-1} \geq (\sigma - 1) g_{k-1}^T d_{k-1}. \quad (50)$$

Equations (50), (32), and (21) imply that

$$\left| \frac{g_k^T d_{k-1}}{d_{k-1}^T y_{k-1}} \right| \leq \frac{\sigma}{1 - \sigma}. \quad (51)$$

It follows from the definition of ϑ_k , (51), (28), and (30) that

$$\begin{aligned} \|\vartheta_k\| &\leq \|\delta_k\| + t \left| \frac{g_k^T s_{k-1}}{d_{k-1}^T y_{k-1}} \right| \|d_{k-1}\| \\ &= \|\delta_k\| + t \left| \frac{g_k^T d_{k-1}}{d_{k-1}^T y_{k-1}} \right| \|s_{k-1}\| \\ &\leq \bar{\gamma} + t \frac{\sigma}{1 - \sigma} 2B. \end{aligned} \quad (52)$$

So, we have

$$\begin{aligned} \sum \|u_k - u_{k-1}\|^2 &\leq 4 \sum \|r_k\|^2 \leq 4 \sum \frac{g_k^2}{\|d_k\|^2} \\ &\leq 4 \left(\bar{\gamma} + t \frac{\sigma}{1 - \sigma} 2B \right)^2 \sum \frac{1}{\|d_k\|^2} \\ &< \infty. \end{aligned} \quad (53)$$

The proof is completed. \square

Gilbert and Nocedal [5] introduced property (*) which is very important for the convergence properties of the conjugate gradient methods. We are going to show that method with β_k^{MDL} possesses such property (*).

Property ().* Consider a method of forms (2) and (3). Suppose that

$$0 < \gamma \leq \|g_k\| \leq \bar{\gamma}, \quad \forall k \geq 1. \quad (54)$$

We say that the method has property (*), if for all k , there exist constants $b > 1$, $\lambda > 0$ such that $|\beta_k| \leq b$ and if $\|s_{k-1}\| \leq \lambda$ we have $|\beta_k| \leq 1/2b$.

In fact, by (50), (21), and (42), we have

$$\begin{aligned} d_{k-1}^T y_{k-1} &\geq (\sigma - 1) g_{k-1}^T d_{k-1} \geq c(1 - \sigma) \|g_{k-1}\|^2 \\ &\geq (1 - \sigma) c \gamma^2. \end{aligned} \quad (55)$$

Using this, (28), (29), and (30) we obtain

$$|\beta_k^{\text{MDL}}| \leq \frac{(2L + t) \|g_k\| \|s_{k-1}\|}{(1 - \sigma) c \gamma^2} \leq \frac{2(2L + t) \bar{\gamma} B}{(1 - \sigma) c \gamma^2} =: b. \quad (56)$$

Note that b can be defined such that $b > 1$. Therefore, we can say $b > 1$. As a result, we define

$$\lambda := \frac{(1 - \sigma) c \gamma^2}{2b(2L + t) \bar{\gamma}}, \quad (57)$$

we get from the first inequality in (56) that if $\|s_{k-1}\| \leq \lambda$, then

$$|\beta_k^{\text{MDL}}| \leq \frac{(2L + t) \bar{\lambda}}{(1 - \sigma) c \lambda^2} = \frac{1}{2b}. \quad (58)$$

Let N^* denote the set of positive integers. For $\lambda > 0$ and a positive integer Δ , denote

$$K_{k,\Delta}^\lambda := \{i \in N^* : k \leq i \leq k + \Delta - 1, \|s_{k-1}\| > \lambda\}. \quad (59)$$

Let $|K_{k,\Delta}^\lambda|$ denote the number of elements in $K_{k,\Delta}^\lambda$. From the previous property (*), we can prove the following lemma.

Lemma 7. Suppose that Assumption A holds. Consider MDL method, where α_k is obtained by the strong Wolfe-Powell line search in which $\sigma < 1/3$. Then if (42) holds, there exists $\lambda > 0$ such that, for any $\Delta \in N^*$ and any index k_0 , there is an index $k \geq k_0$ such that

$$|K_{k,\Delta}^\lambda| > \frac{\Delta}{2}. \quad (60)$$

The proof of this lemma is similar to the proof of Lemma 3.5 in [4]. In [4], authors proved that method with (19) has this property, if the search direction d_k satisfies the sufficient descent condition (21). In our paper, we do not need this assumption, since the directions generated by MDL method with strong Wolfe-Powell line search always possess the sufficient descent condition (21). So, we omit the proof of this lemma.

According to the previous lemmas and theorems, we can prove the following convergence theorem for the MDL.

Theorem 8. Suppose that Assumption A holds. Consider MDL method, if α_k is obtained by strong Wolfe-Powell line search with $\sigma < 1/3$. Then we have $\liminf_{k \rightarrow \infty} \|g_k\| = 0$.

Proof. We proceed by contradiction. If $\liminf_{k \rightarrow \infty} \|g_k\| > 0$, then (42) must hold. Then the conditions of Lemmas 6 and 7 hold. Defining $u_i = d_i / \|d_i\|$, we have for any indices l, k , with $l \geq k$,

$$\begin{aligned} x_l - x_{k-1} &= \sum_{i=k}^l x_i - x_{i-1} \\ &= \sum_{i=k}^l \alpha_{i-1} d_{i-1} = \sum_{i=k}^l u_{i-1} \|s_{i-1}\| \\ &= \sum_{i=k}^l \|s_{i-1}\| u_{k-1} + \sum_{i=k}^l \|s_{i-1}\| (u_{i-1} - u_{k-1}). \end{aligned} \quad (61)$$

Equation (61), $\|u_i\| = 1$, and (28) give

$$\begin{aligned} \sum_{i=k}^l \|s_{i-1}\| &\leq \|x_l - x_{k-1}\| + \sum_{i=k}^l \|s_{i-1}\| \|u_{i-1} - u_{k-1}\| \\ &\leq 2B + \sum_{i=k}^l \|s_{i-1}\| \|u_{i-1} - u_{k-1}\|. \end{aligned} \quad (62)$$

Let $\lambda > 0$ be given by Lemma 7, and define $\Delta := \lceil 8B/\lambda \rceil$ to be the smallest integer not less than $8B/\lambda$. By Lemma 6, we can find an index $k_0 \geq 1$ such that

$$\sum_{i \geq k_0} \|u_{i-1} - u_{k-1}\|^2 \leq \frac{1}{4\Delta}. \quad (63)$$

With this Δ and k_0 , Lemma 7 gives an index $k \geq k_0$ such that

$$|K_{k,\Delta}^\lambda| > \frac{\Delta}{2}. \quad (64)$$

For any index $i \in [k, k + \Delta - 1]$, by Cauchy-Schwartz inequality and (63),

$$\begin{aligned} \|u_i - u_{k-1}\| &\leq \sum_{j=k}^i \|u_j - u_{j-1}\| \\ &\leq (i - k + 1)^{1/2} \left(\sum_{j=k}^i \|u_j - u_{j-1}\|^2 \right)^{1/2} \\ &\leq \Delta^{1/2} \left(\frac{1}{4\Delta} \right)^{1/2} = \frac{1}{2}. \end{aligned} \quad (65)$$

From these relations (65) and (64) and taking $l = k + \Delta - 1$ in (62), we get

$$2B \geq \frac{1}{2} \sum_{i=k}^{k+\Delta-1} \|s_{i-1}\| > \frac{\lambda}{2} |K_{k,\Delta}^\lambda| > \frac{\lambda \Delta}{4}. \quad (66)$$

Thus, $\Delta < 8B/\lambda$, which contradicts the definition of Δ . The proof is completed. \square

4. Numerical Results

From (26) and (27), the MDL method can be considered as

- (i) form 1: a modification form of DL method;
- (ii) form 2: a modification form of MHS method;
- (iii) form 3: a modification form of DY method.

In form 1, the β_k^{HS} in β_k^{DL} is replaced by β_k^{MHS} . By this modification, we can guarantee the nonnegativity restrictions in DL method. In form 2, β_k^{MDL} is obtained by β_k^{MHS} adding an adjusting term $-t(g_k^T s_{k-1} / y_{k-1}^T d_{k-1})$ which contains some Hessian information of the objective function. In form 3, $\beta_k^{\text{MDL}} = \beta_k^{\text{DY}} (1 - \cos \bar{\theta}_k) - t(g_k^T s_{k-1} / d_{k-1}^T y_{k-1})$ shows that β_k^{MDL} is obtained by multiplying β_k^{DY} with $(1 - \cos \bar{\theta}_k)$ and adding the second term $-t(g_k^T s_{k-1} / y_{k-1}^T d_{k-1})$.

From the above convergence analysis, we know that MDL method has stronger convergent properties than DL method, and similar convergent properties with MHS method and DY method. So, in this section, we test the following four CG methods:

- (i) MDL method: method of the forms (2) and (3), in which β_k is computed by β_k^{MDL} (26);
- (ii) DL method: method of the forms (2) and (3), in which β_k is computed by β_k^{DL} (19);
- (iii) MHS method: method of the forms (2) and (3), in which β_k is computed by β_k^{MHS} (23);
- (iv) DY method: method of the forms (2) and (3), in which β_k is computed by β_k^{DY} (9).

TABLE I: Numerical results.

Problem	Dim	MDL	DL	MHS	DY
ROSE	2	35/349/83	<i>F</i>	38/267/91	63/800/106
FROTH	2	18/88/29	9/25/18	15/84/26	16/38/26
BADSCP	2	28/275/64	36/510/96	42/362/96	<i>F</i>
BADSCB	2	26/446/48	<i>F</i>	28/452/50	<i>F</i>
BEALE	3	16/87/27	11/81/22	14/83/25	47/193/74
JENSAM	2	11/31/21	<i>F</i>	11/31/21	11/31/21
HELIX	3	49/347/81	28/164/54	47/390/73	80/406/126
BARD	3	18/38/26	24/145/37	18/86/26	48/148/77
GAUSS	3	4/9/5	3/7/4	4/9/5	4/9/5
SING	4	134/501/209	78/396/124	111/411/172	650/3254/1104
WOOD	4	102/613/182	179/865/306	207/1352/365	<i>F</i>
KOWOSB	4	39/178/66	46/383/72	53/259/88	462/1760/796
BIGGS	6	18/279/25	85/564/14	20/286/31	210/644/342
OSB2	11	268/1001/445	185/888/293	186/701/310	<i>F</i>
WATSON	20	1455/3587/2274	1426/4240/2255	1922/4843/3018	548/1480/864
ROSEX	8	36/446/90	26/421/62	38/362/93	63/764/100
	50	46/548/101	32/469/84	44/412/101	86/707/146
	100	45/459/99	23/445/57	46/414/102	71/856/112
SINGX	4	134/501/209	78/396/124	111/411/172	650/3254/1104
PEN1	2	5/18/12	12/182/34	5/18/12	5/18/12
PEN2	4	10/82/26	12/89/27	11/133/29	32/167/57
	50	131/764/254	405/1453/683	136/1056/256	121/724/242
VARDIM	2	3/9/7	3/9/7	3/9/7	3/9/7
	50	10/52/36	10/52/36	10/52/36	10/52/36
TRIG	3	13/129/27	11/82/25	15/225/27	162/974/267
	50	38/320/70	38/222/68	38/225/71	206/1662/290
	100	48/340/90	43/425/76	48/294/90	225/3077/286
BV	3	9/17/11	12/25/16	11/20/13	13/27/18
	10	64/171/97	50/148/81	64/172/99	59/163/93
IE	200	5/59/7	6/13/8	5/59/7	6/61/8
	500	5/11/7	6/13/8	6/13/8	6/13/8
TRID	3	14/33/18	10/26/17	14/33/18	15/84/21
	200	31/68/39	30/66/37	31/68/39	36/78/42
BAND	3	7/64/12	9/20/13	7/64/12	7/64/12
	50	19/670/26	15/278/23	19/670/26	<i>F</i>
	100	18/712/27	16/373/26	18/712/27	<i>F</i>
	500	18/677/26	16/339/27	18/677/26	<i>F</i>
LIN	1000	1/3/3	1/3/3	1/3/3	1/3/3
LIN1	10	1/3/3	1/3/3	1/3/3	1/3/3

The step length α_k in all methods is determined such that the strong Wolfe-Powell conditions (31) and (32) hold with $\delta = 0.01$ and $\sigma = 0.1$.

The test problems are drawn from [14]. The numerical results of our tests are reported in Table I.

The column problem represents the problem name in [14], Dim represents the dimension of the problems. The numerical results are given in the form of $I/F/G$, where I , F , and G denote the numbers of iterations, function evaluations and gradient evaluations, respectively. The stopping condition is $\|g_k\| \leq 10^{-6}$. Since we want to compare the

performance of the different methods, in the numerical results, we omit the problems if all the four methods perform equally. The notation *F* means that, for this problem, the corresponding method fails.

5. Conclusions

In this paper, based on β_k^{DY} and β_k^{DL} , a new formula is proposed to compute the parameter β_k of the conjugate gradient methods. The main motivations are to improve both

the convergence properties and numerical behavior of the conjugate gradient method. For general conjugate gradient methods, in order to get the global convergence results, the methods are required to possess the following major properties:

- (1) the generated directions d_k are descent directions;
- (2) the parameters β_k are nonnegative.

In addition, to ensure that the methods have robust and efficient numerical behavior, the parameter β_k needs to approach zero, when the small step s_k occurs.

From the convergence analysis of this paper, we know that the directions d_k generated by MDL method are descent directions, which is not true for DY or DL methods, and the proposed MDL method is globally convergent for general functions. In the previous section, we compare the numerical performance of the MDL method with the DY, MHS, and DL methods. From the convergence analysis and numerical results, comparing with the DL, DY, and MHS method, we can have the following.

- (a) MDL method versus DL method: from the computational point of view, for most of the test problems, MDL method performs quite similarly with DL method. There are 15 problems in which MDL method outperforms the DL method and 18 problems in which DL method outperforms the MDL method. But, from the convergent point of view, the MDL method outperforms the DL method.
- (b) MDL method versus DY method: the convergence properties of MDL method are similar to DY method. By comparing the numerical results of MDL method with DY method, there are 27 test problems in which MDL method outperforms the DY method and only 4 test problems in which DY method outperforms the MDL method. Therefore, we could say that MDL method is much better than the DY method in numerical behavior.
- (c) MDL method versus MHS method: they possess similar convergence properties; the numerical results show that MDL method performs little better than the MHS method.

Acknowledgments

This research was supported by Guangxi High School Foundation Grant no. 2013BYB210 and Guangxi University of Finance and Economics Science Foundation Grant no. 2013A015.

References

- [1] G. Zoutendijk, "Nonlinear programming, computational methods," in *Integer and Nonlinear Programming*, J. Abadie, Ed., pp. 37–86, North-Holland Publishing, Amsterdam, 1970.
- [2] M. J. D. Powell, "Restart procedures for the conjugate gradient method," *Mathematical Programming*, vol. 12, no. 2, pp. 241–254, 1977.
- [3] M. J. D. Powell, "Nonconvex minimization calculations and the conjugate gradient method," in *Numerical Analysis*, vol. 1066 of *Lecture Notes in Mathematics*, pp. 122–141, Springer, Berlin, Germany, 1984.
- [4] Y.-H. Dai and L.-Z. Liao, "New conjugacy conditions and related nonlinear conjugate gradient methods," *Applied Mathematics and Optimization*, vol. 43, no. 1, pp. 87–101, 2001.
- [5] J. C. Gilbert and J. Nocedal, "Global convergence properties of conjugate gradient methods for optimization," *SIAM Journal on Optimization*, vol. 2, no. 1, pp. 21–42, 1992.
- [6] G. Li, C. Tang, and Z. Wei, "New conjugacy condition and related new conjugate gradient methods for unconstrained optimization," *Journal of Computational and Applied Mathematics*, vol. 202, no. 2, pp. 523–539, 2007.
- [7] Z. Wei, S. Yao, and L. Liu, "The convergence properties of some new conjugate gradient methods," *Applied Mathematics and Computation*, vol. 183, no. 2, pp. 1341–1350, 2006.
- [8] Y. Shengwei, Z. Wei, and H. Huang, "A note about WYL's conjugate gradient method and its applications," *Applied Mathematics and Computation*, vol. 191, no. 2, pp. 381–388, 2007.
- [9] H. Huang, S. Yao, and H. Lin, "A new conjugate gradient method based on HS-DY methods," *Journal of Guangxi University of Technology*, no. 4, pp. 63–66, 2008.
- [10] L. Zhang, "An improved Wei-Yao-Liu nonlinear conjugate gradient method for optimization computation," *Applied Mathematics and Computation*, vol. 215, no. 6, pp. 2269–2274, 2009.
- [11] L. Zhang, "Further studies on the Wei-Yao-Liu nonlinear conjugate gradient method," *Applied Mathematics and Computation*, vol. 219, no. 14, pp. 7616–7621, 2013.
- [12] Z. Dai and F. Wen, "Another improved Wei-Yao-Liu nonlinear conjugate gradient method with sufficient descent property," *Applied Mathematics and Computation*, vol. 218, no. 14, pp. 7421–7430, 2012.
- [13] Y. Dai, J. Han, G. Liu, D. Sun, H. Yin, and Y.-X. Yuan, "Convergence properties of nonlinear conjugate gradient methods," *SIAM Journal on Optimization*, vol. 10, no. 2, pp. 345–358, 1999.
- [14] J. J. Moré, B. S. Garbow, and K. E. Hillstom, "Testing unconstrained optimization software," *ACM Transactions on Mathematical Software*, vol. 7, no. 1, pp. 17–41, 1981.

Research Article

Path Transmissibility Analysis Considering Two Types of Correlations in Hydropower Stations

Baoping Zhi and Zhenyue Ma

School of Hydraulic Engineering, Faculty of Infrastructure Engineering, Dalian University of Technology, Room 330, Building 3 of Lab, Dalian, Liaoning Province 116023, China

Correspondence should be addressed to Zhenyue Ma; dmzy@dlut.edu.cn

Received 16 May 2013; Accepted 4 August 2013

Academic Editor: Daniel Dias-da-Costa

Copyright © 2013 B. Zhi and Z. Ma. This is an open access article distributed under the Creative Commons Attribution License, which permits unrestricted use, distribution, and reproduction in any medium, provided the original work is properly cited.

A new vibration model is built by introducing the head-cover vibration transfer path based on a previous analysis of the vertical vibration model for hydropower station units and powerhouses. This research focuses on disturbance- and parameter-related transfer paths in a practical situation. In a complex situation, the application of the stochastic perturbation method is expanded using an algebra synthesis method the Hadamard product, and theoretical analyses, and numerical simulations of transfer paths in the new vibration model are carried out through the expanded perturbation method. The path transfer force, the path transmissibility, and the path disturbance ranges in the frequency domain are provided. The results indicate that the methods proposed in this study can efficiently reduce the disturbance range and can accurately analyze the transfer paths of hydraulic-source vertical vibration in hydropower stations.

1. Introduction

Hydraulic vibration is the main vibration source in hydropower station units and powerhouses. The vertical vibration in units is usually caused by hydraulic pressure fluctuations or other loads on the water turbine's flow passage components. Field and model tests have shown that there are three main vibration transfer paths running from the water turbine to the powerhouse [1]: (1) runner-shaft-bearing-fixed components (machine frame, head-cover-powerhouse); (2) flow pressure-spiral case-powerhouse; and (3) runner-runner negative pressure region-head cover-powerhouse. Previous studies concerning the vertical vibration produced by a hydraulic source mainly focus on path (1), while the effects of paths (2) and (3) are usually ignored [2]. However, as the scale and capacity of hydropower stations increase, the flow passage area of the head-cover system continually increases, with corresponding increases in the vibration of the head-cover system. Therefore, the influence of the head-cover system becomes more important in the hydraulic vibration transfer path, and ignoring path (3) will produce a larger error. Therefore, it is imperative that the contribution of path (3) should be analyzed; more specifically, the contribution of the

vibration of the head-cover system of the hydropower station vertical vibration transfer should be analyzed. However, due to the presence of randomness, it is difficult to clearly and accurately describe the contribution of this transfer path to the structural vibration.

Theoretical analyses of the vibration transfer path can be classified as a stochastic structural system problem. At present, the Monte-Carlo numerical simulation method (MCSM) [3, 4] and the perturbation method [5–7] are the most popular analysis methods. MCSM is used less frequently because of the large amount of computation required when dealing with a large-scale structure. Conversely, the perturbation method is applied by many researchers in various fields. Collins and Thompson [8] initially employed the perturbation method to analyze stochastic dynamical systematic characteristics in 1969; the perturbation method was later employed in a static analysis by Hisada and Nakagiri [9] and in a dynamic analysis by Liu et al. [10]. Kronecker algebra was introduced to the expansion of the perturbation method by Vetter [11]. After several decades of development, relevant studies on perturbation theory were quite abundant. The primary methods included the L-P method [12], the multiple scale method [13, 14], the average method [15], the KBM

(Krylov-Bogoliubov-Mitropolsky) method [15, 16] and the singular perturbation method [17, 18]. Recent developments include the homotopy perturbation method [19]. In the analysis of transfer paths combined with the perturbation method, Zhang et al. built a theoretical model for vibration transfer path analysis by implementing the perturbation method with Kronecker algebra in the static analysis [20], the dynamic analysis [21] and the reliability analysis [22, 23]. This model has been used for the analysis and design of mechanical components. Computations of the transfer path considering multi-vibration sources have been carried out by Zhao and Zhang [24] based on Zhang's research. These results have been used for isolation vibration analysis. The above research studies focus on additive disturbance analysis. Using multiplicative disturbance analysis, Gao et al. separately analyzed the dynamical characteristics of a truss structure by using the interval factor method [25], the random factor method [26], and nonstationary random excitation [27]. Ma et al. conducted a dynamical characteristic analysis of a linear [28] and nonlinear [29] truss structure using fuzzy variables. In 2010, a two-factor method was proposed by Ma et al. [30], which considers two multiplicative disturbances. However, because of the limitations of these methods, they have not been applied to transfer path analysis with respect to a multiplicative disturbance. Furthermore, previous studies have not jointly analyzed these two types of disturbances. In practice, the two types of disturbances always exist together, and there are some correlations between these two disturbances. There are some correlations among the parameters of the structure as well. Thus, the previous studies were not based on an accurate analysis because they only considered a single disturbance, neglected the correlations between disturbances, or neglected the correlations among parameters. Therefore, it is necessary to jointly analyze the problem of the vibration transfer path of time-invariable parameters for the two types of disturbances and their related parameters. Only a few studies have reported on the two types of correlations in perturbation theory. Previous studies on correlations ignored the two types of correlation or converted relevant variables into irrelevant variables. These analyses did not consider the effects of correlations and thus were not rigorous. At present, only a few researchers have attempted to explore this aspect. Some examples include studies on molecular chemistry [31], nuclear physics [32], and vocal vibration [33, 34]. Of these studies, only the study on vocal vibration considered the correlation parameters, but it did not involve the perturbation method. At present, there are few available studies on structural analysis. Pirrotta [35] conducted a perturbation analysis of delta-correlated processes, but he did not study the correlation between parameters; Ambrogio [36] described the correlations by considering the correlation coefficient between additive and multiplicative disturbances for one parameter, but he also did not refer to the correlation between parameters. Husain et al. [37] solved the problem of parameter correlation, but they only considered computational results and did not extend their results to improve the perturbation method. Khodaparast et al. [38] corrected the structure variation model, but they ignored the correlation between modified parameters and measurement values. This study

focuses on the application of perturbation theory with two types of correlation from the perspective of structure analysis.

Hydropower station units and powerhouses are large-scale structures. Most of the parameters' disturbances should be less than 10% of their mean values in such a large structure. Therefore, problems regarding hydropower stations can be solved by the perturbation method. First, the head-cover system is introduced, which has the same vibration source as a path (1); the elastic foundation constraint is selected; and a new vibration model is built on the basis of the previous vertical vibration model. Furthermore, a method for solving the path transfer force is proposed using the general method of dynamic analysis. Second, for the test signal, correlations between the two types of disturbances and correlations between the parameters are considered based on the single disturbance vibration path analysis. By using the coefficient of variation algebra synthesis method [39], Kronecker algebra [11], and the Hadamard product [40], gradient-sorting estimations of the transfer paths in the frequency domain are carried out, and methods for determining the transfer force and transmissibility and their disturbances are proposed. Finally, the method described in this paper is verified using the model of a large hydropower station.

2. Analysis Model with the Introduction of a Head-Cover System

For a hydroelectric generating unit, regardless of whether it has a suspension or umbrella structure, the weight of its rotating parts is successively transferred to the reinforced concrete machine foundation through the thrust bearing, frame (suspension units containing the stator frame), and sole screw. The head-cover system is always fixed on the base ring strengthening plate, and the head-cover system and the strengthening plate are considered to be one part. Taking a vertical vibration characteristic analysis of the umbrella unit as an example, the model contains a shaft system, thrust bearing, and lower bracket (see Figure 1). The heavy shaft can be simplified as a massless elastic continuous beam, and then its mass can be regarded as a mass attached to three nodes, m_1 , m_2 , and m_3 . m_1 can be defined as the mass of the excitation rotor and the shaft, the half shafting mass, which is measured from the heavy shaft top to the rotor frame, and another mass added on top of the heavy shaft; m_2 can be defined as the mass of the central body of the rotor frame, the half mass of the whole gate arm, and the half mass of the whole shaft; and m_3 can be defined as the mass of the water, turbine runner, the additional mass of water and the half shafting mass, which is measured from the rotor frame to the hydraulic turbine. The rotor gate arm can be simplified as a massless elastic continuous rod, and then its mass can be assigned to the runner margin and the central body of the rotor frame. k_4 can be defined as the sum of the vertical stiffness of the whole gate arm, and m_4 can be defined as the lumped mass of the runner margin. The outer end of the lower bracket is fixed to the concrete foundation. The lower bracket gate arm can then be simplified as a gravity-free beam if the coupling effect of the foundation is ignored. k_{52} can be defined as the vertical

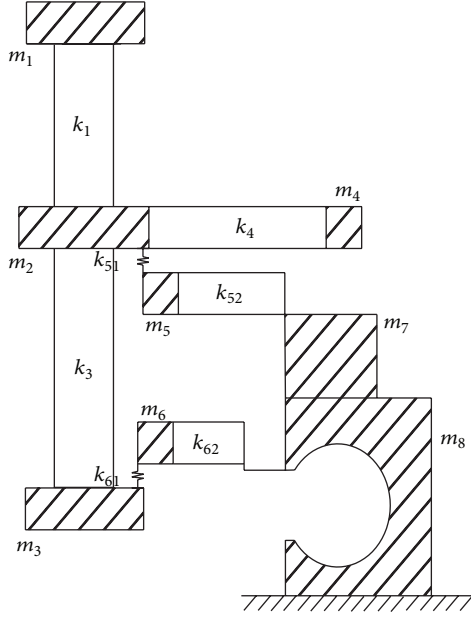


FIGURE 1: Simplified model of the coupling system between the umbrella unit and the powerhouse.

stiffness of the lower bracket gate arm. m_5 can be defined as the lumped mass of one end of the lower bracket, which is close to the heavy shaft, and the half mass of the gate arm; m_5 can be connected to m_2 by the thrust bearing, which is simplified by an equivalent stiffness k_{51} .

With the introduction of the head-cover system, the vibration transfer path is as follows: first, the hydraulic vertical vibration is transferred to the head cover by the heavy shaft seal and guide bearing in the water turbine runner chamber; next, the vibration is transferred from the head cover to the spiral case base ring strengthening plate, which is connected to the outer end of the head cover; and finally, the vibration is transferred to the machine foundation by the wrapped concrete outside the spiral case. Ignoring the coupling effect, the control parts and other additional parts

on the head cover can be regarded as the attached mass of the head-cover system. As the lumped mass is close to the heavy shaft, m_6 can be defined as the mass of the central body and the half mass of the whole head-cover system. The head-cover system can be simplified as a gravity-free beam, and k_{62} can be defined as the vertical stiffness. m_6 can be connected to m_3 by the sealing spring, which lies between the head-cover structure and the water turbine runner. The vertical stiffness of the connection can be simplified by an equivalent stiffness k_{61} .

k_{51} is the series stiffness of the elastic oil tank stiffness (thrust bearing support system) and the oil film stiffness. k_{61} is the series stiffness of the sealing structure stiffness and the clearance water stiffness. These two parameters exhibit a linear relationship because the unit's axial water thrust varies with the unit's conditions. However, k_{51} and k_{61} are simplified as a single stochastic variable in this study.

In the process of examining the unit's vertical vibration, the machine foundation pier can be regarded as an elastic foundation. The structure can be treated as a single node, m_7 , which ranges from the machine foundation pier to the concrete floor in the turbine layer. The structure can be treated as a single node, m_8 , which ranges from the turbine layer to the foundation. The stiffness of this structure is replaced by the equivalent stiffness, which is based on the strengthening plate, spiral structure, and concrete structure. Thus, the hydropower station base is treated by dividing it into two nodes at the connection of the head-cover system and the hydropower station base, where k_{62} is only connected to m_8 .

For the entire model, the form and meaning of the dampness matrix are similar to those of the stiffness matrix. Assuming that the system is linear, the differential equation of the vibration is found from the Lagrange equation:

$$\mathbf{M}\ddot{\mathbf{u}} + \mathbf{C}\dot{\mathbf{u}} + \mathbf{K}\mathbf{u} = \mathbf{F}(t). \quad (1)$$

By merging these dynamical balance equations for the shaft, the rotor, the lower bracket, the head-cover system, and the machine foundation pier, an equation with 8 degrees of freedom and 26 parameters can be obtained, and the total stiffness matrix can be written as

$$\mathbf{K} = \begin{pmatrix} k_1 & -k_1 & 0 & 0 & 0 & 0 & 0 & 0 \\ -k_1 & k_1 + k_3 + k_4 + k_{51} & -k_3 & -k_4 & -k_{51} & 0 & 0 & 0 \\ 0 & -k_3 & k_3 + k_{61} & 0 & 0 & -k_{61} & 0 & 0 \\ 0 & -k_4 & 0 & k_4 & 0 & 0 & 0 & 0 \\ 0 & -k_{51} & 0 & 0 & k_{51} + k_{52} & 0 & -k_{52} & 0 \\ 0 & 0 & -k_{61} & 0 & 0 & k_{61} + k_{62} & 0 & -k_{62} \\ 0 & 0 & 0 & 0 & -k_{52} & 0 & k_{52} + k_7 & -k_7 \\ 0 & 0 & 0 & 0 & 0 & -k_{62} & -k_7 & k_{62} + k_7 + k_8 \end{pmatrix}. \quad (2)$$

The total mass matrix is obtained from the lumped mass:

$$\mathbf{M} = \text{diag}\{m_1, m_2, m_3, m_4, m_5, m_6, m_7, m_8\}. \quad (3)$$

Generally, the characteristics of the vertical vibration source in the hydropower station are unique position, simple

contact surface with structure, and few ingredients. Conversely, the characteristics of the lateral (radial) vibration are multipositions, strong nonlinear contact surface, and complex excitation. For simplifying the model and the calculation, the total structure of the unit's powerhouse is considered as suffering vertical harmonic excitation. The vertical

harmonic excitation is located on the water turbine runner, and the response of the total structure is in a steady state. In addition, the initial phase remains constant throughout the whole process. Setting the steady-state response as $u_i(t) = \bar{U}_i e^{i(\omega t + \varphi_i)}$ and $U_i = \bar{U}_i e^{i\varphi_i}$ yields

$$\begin{aligned} u_i(t) &= U_i e^{i\omega t}, & \dot{u}_i(t) &= i\omega U_i e^{i\omega t}, \\ \ddot{u}_i(t) &= -\omega^2 U_i e^{i\omega t}, \end{aligned} \quad (4a)$$

$$\mathbf{U} = \{u_1, u_2, u_3, u_4, u_5, u_6, u_7, u_8\}^T, \quad (4b)$$

$$\mathbf{F}(t) = \{0, 0, F_0 e^{i\omega t}, 0, 0, 0, 0, 0\}^T. \quad (4c)$$

Substituting (4a)–(4c) into (1) gives the dynamical balance equation of the hydropower station's vertical vibration with the head-cover system in the frequency domain:

$$(-\omega^2 \mathbf{M} + i\omega \mathbf{C} + \mathbf{K}) \mathbf{U} = \mathbf{F}(t). \quad (5)$$

The response vector \mathbf{U} at each node of the structure was obtained by numerical calculations. F_{zhou} and F_{ding} denote the forces that are transferred to the machine foundation pier from the water turbine by the shaft system and the head-cover system, respectively, and can be written as

$$\begin{aligned} F_{\text{zhou}} &= k_{\text{zhou}}(u_3 - u_7) + c_{\text{zhou}}(\dot{u}_3 - \dot{u}_7) \\ &= (k_{\text{zhou}} + i\omega c_{\text{zhou}})(U_3 - U_7) e^{i\omega t}, \end{aligned} \quad (6a)$$

$$\begin{aligned} F_{\text{ding}} &= k_{\text{ding}}(u_3 - u_7) + c_{\text{ding}}(\dot{u}_3 - \dot{u}_7) \\ &= (k_{\text{ding}} + i\omega c_{\text{ding}})(U_3 - U_7) e^{i\omega t}. \end{aligned} \quad (6b)$$

In (6a)–(6b), k_{zhou} and c_{zhou} denote the path stiffness and the path dampness of the vibration path through the shaft system, respectively. Similarly, k_{ding} and c_{ding} denote the path stiffness and the path dampness through the head-cover system, respectively. When calculating the path stiffness and dampness of the shaft system, m_1 and m_4 are treated as dynamic vibration absorbers with dampness.

3. Vibration Path Sorting Considering Two Types of Correlations

In the analysis of a hydropower station, parameters such as the stiffness, mass, and dampness are attributed to the multiplicative disturbances arising from the material properties, manufacturing technology, and other factors. These parameters, obtained by measurement, are attributed to the additive disturbances due to the testing noise and environmental noise. Furthermore, because the testing method and environment are the same for every parameter, the two disturbances of each parameter are interrelated. These parameters are also interrelated by means of continuous structure discretization.

Given the factors mentioned above, the mass, stiffness, and dampness are described as a random vector \mathbf{a} with n random variables, where every random variable involves two

types of disturbances. When the variable disturbance is lower than 15% of the mean value, the stochastic variable can be expressed as

$$a_i = a_i^1 a_i^d + a_i^2. \quad (7)$$

In (7), a_i denotes the i th element in the random vector \mathbf{a} . a_i^1 and a_i^2 denote the multiplicative and additive disturbance of the random variable a_i , respectively. Assuming that their mean values are 1 and 0, respectively, a_i^d denotes the deterministic component of a_i , which represents the mean value after multiple samplings.

According to the coefficient of variation algebra synthesis method [40], calculating the mathematical expectation and variance of (7) yields

$$\begin{aligned} E_{a_i} &= E[a_i^1 a_i^d + a_i^2] = E(a_i^1 a_i^d) + E(a_i^2) = a_i^d, \\ \sigma_{a_i}^2 &= \text{Var}(a_i) = E[(a_i - E_{a_i})^2] \\ &= E[(a_i^1 - a_i^d) a_i^d + a_i^2]^2 \\ &= (a_i^d)^2 \sigma_{a_i^1}^2 + \sigma_{a_i^2}^2 + 2a_i^d \text{Cov}(a_i^1, a_i^2), \end{aligned} \quad (8)$$

where

$$\text{Cov}(a_i^1, a_i^2) = \rho_{a_i^1, a_i^2} \sigma_{a_i^1} \sigma_{a_i^2}, \quad (9)$$

where $\rho_{a_i^1, a_i^2}$ is the correlation coefficient of the multiplicative and additive disturbances contained in the parameter a . If these parameters are interrelated, then

$$\text{Cov}(a_i, a_j) = \rho_{a_i, a_j} \sigma_{a_i} \sigma_{a_j}, \quad (10)$$

where ρ_{a_i, a_j} is the correlation coefficient of the random variables a_i and a_j . Generally, if the random variables follow a normal distribution, their linear transformations and multiplication will also follow a normal distribution. For example, if the vector \mathbf{a} follows a normal distribution, then the function $F_i(\mathbf{a})$ will follow a normal distribution. Using the Taylor expansion, expanding the transfer force F_i at the mean value F_i^d yields

$$\begin{aligned} F_i &= F_i^d + \frac{\partial F_i^d}{\partial \mathbf{a}^T} (\mathbf{a} - \mathbf{a}^d) + O(\mathbf{a}^p) \\ &= F_i^d + \frac{\partial F_i^d}{\partial \mathbf{a}^T} \mathbf{a}^p + O(\mathbf{a}^p), \end{aligned} \quad (11)$$

where

$$\mathbf{a}^p = \mathbf{a} - \mathbf{a}^d = (\mathbf{a}^1 - 1) \mathbf{a}^d + \mathbf{a}^2. \quad (12)$$

Neglecting components of the second order and above, the disturbance of the transfer force is

$$F_i^p = \sum_{k=1}^m \frac{\partial F_i^d}{\partial a_k} a_k^p. \quad (13)$$

In (13), $\partial F_i^d / \partial a_k$ is the partial derivative of F_i with respect to the random variable a_k , which is also the first-order sensitivity of a_k . The covariance of F_i^p and F_j^p is

$$\begin{aligned} \text{Cov}(F_i, F_j) &= E[F_i^p F_j^p] \\ &= E \left[\left(\sum_{k=1}^m \frac{\partial F_i^d}{\partial a_k} a_k^p \right) \left(\sum_{l=1}^m \frac{\partial F_j^d}{\partial a_l} a_l^p \right) \right]. \end{aligned} \quad (14)$$

That is,

$$\begin{aligned} \text{Cov}(F_i, F_j) &= \sum_{k=1}^m \sum_{l=1}^m \frac{\partial F_i^d}{\partial a_k} \frac{\partial F_j^d}{\partial a_l} E(a_k^p a_l^p) \\ &= \sum_{k=1}^m \sum_{l=1}^m \frac{\partial F_i^d}{\partial a_k} \frac{\partial F_j^d}{\partial a_l} \text{Cov}(a_k, a_l). \end{aligned} \quad (15)$$

Equation (16) shows that $\text{Cov}(F_i, F_j)$ of the transfer force F_i and F_j can be expressed by $\text{Cov}(a_k, a_l)$ of the random structure parameter:

$$\text{Cov}(F_i, F_j) = \sum_{i=1}^m \sum_{j=1}^m \frac{\partial F_i^d}{\partial a_k} \frac{\partial F_j^d}{\partial a_l} \rho_{a_k, a_l} \sigma_{a_k} \sigma_{a_l}. \quad (16)$$

If $i = j$,

$$\sigma_{F_i}^2 = \text{Cov}(F_i, F_i) = \sum_{k=1}^m \sum_{l=1}^m \frac{\partial F_i^d}{\partial a_k} \frac{\partial F_i^d}{\partial a_l} \rho_{a_k, a_l} \sigma_{a_k} \sigma_{a_l}. \quad (17)$$

According to Kronecker algebra [11], the corresponding stochastic analysis theory and Hadamard product [41] yield

$$\sigma_{F_i}^2 = \left| \frac{\partial F_i^d}{\partial \mathbf{a}^T} \right|^{[2]} \left(\overline{\rho} \circ (\sigma_a)^{[2]} \right), \quad (18)$$

where the subscript [2] denotes the Kronecker power; that is, $a^{[2]} = a \otimes a$; if a is of order $n \times 1$, then $a^{[2]}$ is of order $n^2 \times 1$. $\overline{\rho}$ is the stacking vector of the matrix of correlation coefficients, which is also of order $n^2 \times 1$. The symbol \circ denotes the Hadamard product. Therefore, $\sigma_{F_i}^2$ is of order 1×1 .

The sensitivity matrix $|\partial F_i^d(a) / \partial \mathbf{a}^T|$ of the transfer force of each parameter is

$$\left| \frac{\partial F_i^d}{\partial \mathbf{a}^T} \right| = \left[\frac{\partial F_i^d}{\partial a_1} \quad \dots \quad \frac{\partial F_i^d}{\partial a_n} \right]. \quad (19)$$

Substituting (19) into (18), the variance of the transfer force F_i for each path can be calculated. Equation (11) only involves the first-order Taylor expansion. A higher-order Taylor expansion will improve the accuracy, but it involves complicated mathematical calculations. Equation (18) shows that the transfer force variance can be directly obtained from the random variables' numerical characteristics. The calculations can thus be simplified because the sample is not included in the mathematical operations. The correlations between parameters are merely modified in (18) and do not

increase the number of calculations required. The transmissibility is defined as the ratio of the amplitudes between the transfer force and the vibration source excitation force:

$$\beta_i = \left| \frac{F_i}{F_0} \right|. \quad (20)$$

Neglecting the disturbance of the excitation force F_0 , based on the random variable algebra synthesis method, the expectation, variance, and transfer coefficient of the transmissibility can be written as

$$E_\beta = E[\beta(a)] = \frac{E(F_i)}{E(F_0)}, \quad (21a)$$

$$\sigma_\beta^2 = \frac{E[F_i]^2}{E[F_0]^2} \left| \frac{\text{Var}[F_i]}{[E(F_i)]^2} \right|, \quad (21b)$$

$$\theta = \frac{E_\beta}{\sigma_\beta}. \quad (21c)$$

The result of a random variable that follows a normal distribution divided by a constant also follows a normal distribution. $E[F_0]$ and $E[F_i]$ are known in the deterministic system, so the variance of the transmissibility will follow a normal distribution. The transfer coefficient is the transfer efficiency of the excitation force. The gradient sorting of the vibration path transmissibility in the frequency domain can be obtained by changing the frequency of the excitation force.

A solution of the vibration transfer path for the two types of disturbances and correlations is proposed based on the above methods. The path transmissibility and its probabilistic characteristic are provided. In this study, the solution only involves the first-order sensitivity of the random parameter and the probabilistic characteristic of the random variable. Additionally, the introduction of the two types of correlations does not involve excessive calculations. Therefore, the calculation accuracy is improved for practical problems.

4. Example Analysis

The main structure of the umbrella unit in a large hydropower station is shown in Figure 2, and the simplified model of transfer path is shown in Figure 1. In this example, the effect of the spiral case and substructure is ignored [41, 42] because their effect is far less than that of the upper structure. The excitation is assumed to be a simple harmonic excitation. The mean values of the random parameters can be obtained from the hydropower station design diagrams. These mean values are $m_1 = 8.28 \times 10^4$, $m_2 = 1.042 \times 10^6$, $m_3 = 3.29 \times 10^5$, $m_4 = 9 \times 10^5$, $m_5 = 1.2 \times 10^5$, $m_6 = 1.15 \times 10^5$, $m_7 = 1.39 \times 10^5$ and $m_8 = 8.92 \times 10^5$, in units of kg; $k_1 = 7.26 \times 10^{10}$, $k_3 = 5.72 \times 10^{10}$, $k_4 = 2.32 \times 10^{10}$, $k_{51} = 2.20 \times 10^{12}$, $k_{52} = 9.41 \times 10^9$, $k_{61} = 1.73 \times 10^8$, $k_{62} = 1.73 \times 10^{10}$, $k_7 = 7.70 \times 10^9$, and $k_8 = 4.26 \times 10^8$, where the unit of the stiffness k is N/m; and $c_1 = 5.48 \times 10^6$, $c_3 = 4.11 \times 10^6$, $c_4 = 1.02 \times 10^7$, $c_{51} = 2.57 \times 10^7$, $c_{52} = 7.51 \times 10^5$, $c_{61} = 2.23 \times 10^5$, $c_{62} = 9.99 \times 10^4$, $c_7 = 1.64 \times 10^6$, and $c_8 = 9.74 \times 10^5$, where the unit of the dampness c is N · s/m. Each parameter comprises

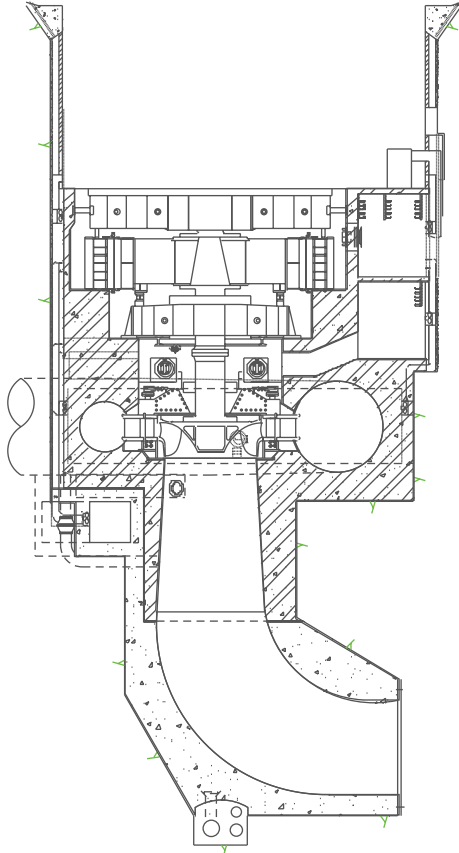


FIGURE 2: Cutaway view of the main structure of hydropower.

two disturbances that follow a normal distribution. The multiplicative disturbance is related to the difficulty of obtaining the parameters. The multiplicative variance coefficients of k_{51} (including the vertical stiffness of the thrust bearing) and k_{61} (the sealing equivalent vertical stiffness between the head cover and runner) are set to 0.10. The equivalent bending rigidity of k_{62} s multiplicative variance coefficient is set to 0.075 because there are many uncertain factors in the control components and other attached components on the head cover. The multiplicative random variance coefficients of the other parameters are set at 0.05. The additive disturbance is related to the measurement range. The standard deviations of the additive random variable with respect to mass and stiffness are set at 10^4 and 10^8 , respectively, according to each parameter's mean value. The variance coefficient of damping is similar to that of the mass and stiffness. In this example, the parameters' disturbances are generated by a function in the MATLAB software, and the sample size is 10000 for each disturbance. All errors are determined to be smaller than 0.1% by comparing the variances and mean values of the generated samples with the corresponding set values. Therefore, the generated sample variances and mean values are used in the study. The correlation function is determined by the generated function. The partial derivative is calculated by the software Mathematica. The coefficient correlation of the generated sample is 0.0329.

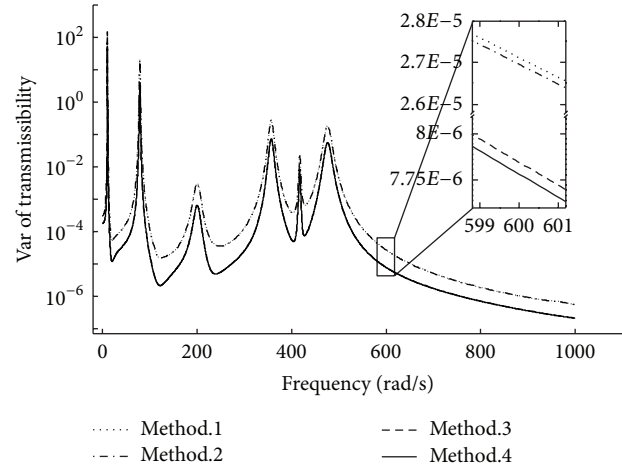


FIGURE 3: Head-cover transmissibility variances in the frequency domain as predicted by the four methods.

Figure 3 displays the transmissibility variances of the head-cover transfer path obtained using different methods. Method 1 does not involve the two types of correlations. The Monte-Carlo simulation is not used in method 1 (due to the inclusion of 26 random variables and because the calculation time is too long, this method only focuses on how each group of variables changes with time, that is, the number of calculations is equal to the sample size). Method 2 (following the method developed by W. J. Vetter in 1973) only involves the correlation with respect to one parameter, which involves the correlations between the disturbances of the parameters. Method 3 (similar to method 2) involves the correlations between parameters instead of the correlations between the disturbances of the parameters. Method 4 involves both types of correlations. The results for method 4 are obtained from (18). Figure 3 displays the characteristic curve of the head-cover system transmissibility variances in the frequency band of 0–1000 rad/s. Figure 4 presents the optimal curve of the two types of correlations for the transmissibility variance range as the correlation coefficient changes. This figure contains two curves: the disturbance curve, which describes the mean values of the results of method 2 subtracted from method 1 and the results of method 4 subtracted from method 3, and the parameter curve, which is similar to the disturbance curve.

Figures 3 and 4 show the following results: (1) compared to the other methods, the variance range for the method that contains two types of correlations is the smallest. This finding indicates that this method significantly decreases the disturbance range under theoretical calculations. The path transmissibility variance decreases by 72.51%. (2) In optimizing the method considering correlations between the disturbances and variances, the range merely decreases by 0.644%. This small decrease may have arisen because the difference between the additive and multiplicative disturbances is large, and the optimizing function is weak. (3) The optimization effect is significant for the method considering the correlations between parameters. The variance range

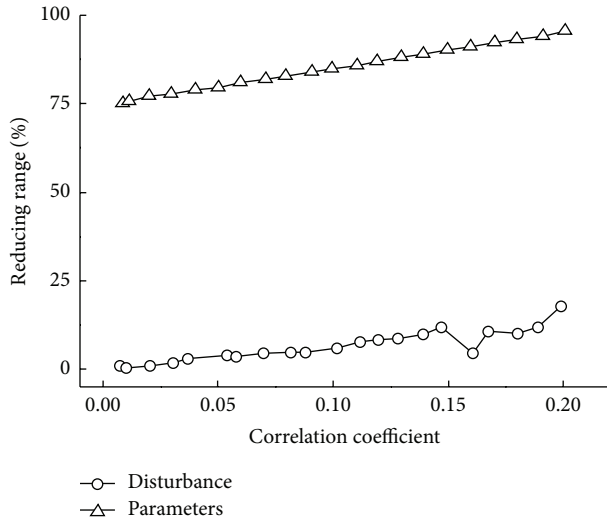


FIGURE 4: Optimization range of the correlation coefficient characteristic curve.

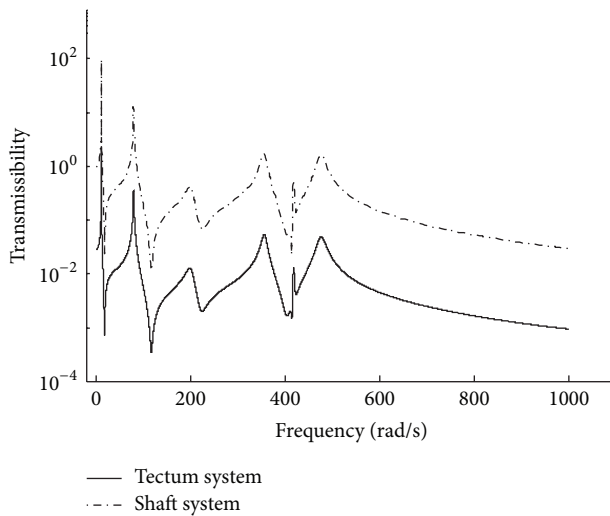


FIGURE 5: Path transmissibility of the excitation frequency curve.

decreases by 75.71% when the correlation coefficient is 0.0085. Thus, neglecting this type of correlation leads to an inaccurate analysis. (4) As the correlation coefficient increases, the optimization of the transmissibility variance is more efficient, and the effect on the disturbance range is more significant. This result demonstrates that the relationship between the optimization range and the correlation coefficients for the parameters is linear and that the relationship between the optimization range and the correlation coefficients for the disturbances is proportional. However, the latter relationship does exhibit some fluctuations.

Figure 5 compares the characteristic curve for each path transmissibility, β_i , to the excitation frequency. This curve shows the ratio between the forces that are transmitted to the machine pier by the corresponding paths and the excitation force of the water turbine hydraulic source. This ratio is

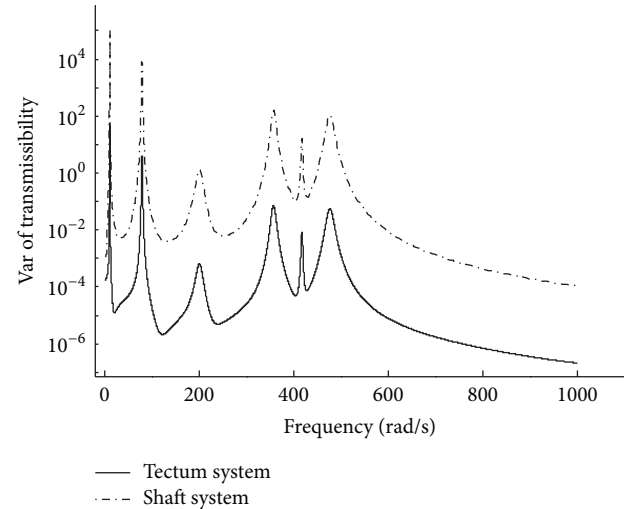


FIGURE 6: Variance of the path transmissibility of the excitation frequency characteristic curve.

equivalent to the amplification coefficient. The curve indicates two results: (1) resonance occurs when the frequency of the excitation force is the same as the natural frequency. The transmissibility reaches its maximum value for each path at this frequency. This result indicates that the path has a large effect on the structural vibration at this frequency. (2) Considering the whole process of vertical vibration transfer, the transmissibility of the head cover is significantly smaller than that of the shafting system. Throughout the entire frequency range, the mean value of the path transmissibility ratio is 32.37. This value indicates that the vibration effect of the head-cover system can be neglected in accurate calculations.

Figure 6 shows that the characteristic curve of the transmissibility variance varies with the excitation frequency for the two types of correlations. This curve reflects the diversion of the transmissibility and indicates the following findings. (1) The path transmissibility variance of the shaft system is greater than that of the head-cover system due to the large number of components and the randomness of these components' parameters. Thus, the variance of a structure with a high level of parameter randomness is large in the transfer path. (2) The variance maximum occurs at the natural frequency. This frequency is determined by the structural parameter, which accounts for the parameter contribution of every transfer path, enabling the transfer force to be obtained from the expectation and variance of the transmissibility.

Figure 7 shows that the characteristic curve of the transfer coefficients varies with the excitation frequency for the two types of correlations. This curve reflects the transfer efficiency of the excitation force. The figure shows that the transfer efficiency of the head-cover system is more efficient than that of the shafting system. Therefore, more attention should be given to the assigned vibration proportion of the shaft and head-cover system in a design.

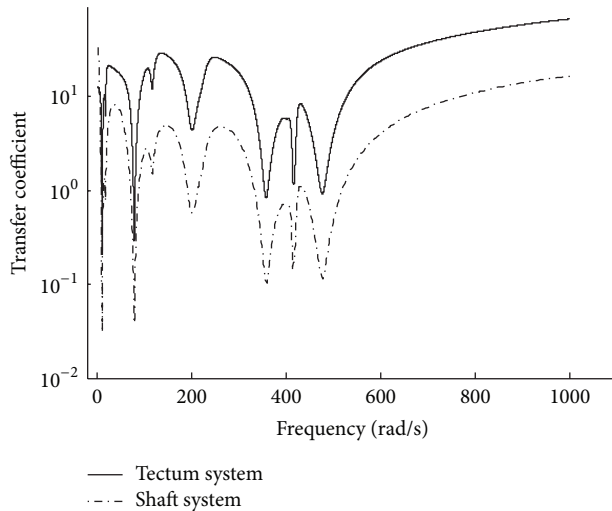


FIGURE 7: Transfer coefficient of the paths of the excitation frequency characteristic curve.

5. Conclusions

- (1) The multivibration source, multipath vibration model, is improved with respect to the coupling effect between hydropower station units and powerhouses by the introduction of a head-cover system. The scalar expression of each vibration transfer path is provided in this study.
- (2) A perturbation analysis of the transfer path is carried out by using a test signal. A complex situation with two types of correlations is considered. Kronecker algebra, the Hadamard product, and probabilistic statistics are employed to develop an analysis method for the transfer path. In the solution process, excessive additional computations are not required because only the numerical characteristics of the random variables are used. The application of the stochastic perturbation method is expanded, and a method for analyzing the vibration transfer path is developed. The analysis method efficiently decreases the disturbance range of the path's contribution. The disturbance ranges of the path transmissibility and the contribution rate are efficiently reduced by considering the two types of correlations. This reduction is significant for the optimization function with respect to the results.
- (3) The simulation results indicate that when the effect of the spiral case and substructure is ignored, the influence on the disturbance range continually increases as the correlation coefficient increases in the hydropower station model. The optimization function of the correlations between parameters is too important to be neglected when calculating the disturbance range.
- (4) In conclusion, the analysis of the proposed model shows that the effect of the water turbine head cover

is not evident in the vertical vibration transfer, but its transfer efficiency is significant.

The analysis of vibration transfer paths of hydropower station units and powerhouses is complicated. Based on the complex disturbances and parameters, the contribution of each transfer path can be calculated by analyzing the sensitivity of the transfer force and the transmissibility of the vibration model in the frequency domain. This study provides a reference for future comprehensive research on the transfer paths of hydropower station units and powerhouses.

Acknowledgment

This research was sponsored by the National Natural Science Foundation of China (51079020).

References

- [1] Z. Y. Ma and Y. X. Dong, *Dynamics of Water Turbine Generator Set*, Dalian University of Technology Press, Dalian, China, 1st edition, 2003.
- [2] Z. Y. Ma and Y. X. Dong, *Vibration and Its Corrective Actions of Water Turbine Generator Set and Power House*, China Water Power Press, Beijing, China, 1st edition, 2004.
- [3] B. N. Singh, D. Yadav, and N. G. R. Iyengar, "Natural frequencies of composite plates with random material properties using higher-order shear deformation theory," *International Journal of Mechanical Sciences*, vol. 43, no. 10, pp. 2193–2214, 2001.
- [4] T. D. Popescu, "Detection and diagnosis of model parameter and noise variance changes with application in seismic signal processing," *Mechanical Systems and Signal Processing*, vol. 25, no. 5, pp. 1598–1616, 2011.
- [5] J. D. Kaplunov, E. V. Nolde, and B. F. Shorr, "A perturbation approach for evaluating natural frequencies of moderately thick elliptic plates," *Journal of Sound and Vibration*, vol. 281, no. 3–5, pp. 905–919, 2005.
- [6] M. Kamiński, "Least squares stochastic boundary element method," *Engineering Analysis with Boundary Elements*, vol. 35, no. 5, pp. 776–784, 2011.
- [7] M. Madani, M. Fathizadeh, Y. Khan, and A. Yildirim, "On the coupling of the homotopy perturbation method and Laplace transformation," *Mathematical and Computer Modelling*, vol. 53, no. 9–10, pp. 1937–1945, 2011.
- [8] J. D. Collins and W. T. Thompson, "Eigenvalue problem for structural systems with statistical properties," *AIAA Journal*, vol. 7, no. 4, pp. 642–648, 1969.
- [9] T. Hisada and S. Nakagiri, "Stochastic finite element analysis of uncertain structural systems," in *Proceedings of the 4th International Conference in Australia on Finite Element Methods in Engineering*, pp. 133–137, 1982.
- [10] W. K. Liu, G. Bestefield, and T. Belytschko, "Vibrational approach to probabilistic finite elements," *Journal of Engineering Mechanics-ASCE*, vol. 114, no. 12, pp. 2115–2133, 1988.
- [11] W. J. Vetter, "Matrix calculus operations and Taylor expansions," *SIAM Review*, vol. 15, pp. 352–369, 1973.
- [12] H. Poincare, *New Methods of Celestial Mechanics, Also History of Modern Physics and Astronomy*, Washington, DC, USA, 1st edition, 1960.

- [13] E. A. Frieman, "On a new method in the theory of irreversible processes," *Journal of Mathematical Physics*, vol. 4, pp. 410–418, 1963.
- [14] A. H. Nayfeh, "A perturbation method for treating nonlinear oscillation problems," vol. 44, pp. 368–374, 1965.
- [15] N. Krylov and N. N. Bogoliubov, *Introduction to Nonlinear Mechanics*, Princeton University Press, Princeton, NJ, USA, 1st edition, 1947.
- [16] N. N. Bogoliubov and Y. A. Mitropolsky, *Asymptotic Methods in the Theory of Nonlinear Oscillations*, Gordon and Breach Science, New York, NY, USA, 1st edition, 1961.
- [17] S. Kaplun, *Fluid Mechanics and Singular Perturbations*, P. A. Lagerstrom, L. N. Howard and Ching-shi Liu, Eds., Academic Press, New York, NY, USA, 1st edition, 1967.
- [18] H. S. Tsien, "The Poincare-Lighthill-Kuo method," *Advances in Applied Mechanics*, vol. 4, pp. 281–293, 1956.
- [19] S. Abbasbandy, "The application of homotopy analysis method to nonlinear equations arising in heat transfer," *Physics Letters A*, vol. 360, no. 1, pp. 109–113, 2006.
- [20] Y. Zhang, S. Chen, Q. Liu, and T. Liu, "Stochastic perturbation finite elements," *Computers and Structures*, vol. 59, no. 3, pp. 425–429, 1996.
- [21] Y. M. Zhang, "Frequency domain transfer degree of vibration transmission path ordering," *Progress in Natural Science*, vol. 17, no. 3, pp. 410–414, 2007.
- [22] Y. M. Zhang, Q. Liu, and B. Wen, "Practical reliability-based design of gear pairs," *Mechanism and Machine Theory*, vol. 38, no. 12, pp. 1363–1370, 2003.
- [23] Y. M. Zhang and Z. Yang, "Reliability-based sensitivity analysis of vehicle components with non-normal distribution parameters," *International Journal of Automotive Technology*, vol. 10, no. 2, pp. 181–194, 2009.
- [24] W. Zhao and Y.-M. Zhang, "Response of vibration transfer path systems with uncertain paths," *Journal of Vibration and Shock*, vol. 28, no. 2, pp. 99–101, 2009.
- [25] W. Gao, "Interval natural frequency and mode shape analysis for truss structures with interval parameters," *Finite Elements in Analysis and Design*, vol. 42, no. 6, pp. 471–477, 2006.
- [26] W. Gao, "Natural frequency and mode shape analysis of structures with uncertainty," *Mechanical Systems and Signal Processing*, vol. 21, no. 1, pp. 24–39, 2007.
- [27] W. Gao, J. J. Chen, T. B. Hu, N. J. Kessissoglou, and R. B. Randall, "Optimization of active vibration control for random intelligent truss structures under non-stationary random excitation," *Structural Engineering and Mechanics*, vol. 18, no. 2, pp. 137–150, 2004.
- [28] J. Ma, J. J. Chen, W. Gao, and Y. Y. Zhao, "Stationary random response analysis of linear fuzzy truss," *Structural Engineering and Mechanics*, vol. 22, no. 4, pp. 469–481, 2006.
- [29] J. Ma, J.-J. Chen, W. Gao, and T.-S. Zhai, "Non-stationary stochastic vibration analysis of fuzzy truss system," *Mechanical Systems and Signal Processing*, vol. 20, no. 8, pp. 1853–1866, 2006.
- [30] J. Ma, W. Gao, P. Wriggers, T. Wu, and S. Sahraee, "The analyses of dynamic response and reliability of fuzzy-random truss under stationary stochastic excitation," *Computational Mechanics*, vol. 45, no. 5, pp. 443–455, 2010.
- [31] H. Shinzawa, T. Genkawa, and W. Kanematsu, "Pressure-induced association of oleic acid (OA) under varying temperature studied by multiple-perturbation two-dimensional (2D) IR correlation spectroscopy," *Journal of Molecular Structure*, vol. 1028, pp. 164–169, 2012.
- [32] B. Allés, A. Buonanno, and G. Cella, "Perturbation theory predictions and Monte Carlo simulations for the 2D $O(n)$ non-linear σ -models," *Nuclear Physics B*, vol. 500, no. 1–3, pp. 513–543, 1997.
- [33] C. J. Butte, Y. Zhang, H. Song, and J. J. Jiang, "Perturbation and nonlinear dynamic analysis of different singing styles," *Journal of Voice*, vol. 23, no. 6, pp. 647–652, 2009.
- [34] L. Chai, A. J. Sprecher, Y. Zhang, Y. Liang, H. Chen, and J. J. Jiang, "Perturbation and nonlinear dynamic analysis of adult male smokers," *Journal of Voice*, vol. 25, no. 3, pp. 342–347, 2011.
- [35] A. Pirrotta, "Non-linear systems under delta correlated processes handled by perturbation theory," *Probabilistic Engineering Mechanics*, vol. 13, no. 4, pp. 283–290, 1998.
- [36] E. G. D'Ambrogio, "The dynamics of complex stochastic models evolution of a correlation function with random fluctuations," *Mathematical and Computer Modelling*, vol. 28, no. 3, pp. 15–20, 1998.
- [37] N. A. Husain, H. H. Khodaparast, and H. Ouyang, "Parameter selection and stochastic model updating using perturbation methods with parameter weighting matrix assignment," *Mechanical Systems and Signal Processing*, vol. 32, pp. 135–152, 2012.
- [38] H. H. Khodaparast, J. E. Mottershead, and M. I. Friswell, "Perturbation methods for the estimation of parameter variability in stochastic model updating," *Mechanical Systems and Signal Processing*, vol. 22, no. 8, pp. 1751–1773, 2008.
- [39] W. Gao, C. Song, and F. Tin-Loi, "Probabilistic interval response and reliability analysis of structures with a mixture of random and interval properties," *Computer Modeling in Engineering & Sciences*, vol. 46, no. 2, pp. 151–189, 2009.
- [40] B. Arazi, "Some properties of Hadamard matrices generated recursively by Kronecker products," *Linear Algebra and its Applications*, vol. 25, pp. 27–39, 1979.
- [41] D. H. Zhao, Y. X. Dong, and Z. Y. Ma, "Static and dynamic analysis for concrete supporting structure of turbine unit," *Hydroelectric Energy Science*, vol. 18, no. 4, pp. 68–71, 2000.
- [42] R. Cardinali, R. Nordmann, and A. Sperber, "Dynamic simulation of non-linear models of hydroelectric machinery," *Mechanical Systems and Signal Processing*, vol. 7, no. 1, pp. 29–44, 1993.